The Investigation of $Ti_3C_2T_x$ MXene Surface Chemistry for Electrochemical Energy Storage

am

Fachbereich Physik

der Freien Universität Berlin

eingereichte Dissertation

zur Erlangung des akademischen Grades

des Doktors der Naturwissenschaften (Dr. rer. nat.)

vorgelegt von

Ameer Al-Temimy

Berlin, Deutschland

July 2022

Erstgutachter   **Zweitgutachter**

Dr. Tristan Petit[x]   Prof. Dr. Klaus Lips[#]

[x]Nachwuchsgruppenleiter Nanoskalige Fest-Flüssig-Grenzflächen, Helmholtz-Zentrum Berlin für Materialien und Energie GmbH (HZB), Deutschland.

[#]Leiter der Abteilung Spins in der Energieumwandlung und Quanteninformatik und Professor des Fachbereichs Physik, Freie Universität Berlin, Deutschland.

The date of defense: 12.09.2023

DEDICATIONS

To the people that I see the world through, my beloved wife Massarah and to my lovely children Yusif and my own 2D daughters Maryam & Marua

To my dear mother who constantly motivated me to be a better person with extremely high standards and father who is the source of constant support

There are many people who pushed me further and further scientifically throughout my life: especially Mr. Masood Abo, Prof. Dr. Sabah Jumaa, Prof. Dr. Ulrich Starke, Dr. Camilla Coletti, and Prof. Dr. Klaus von Klitzing

To DAAD & Germany
I am grateful for the opportunity given to me by the DAAD and I feel super lucky to pursue my postgraduate studies at the great German scientific institutions

Acknowledgments

CONTENTS

Abstract

Electrochemical energy storage devices, such as batteries and supercapacitors, play a pivotal role not only for the increasing demand on renewable energy storage but also for the growing electric vehicles industry. In this context, surface redox (pseudocapacitive) active materials have shown a remarkable increase in both energy and power densities. Titanium carbide $Ti_3C_2T_x$ MXene is an efficient pseudocapacitive 2D material combining high metallic conductivity with hydrophilic surfaces. The $Ti_3C_2T_x$ reveals large capacitance by using sulfuric acid as an electrolyte owing to the surface redox charging mechanism. The electrochemical performance of $Ti_3C_2T_x$ MXene is significantly influenced by interlayer spacing between MXene nanosheets which is altered by the amount of the nanoconfined water and/or intercalants. In this work, X-ray-based techniques were used to study the impact of the MXene surface chemistry as well as its interlayer spacing on its overall electrochemical performance.

$Ti_3C_2T_x$ MXene were investigated using synchrotron-based soft X-ray absorption spectroscopy (XAS) and X-ray photoemission electron microscopy (XPEEM). The XAS peaks are very sensitive to changes in the local chemical environment induced by different types of intercalants and the nanoconfined water between the MXene layers. The oxidation state of the surface Ti atoms in $Ti_3C_2T_x$ has been then extensively investigated as it constitutes a key element in the electrochemical performance. Here we show that the intercalation of organic molecules, like urea, as well as mono- and multi-valent cations such as Li^+, Na^+, K^+, and Mg^{2+} affects the Ti oxidation state in different environments. We show that a controlled higher oxidation state increases the MXene capacitance. In addition, spatially resolved XA spectra were implemented to study the Ti oxidation state of pristine and intercalated single multi-layered $Ti_3C_2T_x$ flakes. On the other hand, the interlayer spacing between $Ti_3C_2T_x$ nanosheets was monitored by X-ray diffraction (XRD). *In situ* XRD patterns taken at different temperatures revealed for the first time the signature of the nanoconfined water in MXene at low temperatures, which shows the coexistence of hexagonal and cubic ice structures.

This work illustrates the significance of the X-ray-based techniques to probe the electronic structure of transition metal oxide surfaces and the nanoconfined water of MXenes in various environments. It paves the way to *operando* XAS combined with electrochemical performance (cyclic voltammogram) which would help to identify the changes in chemical bonds during a redox reaction.

Zusammenfassung

Elektrochemische Energiespeicher, wie Batterien oder Superkondensatoren, spielen eine entscheidende Rolle in Zeiten steigendender Nachfrage an Speichern für erneuerbare Energien, sowie bei der Weiterentwicklung der Elektromobilität. Innerhalb dieses Rahmens konnte die Energie- und Leistungsdichte oberflächenaktiver Materialien, welche fähig sind zu reversiblen Redoxreaktionen (Pseudokapazität), bemerkenswert gesteigert werden. Ein effizientes, pseudokapazitives, zweidimensionales Material stellt Titancarbid in der Form $Ti_3C_2T_x$ MXene dar. Es kombiniert eine hohe metallische Leitfähigkeit mit hydrophilen Oberflächen. Das $Ti_3C_2T_x$ offenbart eine hohe elektrische Kapazität unter Verwendung von Schwefelsäure und aufgrund seiner redox-aktiven Oberfläche. Das elektrochemische Verhalten von $Ti_3C_2T_x$ MXene wird dabei maßgeblich vom Schichtabstand zwischen den einzelnen MXene-Nanosheets beeinflusst. Dieser wird geformt durch Interkalationen und/ oder Wassereinschlüsse. In dieser Arbeit wurde der Einfluss von Oberflächenbeschaffenheit und Schichtabstand auf das allgemeine elektrochemische Verhalten mittels Röntgenspektroskopie studiert.

Um das $Ti_3C_2T_x$ MXene zu untersuchen, wurde die auf Synchrotronstrahlung basierende Röntgenabsorptionsspektroskopie (XAS) sowie die Photoemissionselektronenmikroskopie (XPEEM) verwendet. Die Röntgenabsorption spitze ist sensitiv auf die Änderung der lokalen chemischen Umgebung, hervorgerufen durch verschiedenartige Interkalationen sowie Wassereinschlüsse zwischen den einzelnen MXene-Schichten. Der Oxidationszustand der Ti-Atome an der Oberfläche wurde ausgiebig untersucht und stellt ein Schlüsselelement in der elektrochemischen Funktion dar. Es wird gezeigt, dass der Einschluss organischer Moleküle, wie Harnstoff, ebenso wie einfach und mehrfach geladener Kationen, wie Li^+, Na^+, K^+ und Mg^{2+} die Oxidationsstufe des Ti beeinflussen können. Dabei wurde festgestellt, dass eine höhere Oxidation die Kapazität steigert. Zusätzlich wurde räumlich aufgelöste Röntgenabsorption angewandt um den Zustand des Ti in unveränderten $Ti_3C_2T_x$ Spänen mit dem interkalierter und mehrfachgeschichteter $Ti_3C_2T_x$ Späne zu vergleichen. Die Schichtabstände wurden zusätzlich mittels Röntgenbeugung (XRD) analysiert. Von besonderer Bedeutung ist dabei die Tatsache, *in situ* Röntgenbeugung dass zum Ersten Mal die Signatur von eingeschlossenem Wasser bei niedrigen Temperaturen aufgezeichnet werden konnte, zeigt die koexistenz von hexagonalen und kubischen Eisstrukturen.

Die vorliegende Arbeit zeigt auf, von welcher Bedeutung die Verwendung röntgenbasierter Methoden für die Untersuchung der elektronischen Struktur von übergangsmetalloxidischen Oberflächen und Wassereinschlüssen im MXene in verschiedenen Umgebungen ist. Damit ist der Weg bereitet für operando XAS kombiniert mit elektrochemischer Leistung (cyclic Voltammogram), die helfen würde, die Veränderungen chemischer Bindungen während einer Redoxreaktion zu identifizieren.

CHAPTER ONE

Introduction

1. Introduction

Electrochemical energy storage (EES) devices such as batteries and supercapacitors have witnessed a dramatic demand especially over the last decade. Efficient batteries and/or supercapacitors have become extremely important for the growing industry of the electric vehicle and portable electronic devices. Owing to their outstanding features, such as electrical conductivity and large surface area, two dimensional (2D) materials could play a crucial role in the performance of EES devices. Recently, a large family of 2D materials called MXenes were reported to be promising and efficient materials to boost up the electrochemical performance to large extent. MXenes have a great potential to store energy electrochemically owing to its surface chemistry that can be relatively easy to modify, resulting in a significant alteration in its oxidation state.

1.1 Electrochemical Energy Storage Systems

The energy storage sector has witnessed a growing attention by scientists and policymakers to overcome not only the environmental impacts induced by fossil fuels but also to enhance the capacity and resilience of a national energy grid [1,2]. The EES is a technique where the charges are stored in a chemical form where the loss in energy is limited due to the high conversion efficiency from electrical to chemical energy form and vice versa. The high efficiency of the EES constitutes a cornerstone in the development of clean energy reliable technologies. There are two main fundamental routes for storing electrochemical energy [3]: (i) Through a faradic process involving the oxidation and reduction of electrochemically active surface electrodes, allowing then charges to flow between electrodes through an electrolyte as found in batteries. (ii) Electrostatically at the interface between the electrode and electrolyte as exemplified by supercapacitors. **Figure 1.1**, known as Ragone plot, shows the power and energy densities trade-offs of different energy storage devices. The energy density scale describes how much energy can be stored. The power density scale, on the other hand, represents how quickly the device can be charged and discharged. In batteries, the energy is electrochemically stored but the time required for charging is considered long for a practical use, see **table 1.1**. **Figure 1.1** shows different types of batteries [4] that possess high energy density of about few hundreds of $Whkg^{-1}$, explaining the predominance of this type of EES devices in the market.
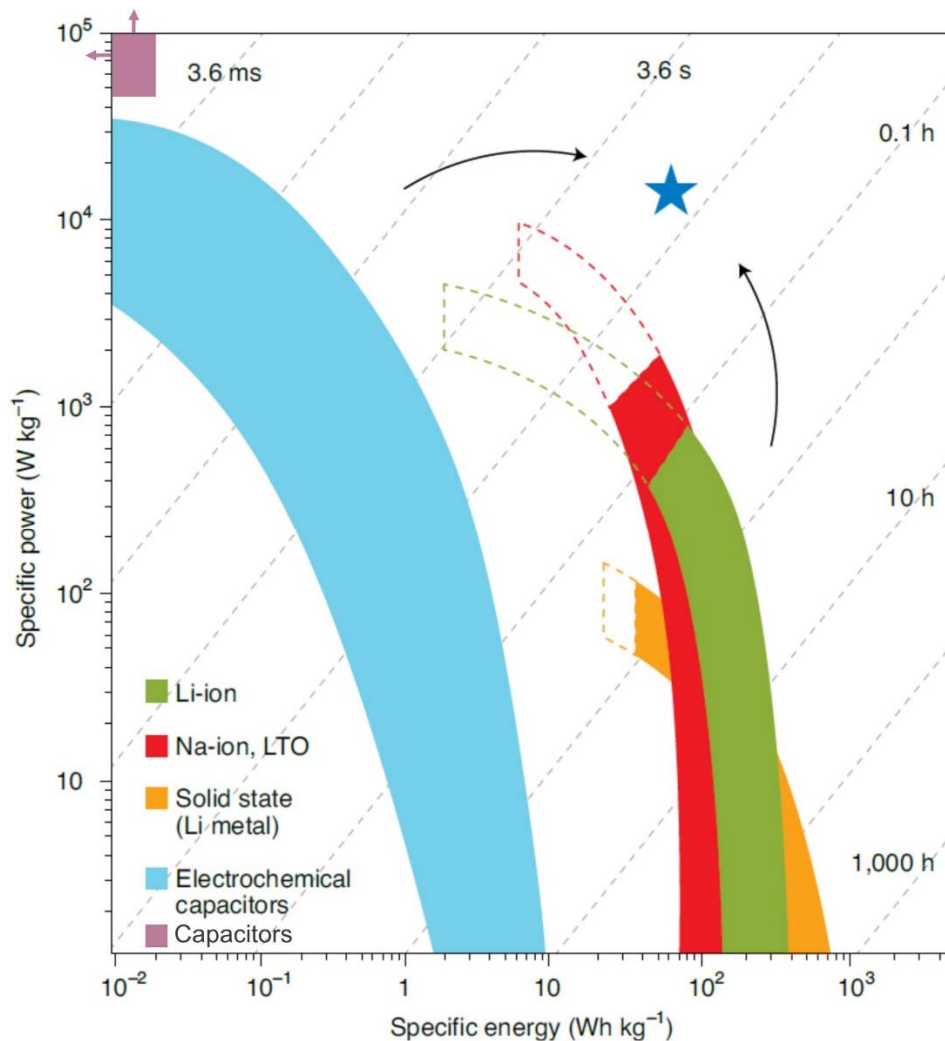
Figure 1.1 Ragone plot demonstrates the energy and power densities of capacitors (purple), electrochemical capacitors (light blue), and different types of batteries (green, red, and orange). The time frame of how fast an EES device can be charged (single charge) is shown as well. The goal is to extend energy and power density regions diagonally as indicated by the blue star which can be obtained via pseudocapacitive active materials, resulting in higher specific energy devices that can be quickly charged. LTO stands for lithium titanium oxide ($Li_4Ti_5O_{12}$). Reproduced with permission from Ref. [5], copyright 2020.

In contrast, supercapacitors, also known as electrochemical capacitors (ECs), store relatively less amount of energy but can be released in a matter of a sub-second. Depending on the storage mechanism, supercapacitors can be divided into electric double layer capacitors (EDLCs) and pseudo-capacitors. In EDLCs, the energy is stored close to the electrode-electrolyte interface, leading to a limited energy density [3]. However, in pseudo-capacitors the energy stored not only near the electrode-electrolyte interface but also via fast surface redox (oxidation and reduction) reactions and intercalation of cations within the electrodes as explained in further details in section 1.2. As a result, a pseudo-capacitor ensures more

3

charges to be stored and short time for charging and discharging, signifying greater power density and cyclability relative to Li-ion batteries (LIB), see **Table 1.1**.

Table 1.1 Typical characteristics of capacitors, EDLCs/ pseudocapacitors, and Li-ion batteries [6].

Function	Capacitors	EDLCs/ Pseudocapacitors	Li$^+$ batteries
Charge time	10^{-3} to 10^{-6} s	1 to 10 s	10 to 60 min
Cycle life	>1,000,000	> 1,000,000/ < 100,000	< 1,500
Storage Mechanism	Electrostatic	Electrostatic/ +Chemical	Chemical
Charge stored	Between charged electrodes	Electrode-electrolyte interface/+ Ion intercalation	Entire electrode
Cell voltage	High	< 3 V	3.6 to 3.7 V
Specific energy (Wh/Kg)	< 0.1	1 to 10	100 to 250
Specific power (kW/Kg)	> 10	0.5 to 20	1 to 3
Efficiency	> 95 %	85 to 95 %	70 to 85 %
Operation Temperature	-40 to 65 °C	-40 to 65 °C	-20 to 45 °C

Therefore, efficient pseudo-capacitive materials are indispensable for the development of energy storage systems with long cycle life and short time for charging and discharging like EDLCs, with battery-like energy density features. The combination of high energy and power densities fulfils the goal mentioned in **Figure 1.1** and will ensure new technologies for energy storage-based applications.

1.2 Electrochemical Charge Storage Mechanisms

A comprehensive understanding of the various charge storage mechanisms is paramount to the development of electrochemical energy storage devices with simultaneous high power and energy densities. Although batteries and supercapacitors are constructed almost similar to each other, however, the energy storage mechanism is significantly different. A battery is an EES device that basically stores chemical energy and converts it into electrical energy via chemical bonds transformation (electrochemical redox reactions). The electrochemical redox

reactions in a battery cell result in a flow of electrons from the negative electrode to the positive one. However, the capacity of rechargeable batteries mainly depends on the diffusion-limited faradaic reactions (charge transfer). Also, intercalation and de-intercalation within the structure of the electrode plays a vital role in charging and discharging cycles, respectively [7,8]. As a result, this slow redox process is translated into a low power density. Since electrochemical redox reactions are taking place in the bulk materials of the electrode, the energy storage mechanism in batteries is accompanied by a phase transformation. On the other hand, the capacity of supercapacitors is via reversible ion adsorption at the surface or in pores, as illustrated in **Figure 1.2 A** and **B**. As no diffusion within the electrode or diffusion-limited faradaic redox reactions are taking place, this route of storage is characterized by rapid charging and discharging within only few minutes, leading to high power density.
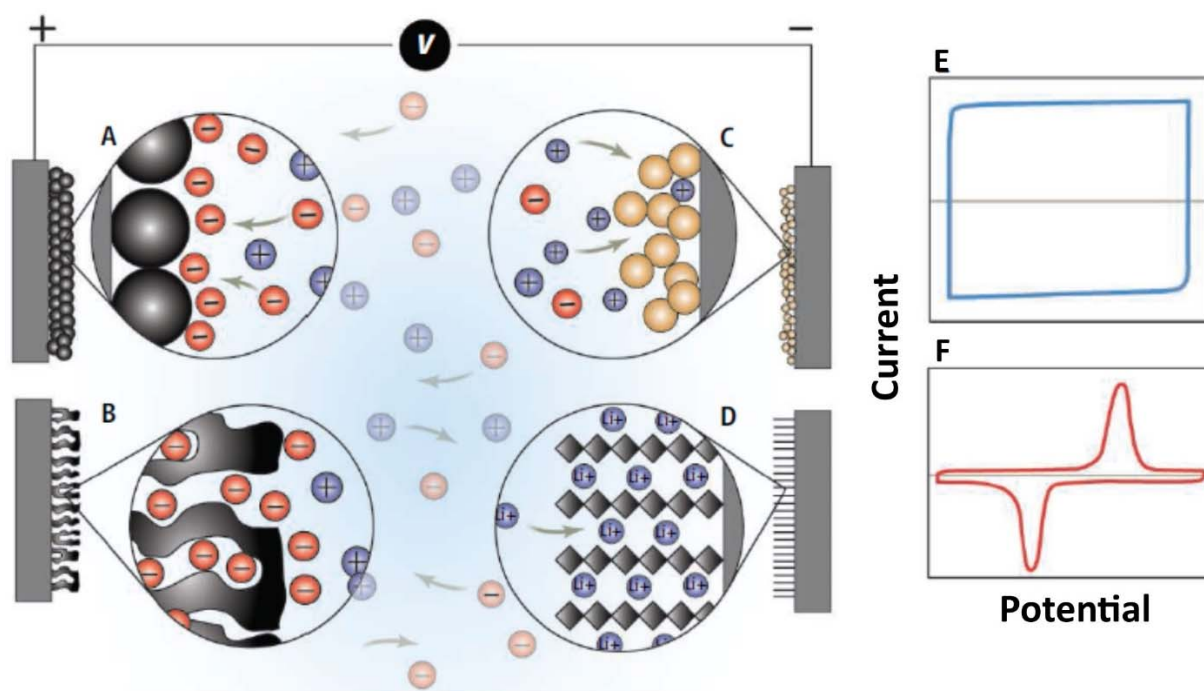
Figure 1.2 Summary of different charge storage mechanisms in supercapacitor- and battery-like materials. In a supercapacitor, the electrodes are constructed from (A) carbon particles or (B) porous carbon, demonstrating negative ions adsorption from the electrolyte on a positively charged electrodes. In pseudocapacitors, the redox pseudocapacitance reaction is illustrated in (C) in hydrous RuO_2 whereas the intercalation pseudocapacitance is shown in (D) where the Li ions are inserted into layers of crystalline structure of electrode materials, like Nb_2O_5. Panels E and F demonstrate typical cyclic voltammogram profiles of supercapacitor and battery electrodes, respectively. Taken and reproduced with permission from Ref. [9], copyright 2014.

Interestingly, a pseudocapacitive material exceeds features of those used in supercapacitors and exhibits faradaic redox reactions at or near the electrode surface which triggers higher

energy density compared to traditional supercapacitors. The significantly faster kinetics of redox reactions distinguishes pseudocapacitive materials from conventional LIB. Therefore, the charge storage mechanism in pceudocapacitive materials can be subdivided into two types: First, surface redox pseudocapacitance where the charge mechanism is assigned to charge transfer taking place at or near the surface of the electrode material (short diffusion) by means of electrochemical ions adsorption, see **panel C of Figure 1.2**. Second, in the intercalation pseudocapacitance, the ions diffuse quickly in and out between the interlayer structures of an electrode material which does not suffer any phase change, as shown in **panel D of Figure 1.2**. The energy storage mechanisms of ECs, also known as pseudocapacitors, are not only demonstrated by materials of inherent pseudocapacitive features but could also be activated via necessary material modifications and/or engineering [10]. The rectangular shape in **Figure 1.2 E** represents a typical cyclic voltammogram (CV) of a conventional supercapacitor where the current exhibits a constant behavior in response to a linear change in the potential. The CV in battery-based materials, however, demonstrates characteristic faradaic peaks, as shown in **Figure 1.2 F**. In this context, the pseudocapacitive nanomaterials are of a great importance for EES devices owing to their performance of high power and energy densities.

1.3 Nanomaterial-based Electrodes

Wide range of nanomaterials can be used for electrode construction in EES devices, however, only those with extraordinary properties in favor of electrochemical storage performance draw the scientific community attention in order to enhance the amount of energy storage within a relatively short time [11,12]. In typical LIB, LiFePO4, Si, LiCoO$_2$, etc., nanoparticles (NPs) with different chemical compositions have revealed a significant enhancement in power density as well as cycling (high scan rate) owing to the short diffusion distances of Li ions within the electrode material [7,13,14]. On the other hand, in EDLCs the carbon onions, exhibit unique zero-dimensional (0D) spherical structures of few nm in diameter, have demonstrated a superior power density performance [15]. Furthermore, due to the flexibility in electrode formation without the need to use any further additives and/or binder, the high aspect ratio of the one-dimensional (1D) nanostructures such as nanotubes and nanowires makes them attractive to be utilized in EES devices [14,16]. It is noteworthy that additives such as carbon nanotubes are widely used in battery electrodes to lower its resistance and moderate the

Ohmic losses (voltage drop due to internal resistance), resulting in a better rate performance [17].

Besides nanoparticles, mesoporous nanomaterials are highly relevant. The high surface area of mesoporous nanomaterials is of great importance in EES materials. In addition, the mesoporosity feature ensures high capacitance and cycling due to the high diffusion of the electrolyte ions throughout the structure of the electrode material. For instance, ordered mesoporous channels in carbide-derived carbon demonstrate a dramatic electrochemical enhancement of about 170 F/g in non-aqueous electrolyte due to the high surface area and the very fast ionic transport [18]. Materials with intrinsic pseudocapacitive behavior, including but not limited to hydrous RuO_2 [19], MnO_2 [20], and Nb_2O_5 [21] have the capability to store considerable amount of energy in a short charging time. The pseudocapacitance performance in Nb_2O_5 demonstrates a specific capacitance of about 400 F/g in non-aqueous electrolyte [22] whereas it was found very high of about 720 F/g in hydrous RuO_2 when an aqueous electrolyte is used, namely, sulfuric acid (H_2SO_4) [19]. Therefore, pseudocapacitive transition metal oxides constitute a promising path capable to improve the electrochemical storage performance. However, transition metal oxides lack in general high electronic conductivity, leading to limit power density and the high cost and low abundance of Ru would hinder large-scale applications. To overcome this difficulty, developing 2D materials with inherent redox active surface sites and high conductivity stimulates further improvement in the electrochemical performance. Interestingly, a new class of 2D materials known as MXenes demonstrate a significant pseudocapacitive electrochemical performance, as discussed in section 1.4.

1.4 MXenes

MXenes are a new class of 2D nanomaterials consisting of few atoms thick layers of transition metal carbides, nitrides, or carbonitrides, discovered at Drexel University in 2011 [23]. MXenes are currently attracting a great attention due to the wide range of possible applications in general and the electrochemical performance in particular for EES. The titanium carbide Ti_3C_2 MXene, a representative member of the large MXenes family and currently the most investigated one, is being applied for many interesting applications such as electromagnetic interference shielding [24], water purification and desalination [25], urea sorption which promises a path toward an artificial kidney [26] and EES devices [27–34]. The large family of

MXene can have at least three different types $M_{n+1}X_n$ (n=1, 2, 3) in terms of the number of the transition metal layers (M) relative to the carbon and/or nitrogen atomic layer (X) such as Ti_2C, Ti_3C_2, and Ti_4N_3 MXenes, see **Figure 1.3**. The representative member $Ti_3C_2T_x$ MXene, where T_x stands for various surface terminations mainly –OH, –O–, and –F, has demonstrated high electrical conductivity up to 10000 S cm^{-1} [35] thanks to the conductive carbide core which facilitates very fast electron access to the surface redox active sites, enabling fully charged device within few seconds. This conductivity is coupled with highly hydrophilic surface nature which renders MXene surfaces electrochemically active. Interestingly, nano-trapped water is found to reside between the $Ti_3C_2T_x$ MXene nanosheets and is strongly hydrogen bonded to –OH/–O– terminations [36,37]. Since the oxygen-containing terminations react to chemical changes, the surface chemistry of $Ti_3C_2T_x$ MXene can be tuned in favor of EES performance.

M₂X — Mono-transition metal MXenes · Solid solution MXenes · Ordered double-transition metal (M) MXenes · Ordered divacancy MXenes

M₃X₂ — Mono-transition metal MXenes · Solid solution MXenes · Ordered double-transition metal (M) MXenes · Ordered divacancy MXenes (N/A)

M₄X₃ — Mono-transition metal MXenes · Solid solution MXenes · Ordered double-transition metal (M) MXenes · Ordered divacancy MXenes (N/A)

M₂X				M₃X₂				M₄X₃			
Sc₂C	Ti₂C	Ti₂N	Zr₂C	Ti₃C₂	Ti₃N₂	Ti₃(CN)	Zr₃C₂	Ti₄N₃	V₄C₃	Nb₄C₃	Ta₄C₃
Zr₂N	Hf₂C	Hf₂N	V₂C	(Ti,V)₃C₂	(Ti₂Nb)C₂	(Ti₂Ta)C₂	(Ti₂Mn)C₂	(Ti,Nb)₄C₃	(Nb,Zr)₄C₃	(Ti₂Nb₂)C₃	(Ti₂Ta₂)C₃
V₂N	Nb₂C	Ta₂C	Cr₂C	Hf₃C₂	(Hf₂V)C₂	(Hf₂Mn)C₂	(V₂Ti)C₂	(V₂Ti₂)C₃	(V₂Nb₂)C₃	(V₂Ta₂)C₃	(Nb₂Ta₂)C₃
Cr₂N	Mo₂C	Mo₁.₃C	Cr₁.₃C	(Cr₂Ti)C₂	(Cr₂V)C₂	(Cr₂Nb)C₂	(Cr₂Ta)C₂	(Cr₂Ti₂)C₃	(Cr₂V₂)C₃	(Cr₂Nb₂)C₃	(Cr₂Ta₂)C₃
(Ti,V)₂C	(Ti,Nb)₂C	W₂C	W₁.₃C	(Mo₂Sc)C₂	(Mo₂Ti)C₂	(Mo₂Zr)C₂	(Mo₂Hf)C₂	(Mo₂Ti₂)C₃	(Mo₂Zr₂)C₃	(Mo₂Hf₂)C₃	(Mo₂V₂)C₃
Mo₂N	Nb₁.₃C	Mo₁.₃Y₀.₆C		(Mo₂V)C₂	(Mo₂Nb)C₂	(Mo₂Ta)C₂	(W₂Ti)C₂	(Mo₂Nb₂)C₃	(Mo₂Ta₂)C₃	(W₂Ti₂)C₃	(W₂Zr₂)C₃
				(W₂Zr)C₂	(W₂Hf)C₂			(W₂Hf₂)C₃			

M: Sc, Y, Ti, Zr, Hf, V, Nb, Ta, Cr, Mo, W, Mn
X: C, N

Legend: Theoretical · Experimental · Solid solution double-M · Ordered double-M · Ordered divacancy

Figure 1.3 The large family of various MXenes is illustrated following the $M_{n+1}X_n$ (n= 1-3) formula, where M represents the transition metal layers and X denotes the carbides and/or nitrides. So far, in addition to experimentally demonstrated (cyan), some of the MXenes are predicted to exist theoretically (grey). To date, there are mainly four types: mono-M element such as Ti_2C, Nb_2C, solid-solution M elements such as $(Ti,V)_3C_2$, $(Cr,V)_3C_2$, and ordered double-M elements such as Mo_2TiC_2 and $Mo_2Ti_2C_3$, and ordered divacancy MXenes such as $Cr_{1.3}C$ and $Mo_{1.3}C$. N/A is not available. Reproduced with permission from Ref. [33] [32]. Copyright 2017 Springer Nature.

1.5 Synthesis of MXenes

Ten years after the discovery of MXenes, different procedures have been adopted to synthesize the $Ti_3C_2T_x$ MXene. Irrespective of the applied procedure, the synthesis mainly requires a selective etching of MXene precursor which is an atomic layered structure known as the MAX phase. Like MXenes, the MAX phase can also be found in different types following the formula $M_{n+1}AX_n$ where A, which links the MXene nanosheets, represents atoms from group 13 and 14 elements of the periodic table, typically Aluminum (Al) [38]. Another study by the Gogotsi group at Drexel University has reported that MXene can be produced via high temperature etching of the MAX phase in a certain environment. For instance, $Ti_4N_3T_x$ MXene was synthesized by etching the Al layer from Ti_4AlN_3 powder using a molten salt at 550 °C under an argon (Ar) atmosphere [39]. It is noteworthy that MXenes can also be synthesized starting from non-MAX phase precursors such as Mo_2CT_x MXene from Mo_2Ga_2C by etching the two Ga layers or the $Zr_3C_2T_x$ MXene from $Zr_3Al_3C_5$ structure by etching Aluminum carbide (Al_3C_3) instead of only Al layer [40–42]. Depending on which synthesis route is adopted, the surface chemistry of MXene is dramatically altered, leading to significant changes in MXene properties. In general, aqueous acidic solutions were applied for the aim of selective etching of the Al layer to produce the $Ti_3C_2T_x$ MXene, which can then be intercalated with various compounds as shown in **Figure 1.4**.
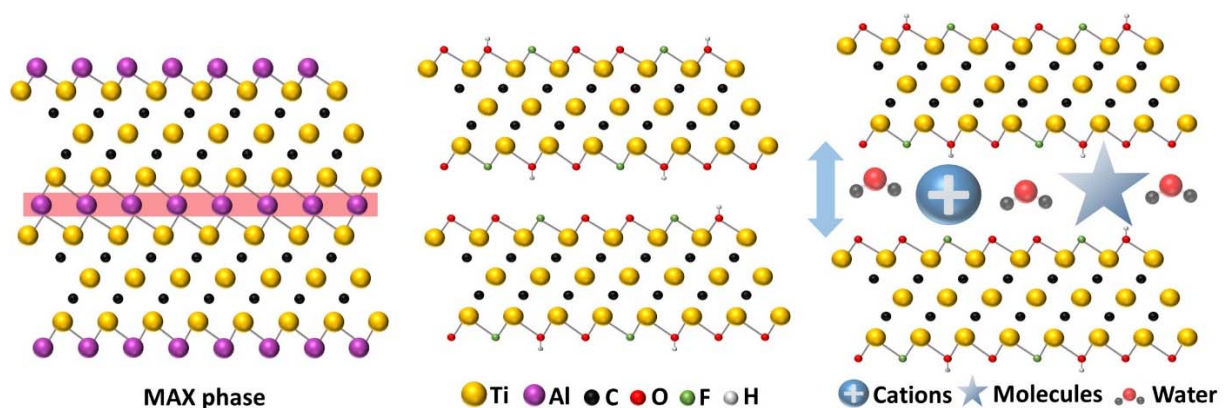
Figure 1.4 Schematic illustration of the $Ti_3C_2T_x$ MXene synthesis from its $Ti_3AlC_2T_x$ layered precursor: Left) the precursor is known as MAX phase which is treated by acids in order to remove the Al layer, this results in middle) selective etching and formation of single or multi-layered $Ti_3C_2T_x$ MXenes. Right) shows delamination of MXenes nanosheet flakes by intercalation of different types of cations or molecules, leading to a great expansion in the interlayer spacing between the MXene nanosheets.

Currently, there are three main methods used to synthesize MXenes: (i) hydrofluoric acid (HF), (ii) HF and lithium chloride (LiCl), and (iii) a mixture of lithium fluoride (LiF) and hydrochloric acid (HCl) [28,43]. The (i) and (ii) methods result in multi-layered $Ti_3C_2T_x$ MXene particles while the third one (iii) results in free-standing $Ti_3C_2T_x$ MXene films. The details of these procedures will be explained in section 2.5. It is noteworthy that these different synthesis procedures result in a dramatic change in the MXene surface chemistry. For example, the –F terminations are significantly reduced in favor of other terminations when the LiF+HCl etching procedure is applied compared to the only HF etching method [44]. Less –F surface terminations result in an increase in the amount of the nanoconfined water that resides between MXene nanosheets [44]. A detailed insight about the nanoconfined water is presented in section 6.2. The surface chemistry along with the nanoconfined water are known to drastically impact a wide range of $Ti_3C_2T_x$ MXenes properties including the electrochemical energy storage performance [32]. As the MXene surface chemistry can be tuned in solvent, changing the environments of MXene is likely to play a vital role in the enhancement of MXene electrochemical performance.

1.5.1 Surface Modifications of $Ti_3C_2T_x$ MXenes

In MXenes, the modification in surface chemistry changes many properties of this 2D material such as electrical conductivity and electrochemical performance. For instance, intercalation and/or environment of MXene, which can be part of the various synthesis procedures of MXene, impact its surface chemistry, implying an alteration in the electronic structure of the surface Ti atoms. MXenes can be intercalated both chemically and electrochemically by various types of polar organic molecules, such as urea and dimethyl sulfoxide (DMSO) or large organic base molecules like tetrabutylammonium hydroxide (TBAOH) [31,45,46]. In addition, wide range of mono and/or multivalent metal cations such as Li^+, Na^+, K^+, Mg^{2+}, and Al^{3+} can also be intercalated between MXene nanosheets, signifying the high flexibility of MXenes [28]. The intercalation process does not only impact the MXene surface chemistry but also acts as a pillar that opens further the galleries between the $Ti_3C_2T_x$ nanosheets, as shown in **Figure 1.4**. Upon intercalation and/or changing environment, the interlayer spacing distance between $Ti_3C_2T_x$ layers was found to be intercalant-dependent and also influences the amount of the nanoconfined water [47], suggesting a great impact on the MXene surface chemistry too. The expansion in the interlayer spacing results in more co-intercalated water which

weakens the interaction between the MXene nanosheet layers. It is noteworthy that sonication of the intercalated MXenes in water leads to a colloidal solution of single and/or multi-layer MXenes that do not demand surfactants for stabilization, indicating an advantage for device printing and coating/films manufacturing [32]. The negative zeta potential nature of MXene flakes leads to electrostatic stability, preventing aggregation of MXenes in colloidal solutions. The colloidal solution of MXene has a great potential for printing technology [48,49], which facilitates the control of the thickness of MXene-based electrodes.

1.5.2 Chemical Treatment of Ti$_3$C$_2$T$_x$ MXenes

Several routes can be followed to modify the surface of MXene, e.g., using ionic compound treatment where the Ti$_3$C$_2$T$_x$ MXenes can be chemically treated in various aqueous solutions such as potassium hydroxide (KOH), potassium acetate (KOAc), and cesium hydroxide (CsOH) [32,50]. Also, treating Ti$_3$C$_2$T$_x$ MXenes with hydrazine monohydrate (HM) would result in modifications in the surface chemistry of MXenes [37]. As –F surface terminations dramatically hinders the electronic structure of the surface Ti atoms, annealing MXene above 500 °C would result in de-functionalization of the –F termination [51]. Furthermore, a recent study has reported a fluorine-free Ti$_3$C$_2$T$_x$ MXene synthesis procedure via alkali treatment [52]. As aqueous solutions (used in this work) were applied to synthesize Ti$_3$C$_2$T$_x$ MXenes from the MAX phase, the concentration of HF is found to have a great impact. In this context, 50% HF would result in a higher percentage of –F terminations and less –OH/–O– terminations relative to the 10% HF concentration [36]. This means that lower HF concentration would result in a higher ratio of oxygen-containing terminations relative to fluorine ones. Any further post-synthesis treatment, delamination, etching, and even storage conditions can modify the surface terminations of MXenes [36]. Besides, metal vacancies are also observed in Ti$_3$C$_2$T$_x$ MXenes and proportionally rely on the concentration of the HF acid [53]. Since the MXene surface terminations are of great importance, the various procedures applied to synthesize Ti$_3$C$_2$T$_x$ MXenes will be discussed in detail in section 2.5.
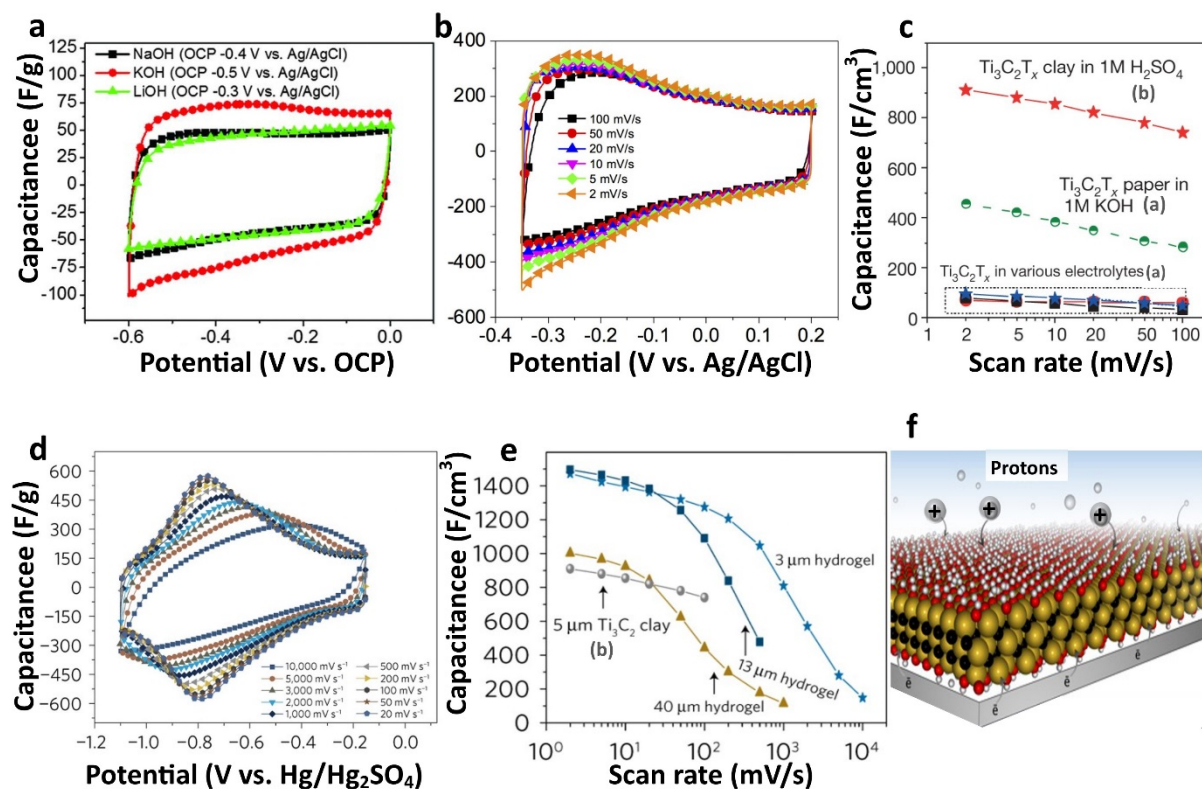
1.6 Electrochemical Performance of MXene

The pseudocapacitors have witnessed great attention by the energy materials community since they offer a great potential to store and deliver high amount of electrical energy [3]. In pseudocapacitive materials, such as MXenes, the electrochemical performance mainly

depends on redox reaction that occurs on the surface of MXene electrodes and intercalation between MXene layers while cycling. The $Ti_3C_2T_x$ MXenes reveal a salient electrochemical performance in a diverse set of aqueous-based electrolyte solutions. In **Figure 1.5 a**, the CVs of the multi-layered $Ti_3C_2T_x$ MXenes (HF only etching method) have demonstrated enhanced gravimetric specific capacitance (C_m) to about tens of farads per gram in alkali-containing hydroxides such as NaOH, KOH, and LiOH aqueous basic electrolytes [28]. For instance, the capacitance of MXene in KOH was found to be about 70 F/g at low scan rate (2 mV/s). The observed CVs are of typical rectangular shape, showing an electric double layer (EDL) capacitive behavior during cycling in these standard electrolyte solutions.

To shed light on the impact of the interlayer spacing and thickness of the multi-layered $Ti_3C_2T_x$ particles, the paper-like MXene electrodes, prepared by delamination with DMSO that shows a large interlayer spacing and few-layer thick $Ti_3C_2T_x$ flakes, were investigated [28]. Accordingly, the C_m was found to increase almost twice to ~130 F/g at low scan rate (2 mV/s) in KOH electrolyte [28], indicating that more K^+ ions were intercalated owing to the resulted larger spacing between the MXene layers that eventually results in better electrochemical performance, see **Figure 1.5 a**.

In transition metal oxide-based electrodes, acidic electrolytes are of great advantages due to their high conductivity as well as the protons small size that trigger a considerable capacitance owing to the fast surface redox reactions [3]. Therefore, the freestanding $Ti_3C_2T_x$ film-based electrode (LiF+HCl method) in 1M H_2SO_4 electrolyte at 2 mV/s scan rate discloses a remarkable gravimetric and volumetric capacitance of 245 F/g and up to 900 F/cm^3 with excellent cyclability and rate performances as shown in **Figure 1.5 b, c** , respectively [43]. On the other hand, controlling the porosity of the $Ti_3C_2T_x$ electrodes enhances further the electrochemical performance of MXene's pseudocapacitance. Indeed, **Figure 1.5 d** shows that a 13 µm thick macroporous $Ti_3C_2T_x$ electrode in 3M H_2SO_4 electrolyte reveals exceptional gravimetric and volumetric capacitances of about 310 F/g and 1500 F/cm^3, respectively [54]. This volumetric capacitance reaches even the previously unmatched volumetric performance of the costly RuO_2 material. In addition, **Figure 1.5 e** shows a comparison between $Ti_3C_2T_x$ electrodes of different thicknesses in terms of volumetric capacitance. The electrochemical performance of MXene was found thickness-dependent [43,54]. The investigation of a 90 nm thick $Ti_3C_2T_x$ electrode in 3M H_2SO_4 unveils capacitance up to 450 F/g with extraordinary rate performance

[54]. **Figure 1.5 f** illustrates the pseudocapacitance mechanism of $Ti_3C_2T_x$ MXene electrode in H_2SO_4 electrolyte which drives the highest capacitance shown in **Figure 1.5 c**.


Figure 1.5 Electrochemical performance of differently prepared $Ti_3C_2T_x$ MXene electrodes in various types of electrolytes. (a) CV profiles of HF-only prepared MXene in basic electrolytes, namely, LiOH, NaOH, and KOH, NaOH at 20 mV/s. (b) CV profiles of LiF+HCl prepared MXene in 1M H_2SO_4 demonstrate a good rate performance up to 100 mV/s with 82% retention. (c) Comparison of the rate performances in terms of the volumetric capacitance in basic and acidic electrolytes. (d) CV profiles of 13 μm thick macroporous $Ti_3C_2T_x$ electrode in 3M H_2SO_4 uncover exceptional capacity performance even at potential of 10000 mV/s with ~70% retention. (e) Rate performances of different MXene thickness electrodes in terms of the volumetric capacitance in 3M H_2SO_4 compared to the MXene electrode described in b. (f) A representation image, taken from Ref. [55], highlights the redox reaction at the $Ti_3C_2T_x$ surfaces via bonding and debonding process of hydrogen protons, changing MXene surface chemistry. In panel (f), the atoms in metallic gold, black, red, and white stand for titanium, carbon, oxygen, and hydrogen. Also, for clarity, the size of protons were magnified to highlight the bonding/debonding process on MXene surface. Reproduced with permission from Ref. [28,43,54]. Copyright 2013, 2014, and 2017.

To shed light on the pseudocapacitance mechanism, the hydrated protons (H^+) in H_2SO_4 electrolyte are very important as bonded with the MXene oxygen surface terminations when the $Ti_3C_2T_x$ electrode is negatively charged. While at a positively charged $Ti_3C_2T_x$ electrode, the H^+ are decoupled. This bonding/debonding process of H^+ drives a proton-coupled electron transfer between surface Ti and O-containing terminations in $Ti_3C_2T_x$ MXene, suggesting a

reversible change in the oxidation state of MXene surface Ti atoms. The electrochemical redox reaction at the $Ti_3C_2T_x$ MXene surfaces can be described with the following formula:

$$Ti_3C_2O_x\ (OH)_y\ F_{2-x-y} + \delta \bar{e} + \delta H^+ \rightarrow Ti_3C_2O_{x-\delta}\ (OH)_{y+\delta}\ F_{2-x-y}$$
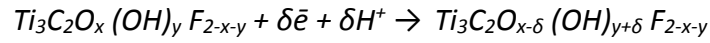
where δ is the number of electrons taking part in this redox reaction, which is found to be 0.3 owing to the fact that every Ti atom in $Ti_3C_2T_x$ MXene shares 0.1 electron [34]. Lukatskaya *et al.* have shown in a study [34], which used XAS at the Ti K-edge (see section 2.2.2), that the electrochemical voltage window used for $Ti_3C_2T_x$ MXene in 1M H_2SO_4 ranges from -0.35 V to less than +0.4 V versus silver-silver chloride (Ag/AgCl) reference electrode. This applied voltage range of -0.35 V to +0.4 V is crucial as it is considered to be a safe voltage region to fulfill a reversible change of the Ti oxidation state. Therefore, owing to the limited voltage window ~1.0 V of MXenes in aqueous electrolytes, organic or ionic liquid electrolytes were also investigated [56–58]. An extended voltage window enhances the amount of the stored energy as well as the cycle life in EES applications. Using an organic or ionic electrolyte results in a wide voltage window up to 3.0 V, however, non-aqueous electrolytes suffer poor conductivity due to the big size of ions, affecting eventually the intercalation process during cycling.

Over the last few years, the MXene electrochemical behavior was investigated to further enhance the energy storage capability along with excellent rate performance. In this context, *in situ* X-ray diffraction (XRD) [28], X-ray absorption spectroscopy (XAS) [34], nuclear magnetic resonance (NMR) [44], and Raman [59] techniques were applied to deeply understand the impact of cations intercalation, electrolytes, and synthesis procedures on the redox process and Ti oxidation state of MXene while cycling. Owing to the significant role of the charge transfer between the surface Ti and O atoms during the redox processes in $Ti_3C_2T_x$ MXene, *in situ* XAS at the Ti K-edge [34] was employed to probe the bonding/debonding impact on the Ti oxidation state. Also, by using density functional theory (DFT), a theoretical study of the $Ti_3C_2T_x$ MXene unveils its redox process in H_2SO_4 electrolyte [60]. Therefore, the impacts of flake/particle thickness, intercalation, and electrolyte on the Ti oxidation state have become extremely important to better understand the exceptional electrochemical performance of $Ti_3C_2T_x$ MXene electrodes.

1.7 Motivation

The key elements in enhancing the electrochemical energy storage performance of $Ti_3C_2T_x$ MXenes are the surface chemistry, interlayer spacing (intercalation and nanoconfined water), and flakes/particles thickness. These key elements are tightly connected in MXenes and are known to dramatically affect the oxidation state of the surface Ti atoms, demanding deep understanding and advanced characterizations sensitive to the Ti electronic structure. Understanding thoroughly the impact of the aforementioned key elements would help to guide us toward higher electrochemical performance.

XAS, see details in section 2.2, is a very sensitive technique to changes in the electronic structure of a sample. The electronic transitions from core-level to unoccupied states can be probed by XAS, enabling to measure the electronic and chemical environment of an absorbing atom. The XAS sensitivity at the Ti L-and O K-edges was employed to investigate the oxidation state of the surface Ti atoms, changes in surface chemical bonds, and nanoconfined water in $Ti_3C_2T_x$ MXenes. In order to have a comprehensive understanding about the nature of the chemical bonds at different environments, different cation intercalated MXenes dispersed in water and sulfuric acid were investigated by XAS. To monitor the changes in Ti chemical bonds, *ex situ*, *in situ*, and *operando* XAS approaches were employed to carefully assign the oxidation state of the surface Ti atoms. In particular, since $Ti_3C_2T_x$ electrodes in H_2SO_4 electrolyte results in a high capacitance, *ex situ* and *in situ* XAS measurements were performed. As constitute a main building block in MXene electrodes, single flakes/particles of mono- and multi-layered $Ti_3C_2T_x$ MXene were investigated. Furthermore, *in situ* spatially resolved XAS measurements at low temperatures were conducted to monitor the impact of nanoconfined water on the Ti electronic structure. In parallel, the change in $Ti_3C_2T_x$ MXene structure was studied by XRD technique, which allows to measure the interlayer spacing between MXene nanosheets.

To this aim, as soft X-ray photons are needed to investigate the Ti L-and O K-edges, the *ex situ* and *in situ* XAS measurements presented in this work were carried out at the LiXEdrom and SPEEM beamline end-stations operated by BESSY II synchrotron facility. The post-synthesis sample preparation processing for XAS and XRD measurements were conducted in the chemistry lab at the Energy Materials *In situ* Laboratory Berlin (EMIL). In this work, special

attention was given to correlate the X-ray based findings of Ti$_3$C$_2$T$_x$ MXenes with their electrochemical performance. The structure of this PhD dissertation is briefly outlined below:

Chapter Two addresses the fundamental principles of the different X-ray based techniques used to obtain information about the Ti oxidation state and nature of the local chemical bonds of pristine and intercalated MXenes in different environments. The experimental methodologies used to conduct *ex situ*, *in situ*, and *operando* measurements will be explained.

Chapter Three shows the impact of urea intercalation between multi-layered Ti$_3$C$_2$T$_x$ MXene layers in terms of the surface chemistry, Ti oxidation state in different environments, and the electrochemical performance. Furthermore, using a spatially resolved XAS technique allows for mapping the oxidation state of a single multi-layered Ti$_3$C$_2$T$_x$ flake before and after urea intercalation. The work presented in this chapter was performed in close collaboration with Prof. Gogotsi and all of the MXene samples were synthesized by his group at Drexel University in Philadelphia, USA.

Chapter Four presents a comprehensive study about the impact of the intercalation of various metal cations such as Li$^+$, Na$^+$, K$^+$, and Mg^{2+} on the MXene surface chemistry. It shows that the Ti oxidation state is cation-dependent. This work reveals for the first time *ex situ* and *in situ* XA spectra of MXene in H$_2$SO$_4$ environment and *operando* measurements at the Ti L-edge of different cation-intercalated multi-layered Ti$_3$C$_2$T$_x$ MXenes biased at a negative potential. Furthermore, this chapter shows the impact of the H$_2$SO$_4$ environment on the MXene interlayer spacing. The MXene samples were synthesized by Naguib group at Tulane University in New Orleans, USA.

Chapter Five demonstrates the impact of the thickness of multi-layered Ti$_3$C$_2$T$_x$ MXenes on the Ti oxidation state by using spatially resolved XAS. The latter is extremely important as individual multi-layered MXene particles are the building blocks for electrode manufacturing, which influence the overall electrochemical performance of MXene electrodes. Indeed, the Ti oxidation state in pristine, Li-, and Mg-intercalated Ti$_3$C$_2$T$_x$ was found to be thickness-dependent, while Na- and K-intercalated Ti$_3$C$_2$T$_x$ particles did not reveal differences upon changing the particle thickness. The MXene samples were synthesized by Naguib group at Tulane University in New Orleans, USA.

Chapter Six focuses on the impact of MXene nanoconfined water on the surface chemistry and interlayer spacing at different temperatures. This chapter discloses a change in MXene surface chemistry driven by the inherent nanoconfined water that resides between the $Ti_3C_2T_x$ layers, as manifested by spatially resolved XA spectra at the O K- and Ti L-edges. Interestingly, upon freezing the nanoconfined water in MXene, *in situ* XRD technique at low temperature unveils diffraction patterns of cubic and hexagonal ice structures. Also, the interlayer spacing between the $Ti_3C_2T_x$ nanosheets was dramatically increased at low temperatures and does not restore its initial value measured at room temperature (RT). The changes in the interlayer spacing lead to a great impact on the electrochemical performance of $Ti_3C_2T_x$ MXene electrodes. The MXene samples were synthesized by the Gogotsi group at Drexel University in Philadelphia, USA.

Chapter Seven presents conclusions of what has been done in this PhD work and gives an outlook for further studies.

CHAPTER TWO

Experimental Methods

2.1 Introduction

As previously mentioned in chapter one, advanced techniques are urgently needed in the characterization of $Ti_3C_2T_x$ MXene in different environments. One of which needs to be focused on is the Ti oxidation state which offers a pathway to enhance the MXene electrochemical performance as well as to understand the pseudocapacitance mechanism. In this context, XAS technique fits very well owing to its sensitivity to changes in local chemical bonds of nanostructure and 2D materials in/under different environments/conditions. The use of synchrotron facility is required to offer soft X-ray (100-1000 eV) with high brilliance, high photon flux, and tunable energy, allowing to select an energy range of interest [61]. The X-ray spectroscopy and microscopy techniques available at BESSY II synchrotron facility were used to investigate different MXenes samples. In this PhD dissertation, the presented data were conducted at the LiXEdrom and SPEEM end-stations. Moreover, other characterization techniques were also used to investigate MXenes, which are detailed in section 2.4.

2.2 X-ray Absorption Spectroscopy (XAS)

XAS [27,34,62] is an element-selective and site-specific spectroscopic technique that is sensitive to the surface chemistry of metal oxide materials in different environments. In particular, the characterization of transition metal L-edges is very sensitive to the metal chemical environment and has been used to distinguish various Ti oxide species [63,64]. The XAS-based experiments are best performed at a synchrotron facility where the tunable and brilliant X-ray light can be provided. In this work, owing to its sensitivity of Ti L-edge and O K-edge, soft X-ray range was utilized in order to investigate the Ti L-edge and O K-edge to highlight the impact of different environments on the surface chemistry, Ti oxidation state, and the nature of local chemical bonds in $Ti_3C_2T_x$ MXenes.

2.2.1 XAS Principle

In general, as soft X-ray light interacts with matter, the incident photon energy of the X-ray decreases due to a transfer of energy to atoms. This leads to the absorption of X-ray photon by a core-level electron which is then excited to an unoccupied level, such as the conduction band, of a material of interest. This is known as X-ray absorption process which is detected by XAS technique. To emphasize this process, upon energy absorption of an incident X-ray photon of few hundreds of eVs, the core-level electrons can be excited to an unoccupied state, leaving

a hole behind as can be seen in **Figure 2.1 a**. If the energy of the incident X-ray light is equal to an absorption resonance, this leads to the so-called absorption edge of a chemical element desired to be investigated, see section 2.2.2. This means it is the energy difference between the initial and the final states.
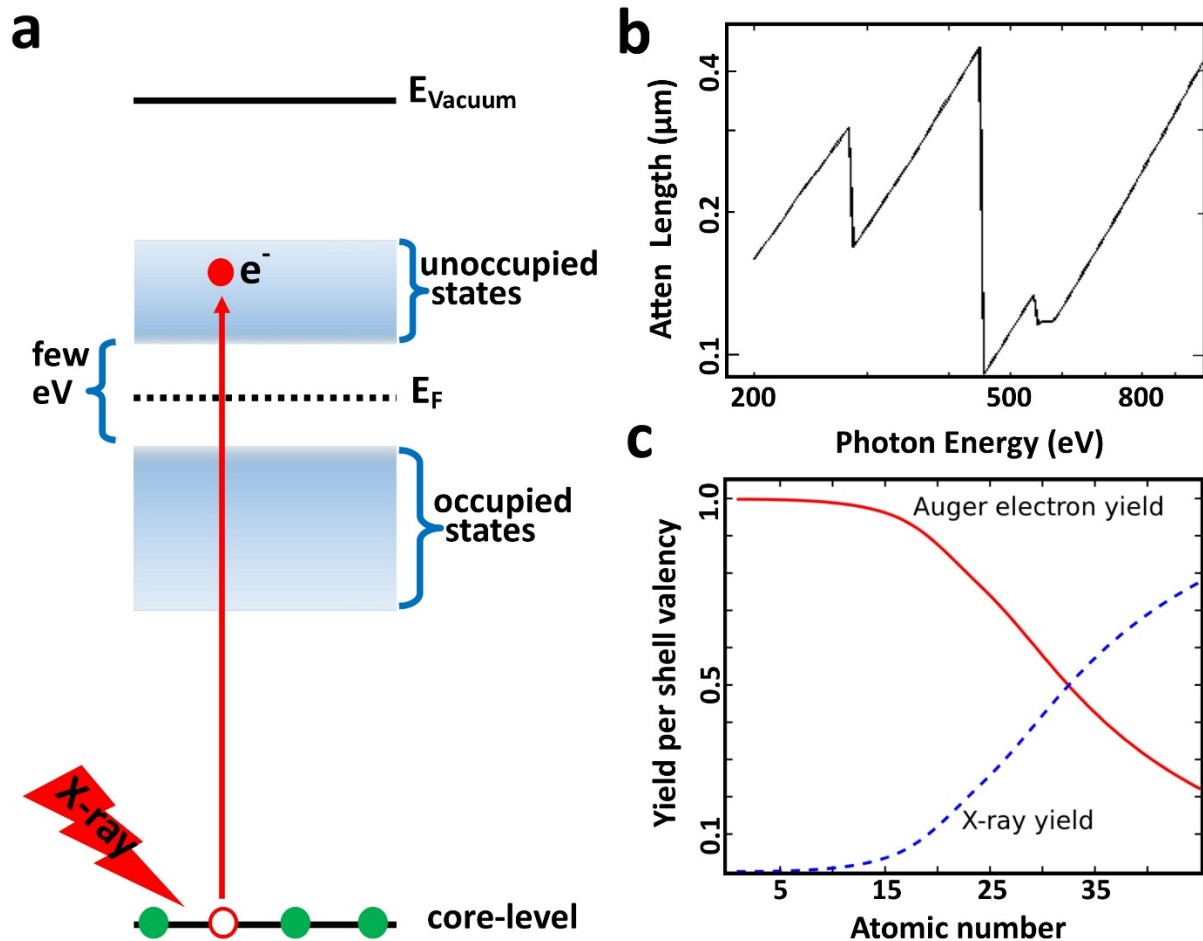
Figure 2.1 X-ray absorption spectroscopy principle. (a) An illustration of X-ray light absorption by a core-level electron that is excited to an unoccupied state above Fermi energy level (E_F). (b) The attenuation length of X-ray light for $Ti_3C_2O_2$ MXene as a function of the incident photon energy at fixed angle of 90° and density of 4.54 g/cm^3, calculated using Ref. [65]. (c) Auger electron vs. X-ray fluorescence yields as a function of the atomic number of a material of interest, taken from Ref. [66].

On the other hand, the concept of the absorption of X-ray light is to measure the difference in intensity between incident and transmitted light owing to the attenuation coefficient of a material of interest. Thus, XAS in transmission mode is a direct approach to measure the X-ray absorption (XA) spectra. However, in the soft X-ray range the light will be completely attenuated within only a sub-micrometer of a material as shown in **Figure 2.1 b**. Hence, the transmitted intensity will be extremely weak and thus will be difficult to detect. Therefore, by

using soft X-ray range, the measurement in transmission mode is only possible for very thin samples.

This leads to find another approach to record the XA spectra. The created core-hole shown in **Figure 2.1 a** by the X-ray absorption process will be then filled with an outer shell electron, releasing energy transferred to either an Auger electron (electron yield) or released through a photon (fluorescence yield). Detecting either yields of electrons or photons would quantify the absorption cross section. The percentage of these two yields strongly relies on the atomic number of a material of interest, as can be seen in **Figure 2.1 c**. For small atomic number, the electron yield is then predominant relative to X-ray fluorescence yield and vice versa.

In this context, if an electron is emitted, the XAS data will be recorded by electron yield (EY) detection mode. The EY detection mode is widely employed to characterize solid samples with soft X-ray range. As the soft X-ray incident photon energy is small, electrons at and/or near the surface remove the material, signifying a positive charge sample. Thus, the drain current of the sample to ground will be detected by a Keithley (electrically connected to a copper stage attached to the manipulator), recording the XA spectra with total electron yield (TEY) detection mode. The XAS measurements in TEY mode are recorded via the integration of the emitted photoelectrons as a function of X-ray energies. Owing to the low free mean path of the photoelectrons (see section 2.2.3), the TEY detection mode is a surface sensitive technique [67]. The typical probing depth of TEY mode is in the range of 10 nm [68–70]. By using an electron energy analyzer, XA spectra can be recorded from the secondary photoelectrons in partial electron yield (PEY) detection mode. In PEY, electrons experience energy-based discrimination as in SPEEM end-station where spatially resolved images can be also acquired, explained in section 2.2.3. The PEY is even more surface sensitive detection mode with a probing depth up to 10 nm [71]. Therefore, the EY detection mode is not able to probe the bulk properties of a material. In this dissertation, the dried samples of pristine, urea-, Li-, Na-, K-, and Mg-intercalated $Ti_3C_2T_x$ MXenes were characterized by XAS in TEY and PEY detection modes. The results were published [72–74] and presented in chapters three to six.

Alternatively, the electron decay to fill the core-hole is going to emit light (fluorescence) that can be detected by either a photodiode or an energy dispersive detector (see section 2.2.3). In this case, the XAS data will be recorded in fluorescence yield (FY) mode. If the light is

detected integrally by a photodiode, the XA spectra will be recorded by total fluorescence yield (TFY) detection mode which probes a depth of about 200 nm [75,76], indicating a bulk sensitive mode. The TFY detection mode was used for XAS measurements of samples dispersed in water when the light is emitted through an X-ray transparent membrane and is detected by a photodiode positioned very close to the membrane window, as shown in Figure 2.3. On the other hand, if the emitted fluorescence light is discriminated by an energy dispersive detector, the XAS data are recorded in partial fluorescence yield (PFY) mode. The PFY detection mode requires either a monochromator that covers the range of the X-ray fluorescence or an energy sensitive detector, see section 2.2.3. The PFY detection mode was used for XAS measurements of MXene samples exposed to sulfuric acid with and without applied potential.

2.2.2 XAS Measurements of Titanium Oxides

Figure 2.2 a shows, as an example, the absorption edge of Ti chemical element (Ti L-edge) of various titanium oxide species, offering valuable information about the difference in the corresponding local chemical environment. One of which is that the pre-edge onset energy position feature of the XA spectra shifts to lower energies (highlighted by a solid yellow line in **Figure 2.2 a**) as going from titanium dioxide (TiO_2) to titanium monoxide (TiO), since the oxidation state of titanium changes from Ti^{4+} to Ti^{2+}, respectively. This demonstrates the sensitivity of XA spectra at the Ti L-edge to changes in the Ti electronic structure, indicating its usefulness to investigate the Ti oxidation state in $Ti_3C_2T_x$ MXenes. In $Ti_3C_2T_x$ MXenes, the electronic structure of the Ti atoms are expected to alter upon changes in the surface chemistry and surface terminations. Also, XAS at the Ti K-edge is known to be sensitive to changes in the Ti oxidation state of Ti^{4+} relative to Ti^{2+} [34] as shown in **Figure 2.2 b**. However, as MXene is the material of interest, an experimental study has shown that even at biased potential the XA spectra at Ti K-edge of $Ti_3C_2T_x$ are almost identical (see **Figure 2.2 b**) [34], indicating that the Ti L-edge on the other hand is more sensitive to valence electrons of t_{2g} and e_g orbitals that are involved in the Ti–O chemical bonds as detailed in the following. Therefore, the Ti L-edge XA spectra of different titanium oxide species, shown in **Figure 2.2 a** can be used as a guide to identify the chemical nature of the Ti atoms in $Ti_3C_2T_x$ MXenes. As the Ti oxidation state of the Ti atoms in $Ti_3C_2T_x$ samples is a key element in enhancing the

electrochemical performance, a deep understanding of the mutual Ti and O chemical bonds is essential, suggesting XAS measurements at the Ti L- and O K-edges.
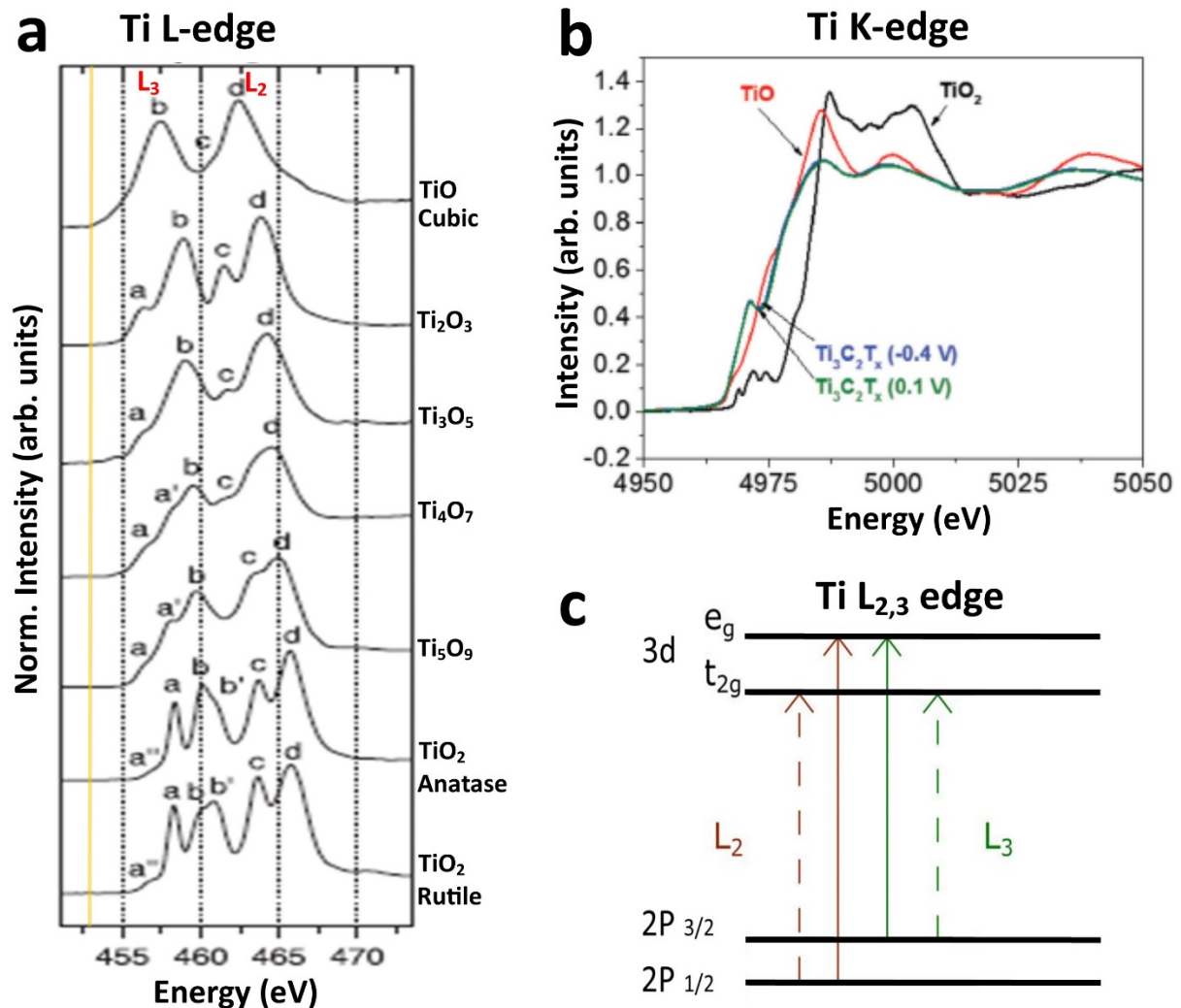
Figure 2.2 X-ray absorption spectra. (a) Experimentally measured Ti L-edge of different oxide species reveal high sensitivity to even small changes in the Ti valence state, taken and modified from Ref. [63], copyright 2007. (b) Ti K-edge spectra of TiO_2 and TiO compared to $Ti_3C_2T_x$ MXene in 1M sulfuric acid at biased potential of -0.4 V and 0.1 V, blue and green respectively. Reproduced with permission from Ref. [34]. (c) Schematic of the X-ray absorption transitions in TiO_2 material.

What determines the Ti L-edge profile in oxides? The Ti L-edge is related to transitions from Ti $2P_{3/2}$ and Ti $2P_{1/2}$ core levels to an unoccupied Ti 3d state and are denoted L_3 and L_2 absorption edges, respectively. The energy range of the Ti $L_{3,2}$ edges is between ~453.0 and 475.0 eV. Owing to the ligand field caused by binding with oxygen atoms, the $L_{3,2}$ absorption edges are each split into two sub-bands. These two bands are related to electronic states with t_{2g} and e_g symmetries, shown in **Figure 2.2 c**. The $L_{3,2}$ absorption edges of 3d transition metals contain

local chemical information, one of which is the valence state. Therefore, the $L_{3,2}$ edges reflect the covalent bonding states that originated from strong interactions between titanium and oxygen atoms. A crucial feature is that the e_g band is very sensitive to the local chemical environment due to the interaction between Ti e_g orbitals and 2p orbitals of the neighboring/surrounding oxygen atoms [77,78]. For example, the TiO_2 XAS profile splits into t_{2g} and e_g sub peaks, leading to four absorption peaks. On the contrary, TiO exhibits only two peaks which indicates no further split in the $L_{3,2}$ absorption edges (see **Figure 2.2 a**). This difference between TiO and TiO_2 XA profiles is due to the presence of two electrons on the $2t_{2g}$ level of TiO which leads to screen the created core hole [77,78], preventing further transitions. On the other hand, as no electrons existed on the $2t_{2g}$ level for TiO_2, very poor screening allows for more transitions to take place, leading eventually to four absorption lines as can be seen in **Figure 2.2 c**. As a result, significant differences can be observed in TiO_2 relative to the TiO in terms of their XA spectra signatures such as: (i) Pre-edge onset energy position is shifted to lower energies in TiO compared to TiO_2 materials. (ii) Four and two absorption lines in TiO_2 and TiO, respectively.

On the other hand, the O K-edge XA spectra of Ti oxide samples show mainly transitions between oxygen 1s and 2p states hybridized with the unoccupied Ti 3d orbitals with t_{2g} and e_g symmetries in the energy range 529.0-535.0 eV [63,78]. The O K-edge spectra exhibit a second set of absorption bands in the energy region 537.0-546.0 eV, which are assigned to transitions from O 2p states hybridized with Ti 4s and 4p states [63,78].

2.2.3 XAS End-Stations

In this PhD work, two end-stations were used in order to carry out the XAS characterization of $Ti_3C_2T_x$ MXenes. These end-stations are LiXEdrom and SPEEM that are connected to the U49-2_PGM1 and UE-49-PGMA beamlines of BESSY II synchrotron light source, respectively. The full technical details of these end-stations and the beamlines can be found in Ref. [79–82].

The LiXEdrom can be used to investigate the material in different environments such as dried, dispersed in liquid, and also during electrochemical reactions in electrolyte. The LiXEdrom end-station is equipped with different manipulators, one of which ends with a copper plate to ensure a conductive stage at which solid/dried samples can be placed. The XA spectra of solid/dried samples are recorded in TEY detection mode, as explained earlier in section 2.2.1.

The operating pressure in the main chamber of LiXEdrom is about 10^{-6} mbar in order to avoid attenuation of the soft X-ray light. As the main chamber is under vacuum conditions, the XAS study of liquid samples is a challenge. To overcome this difficulty, a flow cell, attached to another manipulator, is equipped with X-ray transparent silicon nitride (Si_3N_4) membrane window to separate the liquid from the necessary vacuum conditions [83].
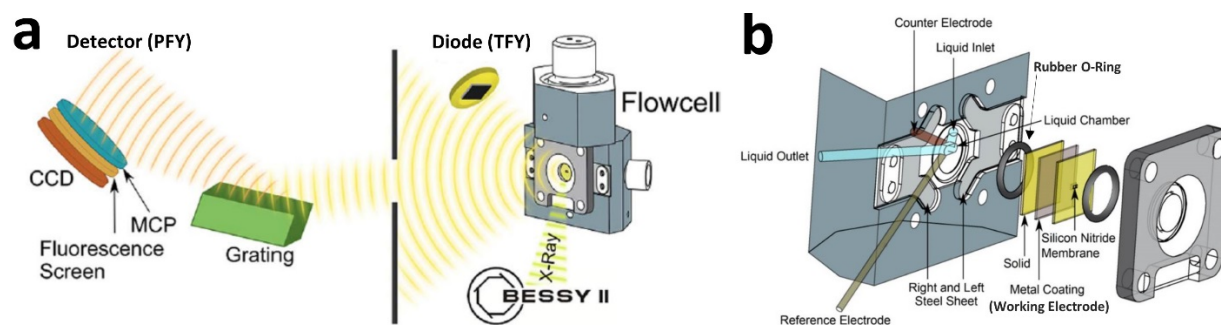

Figure 2.3 XAS study in liquid environment. (a) Scheme of energy dispersive XAS experiment where a Si_3N_4-based membrane flow-cell is used to study MXene liquid/dispersed samples and *in situ* XAS electrochemical reaction. The emitted fluorescence light passes through the membrane reaching either a photodiode or an energy analyzer detector if a specific energy range of interest needs to be discriminated. In both cases, the XA data will be recorded in FY detection mode. An energy analyzer consists of stack of micro-channel plates (MCP), a phosphorous screen, and a charge coupled device (CCD). (b) Detailed view of the electrochemical cell shows that the membrane is metal coated (gold) to ensure a good conductivity and serves as a working electrode. A counter and reference electrodes are placed inside the liquid chamber within the flow cell. Reproduced with permission from Ref. [83], copyright 2014.

Figure 2.3 a shows an electrochemical flow cell made of polyether ether ketone (PEEK) material, known for its excellent chemical resistance property, which can be attached to the manipulator inside the main chamber. The flow cell is sealed by two rubber O-rings which moderate the pressure while tightening the four screws to minimize the risk of breaking the extremely thin (tens of nm) Si_3N_4 membrane, as shown in **Figure 2.3 b**. The membrane itself is a customized small window located in the middle of a silicon (Si) wafer and is purchased from Silson Ltd., United Kingdom. On the back side of the membrane, a small chamber accommodates a flow-through of liquid sample or an electrolyte. A steady flow is achieved by using a syringe pump that pushes the liquid with a defined flow rate during the experiment through the inlet and outlet ports, see **Figure 2.3 b**. To study electrochemical reactions, this cell is equipped with a 1.6 mm in diameter platinum (Pt) rod counter electrode (Goodfellow, GmbH) and Ag/AgCl reference electrode (Innovative Instruments, Inc.). Irrespective to the aim

of the experiment, the XAS data will be recorded with fluorescence yield (FY) as mentioned earlier in section 2.2.1.

Unlike LiXEdrom setup, the SPEEM end-station, see **Figure 2.4 a**, is an essential tool for X-ray photoemission electron microscopy (XPEEM) measurements and is equipped with an Elmitec PEEM-III energy microscope/analyzer, allowing for spatially resolved investigations of nanostructures via XAS chemical maps. The XAS characterization is obtained with spatial resolution down to 30 nm [79] of individual nanostructures. Since soft X-ray range is used to irradiate solid samples, secondary surface photoelectrons emitted from the first several nanometers within a material of interest can be ejected due to short inelastic mean free path for electrons in solids (see **Figure 2.4 b**). These electrons at every single energy are the source of spatially resolved XAS imaging as transferred to projective optics and focused onto a CCD camera as shown in **Figure 2.4 a**. The surface electrons that are ejected from the material are enabled to reach the energy detector in vacuum due to a high potential difference applied between the solid sample and the energy analyzer. This leads to record the XAS data in PEY detection mode.
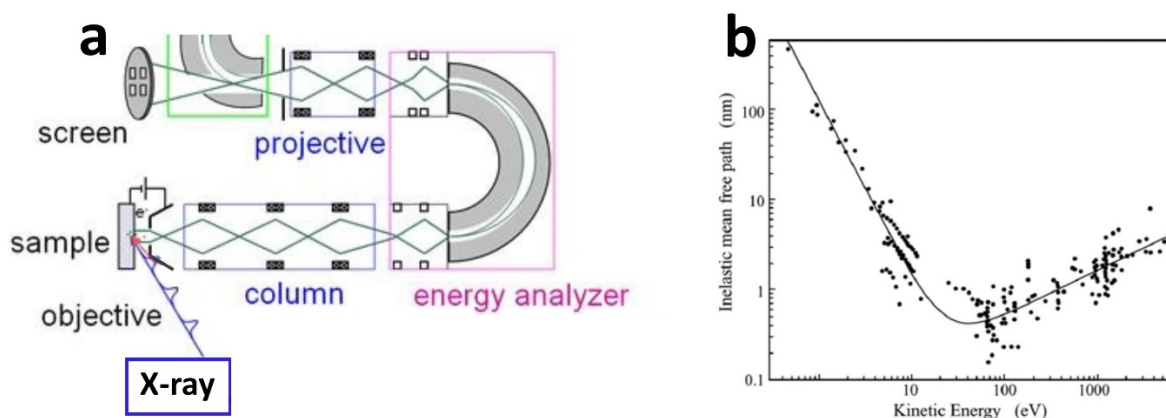
Figure 2.4 Sketch of XPEEM instrument demonstrates the path of the electrons through the energy analyzer which allows the XPEEM to image nanostructures by means of detection of secondary photoelectrons generated upon X-ray illumination, taken and mod from Ref. [81]. (b) Universal curve plot of inelastic mean free path for electrons in solid samples as function of kinetic energy, taken with permission from Ref. [84].

SPEEM end-station can therefore only be used to study solid/dried samples. In contrast to LiXEdrom, the pressure of the main chamber where the samples are placed inside a sample holder is about 10^{-10} mbar, indicating the necessity for ultra-high vacuum (UHV) conditions. The nanometer-scale spatial resolution opens a new horizon to visualize changes in the local

chemical bonds by varying the incident X-ray photon energy across the absorption edge of interest and record an image at every single energy value. Importantly, SPEEM is equipped with various special sample holders allowing for *in situ* XAS measurement at different temperatures in a range of ~110-600 K [79]. The low temperatures range below RT is obtained by using liquid helium (He) to cool down the whole manipulator of which the sample holder is mounted. In addition, SPEEM can also be equipped with sample holders of only annealing capabilities of up to ~1000 °C (1273 K).

2.2.4 Experimental and Data Analysis

All of the MXene samples used in this work were synthesized at our collaborator facilities, namely, at Drexel and Tulane Universities. The details of the synthesis procedures of MXene samples used in this work are shown later in section 2.5. If samples are not already dispersed in water, the MXene samples were received as powders. Thereafter, at EMIL, the powders are dispersed in Milli-Q (18.2 MΩ.cm) water and sonicated for 90 min. For the *ex situ* study of MXenes initially dispersed in water, the sonicated pristine and intercalated MXene powders were centrifuged at 3500 rpm for 15 min. Shortly before drop cast deposition, the samples were further sonicated for several minutes in order to ensure a homogeneous suspension (ink-like). For liquid MXene samples, a membrane-based flow cell was used for XAS measurements in TFY and PFY detection mode by using LiXEdrom, as described in details in section 2.3.2.

Solid samples measured in TEY mode under vacuum conditions (LiXEdrom) were drop cast on conductive Si substrates and dried in air for about three hours prior to introduction into vacuum chamber. One the other hand, samples measured in PEY mode (XPEEM) were spin coated on similar conductive Si substrates and dried in air for about ten minutes prior to introduction into UHV chamber. Please note that the XA spectra of anatase TiO_2 NPs at the Ti L-edge were used as a reference to calibrate XAS end-station beamline shift. The anatase TiO_2 NPs (PL-TiO, Plasmachem, GmbH) have an average particle size of 4–8 nm and were stabilized by a 10 wt% nitric acid (HNO_3) solution.

In chapter three, the Ti L-edge was normalized to the dried $Ti_3C_2T_x$ MXenes L_3 (t_{2g}) peak at 458.1 eV. The mapping of the O content distribution over individual MXene flakes/particles is obtained from the difference of averaged X-PEEM micrographs at the O K-edge of the t_{2g} and e_g region (530.0-534.5 eV) relative to the background one (524.5-529.0 eV). For dispersed in

water MXene samples (ink-like), 50 nm thick Si_3N_4 membranes were utilized to isolate the liquid environment from the vacuum chamber (10^{-6} mbar). Accordingly, the energy of the O K-edge of MXene samples was calibrated to the water pre-edge at 535.0 eV. For clarity, the intensity of the O K edge XA spectra was normalized to the intensities before and after the water main edge. Each XA spectrum is the average summation of two or three spectra with sensitivity of 0.1 eV.

In chapter four, the drop cast samples in *ex situ* studies were characterized by XAS using TEY detection mode at the LiXEdrom end-station. For $Ti_3C_2T_x$-electrolyte samples, H_2SO_4 of 10mM concentration was added to the ink-like suspension followed by a short sonication for several minutes in order to get a homogeneous colloidal used for the *ex situ* study of MXene samples initially dispersed in H_2SO_4. The Ti L-edge XA spectra were normalized to the background signal before 455.0 eV and after 470.0 eV the edge features. Each *ex situ* XA spectrum at the Ti L-edge is the average of two or three spectra measured at different positions.

For MXene in H_2SO_4 environment, membrane-based electrochemical flow cell enabled to perform *in situ* XAS experiments measured in PFY mode. The Si_3N_4 membranes had a window size of 1.0 mm × 0.5 mm used to isolate the liquid environment from the vacuum chamber (10^{-6} mbar). The window is composed of a 75 nm-thick Si_3N_4 membrane coated with 5 nm Cr (adhesive layer) and 10 nm Au. The MXene samples (initially dispersed in water similar to samples used in the *ex situ* study) were drop-cast on the Au-coated membrane and drying in air. The electrochemical reaction was conducted in a three electrode system using an Ag/AgCl reference electrode and a Pt counter electrode. The Ti L-edge XA spectra were measured with PFY mode and normalized to the background signal before 455 eV and after 470 eV the edge features. Each *in situ* XA spectrum (before and after bias potential) at the Ti L-edge is the average of four to six spectra measured at different positions of the X-ray transparent window.

In chapter five, XPEEM was utilized to obtain spatially resolved XA spectra of pristine and cation-intercalated $Ti_3C_2T_x$ samples. Subsequently, the ink-like samples were spin coated in air on Si conductive substrates to obtain individual multi-layered particles. The XA spectra were measured in PEY detection mode. Due to the difficulty to find similar particles in thickness, we focused the study on two individual particles having comparable thickness per each sample. It is worth noting that the X-PEEM technique could also provide valuable information about

the thickness of the multi-layered MXene particles. The height of the thick multi-layered MXene particles above the substrate can be measured from the shadow region. The thickness of the multi-layered MXene particles is calculated via multiplying the length of the shadow region by the tangent of the incident angle (16°) of the X-ray beam. On the other hand, particles without shadow are below 30 nm in thickness and those particles shining a signal from the Si substrate are below 10 nm. Each XA spectrum is the average summation of two or three spectra with sensitivity of 0.1 eV.

In chapter six, thin film $Ti_3C_2T_x$ MXene is obtained by spin coating on a conductive Si substrate. Thin conductive samples are required by XPEEM tool to avoid charging up while measuring, otherwise, may seriously harm the instrument. For XA measurements at low temperature, the sample is then placed on a special customized sample holder that allows for measurements within a temperature range of ~110-600 K [79]. In an attempt to freeze the entire nanoconfined water quickly, as cooling the manipulator to which the special sample holder needs to be introduced takes few hours, the $Ti_3C_2T_x$ sample was directly transferred to ~80 K cold manipulator to avoid and/or minimize desorption under UHV conditions. After temperature equilibrium, the *in situ* measurement is commenced and the XA spectra were recorded at the Ti L- and O K-edges in PEY mode under UHV conditions. Since the operation temperature of the sample holder lies within a range of ~110-600 K [79], the XA measurement of $Ti_3C_2T_x$ MXene at 773 K was performed by using only-annealing sample holder [79], see section 2.2.3. Irrespective to the thickness of the $Ti_3C_2T_x$ MXene film, the probing depth provided by X-PEEM PEY detection mode is up to 10 nm, implying the study of several layers of $Ti_3C_2T_x$ MXenes. Each XA spectrum is the average summation of three spectra with a sensitivity of 0.1 eV.

In order to better highlight the evolution of peak position and area with temperatures, a peak fitting of the XA spectra at the O K-edge was performed using Igor Pro software/ Multi-peak fit version 2.22 (Gaussian Function). The peak fitting parameters were let to be completely free (no constraints applied), however, the background/baseline removal was fixed for all spectra. Owing to a better fit convergence, the peak fitting was found to contain six and five peaks at temperature ranges of 220-270 K and 280-300 K, respectively.

A peak fitting was also conducted on XRD spectra of drop cast MXene samples at low temperatures, using a compatible dome-like chamber, see details in section 2.4.1. The peak fitting was very useful to demonstrate the peak position and area of XRD ice structures at 220 K. The background/baseline removal was fixed for all spectra and the peak fitting parameters were free without any constraint. By using Igor Pro software/ Multi-peak fit version 2.22 (Gaussian Function), the XRD peak fitting calculation of ice-related XRD spectra was obtained.

2.3 Experimental XAS Measurements of MXenes

As mentioned earlier in section 1.7, *ex/in situ* soft XAS was employed to investigate the $Ti_3C_2T_x$ MXenes before and after intercalation in different environments throughout this PhD work. The results and discussion are presented in chapter three to six. The related experimental details are discussed below.

2.3.1 XAS Measurements of Dry MXenes

The solid pristine and intercalated $Ti_3C_2T_x$ MXene samples were obtained by drop cast or spin coating of ink-like MXene on a Si substrate. For XAS measurements of dry MXenes, drop cast $Ti_3C_2T_x$ samples need about a couple of hours to be completely dried while spin coated ones require only several minutes to dry. Thick samples are not suitable for XPEEM experiment due to a possible charging up effect while measuring. This is why only thin particle/film of $Ti_3C_2T_x$ MXene is required by XPEEM tool, which is obtained by spin coating procedure described in Ref. [85]. Irrespective of the post-synthesis preparation and thickness of MXenes samples, the XAS characterization of the dried $Ti_3C_2T_x$ samples were recorded by EY detection mode.

2.3.2 XAS Measurements of Hydrated MXenes

The *in situ* XAS investigation of the EES materials in different environments has become very important in order to fundamentally understand the pseudocapacitive storage mechanism. As aqueous electrolytes such as H_2SO_4 demonstrates a high gravimetric capacitance in $Ti_3C_2T_x$ MXenes (**see Figure 1.5**), the *in situ* study of $Ti_3C_2T_x$ MXene in water and H_2SO_4 environments have been conducted. The *in situ* and *ex situ* studies of $Ti_3C_2T_x$ MXene samples were carried out at LiXEdrom end-station. Using the soft XAS technique for *in situ* study of $Ti_3C_2T_x$ is complicated. As shown in **Figure 2.3 a**, the soft X-ray is focused on a transparent Si_3N_4 membrane window that is located in the middle of the aperture of the flow cell. **Figure 2.5 a** illustrates a 50 nm thick Si_3N_4 membrane (Plano GmbH) with a square shape window (0.5mm

× 0.5mm) that is used to isolate the dispersed in water MXenes from the needed vacuum conditions (10^{-6} mbar) for soft XAS measurements. The emitted light traverse through the membrane is then collected by a photodiode (XUV-100 silicon photodiode from AMS Technologies). As a result, TFY detection mode is employed to characterize pure water, dispersed multilayered $Ti_3C_2T_x$, u-$Ti_3C_2T_x$, and 1M urea in water samples, see chapter three [72]. To maintain a stable flow of MXene samples during the experiments, a Legato 270 syringe pump (KD Scientific Inc.) was operated in push-pull mode with a flow rate of 1 mL/min.
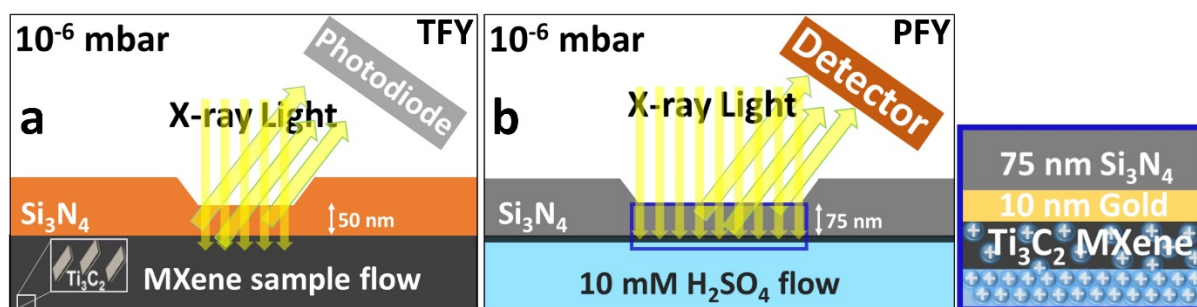
Figure 2.5 Schematic of Si_3N_4 membrane flow cell used for *in situ* XAS measurements to validate the impact of different environments on the surface chemistry of pristine and intercalated $Ti_3C_2T_x$ MXenes. (a) Shows the detection of fluorescence light that pass through a 50 nm thick membrane from a flow of $Ti_3C_2T_x$ MXene dispersed in water by a photodiode (XA spectra recorded in TFY mode). (b) Demonstrates an electrochemical flow cell with a 10 nm gold-coated membrane window. The cation-intercalated $Ti_3C_2T_x$ MXenes were drop cast on the membrane and dried in air before mounting into the cell. Then, 10 mM H_2SO_4 electrolyte was flown through using a syringe pump. The XA spectra are recorded by PFY detection mode. The panel on the right, zoom in of the blue rectangular region shown in (b), highlights the 10 nm gold layer coated silicon nitride membrane and the rapid diffusion of the electrolyte's protons through MXenes samples, driving proton-coupled electron transfer on MXene surfaces.

Alternatively, for the purpose of studying the electrochemical reaction of $Ti_3C_2T_x$ with H_2SO_4 electrolyte, the fluorescence light travel through the Si_3N_4 membrane window is detected in PFY mode as shown in **Figure 2.5 b**. **Figure 2.5 b** demonstrates 1.0 mm × 0.5 mm transparent window composed of a 75 nm-thick Si_3N_4 membrane coated with a 10 nm layer of gold (Au). To ensure a stable and homogeneous coating of Au layer, 5 nm chromium (Cr) is used as an adhesive layer between the Au layer and Si_3N_4 membrane. The electrochemical reaction was conducted in a three-electrode system, see **Figure 2.3 b**. To study the electrochemical reaction of the multi-layered $Ti_3C_2T_x$ MXenes with H_2SO_4, the MXene powder was first dispersed in water until the ink-like solution is obtained as explained in section 2.2.4. Thereafter, the multi-layered Na-, K-, and Mg-intercalated $Ti_3C_2T_x$ samples were drop cast on the Au side of the

membrane and left to dry in air. Initial measurements using a flow of 1 M H_2SO_4 with the aforementioned syringe pump have uncovered a rapid degradation of the Au current collector under an applied potential, which was not the case with 10 mM H_2SO_4 flow. Therefore, this relatively low H_2SO_4 concentration was chosen for this study. The close-up schematic, right panel of **Figure 2.5**, demonstrates the diffusion of protons through the dried drop cast MXene samples during the flow of the 10 mM H_2SO_4 electrolyte. In this way, *in situ* XAS experiments of Na-, K-, and Mg-intercalated $Ti_3C_2T_x$ were conducted to validate the impact of aqueous acidic environment and applied potential on the Ti electronic structure.

2.4 Other Characterization Techniques

Other *ex/in situ* measurements were conducted, in addition to the soft XAS, to study several important properties of $Ti_3C_2T_x$ MXenes before and after intercalation as well as in different environments.

2.4.1 *In Situ* XRD

XRD is a powerful technique that has been used extensively to investigate the atomic and molecular structure, composition, and interlayer spacing of a material. Thus, XRD is not a spectroscopic but a geometric technique as the diffracted angle provides valuable structural information such as the interlayer spacing (*d*-spacing) between planes of periodic atoms of a material of interest. In XRD, if the wavelength of the X-ray light is fixed, the peak position (the diffraction angle) is a function of distance between planes (d_{hkl}), giving information about the *d*-spacing. To understand that, the diffraction pattern is acquired when a monochromatic X-ray beam is focused on a material and then scattered by planes of arranged atoms of a material, as shown in **Figure 2.6 a**. Thereafter, the scattered X-ray angles by that material and their intensities are detected. Only if the scattered X-rays interfere constructively among each other, XRD patterns are measured. Since constructive interference has to be satisfied, the path difference between the incident and diffracted beams is an essential factor and depends on the X-ray angle of incidence relative to crystal planes, as described by Bragg's equation:

$$n\lambda = 2d \sin\theta$$

where n is a multiple integer, λ is the wavelength of the X-ray, and θ is the angle of incidence of the X-ray beam. Thus, Bragg diffraction order peaks result from constructive interference between periodic structures of atoms, clusters, pores, and etc. Therefore, XRD technique can be used to investigate the interlayer spacing of $Ti_3C_2T_x$ MXene before and after intercalation

with molecules, cations, and protons. *In situ* XRD measurements can thus provide valuable information on the structure of MXenes before and after physical or chemical treatments. For instance, the *d*-spacing between $Ti_3C_2T_x$ nanosheets reveals a major impact on the overall electrochemical performance [28,32]. In this context, the amount of stored charges in $Ti_3C_2T_x$ MXene is found to be greatly altered as the *d*-spacing experiences expansion or contraction [28]. As the nanoconfined water is accommodated between the $Ti_3C_2T_x$ nanosheets, the amount of the water in confinement was also found to have a major impact on MXene conductivity and electrochemical performance [32,51].

Since the nanoconfined water impacts many properties such as optical transparency, electrical resistivity, and pseudo-capacitance of $Ti_3C_2T_x$ Mxenes [32], a recent study has reported a calculated XRD patterns of mixed water layers, namely, monohydrated (1W) and bihydrated (2W) $Ti_3C_2T_x$ nanosheets [86]. Also, the experimental findings show that $Ti_3C_2T_x$ interlayer spacing shrinks by ~3.5 Å as the relative humidity (RH) drops down from 95% to 5% [86].
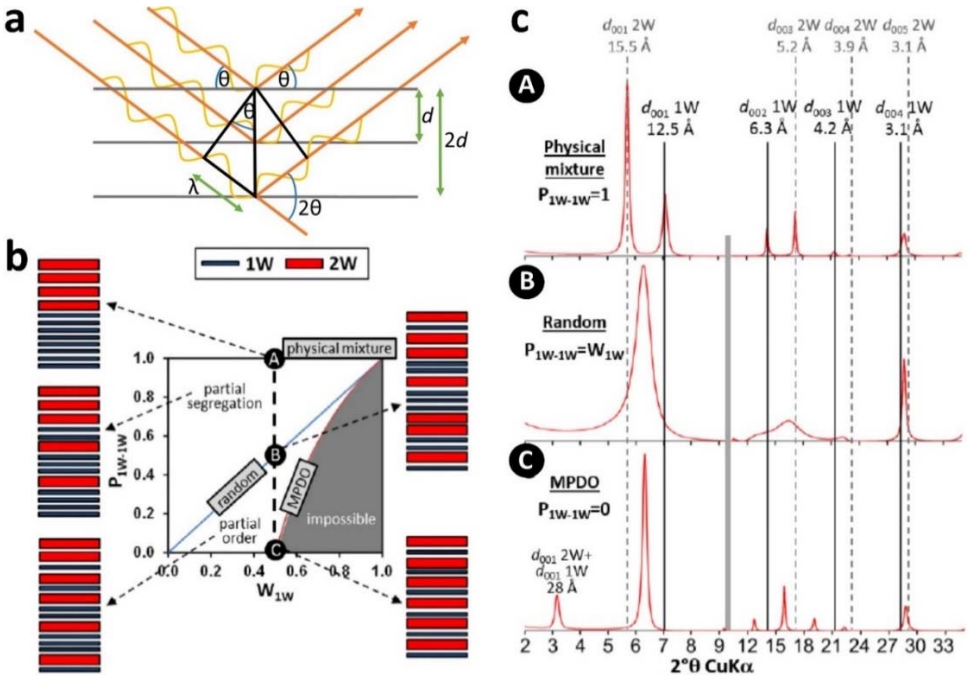
Figure 2.6 (a) Schematic representation of the Bragg equation where XRD patterns are recorded when the intensities of the diffracted X-rays, departs crystal planes at a certain angle, fulfill the Bragg equation. (b) A model shows the probability of mainly three different categories of mixed layers described by the P_{1W-1W} parameter as a function of W_{1w}: A) Physical mixture, B) random, and C) MPDO interstratification. (c) Calculated XRD pattern of these mixed layers with an assumption of equal proportions of 1W and 2W layers (W_{1w}= 0.5) and different parameters of P_{1W-1W}. Please note that the P_{1W-1W} is the probability parameter to find two successive 1W layers while W_{1w} stands for the relative proportion of 1W layers. Reproduced with permission from Ref. [86].

Figure 2.6 b discloses a range of potential stacking sequence by these mixed layers of MXenes that is described by P_{1W-1W} parameter as a function of the relative proportion of 1W (W_{1w}), suggesting three main different categories of mixed layers: (i) Physical mixture as well as partial segregation or order, (ii) random, and (iii) and maximum possible degree of ordering (MPDO) interstratification. A regular coexistence of hydrates (1W and 2W) is then plausible in MXene interstratified crystals [86]. Therefore, the mixture of interstratified hydrate layers plays a vital role and thus enables XRD patterns in $Ti_3C_2T_x$ MXene [86]. For clarity, XRD patterns of these mixed layers assume equal proportion of 1W and 2W (W_{1w}= 0.5) with respect to different P_{1W-1W} parameter values. The XRD spectra were collected based on the sum of *00l* reflection plane series of both 1W and 2W periodic structures. **Figure 2.6 c** demonstrates the corresponding XRD patterns of these mixed 1W and 2W MXene layers described in (i), (ii), and (iii), indicating a significant difference in *d*-spacing of MXenes. Further calculation based on expansions or contractions in the *d*-spacing may provide information about local bond lengths, giving an insight about MXene surface chemistry. As the operation temperature of EES devices ranges from -40 °C to 65 °C (see **Table 1.1**), *in situ* XRD study of $Ti_3C_2T_x$ MXene at temperatures below RT becomes crucial. Importantly, the XRD technique has also shown the capability to detect the ice fingerprint of water in confinement upon freezing [87].

To enable *in situ* XRD measurements of MXene below RT, a customized low temperature-assisted dome-like chamber was built in-house, allowing for cooling and heating the samples between 220 K to 300 K (see **Figure 2.7 a**). **Figure 2.7 a** shows a setup of in-house constructed dome-like chamber compatible with our Bruker XRD setup, which enables XRD measurements at temperatures from 220 K to 300 K. To avoid water condensation at low temperatures, near ambient pressure (NAP) conditions was applied inside the dome-like chamber. The *in situ* XRD measurements were carried out on drop cast $Ti_3C_2T_x$ MXene on a Si substrate, as shown in **Figure 2.7 b**. When the temperature is decreased below RT, NAP conditions was established as soon as the sample temperature is around 280 K to reduce as much as possible the time at which the sample is exposing to vacuum conditions. The essential parts needed for this customized low temperature-assisted dome-like chamber are described in detail at the end of this section.

In this work, by using the dome-like chamber, *in situ* XRD measurements at temperature range of 220 K to 300 K were used to reveal the ice structure of the nanoconfined water in MXenes.

This approach allows not only to detect the nanoconfined water fingerprint but also its impact on the 002 diffraction order peaks of $Ti_3C_2T_x$ MXene. To make sure that the water signature belongs to the nanoconfined water, XRD pattern of Si reference substrate was also measured. Following the same experimental procedure but with introducing ambient air into the dome-like chamber, XRD patterns of MXene and Si substrate under air pressure of 256 mbar were performed in order to have further quantitative data related to XRD pattern of ice structures, see chapter six.

- *Technical details of the XRD measurements:*

 In this work, XRD patterns were collected by using Cu Kα radiation at 1.54187 Å wavelength. The XRD patterns presented in chapter three and six were collected via a Bruker D8 diffractometer using Cu Kα radiation. Each XRD profile of the nanoconfined water is the average summation of two scans between 3°–40° of 2θ values with 0.02° step width per 0.25s. However, the diffraction pattern of the cation-intercalated and pristine $Ti_3C_2T_x$ (chapter four) was obtained using a Rigaku DMAX 2200 Cu Kα X-ray diffractometer. The scans were conducted with a step size of 0.02°, 1° per s dwell time, and 3°–65° of 2θ values.

- *The different parts needed for the dome-like chamber setup are:*

Briefly, the sample stage shown in **Figure 2.7 a**, where MXene sample is placed on, is made from Cu due to its remarkable heat conductivity. The table underneath consists of a Peltier element and a Brass heat exchanger mounted in a sandwich assembly. The required tempered oil for the heat exchanger is supplied by a Julabo chiller. On the other hand, the Lakeshore controller (LS336) ensures the fine-tuning of the temperature. The temperature feedback comes from a Pt100 sensor which is mounted in the center of the sample table and is very close to the sample of interest to be studied. As the output of the proportional–integral–derivative (PID) loop controller of the LS336 is an analog signal of a low power, it is powered up by the so-called Hyginn V/I converter with a ±2 A signal. The temperature accuracy and stability provided by this setup is 1 mK and less than 5 mK, respectively. A scroll pump from Edwards Inc. was used to reach the desired NAP pressure conditions. This dome-like chamber was designed and constructed by the sample environment department at Helmholtz Zentrum Berlin für Materialien und Energie.
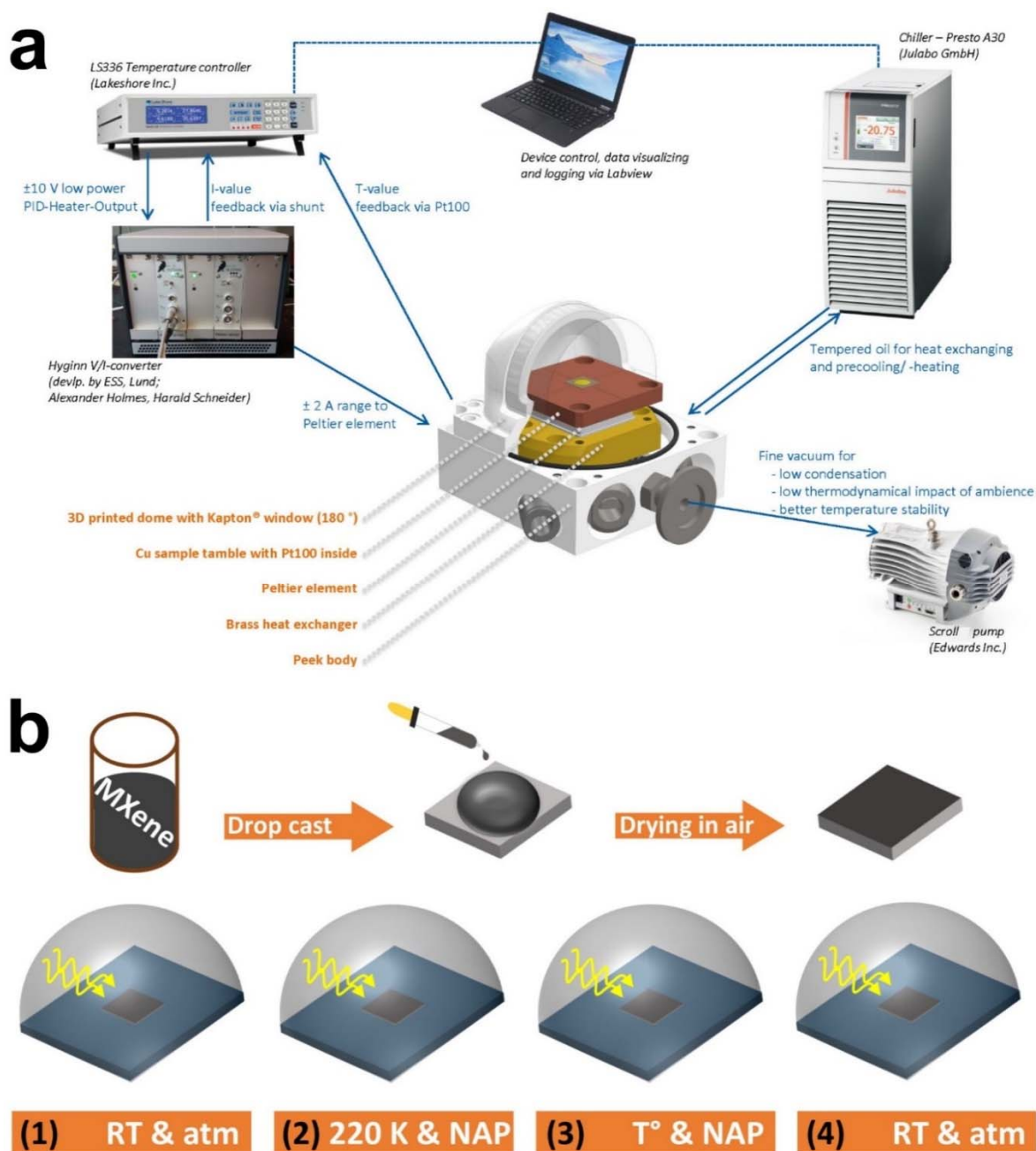
Figure 2.7 In-house constructed low temperature-assisted dome-like chamber enables *in situ* XRD measurements in the range of 220-300 K. (a) Schematic illustrates the necessary devices for the operation of the dome-like chamber to ensure in *situ* XRD measurement at low temperatures. Owing to its significant heat conductivity, the sample is placed on a Cu stage. By using a Peltier element, low vacuum, and chiller, a desired temperature can be obtained. To be transparent to X-ray light, the XRD measurement was possible via a 180° transparent Kapton tape window. (b) The preparation of the MXene sample prior to mounting onto the stage of the dome-like chamber. The steps of the cycle are shown underneath: First (1), at RT and atmospheric (atm) pressure, Second (2), at 220 K and near ambient pressure (NAP), Third (3), stepwise heating (220, 240, 260, 270, 280, 290, and 300 K) under NAP conditions, Fourth (4), measuring at RT and atm. For clarity, the full space transparent dome illustration in panel b is just to highlight the sample position and the penetration of the X-ray through the Kapton tape.

2.4.2 Electrochemical Measurements

In an electrochemical process, the flow of electrons is related to chemical changes. Thus, electrochemical measurement is a useful tool to probe charge transfer between electrode and electrolyte, changing the oxidation state of the electrode material. The change in the oxidation state is known as a redox reaction which stands for reduction and oxidation processes while cycling. When an atom/ion/molecule receives an electron, the oxidation state is decreased (reduction process) but if it grants an electron, the oxidation state is increased (oxidation process). The electrochemical performance can be obtained from CV measurements in order to find out the capacitance and the presence of redox reactions of a material. As shown in **Figure 1.5 E**, **F**, and section 3.4, a CV profile is acquired when a specific range of potential is applied on an electrode at a certain scan rate and collects the current response accordingly. In CV measurements, the scan rate is an important parameter which stands for a gradual linear variation of an applied potential per second.

As a result of remarkable energy storage, sulfuric acid was used as an electrolyte with $Ti_3C_2T_x$ MXene-based electrodes. The concentration of the used sulfuric acid electrolyte was 1M. The electrochemical measurements were conducted in Swagelok cell [32,34,43] equipped with three electrodes system, where MXene is the working electrode, activated carbon is the counter electrode, and Ag/AgCl is used as a reference electrode. As the potential is swept from positive to negative values (cathodic), the Ti atoms in $Ti_3C_2T_x$ MXene electrode are reduced. Whereas in a reverse potential scan, from negative to positive voltages (anodic), the Ti atoms in $Ti_3C_2T_x$ electrode are oxidized. In this context, an experimental study utilizes XA spectra at the Ti K-edge (see **Figure 2.2 b**) show an increase in the oxidation state of surface Ti atoms from +2.33 to +2.43 when an anodic potential is applied on $Ti_3C_2T_x$ electrode in 1M H_2SO_4 [34]. This experimental study shows that the electrochemical performance of $Ti_3C_2T_x$ MXene electrode in 1M H_2SO_4 electrolyte is dominated by true pseudocapacitive behavior. In agreement with this study [34], a theoretical study has reported that despite EDL behavior works against the redox-based one, the overall electrochemical behavior of $Ti_3C_2T_x$ MXene in 1M H_2SO_4 is predominately pseudocapacitive [88].

- *Electrochemical performance calculations:*

In our MXene electrochemical performance calculations (see **Figures 3.2** and **3.3**), multilayer powders of $Ti_3C_2T_x$ or u-$Ti_3C_2T_x$ were mixed with polytetrafluoroethylene (60 wt.% in water, Sigma Aldrich) to form a weight ratio of 95:5 for the working electrode films. Similarly, activated carbon (AC) films were prepared by mixing 5 wt.% polytetrafluoroethylene (60 wt.% in water, Sigma Aldrich) with 95 wt.% YP50 (Kuraray, Japan). Electrodes were formed by rolling the mixtures into 100 μm thick films followed by drying in a vacuum oven at 70 °C overnight.

The electrochemical tests of CVs were conducted at RT using a VMP3 electrochemical workstation (BioLogic, France). CVs were recorded using a VMP3 at scan rates ranging from 5-100 mV/s after pre-cycling electrodes at 5 mV/s for 50 cycles. The 3-electrode measurements were performed in 1M H_2SO_4 electrolyte, in which $Ti_3C_2T_x$ and u-$Ti_3C_2T_x$ electrodes were employed as the working electrodes with over-capacitive activated carbon and Ag/AgCl as the counter and reference electrodes, respectively. Gravimetric, areal, and volumetric capacitances were calculated based on the weight, area, and volume of the active materials, respectively. The details of the calculations are as following:

The gravimetric specific capacitance, C_m (F/g), of the electrode materials was calculated from the CV curves by integrating the discharge portion according to the following equation:

$$C_m = \frac{1}{Vmv} \int i \, dV$$

where *i* is the current (mA), *V* is the potential window (V), v is the scan rate (mV/s), and *m* is the mass of the active material (mg).

Areal capacitance values (F/cm^2) C_A were estimated by multiplying the gravimetric capacitance with the areal mass loading (~20 mg/cm^2) of the working electrodes.

$$C_A = C_m * mass\ loading$$

Volumetric capacitance (F/cm^3) values were estimated by normalizing the areal capacitance with the thickness (100 μm) of the working electrodes.

$$C_V = C_A / thickness$$

2.4.3 Thermogravimetric Analysis and Mass Spectrometry

Thermogravimetric analysis coupled with Mass Spectrometry (TG-MS) is a useful technique to identify evolved material decomposition during the heating process, typically from RT to about 1000 °C, in an inert gas environment. The TG tool utilizes the change in the sample weight as a function of the annealing temperatures to gain information about the material such as stability, desorption, and dehydration. Owing to the annealing process, the TG resultant sample gas enters a mass spectrometer to identify the evolved compounds by means of ions separation. The ions are separated by electromagnetic fields according to their mass to charge ratio. The signature of ions are then disclosed by a detector to find out the constituents of the evolved gas from the sample.

In this study, the thermogravimetric analysis (SDT Q 650) and mass spectrometer (110/220V) measurements were performed under constant flow of helium. The TG-MS experiments were carried out at temperatures ranging from RT to 400 °C on pristine and urea-intercalated MXene powder samples to examine the dehydration and the decomposition of urea. This TG-MS experiment is essential to validate urea intercalation at RT in multi-layered $Ti_3C_2T_x$ MXene as a previous study [89] has reported the decomposition of intercalated urea in $Ti_3C_2T_x$ into ammonium and carbon dioxide at about 60 °C. It is noteworthy that XAS experiments of urea-intercalated MXene were conducted only at RT. Since pristine and urea-intercalated $Ti_3C_2T_x$ MXenes have the same 002 diffraction order peak, the TG-MS experiments were performed on urea-intercalated $Ti_3C_2T_x$ to confirm the urea intercalation in $Ti_3C_2T_x$ MXene, as explained in section 3.3.

2.5 Sample Preparation of $Ti_3C_2T_x$ MXenes

For this work, three different synthesis routes were adopted to produce $Ti_3C_2T_x$ MXenes. The details of these various methods are shown below. The main difference is that the surface chemistry is dramatically altered as the ratio of the different surface terminations is largely influenced.

2.5.1 Multilayered $Ti_3C_2T_x$ MXenes Particles (HF Method)

Multi-layered $Ti_3C_2T_x$ MXenes particles were synthesized from the respective precursor Ti_3AlC_2 by Gogotsi's group at Drexel University. To make $Ti_3C_2T_x$, 1 g of Ti_3AlC_2 (<37 μm particle size) powder was added into 10 mL of 10% HF (50%, Fisher Scientific) solution for 2 min. The

solution was stirred for 24 h at 35 °C. The obtained multilayered $Ti_3C_2T_x$ was repeatedly washed with deionized water, followed by centrifugation and decantation until the pH of the suspension reached ~6.0. After the final centrifugation, the sediment of each $Ti_3C_2T_x$ MXene was collected via vacuum-assisted filtration, and the obtained $Ti_3C_2T_x$ powder was kept under vacuum at RT to prevent any deterioration due to oxidation. This synthesis procedure does not result in any molecules and/or cations intercalation. Intercalation between $Ti_3C_2T_x$ MXene nanosheets is extremely important in terms of many MXene-based applications. To study the impact of urea intercalation on the $Ti_3C_2T_x$ MXene, the adsorption of urea was performed in aqueous solution with an initial urea concentration of 5 g/dL at RT. 2 g of $Ti_3C_2T_x$ MXene powder was added to 50 mL of aqueous urea solution and mixed by hand for approximately 6 min, followed by shaking at 150 rpm for an hour. Afterwards, the $Ti_3C_2T_x$/urea suspension was centrifuged at 1000 rpm for 2 min. Both the precipitate and supernatant were reserved for analysis. The resulting urea intercalated $Ti_3C_2T_x$ (u-$Ti_3C_2T_x$) and the pristine $Ti_3C_2T_x$ precipitates were dried via vacuum-assisted filtration and used for further analysis. For example, only prior XRD measurements shown in **Figure 3.1**, both samples were also vacuum annealed at 110 °C for 12 hours to remove any intercalated water. For other experiments than this specific XRD, the samples were not annealed prior characterization.

2.5.2 Multilayered $Ti_3C_2T_x$ MXenes Particles (HF+LiCl Method)

The Ti_3AlC_2 MAX phase was synthesized by Naguib`s group at Tulane University, details are reported by Huang and Mochalin [90]. Powders of titanium (Alfa Aesar, -325 mesh), aluminum (Alfa Aesar -325 mesh), and graphite (Alfa Aesar, APS 7–15 µm) were mixed in an atomic ratio of 3.00:1.10:1.88 in a Turbula T2F mixer for 3 h using zirconia balls, then the powders were annealed in a tube furnace under flowing argon at 1600 °C for 2 h with a heating rate of 10 °C/min. Cation-intercalated $Ti_3C_2T_x$ MXene samples were produced similarly to Ghidiu et al. [47]. The Ti_3AlC_2 powder was ground to -325 mesh and slowly added to a solution of LiCl in 10% wt HF in ratios of 1 g of Ti_3AlC_2 to 10 mL of the etchant, with a 1:5 molar ratio of Ti_3AlC_2 to LiCl. The etching was carried out at RT with stirring for 24 h and that would result in the delamination of the MXene nanosheets. This was followed by washing with excess deionized water until a pH > 6 was reached. The still wet powders were soaked in 37% HCl (30 mL per every 1 g powder), centrifuged, and the supernatant was discarded. This step was repeated for a total of 5 cycles of acid washing. The powders were again washed with excess deionized

water until a pH > 6 was reached. Despite the several washing steps, some Li cations may remain intercalated. The wet powders were divided into 5 equal portions, and one portion was soaked in 1 M LiCl, 1 M NaCl, 1 M KCl, 0.5 M MgCl$_2$, or deionized water (40 mL solution for each gram of powder) for 1 h, after which the solutions were centrifuged, and supernatants discarded. This was followed by repeating the soaking of the wet powders in fresh solutions, listed above, for 24 h. Then, the mixtures were washed with deionized water 3 times, discarding supernatants at each step. Finally, the intercalated powders of Li−, Na−, K−, and Mg−Ti$_3$C$_2$T$_x$ MXenes and the pristine Ti$_3$C$_2$T$_x$ MXene were dried by vacuum-assisted filtration.

2.5.3 Single and Few Layer Ti$_3$C$_2$T$_x$ MXene Flakes (LiF+HCl Method)

In this method, the synthesis procedure to produce the Ti$_3$C$_2$T$_x$ MXene is obtained by selective etching of Ti$_3$AlC$_2$ MAX phase (from Materials Research Center, Ukraine) in a mixture of LiF and HCl [91]. These MXene samples were synthesized by Gogotsi's group at Drexel University. This synthesis method results in a spontaneous delamination of the MXene nanosheets owing to the intercalation of Li$^+$ ions. Therefore, the interlayer spacing becomes larger and the surface chemistry is altered relative to the HF only method. The details are when 2 g of Ti$_3$AlC$_2$ MAX phase powder (Material Research Center, Ukraine) was allowed to react with premixed solution of etchants containing 3 g of LiF and 20 mL of 9 M HCl which is continuously stirred for 18 h at RT. In order to render the pH of the supernatant the value of 5, the mixture of the acid is then repeatedly washed with 150 mL of deionized water (DI) for 3-5 cycles. After the fourth wash cycle, 30 mL of DI water was added to the sediment, shake vigorously and centrifuged at 3500 rpm for 30 min. Thereafter, the dark colored supernatant consisting of the delaminated Ti$_3$C$_2$T$_x$ MXene flakes is used and then was filtered to produce the free-standing film.

CHAPTER THREE

Impact of Urea Intercalation on the Ti$_3$C$_2$T$_x$ Electrochemical Performance

3.1 Motivation

As mentioned in chapter one, the operation of EES devices using 2D nanomaterials with intrinsic pseudocapacitive behavior relies greatly on their surface chemistry. Therefore, below are the targets that triggered me to pursue the investigation of pristine and urea intercalated $Ti_3C_2T_x$ MXenes.

1- What is the impact of urea intercalation on the surface chemistry of multi-layered $Ti_3C_2T_x$ MXenes, as dried in air or dispersed in water?

2- Each MXene sample consist of many multi-layered $Ti_3C_2T_x$ flakes, the mapping of the Ti oxidation state of a single flake has become substantial before and after urea intercalation.

3- As urea molecule is a relatively big organic molecule, does it change the oxidation state of the surface Ti atoms in $Ti_3C_2T_x$ MXenes?

4- If yes, is there a link? What is the electrochemical performance of urea intercalated $Ti_3C_2T_x$ relative to the pristine $Ti_3C_2T_x$ MXene.

What is the essence of this chapter?

The $Ti_3C_2T_x$ MXenes have shown outstanding properties due to their highly active hydrophilic surfaces coupled with high metallic conductivity. Many applications, including electrochemical properties, rely on the intercalation between $Ti_3C_2T_x$ flakes by ions or molecules, which in turn might alter the $Ti_3C_2T_x$ surface chemistry. In this work, we show that the capacitance, rate capability, and charge carrier kinetics in the $Ti_3C_2T_x$ MXene electrodes are remarkably enhanced after urea intercalation (u-$Ti_3C_2T_x$). In particular, the areal capacitance increased to 1100 mF/cm^2, which is 56% higher than that of pristine $Ti_3C_2T_x$ electrodes. We attribute this dramatic improvement to changes in the $Ti_3C_2T_x$ surface chemistry upon urea intercalation. The oxidation state and the oxygen bonding of individual $Ti_3C_2T_x$ flakes before and after urea intercalation are probed by soft XAS at the Ti L- and O K-edges with 30 nm spatial resolution in vacuum. After urea intercalation, a higher Ti oxidation state is observed across the entire flake compared to pristine the $Ti_3C_2T_x$. Additionally, *in situ* XAS of u-$Ti_3C_2T_x$ aqueous dispersions reveal a higher Ti oxidation similar to dry samples, while for pristine the $Ti_3C_2T_x$ the Ti atoms are significantly reduced in water compared to dry samples.

3.2 Research Background

The EES systems with high capacitance, fast rate capabilities, and low-cost electrodes are urgently demanded as society transitions to sustainable energy technologies. Thus, MXenes are currently attracting considerable attention for EES purposes [27–30,32,34]. MXenes combine high electrical conductivity with hydrophilic 2D lamellas, enabling the fast and reversible insertion of a variety of intercalants in organic or aqueous environments [92–94]. As explained in chapter one, intercalation of MXenes was found to have a great impact on their surface chemistry and was suggested as a strategy to obtain higher pseudocapacitance performance [95]. Interestingly, urea intercalation has also been applied as a first step to generate nitrogen-doped $Ti_3C_2T_x$ with improved capacitance in aqueous electrolyte [96].

The MXene interlayer distance has been found to be directly proportional to the intercalant's hydration size, and intercalation generally induces a larger spacing between the material layers, as demonstrated by XRD [47]. Despite the relatively large size of urea compared to the interlayer gallery of MXenes, the change in the interlayer distance after intercalation is relatively small owing to the parallel orientation of urea molecules relative to the MXene surface, regardless of the possible surface terminations [26]. It has to be mentioned that in another study, the decomposition temperature of urea was shown to be reduced to ~60 °C when intercalated into MXenes [89]. The impact of urea intercalation on the surface chemistry of pristine $Ti_3C_2T_x$ MXenes and on the ion transportation mechanism of the electrolyte remains largely unexplored, even though they are expected to dramatically impact the pseudocapacitance performance. As previously presented in chapter two, the XAS characterization of transition metal L-edges is highly sensitive to the metal chemical environment and has been used to distinguish the various Ti oxide species [63,64].

While previous XAS reports on $Ti_3C_2T_x$ at the Ti K-edge have shown changes in the Ti oxidation state during cycling under different conditions [27,34] the Ti L-edge can provide further information on the nature of the chemical bonds between Ti atoms and surface groups due to its high sensitivity to metal-ligand coordination [97]. However, the shorter penetration depth of soft X-rays makes *in situ* experiments on thick electrodes much more complicated at the Ti L-edge compared to the Ti K-edge. In previous studies, pristine $Ti_3C_2T_x$ MXenes have also been found to be sensitive to oxidation due to a charge transfer that can take place between surface O and Ti atoms [98,99]. The high chemical sensitivity of XAS at the Ti L-edge was also employed

for *in situ* in aqueous environments using flow cells with thin X-ray transparent membranes [64]. Probing the MXene Ti chemical bonding in different environments is extremely important as electrochemical reactions take place in aqueous media. Nevertheless, XAS in the soft X-ray range has not been applied to MXene so far.

In this chapter, we characterized the electrochemical performance of pristine and u-$Ti_3C_2T_x$ MXene electrodes and correlated it to the nature of Ti−O bonding probed in vacuum and in water using XAS at the Ti L and O K-edges. Spatially resolved oxidation over individual multi-layered $Ti_3C_2T_x$ flakes was characterized by X-PEEM. In addition, in situ XAS was performed on aqueous dispersions of MXenes to observe the effect of solvation on MXene electronic structure. The u-$Ti_3C_2T_x$ MXenes were characterized under similar conditions and demonstrated a significantly higher Ti oxidation state and capacitance compared to the pristine $Ti_3C_2T_x$ MXene. The u-$Ti_3C_2T_x$ based electrode exhibits enhanced capacitance performance and rate capabilities over pristine $Ti_3C_2T_x$ electrodes, the origin of which will be discussed based on XAS characterization in the following.

3.3 MXene's Characterization

First of all, $Ti_3C_2T_x$ and u-$Ti_3C_2T_x$ samples were synthesized via the 10 wt % HF selective etching method as performed according to previously published method in Ref. [91] and shown in section 2.5.1. **Figure 3.1 a** illustrates a schematic of the urea intercalation in $Ti_3C_2T_x$ MXenes. The orientation of urea molecules in the gallery of the MXene flakes shown in **Figure 3.1 a** is based on our previous computational calculations [26]. XRD patterns of the as synthesized pristine $Ti_3C_2T_x$ and u-$Ti_3C_2T_x$ at RT are shown in **Figure 3.1 b**. The u-$Ti_3C_2T_x$ sample shows a (002) diffraction peak at 7° 2θ (corresponding to a c lattice parameter of 25.3 Å), which corresponds well with the c lattice parameter expected for urea intercalated in a planar orientation, as shown in **Figure 3.1 a** [26]. However, a similar spacing was also observed for the pristine MXene as a result of water intercalation [100]. We therefore performed vacuum annealing at 110 °C to remove intercalated water molecules in both samples. The 2θ (002) peak shifted to 8.6° and 6.4° for pristine $Ti_3C_2T_x$ and u-$Ti_3C_2T_x$, corresponding to c lattice parameters of ~20.6 and ~27.6 Å, respectively. The interlayer spacing of pristine $Ti_3C_2T_x$ clearly decreases upon water desorption, which is not observed for u- $Ti_3C_2T_x$. This indicates that the large interlayer spacing for u-$Ti_3C_2T_x$ at RT is not due to water intercalation. The

difference in spacing between the two annealed MXene samples ($\sim$3.5 Å) is similar to that of a previously reported change in kaolinite interlayer spacing after urea intercalation [101].
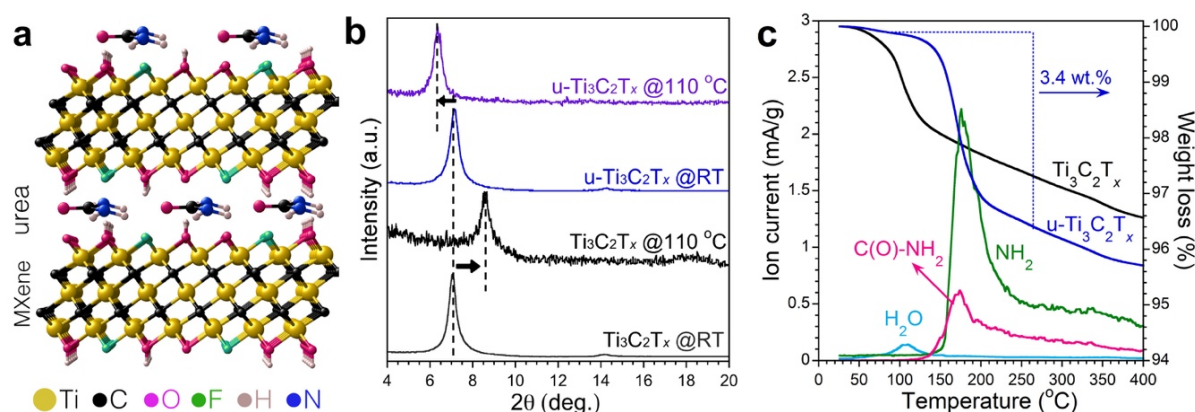
Figure 3.1 (a) Schematic of urea adsorption on $Ti_3C_2T_x$ after addition to an aqueous urea solution. (b) X-ray diffraction patterns of the as-synthesized $Ti_3C_2T_x$ powder ($Ti_3C_2T_x$ @RT), $Ti_3C_2T_x$ after annealing at 110 °C for 12 hours ($Ti_3C_2T_x$ @110 °C), $Ti_3C_2T_x$ after urea adsorption at room temperature for 12 hours (u-$Ti_3C_2T_x$ @RT), and $Ti_3C_2T_x$ after urea adsorption at 110 °C for 12 hours (u-$Ti_3C_2T_x$ @ 110°C). The arrows show the change in position of the 002 diffraction peaks after vacuum annealing at 110 °C, highlighting that the vacuum annealing induces different structural reorientations depending on urea intercalation. (c) Thermogravimetric analysis for pristine $Ti_3C_2T_x$ and u-$Ti_3C_2T_x$, and mass spectrometry from the u-$Ti_3C_2T_x$. Taken with permission from Ref. [72].

To shed light on the nature of the intercalated species, thermogravimetric and mass spectrometric (TG−MS) measurements were performed by Gogotsi group at Drexel University (**Figure 3.1 c**). Our results show decomposition products from urea starting from 130 °C, representing a $\sim$3.4 wt % loss, demonstrating that urea was present in the u-$Ti_3C_2T_x$ at RT. The TG−MS results also show that the interlayer water that exists in pristine $Ti_3C_2T_x$ was largely replaced by urea molecules due to the difference in water weight loss from 2% for pristine $Ti_3C_2T_x$ to < 0.2% in u-$Ti_3C_2T_x$. As the sample environment was dissimilar during the XRD and TG−MS measurements, there is a possibility that urea had already decomposed prior to the XRD measurements performed at 110 °C in vacuum, as has been suggested in a previous study [89]. This will be studied in detail in future work. Irrespective of the urea stability at high temperatures, both XRD and TG−MS measurements demonstrate that urea was intercalated in $Ti_3C_2T_x$ at RT. Please note that annealing was only applied to investigate the interlayer spacing after urea intercalation as well as for TG-MS measurement to make sure no urea decomposition takes place at 110 °C. The annealing is thus not applied for any other measurements presented later in this chapter.

3.4 Electrochemical Performance

The electrochemical behavior of $Ti_3C_2T_x$ and $u\text{-}Ti_3C_2T_x$ MXenes was investigated using three electrode cells in 1 M H_2SO_4 electrolyte. **Figure 3.2 a** shows typical cyclic voltammograms of $u\text{-}Ti_3C_2T_x$ and $Ti_3C_2T_x$ electrodes at a scan rate of 5 mV/s. The broad redox envelop is more prominent in the case of $u\text{-}Ti_3C_2T_x$ compared to $Ti_3C_2T_x$, which can be attributed to the increased accessibility of protons and hydronium ions within the MXene galleries after the intercalation of urea molecules.

The rate retention capability of $u\text{-}Ti_3C_2T_x$ is superior relative to $Ti_3C_2T_x$, as shown in **Figure 3.2 b**. These findings corroborate with the measured XRD, where the enlarged interlayer spacing of $u\text{-}Ti_3C_2T_x$ provides not only a greater number of electrochemically active sites but also facilitates a much faster diffusion of electrolyte ions relative to $Ti_3C_2T_x$ electrode. This leads to that the $u\text{-}Ti_3C_2T_x$ electrode exhibits superior ion transport kinetics relative to $Ti_3C_2T_x$ one.
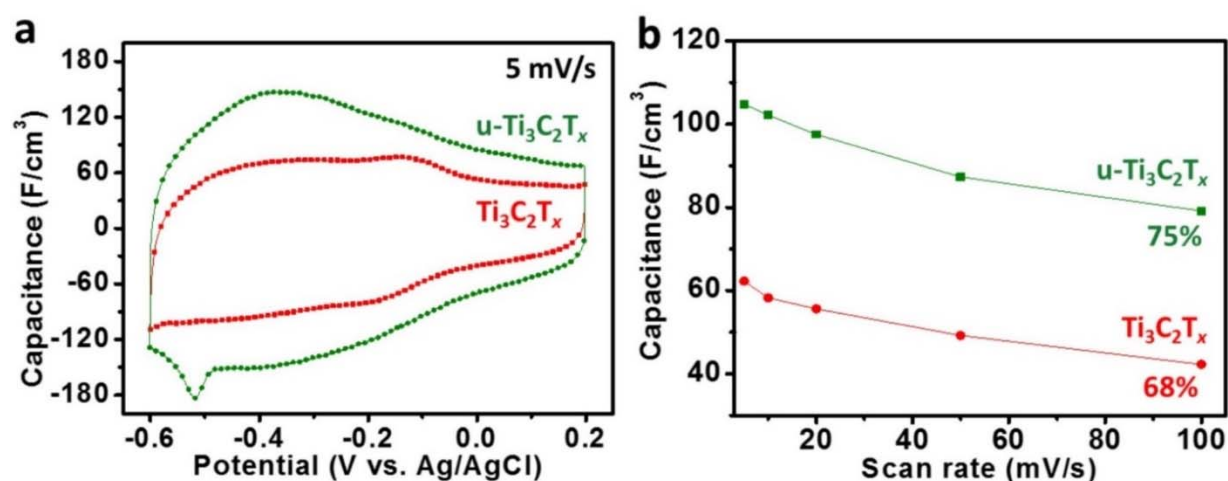
Figure 3.2 Comparison of the electrochemical performance between $Ti_3C_2T_x$ and $u\text{-}Ti_3C_2T_x$ electrodes in 1M H_2SO_4 electrolyte. (a) Cyclic voltammograms at scan rate of 5 mV/s. (b) Volumetric capacitance versus scan rate shows 75% retention in $u\text{-}Ti_3C_2T_x$ relative to 68% for $Ti_3C_2T_x$ electrodes at scan rate of 100 mV/s. Taken with permission from Ref. [72].

Interestingly, there is a small reduction peak at −0.51 V (vs Ag/AgCl) for the $u\text{-}Ti_3C_2T_x$ electrode, which is absent in the case of $Ti_3C_2T_x$. This is probably due to the protonation of urea molecules at low scan rates, as a reduction peak at high scan rates (>20 mV/s) is absent, as shown in **Figure 3.3** as well as the full performance is presented. The areal (volumetric) capacitance of $u\text{-}Ti_3C_2T_x$ increases dramatically and is found to be 1100 mF/cm^2 (110 F/cm^3), which is 56% higher compared to pristine $Ti_3C_2T_x$ electrodes. Note that the volumetric capacitance of u-

$Ti_3C_2T_x$ electrodes (ultrathick electrodes, ~100 μm at a mass loading of 20 mg/cm^2) should not be compared with the few micron thick MXene electrodes (~1−5 μm at a mass loading of 1−3 mg/cm^2) reported by Lukatskaya et al. [54] as the investigated electrode here is powder-based rather than a freestanding film electrode. Optimization of the electrode capacitance in terms of absolute numbers is currently in progress.
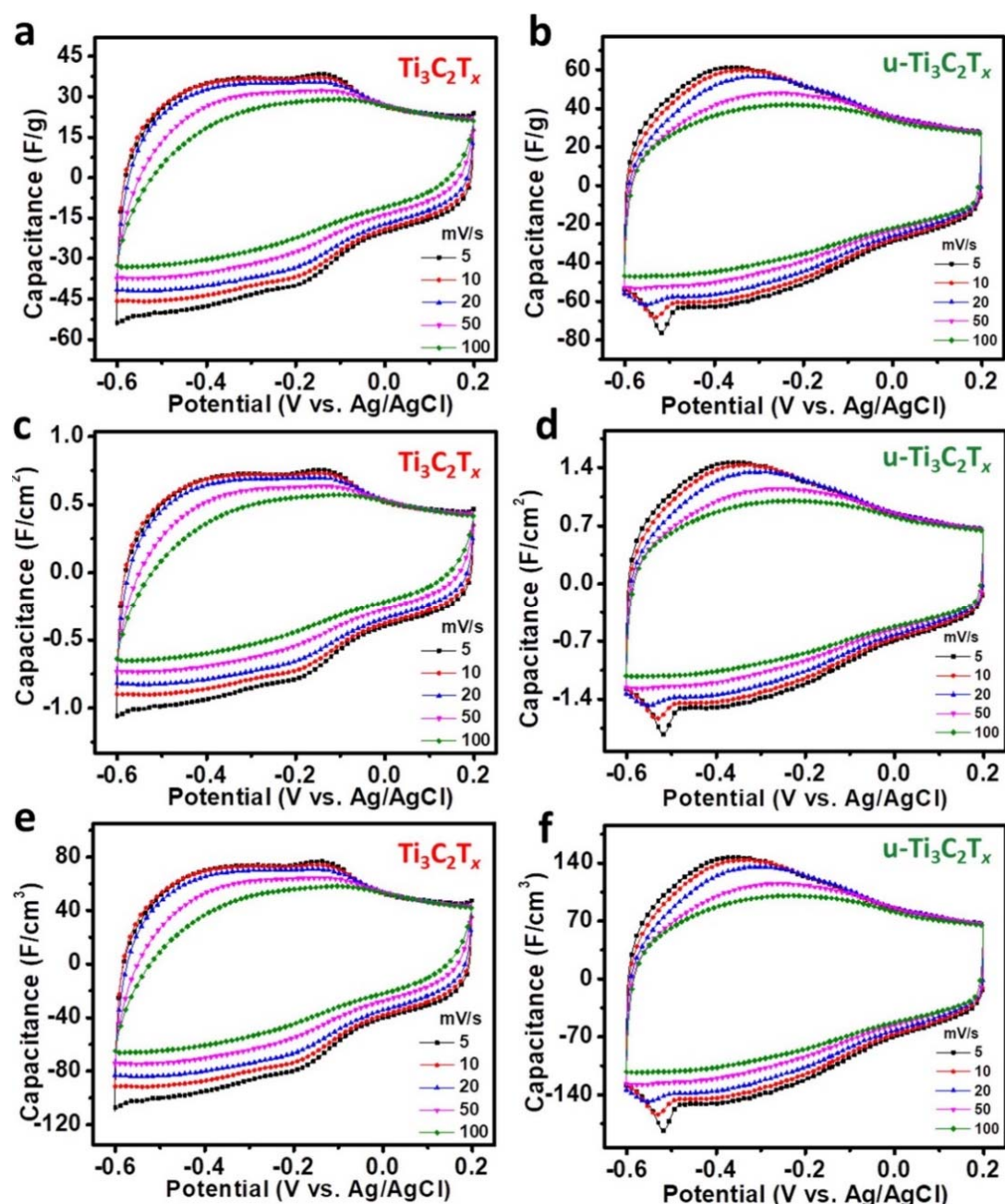
Figure 3.3 Cyclic voltammograms at various scan rates for (a, c, e) $Ti_3C_2T_x$ and (b, d, f) u-$Ti_3C_2T_x$ electrodes normalized with respect to weight, area and volume of the electrodes. Taken with permission from Ref. [72].

3.5 Individual Multilayered Ti₃C₂Tₓ XAS Analysis

The oxidation state of the Ti atoms in $Ti_3C_2T_x$ constitutes a key element in the electrochemical performance. To investigate the oxidation state of the Ti atoms, the XAS technique was applied before and after urea intercalation in different environments. **Figure 3.4 a** shows X-PEEM images taken in vacuum at the Ti L-edge of individual $Ti_3C_2T_x$ MXene flakes before and after urea intercalation. The flakes were found to be a few micrometers in diameter, with sharp edges.
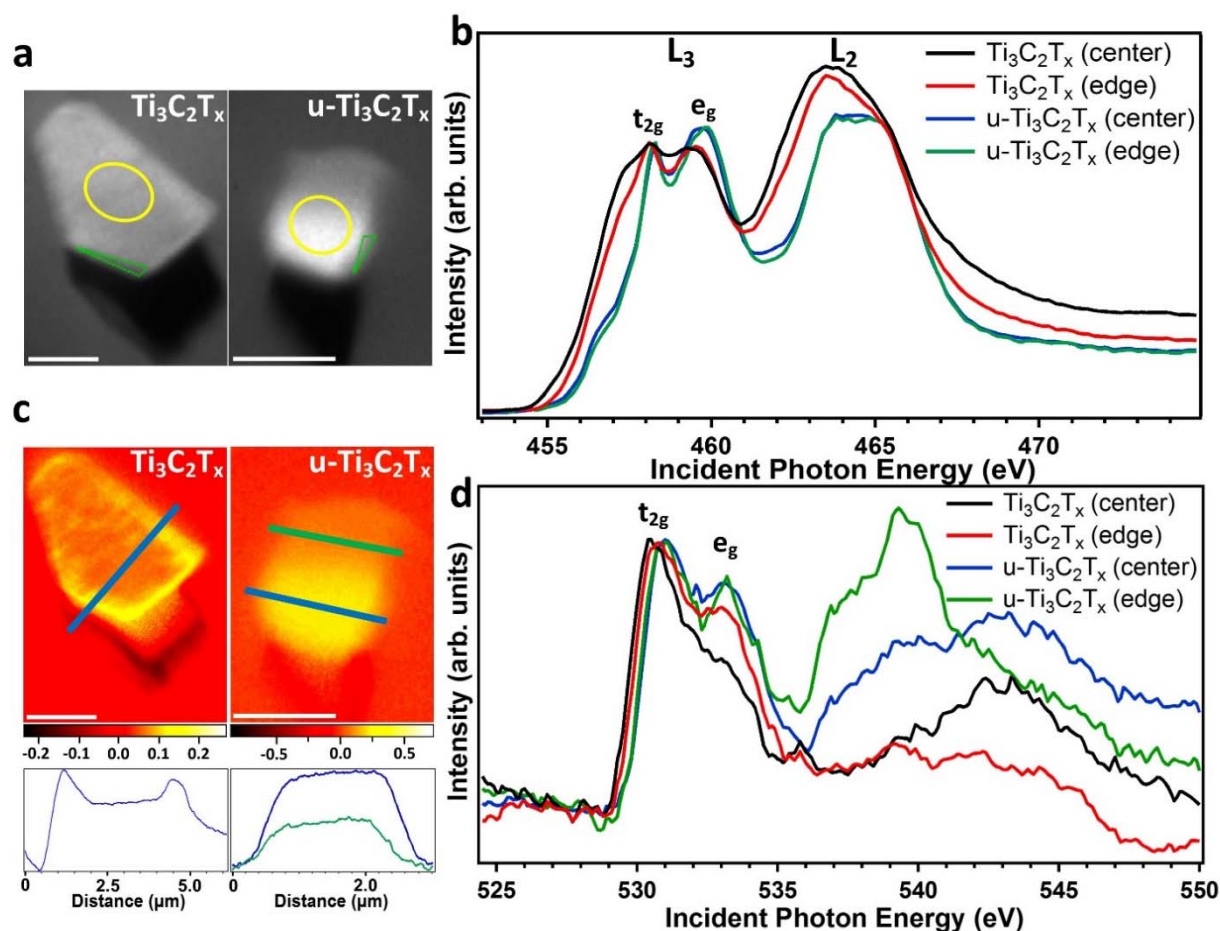
Figure 3.4 (a) X-PEEM micrographs at the Ti L-edge taken at an excitation energy of 463.9 eV (black and white) show individual flakes of pristine $Ti_3C_2T_x$ and u-$Ti_3C_2T_x$ MXenes (scale bar 2 μm). The regions labeled center and edge in (b, d) are highlighted in yellow and green, respectively. (b) X-PEEM Ti L-edge XA spectra of single flakes of pristine $Ti_3C_2T_x$ and u-$Ti_3C_2T_x$ MXenes. (c) Oxygen content distribution over individual MXene flakes obtained from the difference of averaged X-PEEM micrographs at the O K-edge in the t_{2g} and e_g region (530.0–534.5 eV) relative to the background (524.5–529.0 eV), the corresponding line profiles across the flake are shown underneath. (d) X-PEEM O K-edge XA spectra of pristine $Ti_3C_2T_x$ and u-$Ti_3C_2T_x$ MXene samples. Taken with permission from Ref. [72].

The yellow and green marked areas in **Figure 3.4 a** serve to highlight the specific regions denoted as center and edge, respectively, from which XA spectra of the Ti L-edge were extracted from the spectral images. For the $Ti_3C_2T_x$ MXene flake, the splitting of the L_3 edge into t_{2g} and e_g sub-bands was observed at each location on the flake but is more defined at the edge. The onset of the Ti Ledge, shown in **Figure 3.4 b**, also varies between the edge and the center of the flake and is used to estimate the Ti oxidation state. The onset energy shifts from 454.6 eV at the center compared to 455.0 eV at the edge of the flake, corresponding to an estimated oxidation state slightly higher than Ti^{3+} at the center, while the edge position is relatively close to Ti^{4+}. For the $u-Ti_3C_2T_x$ MXene flake, the X-PEEM based XAS reveals that the L_3 feature splits into two pronounced sub-bands corresponding to the t_{2g} and e_g peaks. The pre-edge onset energy of 455.8 eV is independent of location on the $u-Ti_3C_2T_x$ flake and corresponds to a large Ti^{4+} contribution. The Ti atoms are in a significantly higher state of oxidation relative to the pristine $Ti_3C_2T_x$ MXene flake and are homogeneously oxidized over the entire flake.

The oxygen distribution and local bonding environment were also characterized by X-PEEM at the O K-edge. To better visualize the oxygen distribution across the flake, X-PEEM difference images are shown in **Figure 3.4 c**. A higher contrast close to the flake edges demonstrates a higher oxygen content in this region for the pristine MXene, while the oxygen content appears homogeneous after urea intercalation. **Figure 3.4 d** shows a comparison of O K-edge XA spectra for pristine $Ti_3C_2T_x$ and $u-Ti_3C_2T_x$ MXenes at the center and edge positions of the flakes. The MXene spectral features at 530.8 and 533.2 eV are assigned to the t_{2g} and e_g orbitals, respectively. However, for the pristine $Ti_3C_2T_x$, the e_g peak intensity was found to be relatively low in the center, suggesting a lower average oxidation state there relative to the edges. After urea intercalation, the e_g peak at 533.2 eV becomes well resolved, as shown in **Figure 3.4 d**. The O K-edge spectra thus emphasize the similar oxidation state across the $u-Ti_3C_2T_x$ MXene flake, which agrees with the Ti L-edge results. Note that the contribution of intercalated urea possibly appears between 532.5 and 534.0 eV. The features observed between 537.0 and 540.0 eV at the $u-Ti_3C_2T_x$ edge position are attributed to the SiO_2 substrate (**Figure 3.5**). **Figure 3.6** also indicates that the oxygen content on pristine $Ti_3C_2T_x$ is mostly concentrated in the first few hundreds of nanometers from the edge.

The higher Ti oxidation state at the edges of the pristine $Ti_3C_2T_x$ MXene can probably be explained by its higher exposure to water molecules and oxygen from the ambient environment during aqueous dispersion and drying in air. Indeed, the oxidation proceeds faster at the edge positions of a $Ti_3C_2T_x$ flake relative to the basal plane, which has been found to eventually contribute to an overall decrease in conductivity of MXene electrodes [102–105].
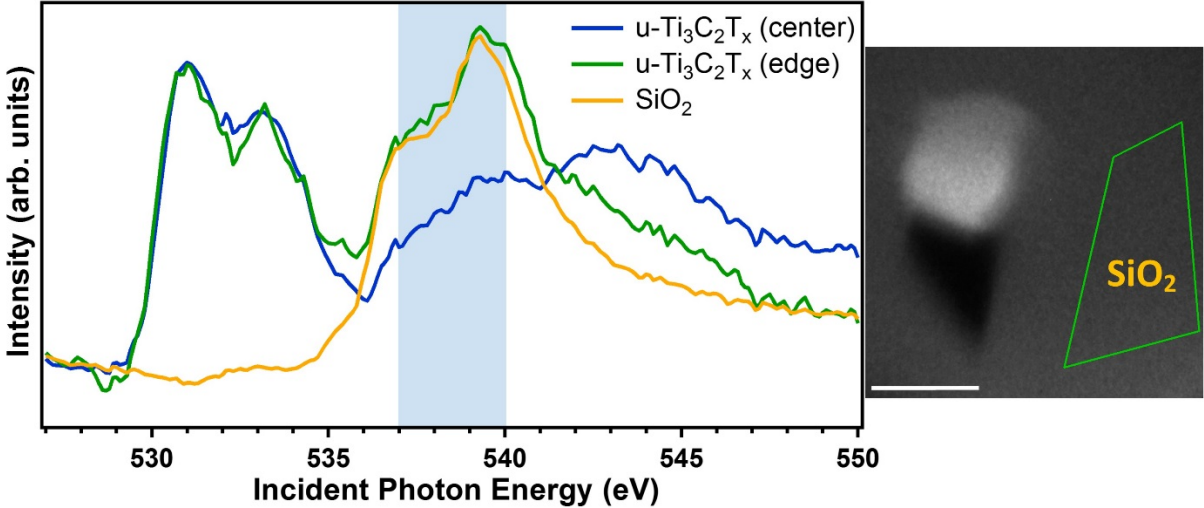
Figure 3.5 X-PEEM O K-edge XA spectra of u-$Ti_3C_2T_x$ MXene sample and to the right is the corresponding micrograph. The spectra show that the XA peak around 537.0-540.0 eV at the edge position relates to the signature of the SiO_2 substrate (scale bar 2 μm). Taken with permission from Ref. [72].
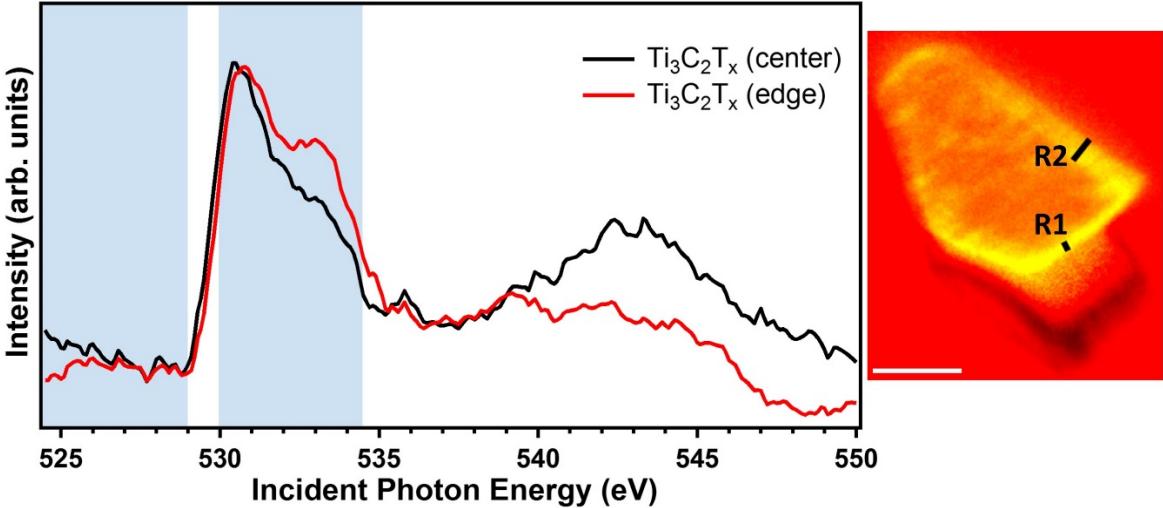
Figure 3.6 X-PEEM O K-edge XA spectra of the pristine $Ti_3C_2T_x$ MXene sample. The corresponding X-PEEM image to the right is obtained from the spectral image difference between the regions from 530.0-534.5 eV compared to the background region from 524.5-529.0 eV in order to illustrate the oxygen distribution over the entire flake. This image highlights the higher oxidation state regions at the edges of the flake. The width of R1 and R2 are about 225 ±30 nm and 635 ±30nm, respectively (scale bar 2 μm). Taken with permission from Ref. [72].

3.6 Liquid/Dried MXene XAS Measurements

As the oxidation state of MXenes strongly influences their redox properties and despite a high Ti oxidation state (close to Ti^{4+}) after urea intercalation, u-$Ti_3C_2T_x$ electrodes exhibit a reversible redox reaction, as evident from the broad redox profile shown earlier in **Figure 3.2 a**. To estimate the origin of the increased Ti oxidation, *in situ* XAS measurements were also directly performed in water. The effects of aqueous solvation on the Ti oxidation state of the MXenes were monitored by comparing the Ti L-edge XA spectra of dried and dispersed pristine $Ti_3C_2T_x$ MXene multilayered powders (**Figure 3.7**).
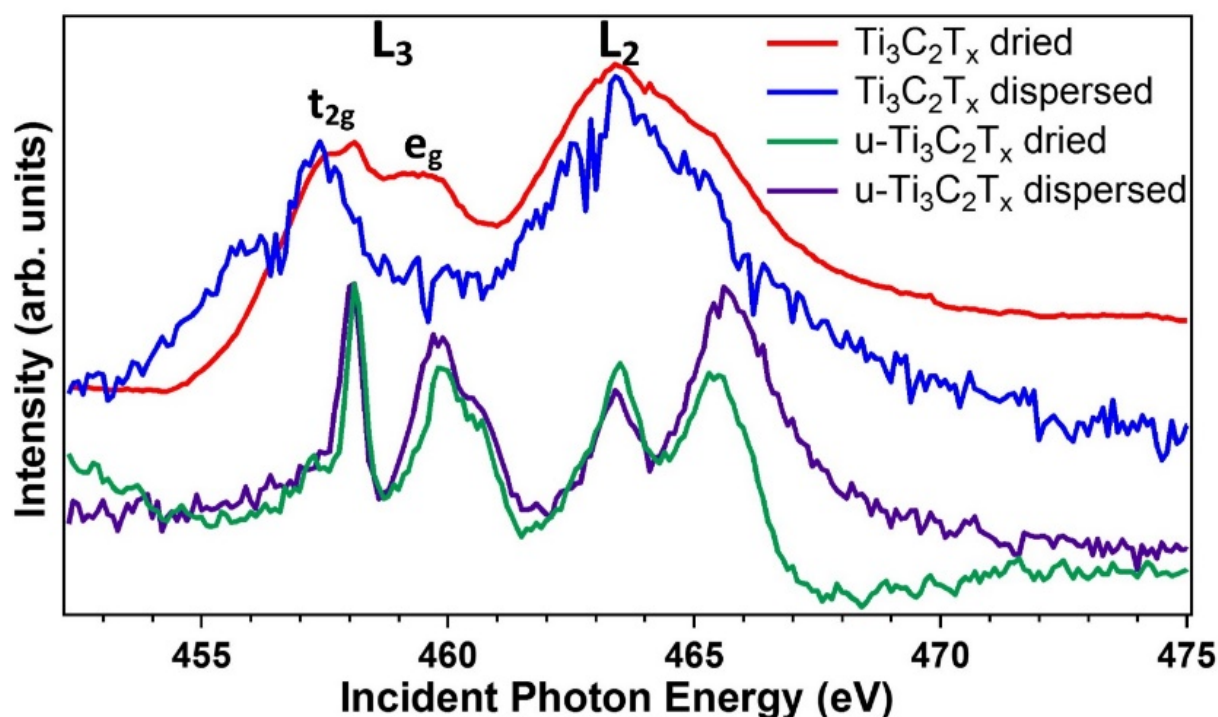
Figure 3.7 Ti L-edge XA spectra of dried and dispersed pristine $Ti_3C_2T_x$ and u-$Ti_3C_2T_x$ MXenes. Dispersed samples in water were characterized by XAS in TFY mode using a flow cell (as shown in section 2.3.2) and dried samples TEY mode in vacuum. Taken with permission from Ref. [72].

For the $Ti_3C_2T_x$ powder dried in air and then characterized under vacuum, the Ti L_3-edge includes a peak at around 458.1 eV and a shoulder at about 459.4 eV, which confirms the coexistence of different Ti species, while the Ti L_2-edge shows a single peak at about 463.4 eV. The XA spectra of the dried $Ti_3C_2T_x$ MXene sample, averaged over a large number of flakes, are very similar to the X-PEEM spectra recorded for individual flakes. On the other hand, the XAS of dispersed $Ti_3C_2T_x$ MXene shows no splitting of the Ti L_3-edge into t_{2g} and e_g states, and a broad peak is detected at 457.4 eV. This new feature is shifted by -0.7 eV compared to the maximum of the L_3 peaks of dried $Ti_3C_2T_x$ sample, indicating a lower oxidation state. Estimation

of the Ti oxidation state from the pre-edge onset suggests a contribution from Ti^{2+} species for the dispersed sample [63].

For u-$Ti_3C_2T_x$ samples, the Ti L-edge XA spectra have similar profiles in both dry and solvated environments, as depicted in **Figure 3.7**. The $L_{2,3}$ edges split into two components separated by about 5.4 eV. The Ti L_2-edge (462.3–467.6 eV) features are broadened relative to the Ti L_3-edge (457.3–461.3 eV) features and are similar to previous reports on TiO_2 materials [78]. The e_g peaks are broader than the t_{2g} peaks, which can be attributed to a larger degree of hybridization of the Ti e_g orbitals with O orbitals [106]. Unlike the pristine $Ti_3C_2T_x$ MXenes, the surface Ti atoms in both dried and solvated u-$Ti_3C_2T_x$ MXenes have an averaged oxidation state close to Ti^{4+}, like in TiO_2. *In situ* O K-edge XAS was also performed for $Ti_3C_2T_x$ and u-$Ti_3C_2T_x$ MXenes dispersed in water, which supports the higher oxygen bonding to Ti atoms on u-$Ti_3C_2T_x$ MXenes, see **Figure 3.8**.
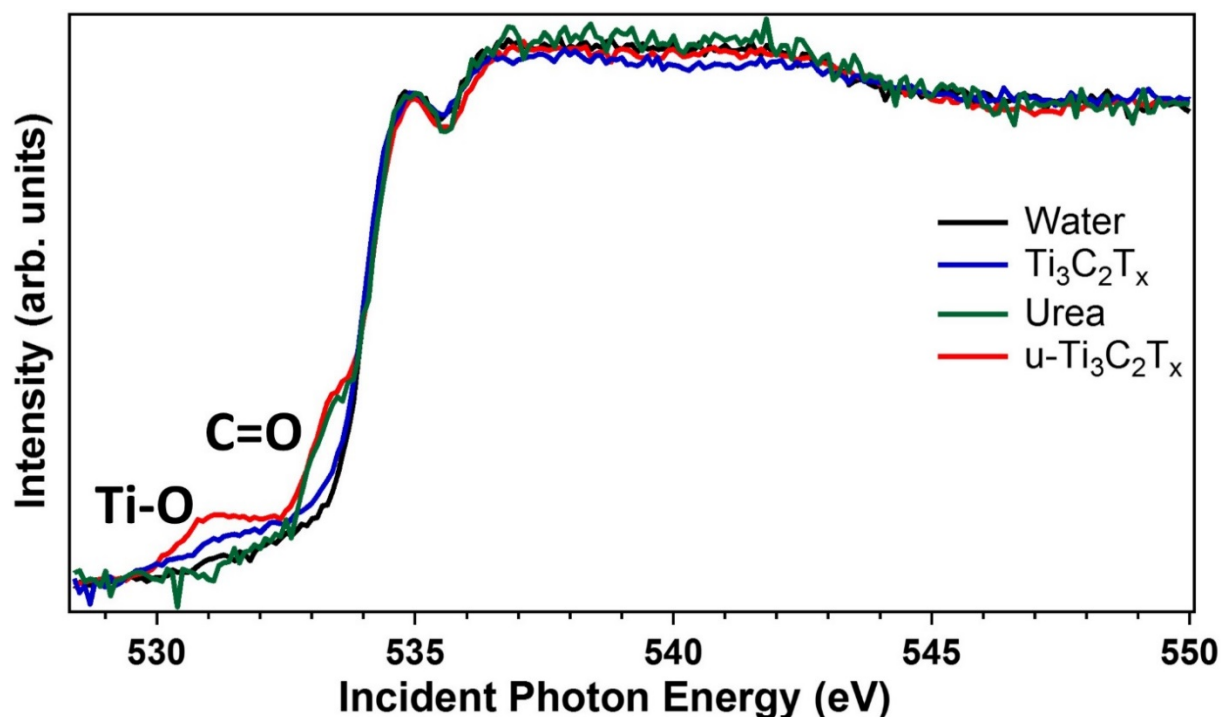
Figure 3.8 O K-edge XA spectra of dispersed in water $Ti_3C_2T_x$ (blue), u-$Ti_3C_2T_x$ (red), urea (green), and pure water (black). These spectra were characterized by XAS in TFY mode using a flow cell. Taken with permission from Ref. [72].

Figure 3.8 is also showing the XA spectra of pure water and a 1M aqueous urea solution for comparison. The main contributions of the XA spectra, namely the pre-edge at 535.0 eV and main/post edges > 535.0 eV are associated with oxygen from water molecules in a liquid hydrogen-bonding environment [107]. Two distinctive shoulders are detected in the pre-edge

region (below 535.0 eV). The broad feature around 531.0 eV is due to Ti-O bonds [64], as also reported in the X-PEEM data analysis. This region is clearly more pronounced after intercalation of urea, which confirms the higher level of Ti oxidation. The shoulder at about 533.5 eV is mostly related to C=O bonds from dissolved urea molecules. Due to the high urea concentration in the dispersion, this contribution is most likely attributed to free urea in solution rather than intercalated urea molecules.

These results demonstrate that the oxidation state of the Ti atoms of the pristine $Ti_3C_2T_x$ samples varies with the sample environment. The averaged Ti oxidation state of the dried $Ti_3C_2T_x$ MXene was found to be close to the Ti^{3+} species, similar to that observed in the X-PEEM results. On the other hand, $Ti_3C_2T_x$ dispersed in water shows a significant contribution from Ti^{2+} species, which is probably induced by a significant increase of the hydroxyl groups at the MXene surface after dispersion in water, inducing a reduction of the Ti oxidation state. No clear e_g peak is observed at the L_3-edges as opposed to the dry sample, showing that no Ti−O bonds with a strong σ-character are detected in water. The same sample has been used for these experiments so that pristine $Ti_3C_2T_x$ MXene may be slightly oxidized upon drying in air [102]. As a result, $Ti_3C_2(OH)_2$ terminations may change to $Ti_3C_2O_2$ terminations, resulting in an increase in the Ti oxidation state to Ti^{3+}.

In contrast, Ti atoms of the u-$Ti_3C_2T_x$ MXene appear highly oxidized both in water and after drying with an estimated average Ti oxidation state very close to Ti^{4+}. It is worth noting that this higher Ti oxidation state does not mean that the MXene samples are transformed into TiO_2, as no signature from TiO_2 is evident in the full XRD pattern shown in **Figure 3.9**.
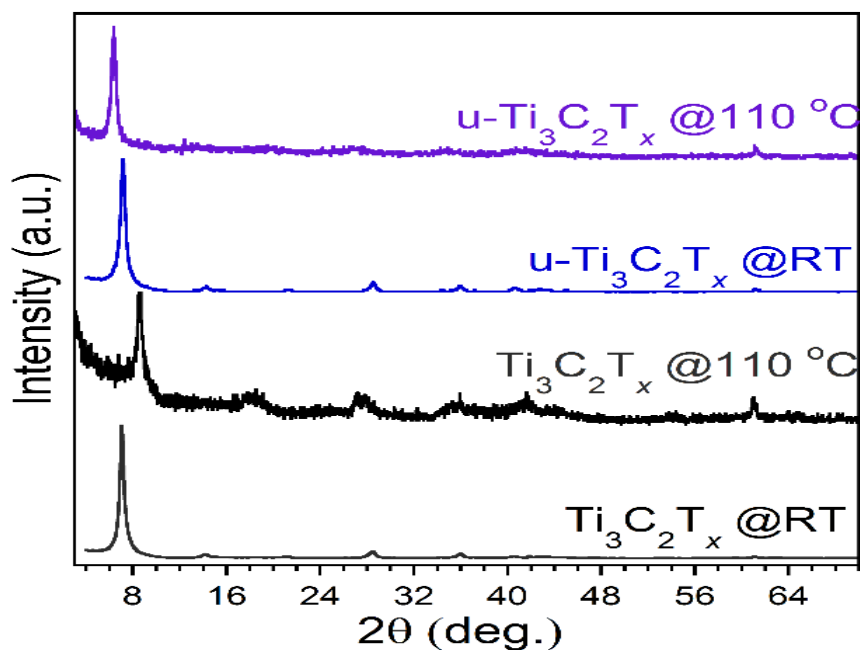
Figure 3.9 Full XRD patterns of the as-synthesized $Ti_3C_2T_x$ powder ($Ti_3C_2T_x$ @RT), $Ti_3C_2T_x$ after annealing at 110 °C for 12 hours ($Ti_3C_2T_x$ @110 °C), $Ti_3C_2T_x$ after urea adsorption at room temperature for 12 hours (u-$Ti_3C_2T_x$ @RT), and $Ti_3C_2T_x$ after urea adsorption at 110 °C for 12 hours (u-$Ti_3C_2T_x$ @ 110°C). Taken with permission from Ref. [72].

Shedding light on the difference in the MXene oxidation state and surface chemistry after urea intercalation requires a thorough understanding of the intercalation mechanism. The interlayer distance of the $Ti_3C_2T_x$ planes after urea intercalation is similar but results from different intercalated molecules (water or urea, **Figure 3.1 b**), and thus weaker van der Waals and hydrogen bonding between the layers [108]. Owing to the size of urea, the urea molecules might occupy considerable space within the interlayer between the MXene sheets with a preference of parallel orientation to the MXene surface [26]. The increased MXene interlayer spacing may facilitate the bonding of oxygen, possibly coming from urea molecules, to the surface Ti atoms, and thus a higher Ti oxidation state is observed. On the other hand, the strong interaction between urea molecules and the Ti atoms on the MXene surface [26] would likely prevent hydroxylation of the surface Ti atoms upon dispersion in water. Higher oxidation occurs over the entire MXene flake for u-$Ti_3C_2T_x$, while only the edges are oxidized in the pristine $Ti_3C_2T_x$ MXene. The higher Ti oxidation of u- $Ti_3C_2T_x$ is apparently not reversible after dispersion in water. The higher oxidation of surface Ti atoms after urea intercalation is most probably related to the observed higher pseudocapacitance. The latter is in full agreement with previous work on TiO_2-Ti_3C_2 nanocomposites showing capacitance about 54% higher

relative to pristine $Ti_3C_2T_x$ electrodes [109]. Furthermore, another study revealed that having a more oxygen terminated surface group in $Ti_3C_2T_x$ MXene led to enhanced electrochemical performance [110].

3.7 Summary

In summary, the areal capacitance of multilayered u-$Ti_3C_2T_x$ powder-based electrodes is found to be 1100 mF/cm^2, reflecting a 56% increase compared to pristine $Ti_3C_2T_x$ electrodes. Interestingly, accelerated diffusion of the electrolyte ions in the presence of urea was observed. We have probed the chemical environment of Ti atoms of both pristine $Ti_3C_2T_x$ and u-$Ti_3C_2T_x$ MXene samples through XAS-based characterization in vacuum and aqueous dispersions. Despite the high observed Ti oxidation state (close to Ti^{4+}), induced by covalent bonding with oxygen atoms, reversible redox reactions have been shown in u-$Ti_3C_2T_x$ electrodes, as is evident from the broad redox profile. This suggests that a higher metal oxidation state constitutes an opportunity to enhance the electrochemical performance in MXene-based electrodes. The XA spectra at the Ti L- and O K-edges show that the electronic structure of $Ti_3C_2T_x$ is dramatically altered after urea intercalation. Using the high spatial resolution of X-PEEM, a direct mapping of the electronic structure of Ti and O atoms over a single $Ti_3C_2T_x$ flake demonstrated higher oxidation at the edges compared to the basal plane of the flake, while homogeneous oxidation was detected over the entire u-$Ti_3C_2T_x$ MXene flake. Finally, in situ XAS measurements in water demonstrated that hydration affects the chemical bonding of Ti atoms in pristine $Ti_3C_2T_x$ MXene. This work illustrates that soft X-ray absorption spectroscopy is a powerful method for probing the electronic structure of oxygen terminated transition metal surface of MXenes in various environments. It paves the way to further investigations on MXene surface chemistry, especially after intercalation with various compounds or cations.

CHAPTER FOUR

Impact of Cations Intercalation and H_2SO_4 Environment on $Ti_3C_2T_x$ using *Ex/In Situ* and *Operando* XAS

4.1 Motivation

The success to find a link between the oxidation state of the surface Ti atoms of $Ti_3C_2T_x$ and a higher electrochemical performance after urea intercalation (chapter one) leads to further deep investigations using mono and/or multivalent metal cations such as Li^+, Na^+, K^+, Mg^{2+} intercalants in different environments. Unlike urea, these cations are already known for their effective redox interaction with the surfaced of metal oxides, suggesting not only a higher electrochemical performance but also better ion ad/desorption in favor of MXene-based membranes. Below are the purposes to study the pristine, Li-, Na-, K-, and Mg-$Ti_3C_2T_x$ MXenes under different conditions.

1- What are the intercalation impacts of Li^+, Na^+, K^+, and Mg^{2+} cations on the surface chemistry of multi-layered $Ti_3C_2T_x$ in different environments?

2- This requires first, *ex situ* study of dried pristine, Li-, Na-, K-, and Mg-$Ti_3C_2T_x$ MXenes initially dispersed in water or sulfuric acid.

3- What is the surface Ti oxidation state and the interlayer spacing of each sample as well as the corresponding electrochemical performance?

4- As we successfully could use the membrane-based electrochemical flow cell, *in situ operando* XAS study of cation-intercalated $Ti_3C_2T_x$ in sulfuric acid under applied potential is urgently need to be addressed to gain more information about the local chemical nature.

What is the essence of this chapter?

Intercalation in $Ti_3C_2T_x$ MXene is essential for a diverse set of applications such as water purification, desalination, electrochemical energy storage, and sensing. The interlayer spacing between the $Ti_3C_2T_x$ nanosheets can be controlled by cation intercalation; however, the impact of intercalation on the $Ti_3C_2T_x$ MXene chemical and electronic structures is not well understood. Herein, we characterized the electronic structure of pristine, Li-, Na-, K-, and Mg-intercalated $Ti_3C_2T_x$ MXenes dispersed initially in water and 10 mM H_2SO_4 using XAS. The cation intercalation is found to dramatically influence the chemical environment of Ti atoms. The Ti oxidation of the MXene increases progressively upon intercalation of cations of larger sizes after drying in air, while interestingly a low Ti oxidation is observed for all intercalated MXenes after dispersion in diluted H_2SO_4. *In situ* XAS at the Ti L-edge was conducted during

electrochemical oxidation to probe the changes in the Ti oxidation state in the presence of different cations in H_2SO_4 aqueous electrolyte. By applying the sensitivity of the Ti L-edge to probe the oxidation state of the surface Ti atoms, we demonstrate that cation-intercalation and H_2SO_4 environment significantly alter the $Ti_3C_2T_x$ surface chemistry.

4.2 Research Background

Owing to their extraordinary properties, MXenes are attracting an enormous attention for many applications ranging from filtration [111], electrochemical energy storage [28–30,32,54], water purification and desalination [25,112–115], to sensing [116–119]. The redox pseudocapacitance has mostly been studied so far with pristine $Ti_3C_2T_x$ MXenes but the energy density of MXene-based electrodes may be enhanced by wide range of cation intercalation due to the fact that MXene interlayer spacing becomes larger [28,120]. The variety of cation intercalation was found to have a notable impact on the overall capacitance [28,45]. For water desalination, efficient and reversible electrochemical ion ad/desorption is required [121]. As a result, for practical separation purposes, laminar membranes with horizontally aligned channels constructed from 2D material such as MXene are a perfect choice. Indeed, attractive separation properties of MXene-based membranes demonstrate rejection toward cations of different sizes and charges in solution.[112] Furthermore, a remarkable study shows MXene membranes with highly ordered nanochannel structures can be employed for gas separation such as H_2 purification and CO_2 capture for zero-emission fossil fuel power plant [122]. Ion intercalation in $Ti_3C_2T_x$ MXenes could be used to tune the MXene interlayer spacing and open new possibilities for molecular separation applications using MXene-based membranes. XRD measurements have shown that the size of hydrated ions influences the interlayer spacing distance between $Ti_3C_2T_x$ nanosheets (**Figure 1a**) [28,119]. The presence of cations between individual MXene sheets does also influence the amount and the structure of the co-intercalated water [119]. As a result, the water mobility is significantly affected by the type, number, and position of the cations within the $Ti_3C_2T_x$ interlayer spacing [123–125]. However, the role of cation intercalation on the surface chemistry of $Ti_3C_2T_x$ MXenes has still been poorly investigated [27], even though it may strongly impact the oxidation state of Ti atoms and thus the chemical reactivity of the MXene layers.

In this chapter, the surface chemistry and metal oxidation state of cation-intercalated $Ti_3C_2T_x$ was probed using XAS. In particular, the characterization of transition metal L-edges is very sensitive to the metal chemical environment [63,64,78]. A shown in chapter two, XAS on $Ti_3C_2T_x$ MXenes intercalated with urea molecules has detected significant changes in the Ti electronic structure [72]. Nevertheless, cations may have a very different mechanism of intercalation between the $Ti_3C_2T_x$ nanosheets because of their smaller size and higher charge, which would affect differently the Ti oxidation state. Furthermore, for electrochemical energy storage applications, aqueous sulfuric acid electrolyte is mostly used but its impact on the $Ti_3C_2T_x$ MXene surface chemistry remains largely unexplored. Herein, the electronic structure of $Ti_3C_2T_x$ MXenes after intercalation with Li^+, Na^+, K^+, and Mg^{2+} is characterized by XAS at the Ti L-edge. *Ex situ* XAS measurements were performed to probe the Ti oxidation state of dried cation-intercalated $Ti_3C_2T_x$ initially dispersed in water or sulfuric acid. Furthermore, *in situ* XAS at the Ti L-edge was performed to track the changes in the oxidation of Na-, K-, and Mg-$Ti_3C_2T_x$ in sulfuric acid under an anodic potential, leading to the electrochemical oxidation of the $Ti_3C_2T_x$ MXenes. The data performed in this chapter are summarized in **Scheme 1**. The evolution of the oxidation state of Ti atoms in the $Ti_3C_2T_x$ MXenes is significantly affected by cation intercalation and exposure to sulfuric acid and is found to be cation-dependent.
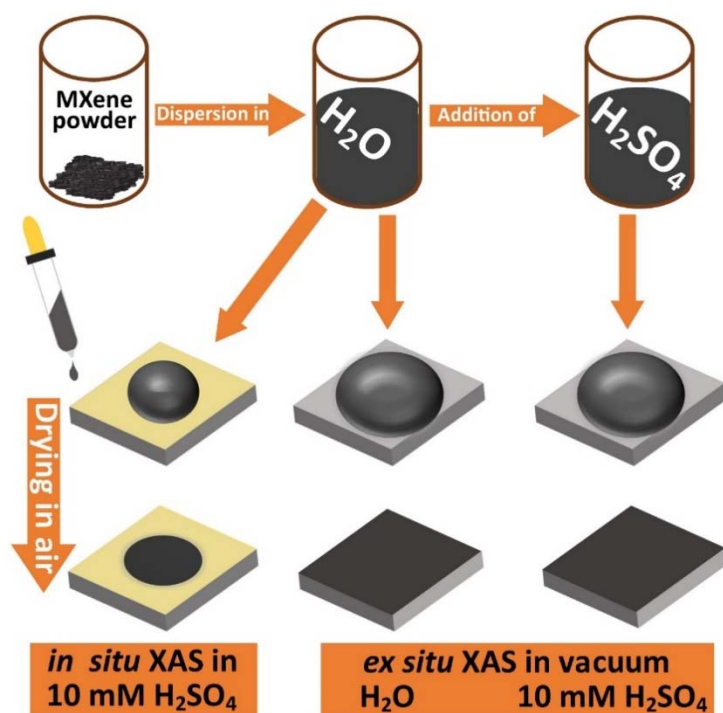
Scheme 1. Schematic of the MXene samples preparation for pristine and cation-intercalated $Ti_3C_2T_x$ films investigated in this work. For *ex situ* and *in situ* XAS, the samples were drop cast on a conductive silicon substrate and on a gold-coated silicon nitride membrane, respectively. The soft X-ray transparent membrane was used in the electrochemical flow cell system as shown in section 2.3.2. Taken with permission from Ref. [73].

4.3 Cation Intercalation in $Ti_3C_2T_x$ MXenes

Figure 4.1 a illustrates a schematic of the pristine (top) and cation intercalated (bottom) $Ti_3C_2T_x$ MXenes. For brevity, the bottom schematic shows the possibility of intercalation by different cations in-between the $Ti_3C_2T_x$ nanosheets. The details of the materials synthesis are shown in section 2.5.2. Based on energy dispersive X-ray spectroscopy (EDS) results, the ratio of Ti to cation in Na-, K-, and Mg-$Ti_3C_2T_x$ MXenes was found to be Ti/Na = 3.00:0.17, Ti/K = 3.00:0.14, and Ti/Mg = 3.00:0.12. It is worth noting that Li cannot be detected using EDS. However, because, like the Na^+ and K^+, the Li^+ cation is monovalent, it is reasonable to assume similar content of Li (0.14−0.17 Li per formula).
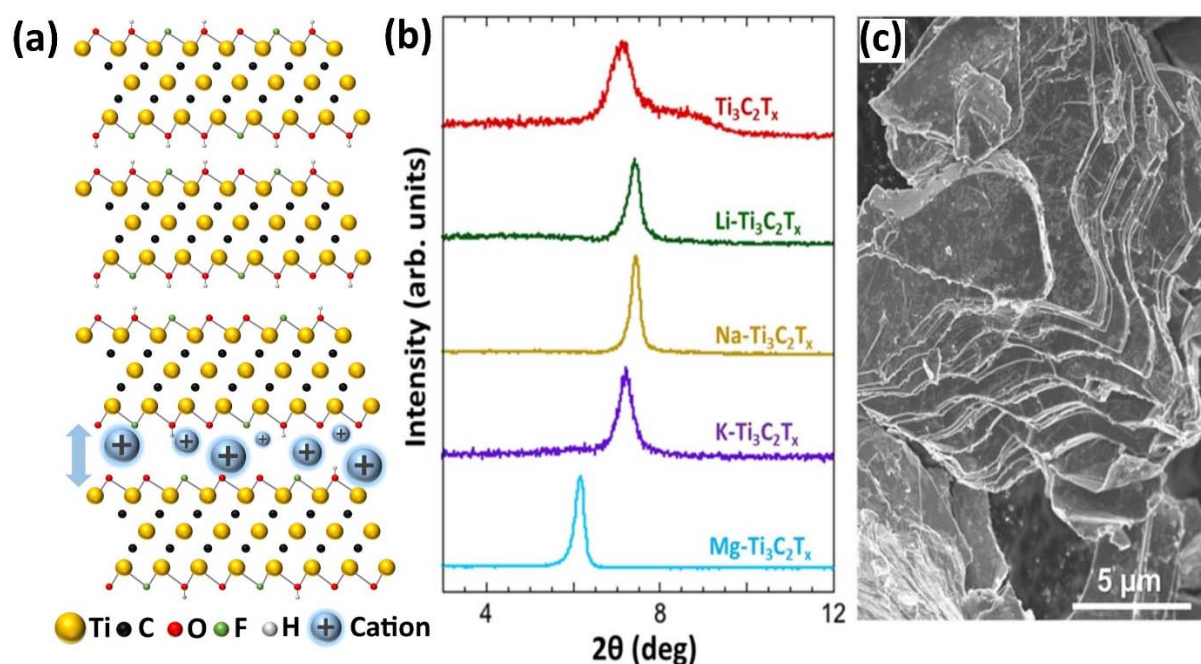
Figure 4.1 (a) Schematic of pristine $Ti_3C_2T_x$ MXenes (top) and cation-intercalated $Ti_3C_2T_x$ MXenes (bottom) showing the possibility to intercalate $Ti_3C_2T_x$ with cations of different sizes (b) Normalized XRD patterns of pristine, Li-, Na-, K-, and Mg-intercalated $Ti_3C_2T_x$ MXenes. (c) A typical representative SEM image of cation-intercalated $Ti_3C_2T_x$ MXenes (this specific SEM image is Na-MXene as an example)**.** Taken with permission from Ref. [73].

Figure 4.1 b shows normalized XRD (002) peak shifts of the intercalated MXenes studied. Because the position of 002 peak is inversely related to the interlayer spacing between the MXene nanosheets (*d*-spacing), the position of this peak can be used to compare the relative interlayer spacing of different MXenes. Li-$Ti_3C_2T_x$, Na-$Ti_3C_2T_x$, and K-$Ti_3C_2T_x$ have a comparable *d*-spacing (with slightly larger spacing for K than for Na and Li) but all of them much smaller than that for Mg-$Ti_3C_2T_x$ (see **Table 4.1**).

Table 4.1: The *c*- lattice parameter of pristine, Li-, Na-, K-, and Mg-intercalated $Ti_3C_2T_x$ MXenes before and after exposure to 10 Mm H_2SO_4. Taken with permission from Ref. [73].

MXene sample	c-lattice parameter (Å)	c-lattice parameter (Å) after exposure to 10 mM H_2SO_4	Difference (Å)
Pristine $Ti_3C_2T_x$	24.76	27.01	+2.25
Li-$Ti_3C_2T_x$	23.81	24.60	+0.79
Na-$Ti_3C_2T_x$	23.69	25.17	+1.48
K-$Ti_3C_2T_x$	24.46	25.24	+0.78
Mg-$Ti_3C_2T_x$	28.58	29.54	+0.96
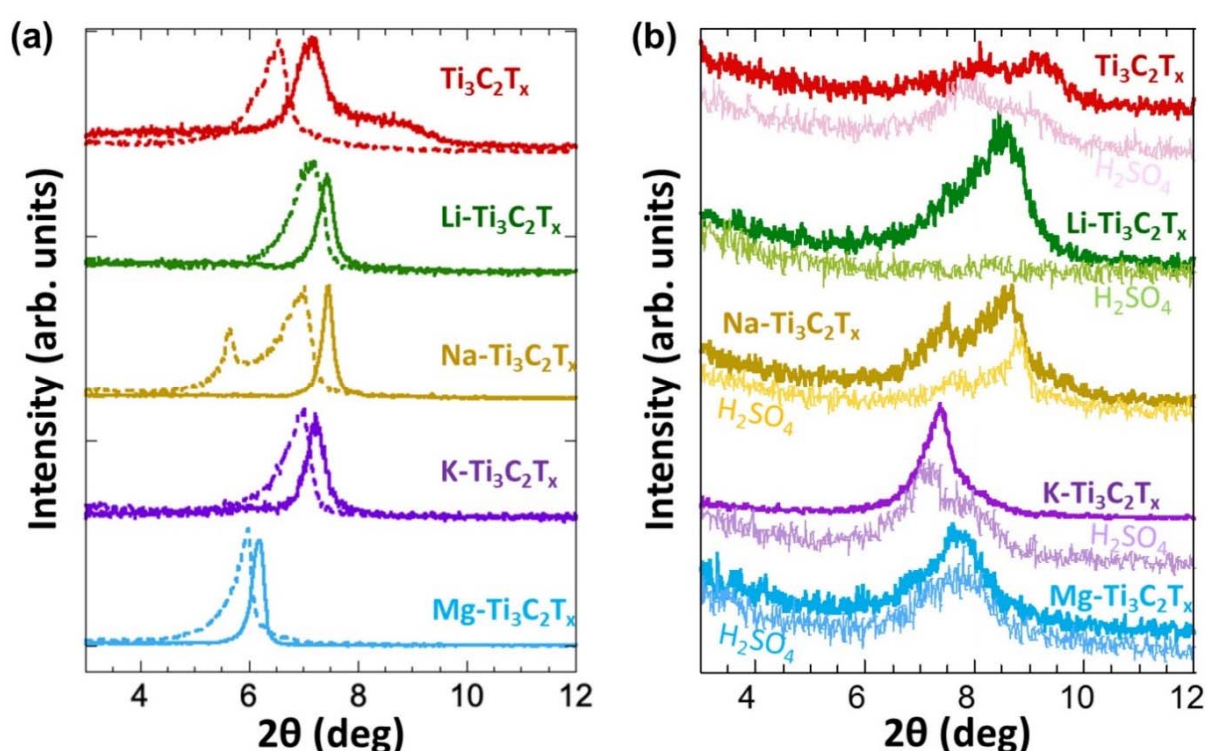
Figure 4.2 Normalized XRD patterns of pristine, Li-, Na-, K-, and Mg-intercalated $Ti_3C_2T_x$ MXenes. Before and after dispersion in H_2SO_4 then dried in (a) air and (b) dried in air followed by vacuum annealing at 110 °C for 4h. In (a) the XRD patterns showing the 002 diffraction order peak before (solid line) and after dispersion in 10 mM H_2SO_4 (dotted line). In (b) thinner lines are for H_2SO_4 dispersed samples after vacuum annealing while thick lines are for as prepared samples after vacuum annealing. Taken with permission from Ref. [73].

This is in agreement with previous reports for cation-intercalated MXenes and suggests that the cations remain hydrated after intercalation [47,86,119]. It is worth noting that two peaks can be observed for the pristine MXene suggesting incomplete removal of Li from in-between the layers during the HCl washing step. Alternatively, the presence of two peaks in pristine

MXene can be attributed to the co-intercalated water from the washing step in-between the layers for some particles. To check this, the pristine MXene sample was characterized by XRD after annealed under vacuum at 110 °C for 4 h. Accordingly, we found that the low-angle peak vanishes, as shown below in **Figure 4.2 b** suggesting that the co-intercalated water might be responsible for the evolution of this peak. **Figure 4.1 c** shows a scanning electron microscopy (SEM) image of a typical multi-layered MXene used in this study. Here, we can clearly see the layered morphology of the MXenes powder.

4.4 *Ex Situ* XAS of $Ti_3C_2T_x$ Initially Dispersed in H_2O

The electronic structure of the intercalated MXene was first characterized ex situ using XAS in TEY detection mode to observe the influence of intercalation with different cations. The cation-intercalated MXene samples were allowed to dry in air at RT before characterization in vacuum (see **Scheme 1**).
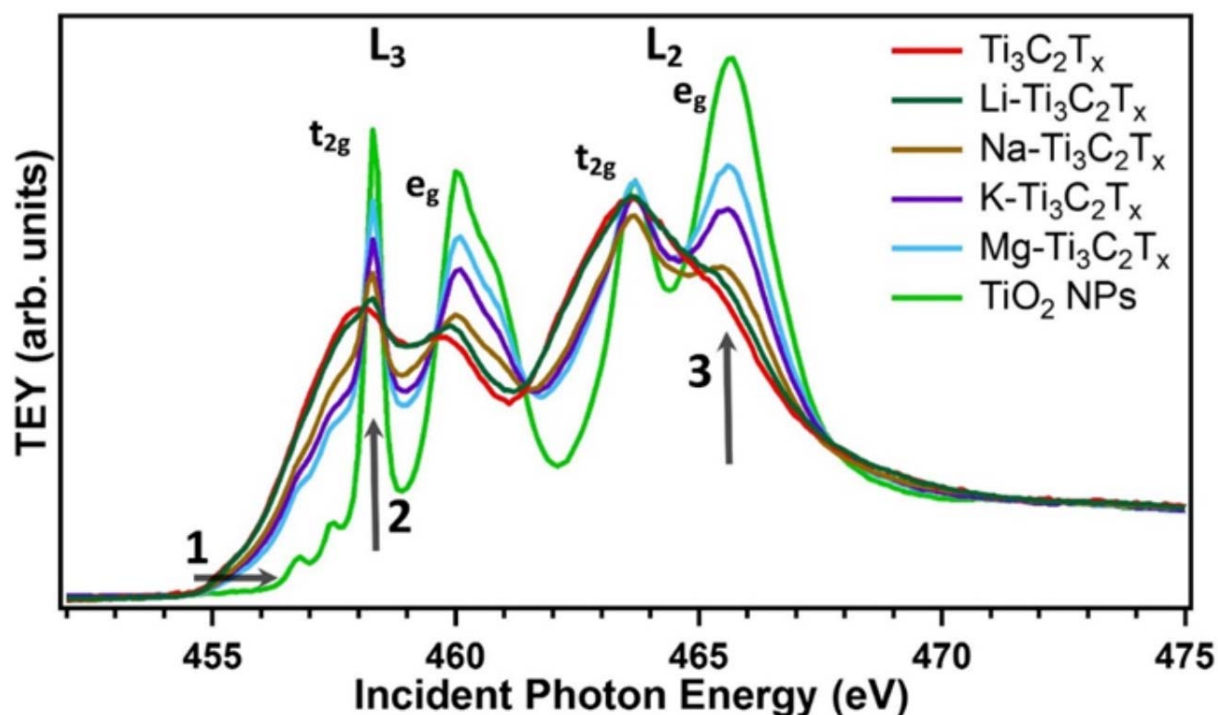
Figure 4.3 Ti L-edge XA spectra of dried pristine, Li-, Na-, K-, and Mg-intercalated $Ti_3C_2T_x$ MXenes initially dispersed in water compared to TiO_2 NPs. XAS was recorded in total electron yield (TEY) mode in vacuum and the XA spectra are normalized to the TEY signal above 470 eV. The XA spectra reveal three distinctive regions. The feature (1) shows higher Ti oxidation state as the pre-edge region shifts to higher energies. The feature (2) shows a progressive increase in the L_3 t_{2g} peak intensity at the expense of the pre-edge region. The feature (3) reveals a systematic increase in the L_2 e_g peak intensity for larger cations. Taken with permission from Ref. [73].

The XA spectra at the Ti Ledge of $Ti_3C_2T_x$ MXenes comprise two doublets related to the Ti L_3- and L_2-edges with 455.0-462.0 eV and 462.0-468.0 eV excitation energies, respectively. As a result, XAS has shown a high sensitivity to the Ti chemical environment, as illustrated in **Figure 4.3**, showing the Ti L-edge XA spectra of pristine, Li-, Na- K-, and Mg-$Ti_3C_2T_x$ MXenes compared to TiO_2 NPs (as a reference).

While the features of the Ti L-edge XAS are relatively similar for pristine and Li-$Ti_3C_2T_x$ MXenes, they differ significantly for Na-, K-, and Mg-$Ti_3C_2T_x$ MXenes. For pristine (Li-) $Ti_3C_2T_x$ MXenes, the Ti L_3-edge includes a peak at 458.1 (458.3) eV and a shoulder at about 459.8 (460.0) eV corresponding to the t_{2g} and e_g bands, respectively. For larger ions, the Ti L_3 t_{2g} peak at 458.3 eV became sharper and the peak maximum is shifted by +0.2 eV compared to pristine MXene while the pre-edge feature decreases progressively. The Ti L_2-edge shows a broad band with a maximum at 463.6 eV, and a faint shoulder is observed at 465.3 eV for Li-$Ti_3C_2T_x$. Intercalation of the $Ti_3C_2T_x$ MXene by Na^+, K^+, and Mg^{2+} cations, on the other hand, results in the splitting of the Ti L_3 edge into well-pronounced t_{2g} and e_g sub-bands at 458.3 and 460.0 eV, respectively. Likewise, the Ti L_2 t_{2g} and e_g peaks are well separated at 463.7 and 465.6 eV, respectively. The Ti $L_{3,2}$ t_{2g} and e_g sub-bands become gradually more intense following the order $Li^+ < Na^+ < K^+ < Mg^{2+}$. Thanks to the highly sensitive e_g band to the local environment [77,78] which guides us to observe that the L_2 e_g to t_{2g} peak-to-peak intensity ratio of cation-intercalated $Ti_3C_2T_x$ was 0.83, 0.88, 0.97, and 1.03 for Li-, Na-, K-, and Mg-$Ti_3C_2T_x$ MXenes, respectively. In comparison to the TiO_2 NPs with a e_g/t_{2g} ratio of 1.25, we can attribute the increase in the e_g component observed for the MXene to the higher amount of surface Ti atoms bonded with oxygen in the $Ti_3C_2T_x$ MXenes.

The pre-edge region around 455.0–458.0 eV is observed to be relatively more intense for pristine and Li-$Ti_3C_2T_x$ than other intercalated $Ti_3C_2T_x$ MXenes (**Figure 4.3**). Note that the onset energy position of the Ti L-edge was found empirically to shift to higher energies for higher Ti valence state [63]. Here, we used the Ti L-edge onset position to have an estimation of the Ti oxidation state. A prominent pre-edge signal and the presence of the single peak L_2-edge suggest a significant contribution of Ti^{3+} and/or Ti^{2+} species [63] in pristine and Li-$Ti_3C_2T_x$. The shift of the pre-edge onset energy to higher energies along with the evolution of the L_2 e_g to t_{2g} peak-to-peak intensity ratio show an increase in the Ti oxidation state. The latter observation suggests that the oxidation of Ti in pristine and Li-intercalated $Ti_3C_2T_x$ MXenes is

close to Ti^{3+} species, whereas the oxidation state of Ti in Na-, K- and Mg- Ti$_3$C$_2$T$_x$ MXenes is gradually closer to Ti^{4+} species. The two low-intensity absorption peaks at 456.8 and 457.5 eV mixed into the L$_3$ edge observed in Na-, K- and Mg-Ti$_3$C$_2$T$_x$ MXenes were previously attributed in TiO$_2$ materials to the strong interaction between poorly screened 3d electrons and the 2p core hole [78]. The appearance of these peaks confirms the relatively higher Ti oxidation state in Na-, K-, and Mg-Ti$_3$C$_2$T$_x$ MXenes after drying in air.

The oxygen bonding was also probed and the XAS at the O K-edge of the cation-intercalated MXene samples are shown in **Figure 4.4**. The XA spectra of pristine, K-, and Mg-Ti$_3$C$_2$T$_x$ reveal two features at 531.0 and 533.3 eV (separated by 2.3 eV) assigned to t$_{2g}$ and e$_g$ peaks of the Ti 3d levels, respectively. In Li- and Na-Ti$_3$C$_2$T$_x$ MXenes, the maxima of the t$_{2g}$ and e$_g$ features appear at 531.6 and 533.5 eV (separated by 1.9 eV), respectively. The t$_{2g}$ and e$_g$ peaks at the O K-edge were found to be separated by about 2.5, 2.1, and 1.6 eV for TiO$_2$, Ti$_2$O$_3$, and TiO, respectively [63].
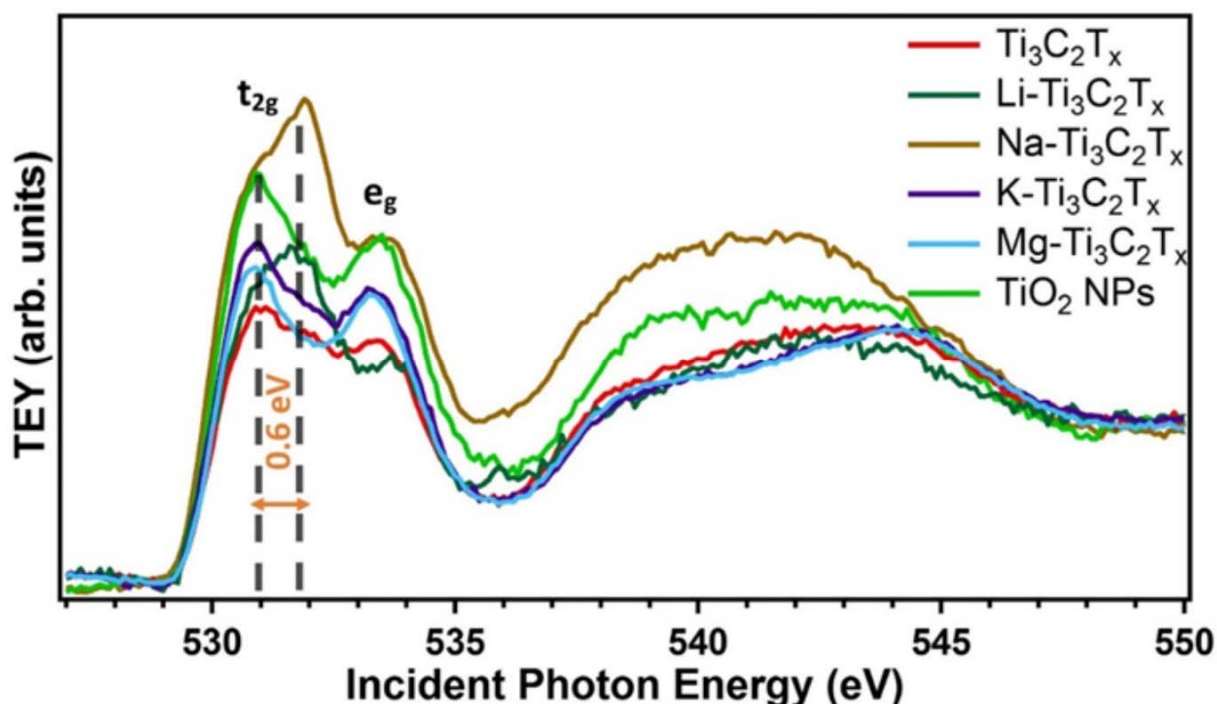
Figure 4.4 O K-edge XA spectra of dried pristine, Li-, Na-, K-, and Mg-intercalated Ti$_3$C$_2$T$_x$ MXene samples and TiO$_2$ MPs dispersed initially in water measured in TEY mode. In Li- and Na- intercalated Ti$_3$C$_2$T$_x$ MXenes, a peak is found at about +0.6 eV compared to the *t$_{2g}$* contribution, which is tentatively attributed to Li–O or Na–O bonds. Taken with permission from Ref. [73].

The intensity of the t$_{2g}$ and e$_g$ peaks is directly related to the degree of covalency of the bond between Ti and O atoms, which becomes stronger with increasing valence state. Therefore,

the O K-edge features can provide further information on the geometry of the metal–oxygen bonding.

In Li- and Na-Ti$_3$C$_2$T$_x$ MXene samples, the t$_{2g}$ peak maximum is shifted by +0.6 eV relative to other MXene samples. This shift may be caused by the deformation of the hybridization because of the distortion of the local octahedral volume [106]. A similar peak has been reported upon Li+ or Na+ ion insertion in TiO$_2$ materials [126,127]. Previous inelastic neutron scattering data showed that Li$^+$ and Na$^+$ ions are located closer to the Ti$_3$C$_2$T$_x$ MXene surface compared to other ions, which may explain the strong distortion of the Ti−O bonds observed only in these cations [123] . For K$^+$ and Mg^{2+} cations, the increase of the e$_g$ component suggests a higher bonding with oxygen atoms, as previously seen with urea intercalation [72].

The XA spectra of pristine and cation-intercalated Ti$_3$C$_2$T$_x$ MXenes at the Ti L- and O K-edges demonstrate a profound impact of Li$^+$, Na$^+$, K$^+$, and Mg^{2+} intercalation on the electronic structure of the Ti$_3$C$_2$T$_x$ MXene. The changes at the Ti L-edge are attributed to a progressive increase in the Ti oxidation state, matching, to a large extent, with the larger interlayer spacing distance following the sequence Li$^+$< Na$^+$< K$^+$< Mg^{2+}, as shown by the XRD data in **Figure 4.1 b**. The exposure of the cation-intercalated MXene samples to air during the drying process has to be taken into consideration. Thus, it is expected that a larger interlayer spacing enables the Ti$_3$C$_2$T$_x$ surface to be more exposed to water and oxygen from ambient air. The cation size is directly correlated to the interlayer spacing but is not the only factor that influences the Ti oxidation state, otherwise the Ti oxidation state should be relatively close for Li-Ti$_3$C$_2$T$_x$ and Mg-Ti$_3$C$_2$T$_x$ as the size of Li$^+$ and Mg^{2+} ions are comparable. The difference in the Ti oxidation state of the Li- and Mg-Ti$_3$C$_2$T$_x$ MXene can be attributed to (i) the difference in the cation valency, which might have an impact on the Ti$_3$C$_2$T$_x$ MXene electronic distribution or (ii) the larger cation hydration shell in Mg-Ti$_3$C$_2$T$_x$ MXene samples. It is noteworthy that in a previous study, the hydration shell was found to have a strong impact on the interlayer distance and to be cation-dependent [47].

4.5 *Ex Situ* XAS of Ti$_3$C$_2$T$_x$ Initially Dispersed in H$_2$SO$_4$

In a second step, the influence of the H$_2$SO$_4$ on the Ti electronic structure was investigated. To this aim, the Ti L-edge of pristine, Li-, Na-, K-, and Mg- Ti$_3$C$_2$T$_x$ MXenes, initially dispersed in a 10 mM H$_2$SO$_4$ electrolyte, were characterized in vacuum shortly after drying in air (see **Scheme**

1). Significant differences were observed as compared to dried samples initially dispersed in water as can be seen in **Figure 4.5**. To check if the cations are still intercalated between the MXene nanosheets, we have performed EDS measurements after the treatment with 10 mM H2SO4. The EDS data show that the ratio of Ti to cation is 3.00:0.04 for Ti/Na, 3.00:0.08 for Ti/K, and 3.00:0.10 for Ti/Mg. Furthermore, as the K L-edge lies within the range of the used soft X-ray, the K$^+$ cations were detected after intercalation as well as after exposure to 10 mM H_2SO_4 (**Figure 4.6**).
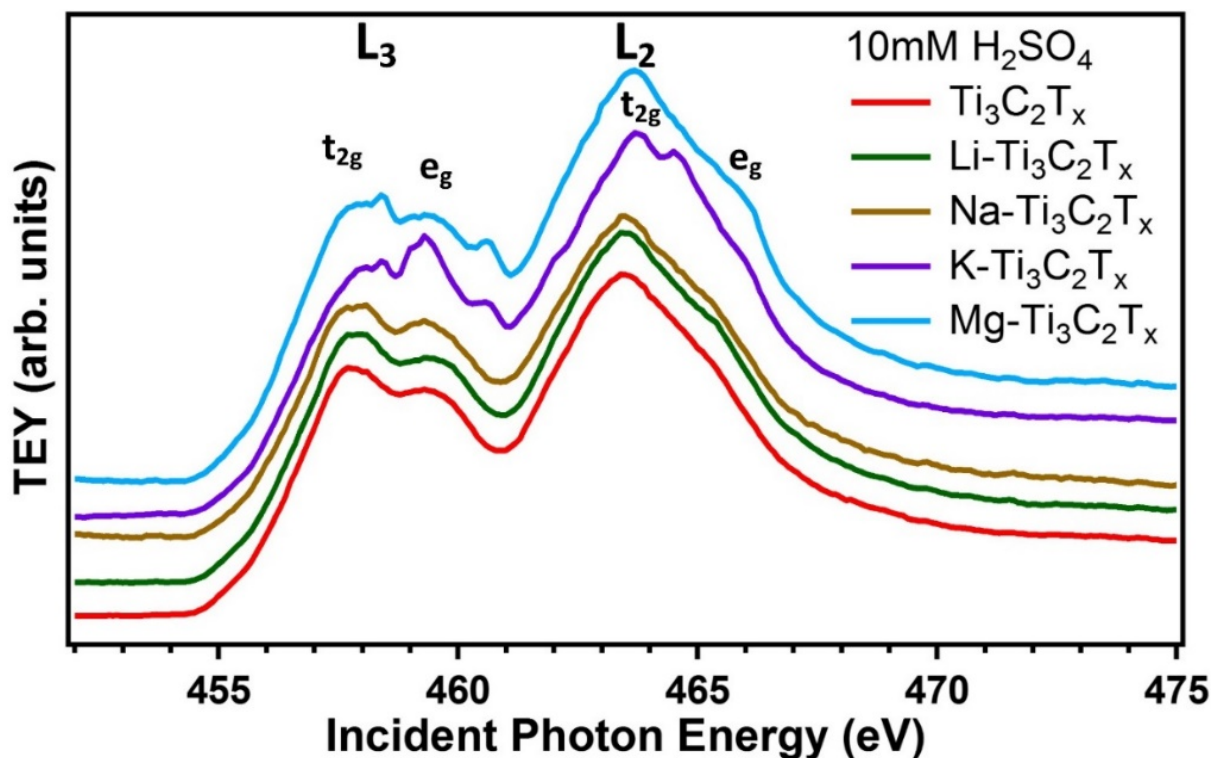
Figure 4.5 Ti L-edge XA spectra of dried cation-intercalated $Ti_3C_2T_x$ MXene samples initially dispersed in 10 mM H_2SO_4 under vacuum conditions. XAS was recorded in the TEY mode and the XA spectra are normalized to the TEY signal above 470 eV. Taken with permission from Ref. [73].
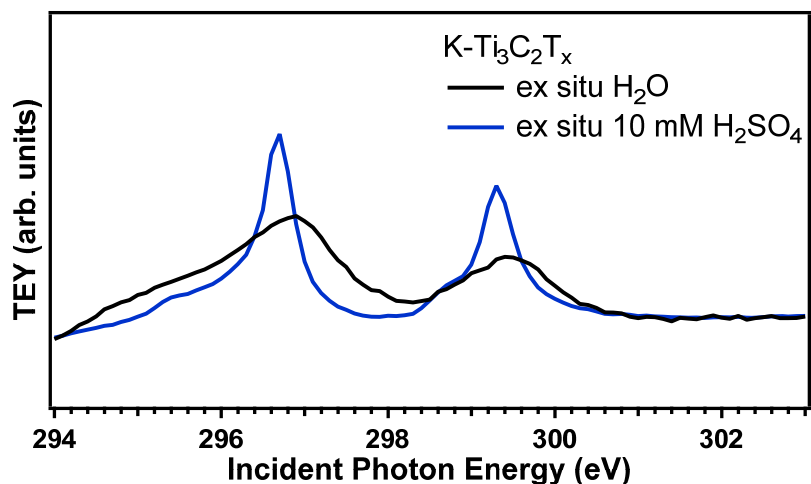
Figure 4.6 XA spectra at the K L-edge measured in TEY mode of dried K-$Ti_3C_2T_x$ MXenes initially dispersed in H_2O and 10mM H_2SO_4 under vacuum conditions. The XA spectra show the two distinctive peaks of the K L-edge after K$^+$ intercalation (black) and then exposure to the 10 Mm H_2SO_4 (blue). Taken with permission from Ref. [73].

The interlayer spacing distance of all samples investigated increases after exposure to 10 mM H_2SO_4 (**Table 4.1 and Figure 4.2**). This is mostly attributed to co-intercalation of H_3O^+ ions as the difference becomes negligible after annealing at 110 °C in vacuum (**Figure 4.2**). In particular, no significant difference is observed in the pre-edge region between the pristine and the cation-intercalated $Ti_3C_2T_x$ MXenes dispersed in 10 mM H2SO4. In pristine, Li-$Ti_3C_2T_x$, and Na-$Ti_3C_2T_x$, the $L_{3,2}$ e_g and t_{2g} have similar profiles which demonstrates a very close oxidation state of the Ti atoms. Interestingly, in K-$Ti_3C_2T_x$ and Mg-$Ti_3C_2T_x$ samples, additional peaks were observed in the $L_{3,2}$ edges at 460.6 and 464.5 eV, respectively. These peaks were previously attributed to distortions typical for Ti in lower valence states than Ti^{4+} species [63].
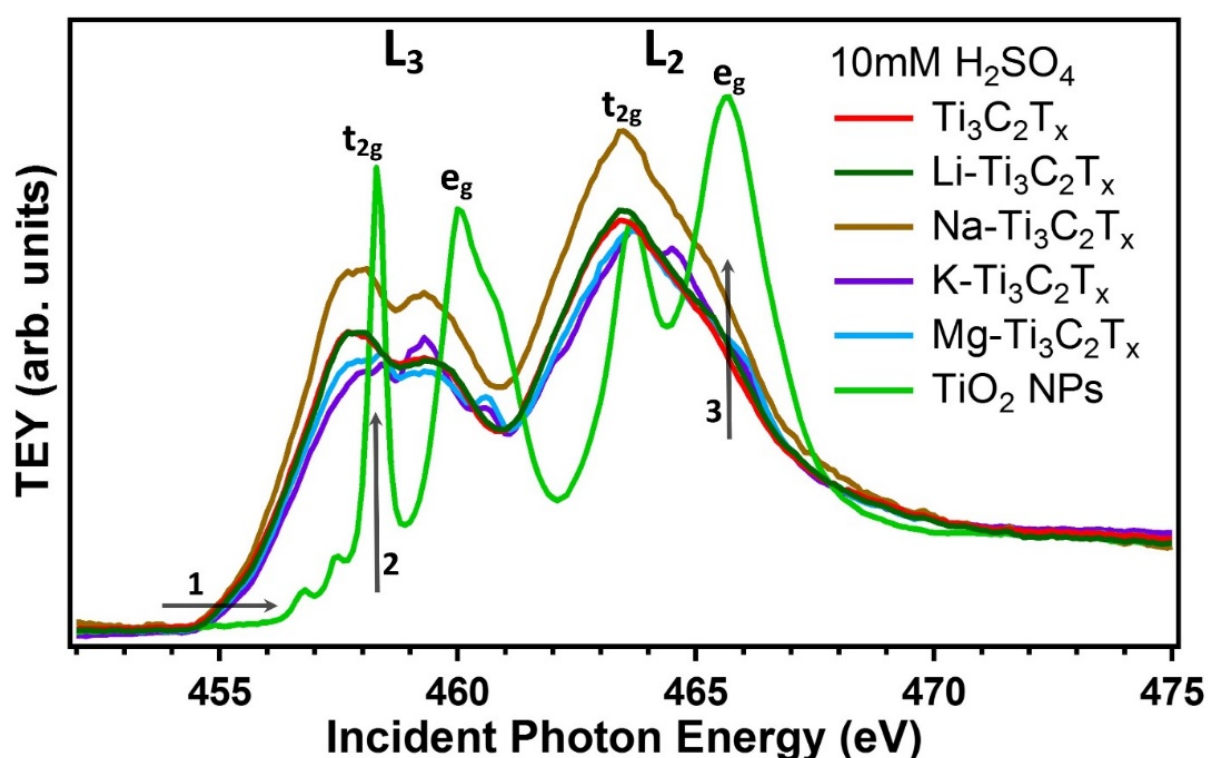
Figure 4.7 XA spectra measured in TEY mode of dried samples (initially dispersed in 10 mM H_2SO_4) under vacuum conditions at the Ti L-edge of pristine, Li-, Na-, K-, and Mg-intercalated $Ti_3C_2T_x$ MXenes. There are three distinctive regions, the feature (1) shows no change in the Ti oxidation state as the pre-edge region of these different cation-intercalated MXenes does not shift relative to each other. The onset energy position of these cation-intercalated $Ti_3C_2T_x$ MXenes significantly shifts to lower energies relative to the TiO_2 NPs. The feature (2) shows no intense L_3 t_{2g} peak, suggesting lower Ti oxidation state compared to the samples initially dispersed in water. The feature (3) reveals no clear L_2 e_g peak intensity, which agrees with the lower observed Ti oxidation state from the other two features. These XA spectra are compared to the Ti L-edge of TiO_2 NPs. Taken with permission from Ref. [73].

Furthermore, the $L_3(t_{2g})$ peak maxima of these samples were found to be shifted by +0.5 eV relative to pristine, Li-, and Na-$Ti_3C_2T_x$ MXenes and were comparable to the t_{2g} peak position

of TiO$_2$ NPs (**Figure 4.7**), whereas a small additional peak appears at 460.6 eV for K- and Mg-Ti$_3$C$_2$T$_x$. This suggests that a small amount of oxidized Ti atoms remain on these samples. However, the main Ti oxidation state remains close to that of the pristine MXene and the spectral changes are not as intense as for the aqueous dispersions (**Figure 4.3**). Likewise, the shoulder at the L$_2$(e$_g$) position of the K- and Mg-Ti$_3$C$_2$T$_x$ is more pronounced compared to other cation-intercalated samples. While the Ti oxidation state in Na-Ti$_3$C$_2$T$_x$ was found to be between Li-Ti$_3$C$_2$T$_x$ and K-Ti$_3$C$_2$T$_x$ after dispersion in pure water, its oxidation state after dispersion in diluted H$_2$SO$_4$ was similar to Li-Ti$_3$C$_2$T$_x$.

Sulfuric acid has a clear impact on the Ti electronic structure of the different MXene samples. Surprisingly, a relatively low oxidation state is found for all cation-intercalated MXenes compared to the MXene initially dispersed in water. The pre-intercalation with H$_2$SO$_4$ manifests that the Ti$_3$C$_2$T$_x$ MXenes are not significantly oxidized after drying in air compared to MXene samples only dispersed in water. This could possibly be related to the higher stability of hydroxylated MXene surface functional groups against oxidation. Storing MXene samples in diluted H$_2$SO$_4$ may be a promising option for protection of MXene layers against oxidation in water or air, which has been previously reported [105]. In previous studies, a lower pH regime was found to impact the surface functional groups as well as observed to enhance the electrochemistry performance [128,129]. This may also relate to the high stability of MXene electrodes in sulfuric acid electrolytes. Further work will be required to better understand the chemical stability of MXenes in sulfuric acid of different concentrations.

4.6 *In Situ/Operando* XAS of Ti$_3$C$_2$T$_x$ under Applied Potential in H$_2$SO$_4$

Complementary to *ex situ* characterization, the observation of the Ti$_3$C$_2$T$_x$ electronic structure directly in aqueous medium is necessary to understand the impact of cation-intercalation on a Ti chemical environment in relevant conditions for applications in energy storage or desalination. Especially, in order to better understand the impact of sulfuric acid on the cation-intercalated Ti$_3$C$_2$T$_x$ electronic structure, the samples solvated in water and dried in air were exposed *in situ* to sulfuric acid (see **Scheme 1**). In addition, the samples were electrochemically oxidized *in situ* by applying an anodic potential. A high electrochemical potential (+0.6 V vs Ag/AgCl) could produce irreversible oxidation of the MXene chosen, as previously reported by Lorencova *et al.* on the pristine Ti$_3$C$_2$T$_x$ MXene [130]. For potentials below +0.4 V versus Ag/AgCl, Lukatskaya *et al.* have shown reversible oxidation of the pristine MXene using *in situ*

XAS at the Ti K-edge, [34]. *In situ* XAS can be performed in the soft X-ray range using an electrochemical flow cell using PFY detection mode [83], as explained in section 2.3.2 and **Figure 2.5 b**.

Figure 4.8 shows the Ti L-edge spectral features of different cation-$Ti_3C_2T_x$ MXenes in the 10 mM H_2SO_4 electrolyte at open potential and +0.6 V versus Ag/AgCl. **Figure 4.8 a** presents the spectral features of Ti L-edge upon introducing the H_2SO_4 to Na-, K-, and Mg-$Ti_3C_2T_x$ samples at an open circuit potential. The 10 mM H_2SO_4 aqueous environment results in different XA spectra features between Na-, K-, and Mg-$Ti_3C_2T_x$ samples compared to their dried counterpart measured under vacuum conditions. After introducing 10 mM H_2SO_4, the Ti oxidation state was found to be the lowest in Na-$Ti_3C_2T_x$ followed by Mg- and K-$Ti_3C_2T_x$ MXenes.
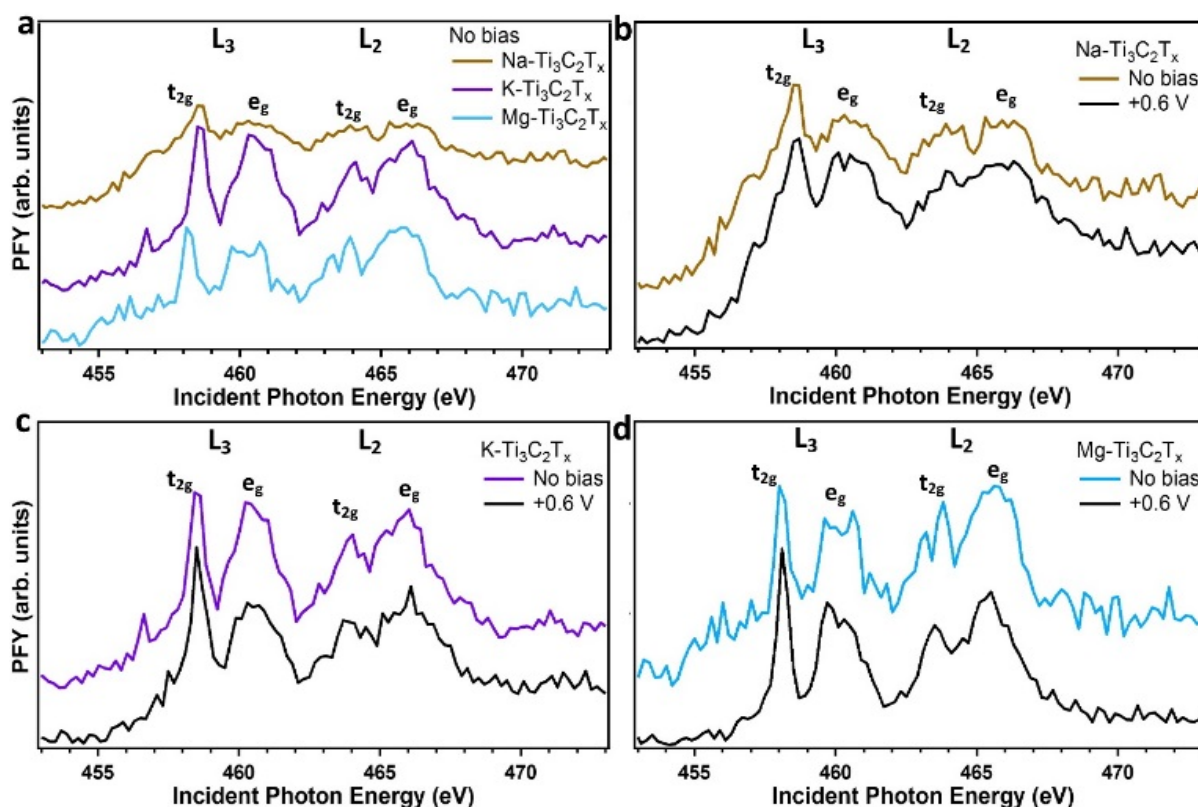
Figure 4.8 *In situ* Ti L-edge XA spectra of different cation-intercalated $Ti_3C_2T_x$ MXenes in 10 mM H_2SO_4 and applied potentials vs. Ag/AgCl. (a) after introducing the sulfuric acid to different cation-intercalated $Ti_3C_2T_x$ MXenes at open circuit potential. (b) Na-$Ti_3C_2T_x$. (c), K-$Ti_3C_2T_x$. (d), Mg-$Ti_3C_2T_x$. The spectrum in black in (b), (c), and (d) corresponds to +0.6 V applied potential. XA spectra were recorded in PFY using an electrochemical flow cell. Taken with permission from Ref. [73].

This estimation is based on the onset energy position and the Ti $L_3(t_{2g})$ peak sharpness. In contrast to the Na-Ti$_3$C$_2$T$_x$, the Ti oxidation state of Mg- and K-Ti$_3$C$_2$T$_x$ MXenes was observed to be relatively higher compared to the dried samples initially dispersed in 10 mM H$_2$SO$_4$ measured under vacuum conditions. Thereafter, we monitored the *operando* XA spectra at the Ti L-edge at +0.6 V applied potential versus Ag/AgCl (**Figure 4.8b-d**).

Figure 4.8 b demonstrates the electrochemical oxidation of the Na-Ti$_3$C$_2$T$_x$ MXene sample. The pre-edge onset energy position shifts to higher energies after applying a positive voltage. This shift confirms a significant increase in the average oxidation state of the Ti atoms at the anodic potential. Additionally, irrespective of the changes associated with the onset energy position: (i) the t_{2g} peak was found to be at 458.5 eV which corresponds to a 0.2 eV shift to higher energies compared to dried sample dispersed in water or XAS detection mode of the peak might become broader in a H$_2$SO$_4$ aqueous environment. (ii) in contrast to the dried sample dispersed in pure water, the L_2 t_{2g}-e_g splitting is unequivocally missing and resembles the trend observed in the dried sample initially dispersed in 10 mM H$_2$SO$_4$.

Unlike Na-Ti$_3$C$_2$T$_x$ MXene, the electrochemical oxidation of K-Ti$_3$C$_2$T$_x$, as shown in **Figure 4.8 c**, does not express a relative shift in the onset energy position at the positive 0.6 V applied potential. Relative to the dried spectrum of K-Ti$_3$C$_2$T$_x$ initially dispersed in water, the $L_3(t_{2g})$ peak becomes more intense and the L_2 t_{2g}-e_g splitting was found to be preserved. It has to be mentioned that the t_{2g} peak was also shifted by 0.2 eV to higher energies relative to the dried sample initially dispersed in water following the tendency observed in the sample initially dispersed in H$_2$SO$_4$. Likewise, the Ti Ledge of the Mg-Ti$_3$C$_2$T$_x$ MXene, as shown in **Figure 4.8 d**, reveals a contribution from the Ti^{4+} species as validated by the intense and sharp t_{2g} peak. The intensity and the sharpness of the t_{2g} peak relative to the pre-edge feature was observed to be more pronounced at +0.6 V applied potential, indicating a higher Ti oxidation state. At the same time, the pre-edge onset is shifted to higher energies, which indicates a higher oxidation at the +0.6 V bias voltage, and the t_{2g} peak itself was found to be much more intense. The cation intercalation and the interaction with sulfuric acid were found to play a significant role in the final oxidation state of Ti atoms. In the Na-Ti$_3$C$_2$T$_x$ sample, a relatively low Ti oxidation was observed, most likely due to the fact that Na$^+$ is located relatively closer to the surface of the MXene sheets compared to K$^+$ and Mg^{2+} cations. A clear oxidation of Ti is then observed at +0.6 V versus Ag/AgCl.

On the other hand, for K- and Mg-Ti$_3$C$_2$T$_x$ samples, the XA spectra recorded at the open circuit potential show that the surface Ti atoms were already quite oxidized. This demonstrates that the initial oxidation in air, as shown in **Figure 4.3**, is irreversible even after exposure to 10 mM H$_2$SO$_4$. The Ti surface atoms can only be reduced if they are exposed to 10 mM H$_2$SO$_4$ before drying in air (**Figure 4.5**). As a result, the impact of electrochemical oxidation is less visible than for Na-Ti$_3$C$_2$T$_x$, which is also confirmed by the smaller current flowing through the K- and Mg-Ti$_3$C$_2$T$_x$ samples during *in situ* measurements at +0.6 V (**Figure 4.9**).
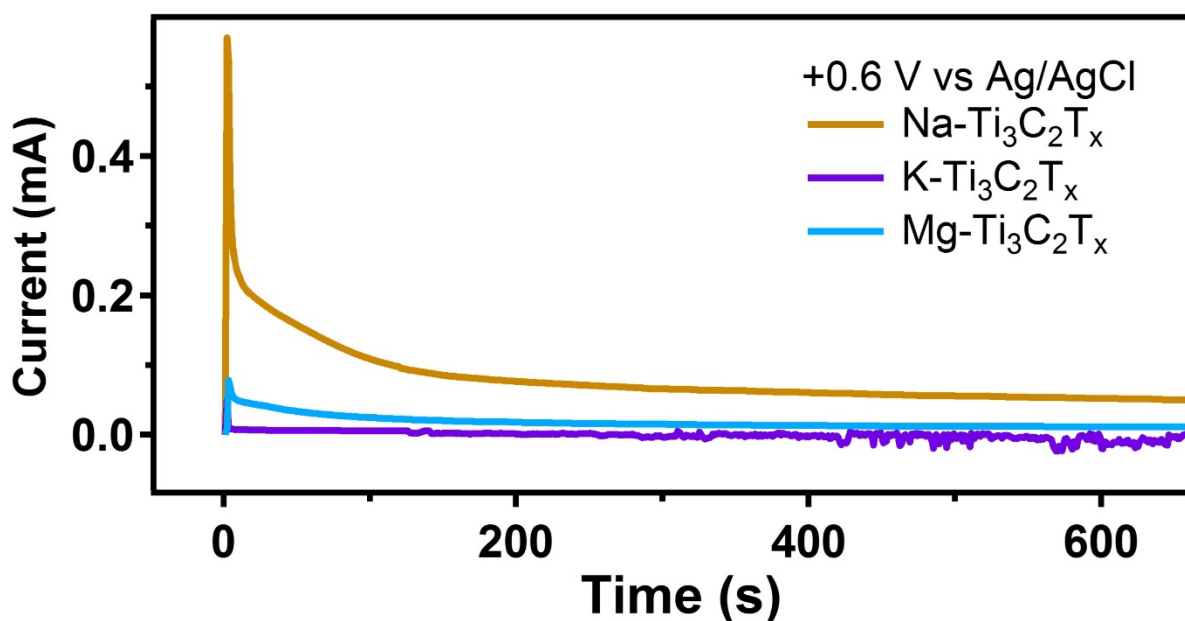
Figure 4.9 *In situ* chronoamperometry shows the current response in Na-, K-, and Mg-Ti$_3$C$_2$T$_x$ MXene samples investigated in this study. These current responses demonstrate that the electrochemical oxidation is achieved within the first minutes. The XA spectra were recorded over several hours and no clear changes were observed over time, therefore irreversible oxidation of the MXene samples was already achieved by the first spectrum collected. Taken with permission from Ref. [73].

In K-Ti$_3$C$_2$T$_x$, no clear shift in the Ti L-edge onset energy position was induced by the positive 0.6 V bias voltage. Nevertheless, L$_3$(t$_{2g}$) was found to be enhanced relative to the eg peak which may indicate a slightly higher Ti oxidation state. For Mg-Ti$_3$C$_2$T$_x$, the anodic potential in H$_2$SO$_4$ has a slight impact on the Ti electronic structure as the pre-edge onset energy position shifts to higher energies and L$_3$(t$_{2g}$) also increases, as shown in **Figure 4.8 d**. As the interlayer spacing is the largest for Mg-Ti$_3$C$_2$T$_x$ (**Figure 4.1b** and **Table 4.1**), the Ti atoms are thus relatively more vulnerable to oxidation.

To make sure that the features observed in the *in situ* XA spectra presented in **Figure 4.8** are real and not correlated to signal-to-noise ratio, **Figure 4.10** is presented below to demonstrate

the XA spectra including error bars calculations. One could easily see that the XA profiles are very well pronounced even with the presence of the error bars calculations.
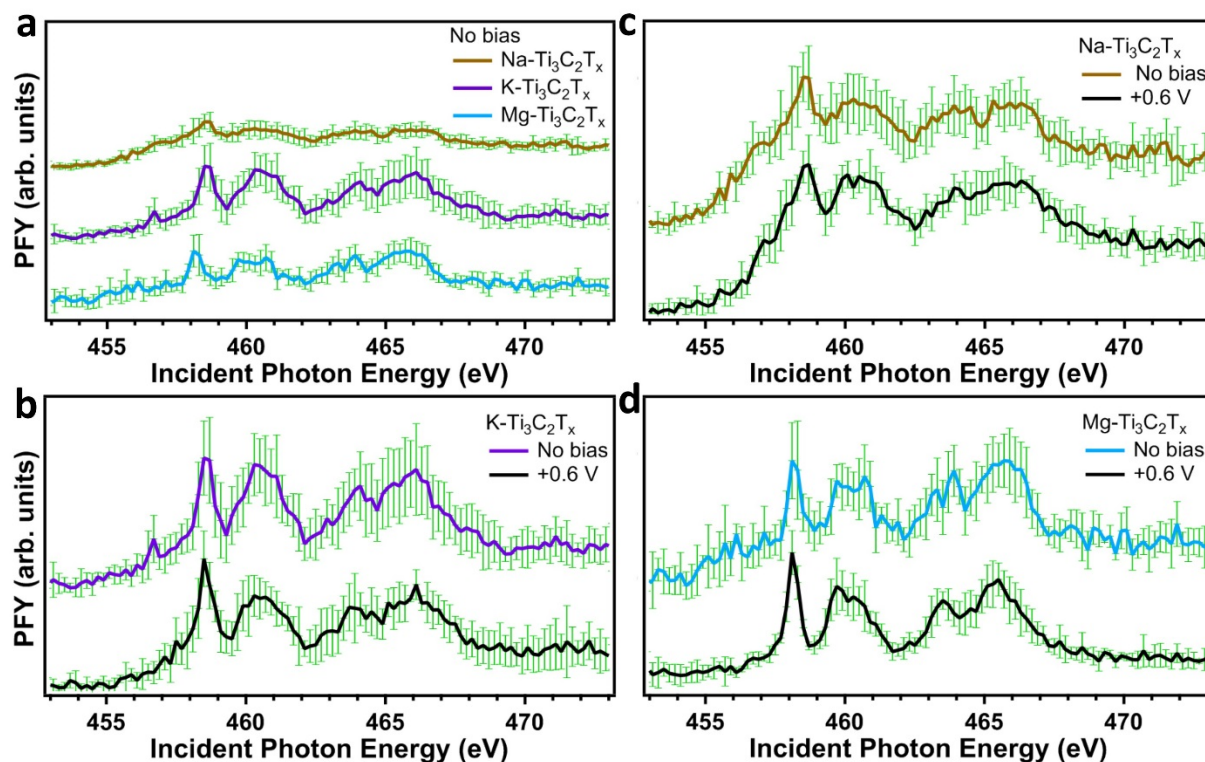
Figure 4.10 *In situ* Ti L-edge XA spectra of different cation-intercalated Ti$_3$C$_2$T$_x$ MXenes in 10 mM H$_2$SO$_4$ and +0.6V applied potentials vs. Ag/AgCl. (a) after introducing the 10 mM H$_2$SO$_4$ to different cation-intercalated Ti$_3$C$_2$T$_x$ MXenes at open circuit potential including the error bar. (b) Na-Ti$_3$C$_2$T$_x$. (c), K-Ti$_3$C$_2$T$_x$. (d), Mg-Ti$_3$C$_2$T$_x$. The spectrum in black in (b), (c), and (d) corresponds to +0.6 V applied potential. The error bar of each XA spectrum is shown in green. Taken with permission from Ref. [73].

4.7 Summary

In this chapter, we investigated the effect of cation-intercalation with Li^+, Na^+, K^+, and Mg^{2+} on the MXene electronic structure using XAS at the Ti L-edge in various environments. After dispersion in water and drying in air, the oxidation state of Ti atoms in $Ti_3C_2T_x$ MXenes is dramatically altered by cation intercalation and is found to progressively increase with larger cations. On the other hand, after dispersion in 10 mM H_2SO_4, the Ti atoms remain largely unaffected by the cation intercalation and have a similar chemical environment to pristine $Ti_3C_2T_x$ MXenes. This suggests that exposure of the MXene to a small amount of H_2SO_4 aqueous solution may protect the MXene surface from oxidation. Finally, the impact of in situ exposure to 10 mM H_2SO_4 and to the application of anodic electrochemical potentials on the Ti oxidation state was also investigated. *In situ* XAS measurements of Na-, K-, and Mg-$Ti_3C_2T_x$ MXenes demonstrated an increase in the average Ti oxidation state upon *operando* electrochemical oxidation (+0.6 V vs Ag/AgCl). This work illustrates that the chemical sensitivity of Ti L-edge XAS may open new chemical insights into cation intercalation and MXene surface oxidation mechanisms. As the oxidation state plays a significant role in the electrochemical performance of $Ti_3C_2T_x$ MXenes, this sensitivity could also be applied to probe electrochemical energy storage and conversion processes on MXenes.

CHAPTER FIVE

The XPEEM Study of Ti Oxidation State and Thickness of Cation-Ti$_3$C$_2$T$_x$ Particles

5.1 Motivation

The XAS spectra of pristine, Li-, Na-, K-, and Mg-$Ti_3C_2T_x$ MXenes at the Ti L-edge were for the first time recorded, as shown in chapter four. This reflects the sensitivity of XAS technique to probe the impact of various cations with different charges and sizes on the surface chemistry of the multi-layered $Ti_3C_2T_x$ MXenes, detecting the changes in the local chemical bonds of the surface Ti atoms. However, the spatially resolved XA spectra of individual multilayered cation-intercalated $Ti_3C_2T_x$ has not been reported yet. Briefly, these are the aims of the work presented in this chapter.

1- What are the XA spectra profile at the Ti L- and O K-edges of single Li-, Na-, K-, and Mg-$Ti_3C_2T_x$ MXene particles?

2- The influence of the flake size of very thin MXenes on the electrochemical performance has been reported [131]. As the multilayered $Ti_3C_2T_x$ particles are the building blocks for manufacturing MXene-electrodes, is the thickness of a single particle influence the Ti oxidation state?

3- The spatially resolved XA spectra at the O K-edge have the potential to map the oxidation state, leading to illustrate the distribution of oxygen content over individual cation-intercalated $Ti_3C_2T_x$ particles

What is the essence of this chapter?

$Ti_3C_2T_x$ MXene is a 2D material possessing highly active hydrophilic surfaces coupled with high metallic conductivity. Cations intercalation between the $Ti_3C_2T_x$ nanosheets has a significant role in many applications such as water purification, desalination, and electrochemical energy storage. The pseudocapacitive charging mechanism involving surface redox reactions at the $Ti_3C_2T_x$ surface enables higher energy densities than electrical double-layer capacitors, and higher power densities than batteries. In this context, the oxidation state of surface Ti atoms involved in redox reactions has a high impact on the capacitance of $Ti_3C_2T_x$ MXene and this can be impacted by cation intercalation. The electronic structure of multi-layered $Ti_3C_2T_x$ particles can be investigated by XAS, while also benefitting from a high spatial resolution of 30 nm from X-ray photoemission electron microscopy. In this chapter, the XA spectra from multi-layered intercalated $Ti_3C_2T_x$ particles of different thicknesses were recorded at the Ti L- and O K-edges. The Ti oxidation state in pristine, Li-, and Mg-intercalated $Ti_3C_2T_x$ was found to be

thickness-dependent, while Na- and K-intercalated $Ti_3C_2T_x$ particles did not reveal differences upon changing thickness. This work demonstrates thickness dependent modification of the MXene surface chemistry upon cation intercalation in different individual $Ti_3C_2T_x$ particles.

5.2 Research Background

The demand for portable electronic devices, electric vehicles, and renewable energy storage devices has increased considerably over the last decade. There is a growing urgent demand for electrochemical energy storage systems where both high energy and high power densities are required simultaneously. As shown in chapter one, the energy density of EDLCs is much lower compared to batteries, but they have very high power density. On the other hand, pseudocapacitors can be charged rapidly in a few minutes or as quickly as less than a minute, achieving power densities exceeding those of batteries [3,132–134]. In pseudocapacitors, high capacitance is usually achieved due to redox reactions between the electrode and the ion from the electrolyte. Significant efforts are currently being directed towards developing 2D materials such as MXenes for electrochemical energy storage due to their potentially large electrode-electrolyte interface. In this contribution, we investigate the impact of cation size (Li^+, Na^+, K^+, Mg^{2+}) on the Ti oxidation state of individual MXene particles after intercalation. The high chemical sensitivity of XAS at the Ti L-edge has been successfully employed to discriminate between various Ti oxide species [63,78]. These oxides can be differentiated because their orbitals differ in their electronic coordination, where TiO, Ti_2O_3, and TiO_2 have two, one, and no electrons, respectively [63,78].

Here, the X-PEEM technique was used to enable acquiring spatially resolved XA spectra of pristine, Li-, Na-, K-, and Mg-$Ti_3C_2T_x$ MXenes under UHV conditions [79]. In this context, we have already demonstrated that cation intercalation by Li^+, Na^+, K^+, and Mg^{2+} in $Ti_3C_2T_x$ MXene can strongly affect the oxidation state of the surface Ti atoms in MXene after drying in air [73]. Nevertheless, no information about the Ti oxidation state on individual multi-layered particles of these cation-intercalated $Ti_3C_2T_x$ MXenes have been considered. Furthermore, the influence of different very thin MXene flake sizes on the electrochemical performance in MXene electrodes has been reported [131]. In the latter study, MXene flakes which are only a few layers-thick were used. To avoid confusion with few-layer single flakes, we will refer to individual multi-layered MXene particles in this chapter, which are comprised of stacked MXene layers having a thickness that can reach several hundreds of nanometers. Because

individual MXene particles are the building blocks for multi-layered MXene electrodes, the particle thickness is expected to influence the electrochemical performance of MXene electrodes. Because MXene-based electrodes are comprised of a wide range of different particle thicknesses, it is necessary to gain insight into how the particle thickness influences the Ti oxidation state.

To do so, the X-PEEM technique was used in this study to characterize pristine, Li-, Na-, K-, and Mg-intercalated $Ti_3C_2T_x$ MXene using XAS at the Ti L- and O K-edges. X-PEEM enables spatially-resolved XA spectra recorded in PEY detection mode over individual particles of multi-layered MXene of different thicknesses. As mentioned in chapter two, the probing depth of the PEY detection mode applied in this study is ≤10 nm. The main focus of this study is to investigate the difference in the Ti oxidation state between thick (~200 to 450 nm) and thin (≤ 30 nm) particles of $Ti_3C_2T_x$ after intercalation by Li, Na, K, and Mg cations. The thickness of the particles is calculated via multiplying the shadow region length by the tangent of the incident angle (16°) of the X-ray beam, see **Figure 5.1**.
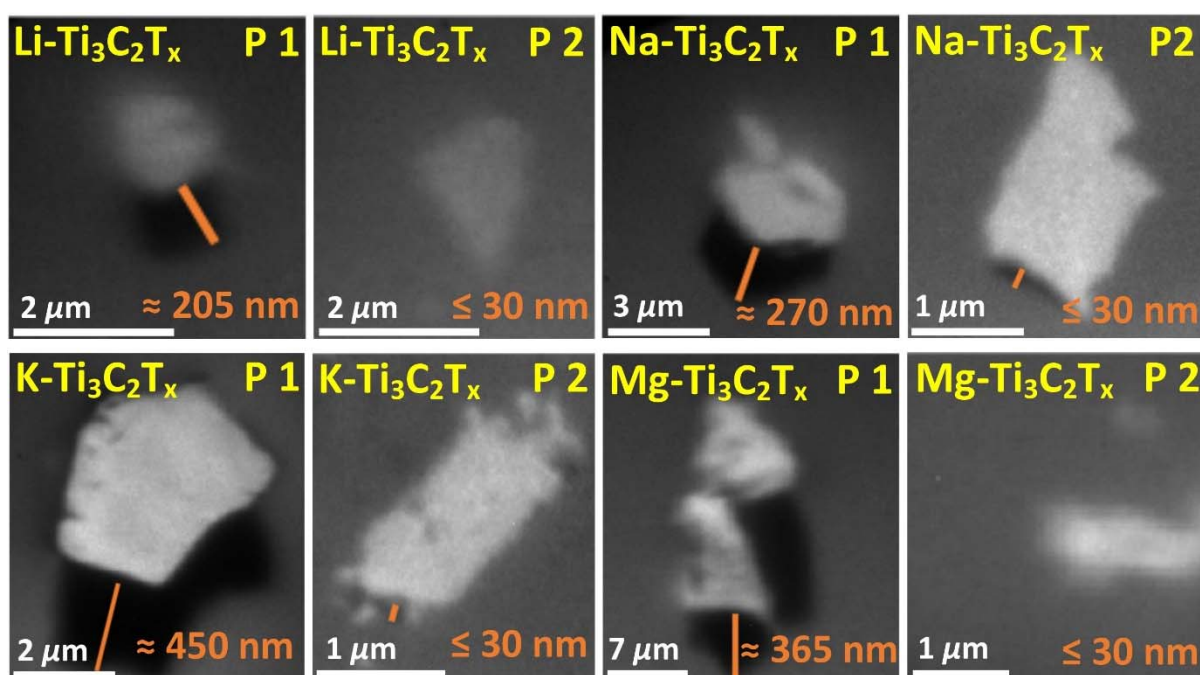
Figure 5.1 X-PEEM micrographs at the Ti L-edge (463.9 eV) show single Li-, Na-, K-, and Mg-$Ti_3C_2T_x$ MXene particles of different thicknesses. The orange line illustrates how large the shadow region. The presented thickness is calculated by multiplying the shadow region length by the tangent of the beam angle (angle is 16°). The flat flakes do not reveal a shadow region which leads to estimate the thickness to be less or equal to 30 nm. Taken with permission from Ref. [74].

Furthermore, spatially resolved oxidation mapping was used to illustrate the distribution of oxygen content over individual cation-intercalated $Ti_3C_2T_x$ particles. In this study, two particles with different thicknesses (thin particles are ≤ 30 nm while thick ones are ≥ 200 nm) were selected for each MXene sample, as shown in **Figure 5.1**. The Ti oxidation state in pristine, Li-, and Mg-$Ti_3C_2T_x$ was found to be thickness-dependent while Na- and K-$Ti_3C_2T_x$ of different thicknesses did not reveal changes in the Ti oxidation state.

5.3 Single Multilayered Pristine $Ti_3C_2T_x$ Particles

Figure 5.2 a shows X-PEEM images recorded at the Ti L- and O K-edges of an individual $Ti_3C_2T_x$ MXene particle. This particle is around two micrometers in diameter, ≤ 30 nm thick, and exhibits sharp edges. XA spectra were integrated over regions near the center and edge positions of the particle, the regions of which are highlighted in yellow and green, respectively. Changes in the Ti oxidation state of the $Ti_3C_2T_x$ MXene particle were observed at different locations across its surface. The splitting of the L_3 edge into t_{2g} (458.1 eV) and e_g (459.4 eV) sub-bands was observed at the center of the particle but is more pronounced at the edge. **Figure 5.2 b** shows that the onset of the Ti L-edge shifts by +0.4 eV at the edge relative to the center of the particle. However, the lack of clear L_2 edge splitting and a shoulder-like e_g sub-band suggests an estimated oxidation state higher than Ti^{3+} at the center and the edge positions.

Since the XA spectra at the Ti L-edge reveal a difference in the Ti oxidation state, the O K-edge was also measured in order to assess any further correlation. **Figure 5.2 c** demonstrates the oxygen distribution and local bonding environment of the $Ti_3C_2T_x$ MXene particle, where the relatively higher contrast close to the edges is indicative of a higher oxygen content. The oxygen content within the particle was found to vary slightly but remain lower relative to the edges as illustrated by the line profile in **Figure 5.2 c**.
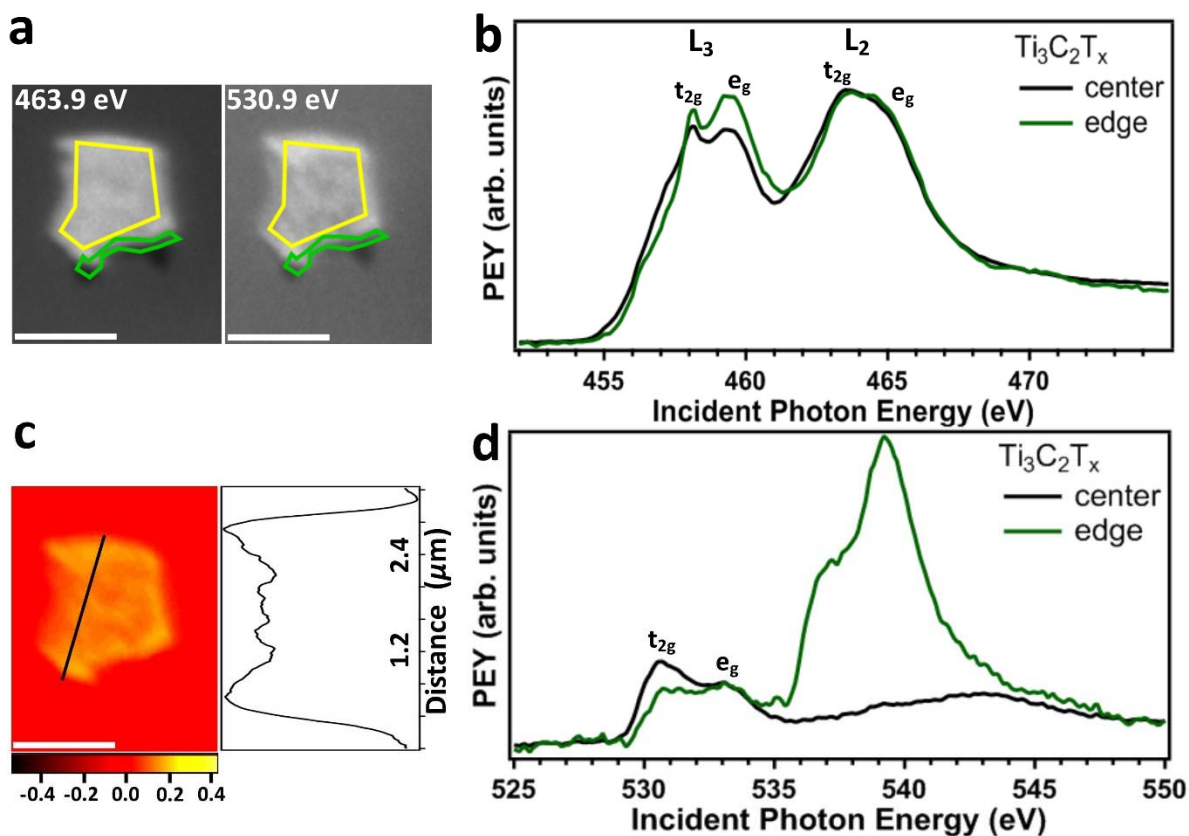
Figure 5.2 (a) X-PEEM micrographs of a pristine multi-layered $Ti_3C_2T_x$ MXene particle at the Ti L- and O K-edges taken at excitation energies of 463.9 eV and 530.9 eV, respectively (scale bar 2 µm). The regions labeled center and edge in b and d are highlighted in yellow and green, respectively. (b) X-PEEM Ti L-edge XA spectra of a single particle of pristine $Ti_3C_2T_x$ MXene. (c) Lateral oxygen concentration over an individual MXene particle obtained from the difference of averaged X-PEEM micrographs at the O K-edge in the t_{2g} and e_g region (530.0-534.5 eV) relative to the background (524.5-529.0 eV), the line profile (the x-axis is the intensity in arb. units) of this particle is shown next to the oxygen concentration distribution map. (d) X-PEEM O K-edge XA spectra of pristine $Ti_3C_2T_x$ MXene. Taken with permission from Ref. [74].

Figure 5.2 d shows a comparison in the XA spectra at the O K-edge for pristine $Ti_3C_2T_x$ MXene at the center and edge positions of the particles. The O K-edge XA spectra demonstrate two main peaks in the energy range between 529.0-535.0 eV which result from the transitions between O 1s and 2p states that are hybridized with empty Ti 3d orbitals. Whereas in the 537.0-546.0 eV region, the O K-edge spectra show a second set of bands which can be attributed to transitions from O 2p states that are hybridized with Ti 4s and 4p states [135]. The strong bands between 537.0-540.0 eV from the edge XAS are characteristic of the SiO_2 substrate, as demonstrated below in **Figure 5.3**.
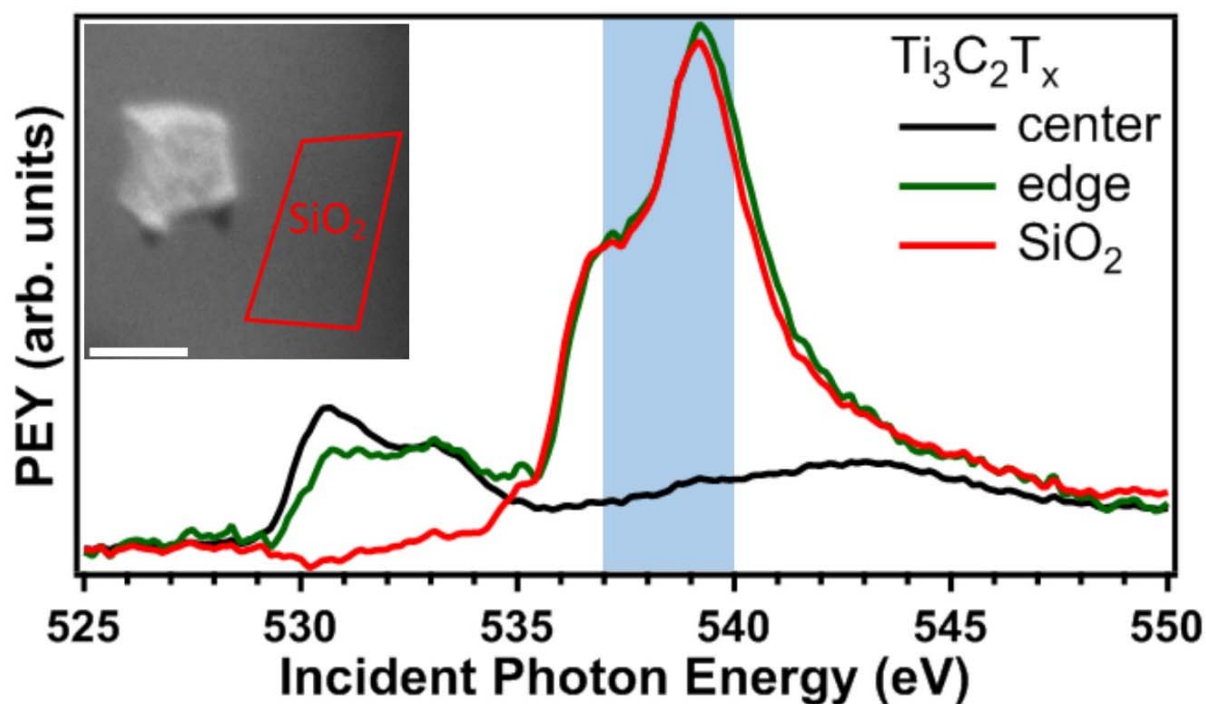
Figure 5.3 X-PEEM O K-edge XA spectra of pristine $Ti_3C_2T_x$ MXene sample and the inset in the left top corner is corresponding to the X-PEEM micrograph. The spectra show that the XA peak around 537.0-540.0 eV at the edge position relates to the signature of the SiO_2 substrate (scale bar 2 µm). Taken with permission from Ref. [74].

We will therefore concentrate the discussion on the 529.0-535.0 eV region in the following. The peaks at 530.6 and 533.1 eV are assigned to the t_{2g} and e_g sub-bands, respectively. Interestingly, the e_g peak was found to be higher in intensity compared to the t_{2g} peak at the edge sites, suggesting a higher oxidation of the edges, which is in agreement with the Ti L-edge. We previously interpreted these findings in chapter three as a slight oxidation induced by oxygen and water molecules from the ambient environment during sample preparation and drying in air [72]. It has to be emphasized that the thickness of the particle shown in **Figure 5.2 a** is very thin (≤ 30 nm). Nevertheless, the difference in the oxidation state between the center and edge is still represented. Indeed, the oxidation proceeds faster at the edges relative to the basal plane in $Ti_3C_2T_x$, resulting in higher resistivity MXene electrodes [102,104,105]. In comparison to a thicker pristine multi-layered $Ti_3C_2T_x$ particle presented in chapter three (**Figure 3.4**), the total average Ti oxidation state was found to be relatively higher for the thin particle.

5.4 Single Multilayered Li-Ti$_3$C$_2$T$_x$ Particles

The pristine multi-layered Ti$_3$C$_2$T$_x$ MXene particle was presented above to probe the impact of cation intercalation between Ti$_3$C$_2$T$_x$ layers on the Ti oxidation state. Individual Li-intercalated Ti$_3$C$_2$T$_x$ MXene particles were then characterized. **Figure 5.4 a** shows X-PEEM images at the Ti L-edge for two Li-Ti$_3$C$_2$T$_x$ particles of different thicknesses. The yellow labeled area indicates the region over which the XA spectra were acquired from, as shown in **Figure 5.4 b**. Thick particles can be identified from the very well pronounced shadow region which is not observed for thin particles. Multi-layered MXene particle 1 XA spectra (about 205 nm thick, see **Figure 5.1**) reveal a very well resolved splitting at the L$_3$ edge into t_{2g} (485.1 eV) and e_g (459.2 eV) peaks. However, no clear splitting was observed in the L$_2$ edge, resulting in a t_{2g} peak at 463.4 eV with a shoulder-like e_g peak. Multi-layered MXene particle 2 is $\leq$ 30 nm thick as no significant shadow is observed (see **Figure 5.1**). This particle shows relatively less pronounced splitting in the L$_3$ edge into t_{2g} (457.8 eV) and e_g (459.2 eV) peaks and the L$_2$ edge reveals only t_{2g} (463.1 eV) as no e_g peak or shoulder-like feature is observed. However, the onset energy position of the Ti L-edge in particle 1 and 2 of Li-Ti$_3$C$_2$T$_x$ MXene was found to be unaffected by the thickness difference. In contrast to particle 2, the L$_3$ e_g peak is higher in intensity relative to the L$_3$ t_{2g} peak in particle 1. The higher L$_3$ e_g to t_{2g} peak intensity ratio and the L$_2$ e_g shoulder feature in particle 1 suggests a higher Ti oxidation state compared to particle 2.

The lateral oxygen concentration in both particles (**Figure 5.4 c**) demonstrates no change in the oxygen distribution, as the line profiles of the corresponding particles show a relatively homogenous oxygen content. **Figure 5.4 d** displays the O K-edge spectra of particle 1 and 2 recorded from the same region of interest where the Ti L-edge XA spectra were acquired in **Figure 5.4 a**. The detection of the SiO$_2$ substrate signature between 537.0 and 540.0 eV at the O K-edge in particle 2 implies a multi-layered MXene particle of probably less than 10 nm thickness. The peaks at 530.5 and 532.6 eV are assigned to the t_{2g} and e_g orbitals in particle 1, respectively. For particle 2, on the other hand, no clear e_g contribution is detected. This observation is in agreement with the XA spectra at the Ti L-edge which manifests a higher oxidation state in particle 1 relative to particle 2. Interestingly, thinner multi-layered Li-intercalated MXene particle demonstrates less Ti oxidation than the thick one. We therefore conclude that thinner particles are not necessarily more oxidized. Therefore, the Ti L-edge and

O K-edge XA spectra present a relatively higher Ti oxidation state in the thick particles. The thickness-dependent Ti oxidation of Li-$Ti_3C_2T_x$ particles is possibly due to a greater intercalation by Li cations between the multi-layered $Ti_3C_2T_x$ MXene nanosheets of thin particles. Regarding the homogeneity of the lateral oxygen concentration, Li cations are known to intercalate very close to the $Ti_3C_2T_x$ surface, suggesting a homogeneous distribution of Li cations which thus serve to effectively shield the Ti atoms at the MXene surface from forming further oxygen bonds [123].
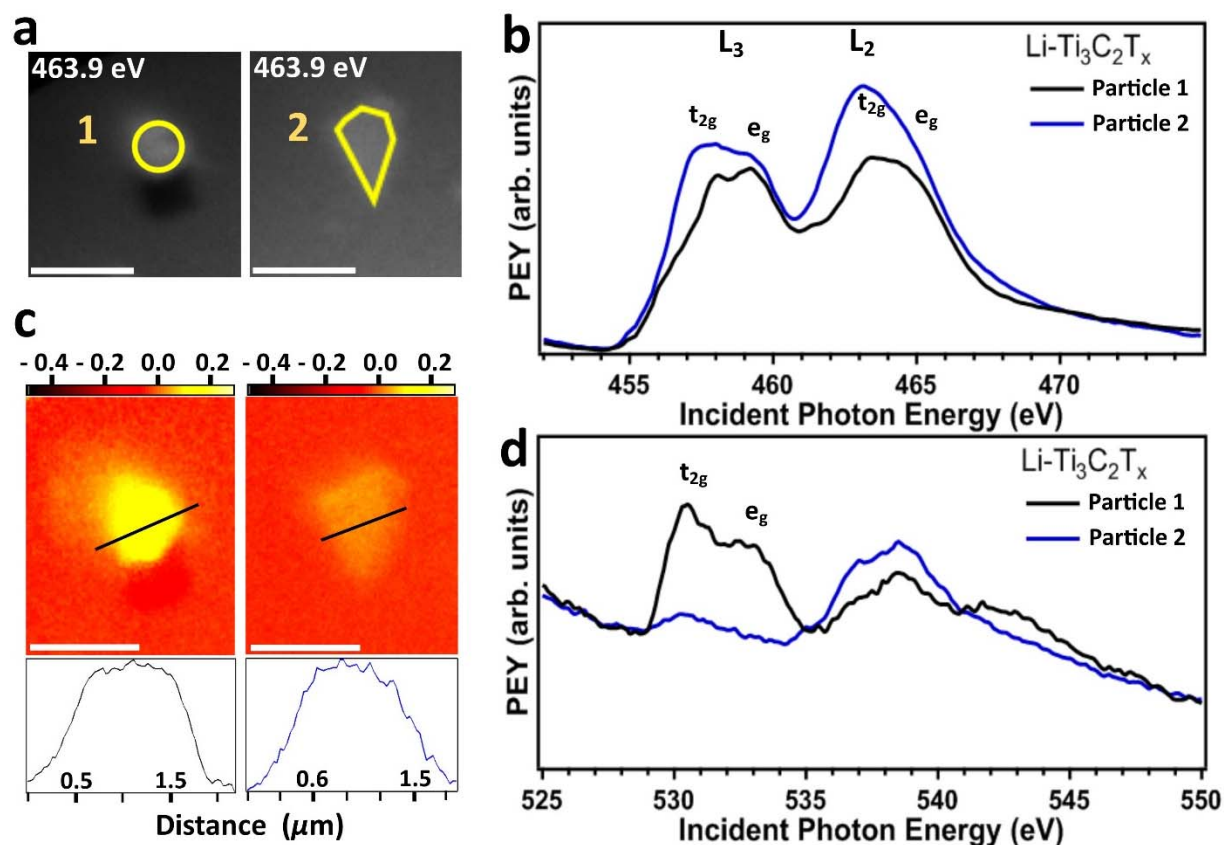
Figure 5.4 (a) X-PEEM micrographs of individual multi-layered Li-$Ti_3C_2T_x$ MXene particles at the Ti L-edge taken at an excitation energy of 463.9 eV (scale bar 2 µm). The investigated region of particle 1 and particle 2 in b and d are labeled in yellow. (b) X-PEEM Ti L-edge XA spectra of the two different Li-$Ti_3C_2T_x$ MXene particles. (c) Lateral oxygen concentration over individual MXene particles obtained for the same energy range described in Figure 5.2 and the line profile (the y-axis is the intensity in arb. units) across each single particle is shown underneath the oxygen concentration distribution map. (d) X-PEEM O K-edge XA spectra of multi-layered Li-$Ti_3C_2T_x$ MXene particles. Taken with permission from Ref. [74].

5.5 Single Multilayered Na-$Ti_3C_2T_x$ Particles

Spatially resolved XA spectra of Na-intercalated multi-layered MXene particles were also measured. The thicknesses of particles 1 and 2 are estimated to be about 270 nm and ≤ 30

nm, respectively (see **Figure 5.1**). The X-PEEM micrographs at the Ti L-edge of these two multi-layered MXene particles are shown in **Figure 5.5 a**. Interestingly, both particles reveal faint splitting at the L$_3$ edge into t_{2g} (458.0 eV) and e_g (459.3 eV) peaks while the L$_2$ edge shows a single peak at 463.5 eV which is related to the t_{2g} sub-band, as illustrated in **Figure 5.5 b**. In agreement with the Ti L-edge fine structure (t_{2g} and e_g peaks), the Ti L-edge onset energy position featured in both Na-Ti$_3$C$_2$T$_x$ particles coincide with each other. Irrespective of the thickness of the Na-Ti$_3$C$_2$T$_x$ particles, the lateral oxygen concentration map is relatively similar and homogeneous across the particles (**Figure 5.5 c**), which is similar to that observed for Li-Ti$_3$C$_2$T$_x$. The XA spectra at the O K-edge of both multi-layered particles were found to agree with one another (**Figure 5.5 d**).
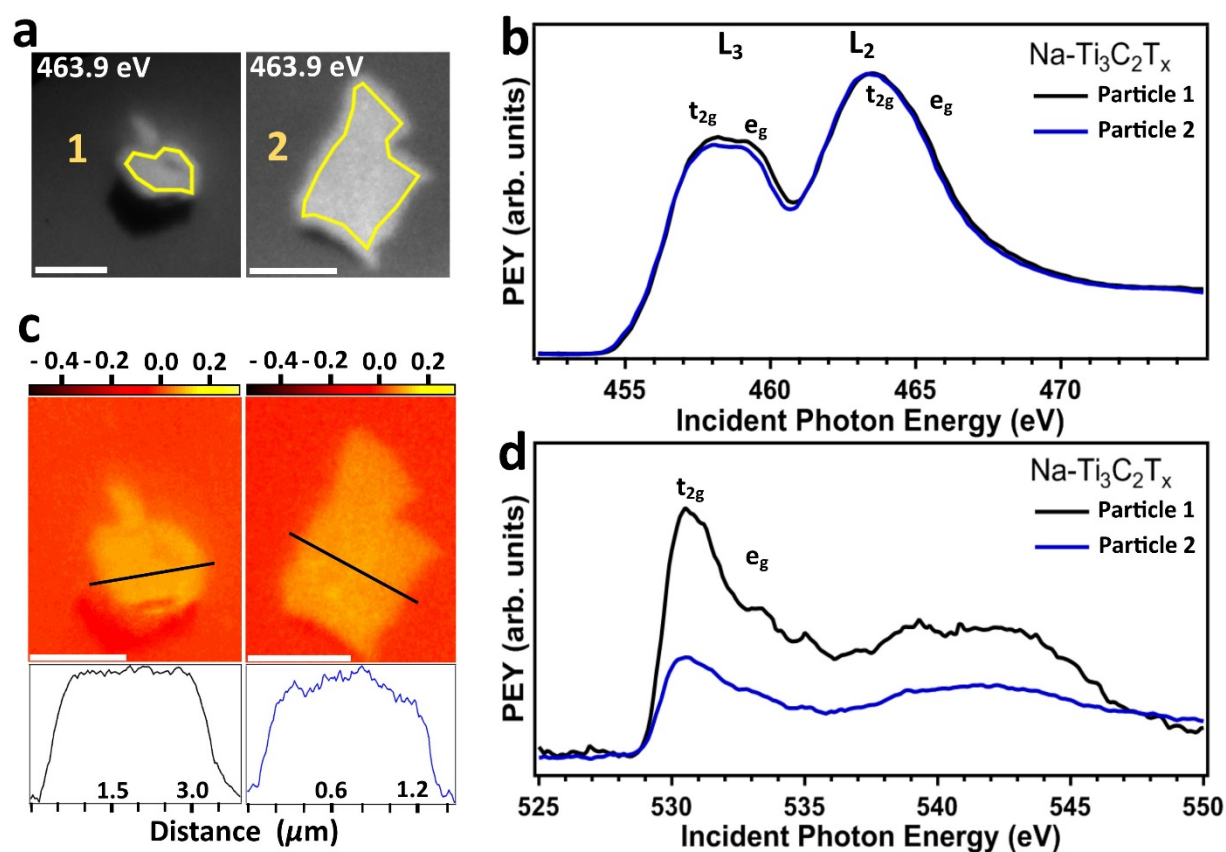
Figure 5.5 (a) X-PEEM micrographs of individual multi-layered Na-Ti$_3$C$_2$T$_x$ MXene particles at the Ti L-edge taken at an excitation energy of 463.9 eV (scale bar 3 μm and 1 μm in particle 1 and 2, respectively). The investigated region of particle 1 and particle 2 in b and d are labeled in yellow. (b) X-PEEM Ti L-edge XA spectra of the two different Na-Ti$_3$C$_2$T$_x$ MXene particles. (c) Lateral oxygen concentration over each individual Na-Ti$_3$C$_2$T$_x$ particle obtained for the same energy range described in Figure 5.2 and the line profile (the y-axis is the intensity in arb. units) across each particle is shown underneath the oxygen concentration distribution map. (d) X-PEEM O K-edge XA spectra of multi-layered Na-Ti$_3$C$_2$T$_x$ MXene particles. Taken with permission from Ref. [74].

The two O K-edge XA spectra signature are similar, with two distinct peaks at 530.7 eV and 533.3 eV, which are attributed to the t_{2g} and e_g orbitals, respectively. This is also observed at the Ti L-edge, and therefore we conclude that there is a comparable oxidation state of the Ti atoms in the two Na-$Ti_3C_2T_x$ MXene particles. As the Ti oxidation state in the multi-layered Na-$Ti_3C_2T_x$ particles is found to be stable irrespective to the particle thickness, the intercalation by Na cations between the multi-layered $Ti_3C_2T_x$ nanosheets might facilitate a relatively homogeneous surface chemistry. It is worth noting that Na cations were also reported to prefer sitting close to the $Ti_3C_2T_x$ surface [123].

5.6 Single Multilayered K-$Ti_3C_2T_x$ Particles

For K-intercalated $Ti_3C_2T_x$ MXene, two different particles of 450 nm and ≤ 30 nm thick (see **Figure 5.1**) were characterized. The spatially resolved X-PEEM micrographs and the corresponding Ti L-edge XA spectra for the K-$Ti_3C_2T_x$ MXene are presented in **Figure 5.6 a and b**, respectively. Despite the large difference in thickness, the Ti L-edge profile of both multi-layered particles was found to be identical. In both particles 1 and 2, a very weak splitting of the L_3 edge into t_{2g} (457.8 eV) and e_g (459.0 eV) peaks was observed, while the L_2 edge shows a single peak at 463.4 eV which is related to the t_{2g} peak, as shown in **Figure 5.6 b**. In line with the Ti L-edge fine structures, the onset energy position in K-$Ti_3C_2T_x$ MXene is found to not be influenced by the thickness of the particles.

However, the lateral oxygen concentration over the particle differs between thick and thin K-$Ti_3C_2T_x$ particles. The line profile across the thicker particle demonstrates inhomogeneous oxygen distribution, whereas the thin particle has a relatively homogeneous oxygen distribution as can be seen in **Figure 5.6 c**. The t_{2g} and e_g peaks of the XA spectra at the O K-edge were found to be at 530.5 eV and 533.2 eV in both particles, respectively (**Figure 5.6 d**). The comparable fine structures at the O K-edge XA profile in both particles leads to a similarity in the Ti oxidation state in multi-layered K-$Ti_3C_2T_x$ MXene particles. This trend observed from O K-edge XA spectra support the similarity in the Ti L-edge XA spectra. Nevertheless, the line profile across the particle reveals differences in the oxygen content environment between thick and thin particles which might be due to the uneven distribution of oxygen atoms in multi-layered $Ti_3C_2T_x$ particles.
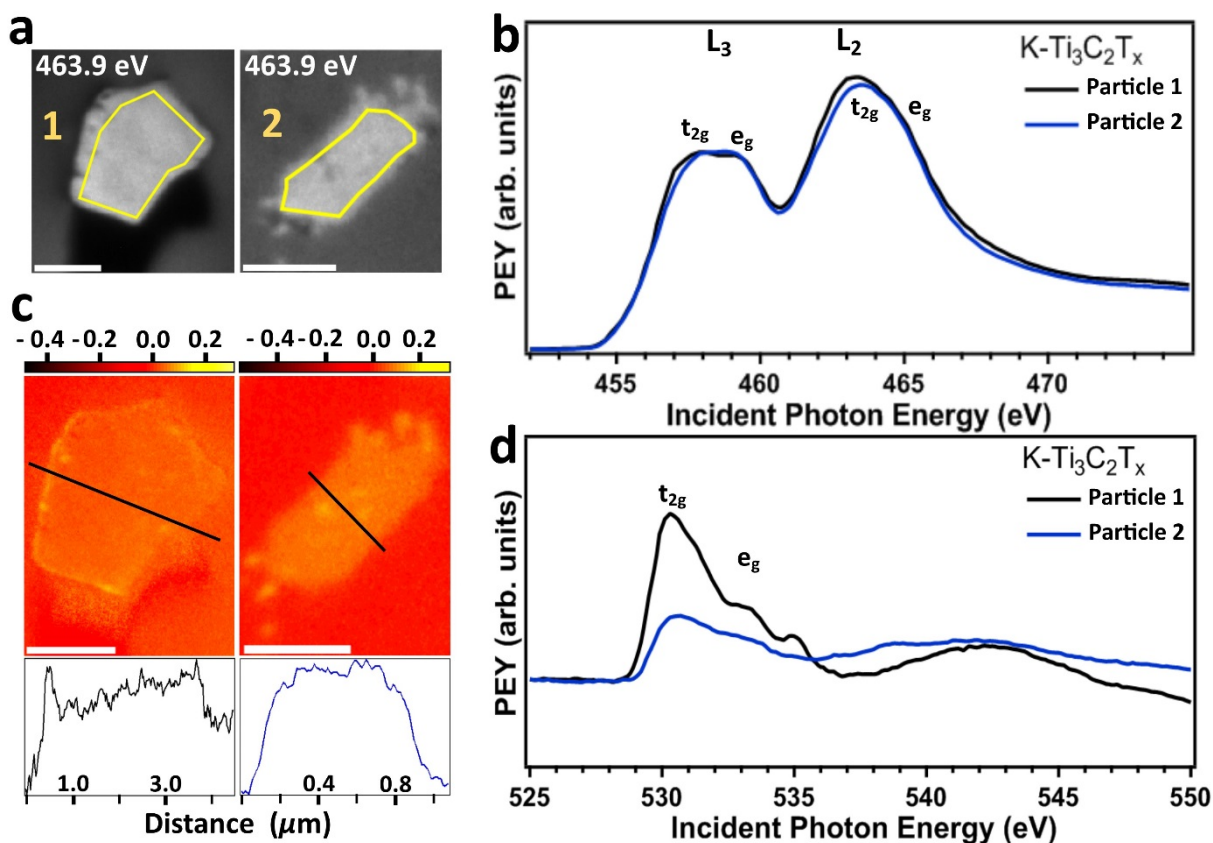
Figure 5.6 (a) X-PEEM micrographs of individual multi-layered K-Ti$_3$C$_2$T$_x$ MXene particles at the Ti L-edge taken at an excitation energy of 463.9 eV (scale bar 2 μm and 1 μm in particle 1 and 2, respectively). The investigated region of particle 1 and particle 2 in b and d are labeled in yellow. (b) X-PEEM Ti L-edge XA spectra of the two different K-Ti$_3$C$_2$T$_x$ MXene particles. (c) Lateral oxygen concentration over each individual K-Ti$_3$C$_2$T$_x$ particle obtained for the same range described in Figure 5.2 and the line profile (the y-axis is the intensity in arb. units) across each particle is shown underneath the oxygen concentration distribution map. (d) X-PEEM O K-edge XA spectra of multi-layered K-Ti$_3$C$_2$T$_x$ MXene particles. Taken with permission from Ref. [74].

5.7 Single Multilayered Mg-Ti$_3$C$_2$T$_x$ Particles

Finally, the impact of intercalation by multivalent cations, such as Mg^{2+}, on the surface chemistry in multi-layered Ti$_3$C$_2$T$_x$ MXene is of a great interest. The thickness of the investigated Mg-intercalated multi-layered Ti$_3$C$_2$T$_x$ particles is about 365 nm and ≤ 30 nm in particles 1 and 2, respectively (see **Figure 5.1**). **Figure 5.7 a** demonstrates X-PEEM spatially resolved micrographs to show individual particles of Mg-Ti$_3$C$_2$T$_x$ MXene at the Ti L-edge. The Ti L-edge XA spectra of both particles demonstrate very similar profiles with a clear splitting in the L$_3$ edge into t_{2g} (458.2 eV) and e_g (459.1 eV) peaks, but the L$_2$ edge shows a single peak at 463.8 eV which corresponds to the t_{2g} peak, as shown in **Figure 5.7 b**. The higher L$_3$ e_g to t_{2g} peak intensity ratio in particle 2 relative to particle 1 indicates a higher Ti oxidation state. The X-PEEM lateral oxygen concentration map over the entire particles is shown in **Figure 5.7 c**.

86

The line profile across particle 1 and 2, shown below the X-PEEM map, demonstrate an inhomogeneous oxygen distribution.
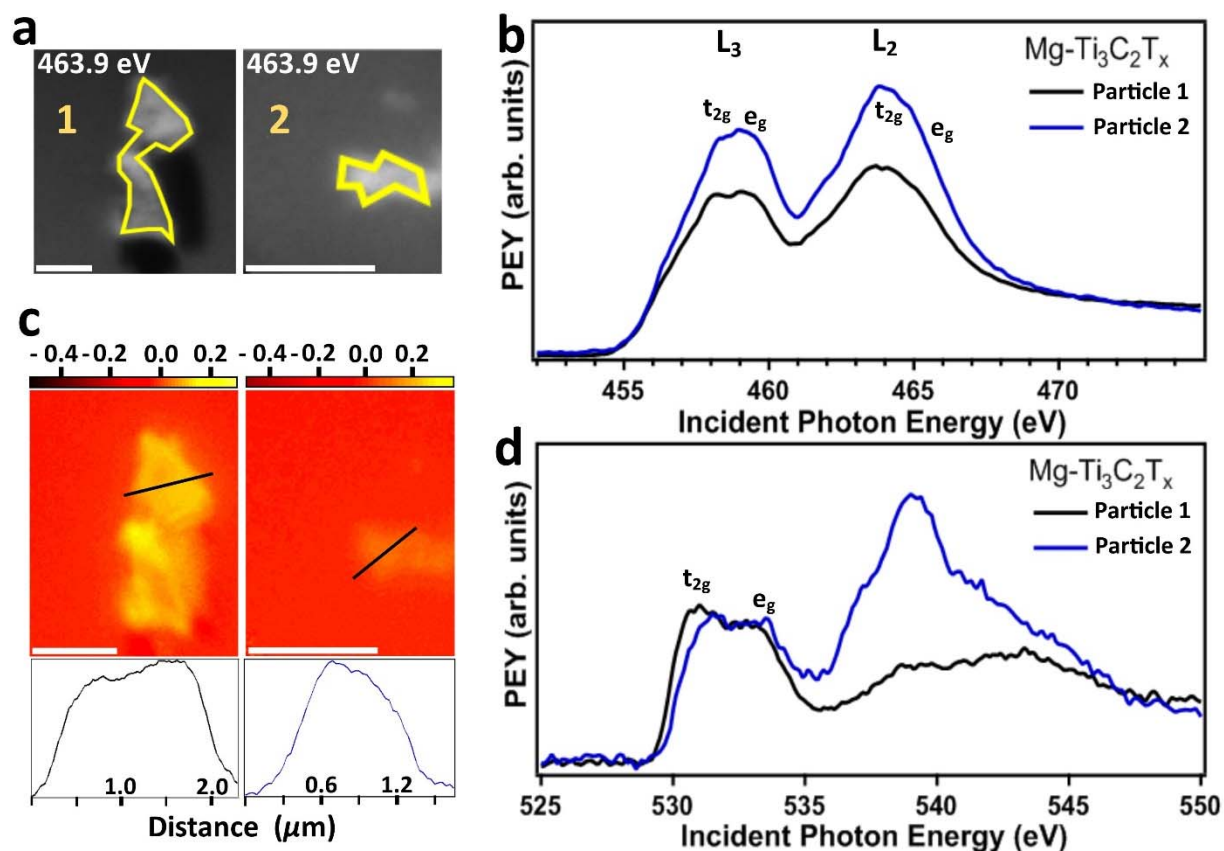
Figure 5.7 (a) X-PEEM micrographs of individual multi-layered Mg-Ti$_3$C$_2$T$_x$ MXene particles at the Ti L-edge taken at an excitation energy of 463.9 eV (scale bar 2 μm). The investigated region of particle 1 and particle 2 in b and d are labeled in yellow. (b) X-PEEM Ti L-edge XA spectra of the two different Mg-Ti$_3$C$_2$T$_x$ MXene particles. (c) Lateral oxygen concentration over each individual Mg-Ti$_3$C$_2$T$_x$ particle obtained for the same range described in Figure 5.2 and the line profile (the y-axis is the intensity in arb. units) across each particle is shown underneath the oxygen concentration distribution map. (d) X-PEEM O K-edge XA spectra of multi-layered Mg-Ti$_3$C$_2$T$_x$ MXene particles. Taken with permission from Ref. [74].

Figure 5.7 d shows the XA spectra at the O K-edge of both Mg-Ti$_3$C$_2$T$_x$ MXene particles. The t_{2g} and e_g peak position was observed at 531.2 eV (531.6 eV) and 532.9 eV (533.0 eV) in particle 1 (particle 2), respectively. It is worth noting that in the Mg-Ti$_3$C$_2$T$_x$ MXene, the distance between the layers are larger after Mg intercalation relative to other cations [47] and Mg cations prefer to be located relatively far away from the MXene surface [119], which paves the way for more oxygen and water molecules from the environment to bond with the Ti$_3$C$_2$T$_x$ surface prior sample's introduction into the UHV system. As a result, a higher average Ti

oxidation state is observed, as supported by the better resolved splitting observed in the L_3 edge.

In comparison between the different cation-intercalated $Ti_3C_2T_x$ samples, the splitting at the L_3 edge is very well pronounced in Li- and Mg-$Ti_3C_2T_x$ which indicates a higher Ti oxidation state compared to Na- and K-$Ti_3C_2T_x$ particles. In this context, the multi-layered Na- and K-$Ti_3C_2T_x$ MXene particles demonstrate also lower e_g to t_{2g} peak ratio at the O K-edge, which can probably be attributed to a comparable impact induced by these cations on the surface chemistry of the $Ti_3C_2T_x$ MXene. In chapter four, XAS recorded in TEY mode showed an increase of the Ti oxidation state after intercalation of cations with increasing cation sizes [73]. We observe here a slight difference of the Ti oxidation state after intercalation of Na and K cations. This difference is most likely related to (i) the relatively larger probing depth of TEY relative to PEY detection modes, (ii) the large amount of particles of different size, geometry, and thickness probed by TEY with a larger X-ray spot and (iii) the MXene environment under UHV conditions in this chapter's measurements (10^{-9} mbar range) compared to standard vacuum (10^{-6} mbar range) conditions applied for chapter's four measurements [73]. The difference in the pressure, along with the comparison between a thick drop cast sample compared to individual particles, may potentially influence the amount of the confined water between the nanosheets of the multi-layered $Ti_3C_2T_x$ MXene and hence the Ti oxidation state. Furthermore, the oxygen distribution over individual particles in the Li- and Na-$Ti_3C_2T_x$ particles is found to be homogeneous, possibly owing to the preferred position of Li and Na cations close to the $Ti_3C_2T_x$ surface [123]. Note that we previously observed O-Na and O-Li bonds at the O K-edge but not on the individual particles investigated in this study. Further X-PEEM studies would be required to understand where these bonds can be found. In K- and Mg-$Ti_3C_2T_x$ MXene, uneven distribution of oxygen was observed, which would also require further investigation in future.

5.8 Summary

By using X-PEEM, the impact of intercalation with Li^+, Na^+, K^+, and Mg^{2+} on the electronic structure of individual multi-layered $Ti_3C_2T_x$ MXene particles was investigated. Spatially-resolved XA spectra at the Ti L- and O K-edges provide extensive information about the Ti and O bonding environment over individual multi-layered MXene particles with approximately 30 nm resolution. For each cation-intercalated multi-layered $Ti_3C_2T_x$ MXene, two individual particles of different thickness and lateral dimensions were characterized. The Ti oxidation state in Na- and K-$Ti_3C_2T_x$ MXene was found to be unaffected by the particle thickness, whereas in Li- and Mg-$Ti_3C_2T_x$ MXene, the Ti oxidation state was found to differ between thin and thick particles. This study highlights that the thickness of individual multi-layered MXene particles, in addition to the interlayer spacing, affect the oxidation state of Ti and surface chemistry of MXene which are critical for electrochemical energy storage. This has to be considered to explain their electrochemical performance of thick electrodes based on such cation-intercalated multi-layered $Ti_3C_2T_x$ particles. The X-PEEM-based XA spectra sensitivity at the Ti L- and O K-edges to the oxidation state of the Ti atoms in MXene can also be applied to investigate the intercalation of other cations in $Ti_3C_2T_x$ and/or other types of MXenes.

CHAPTER SIX

Impacts of Nanoconfined Water in Ti$_3$C$_2$T$_x$ MXene

6.1 Motivation

Nanoconfined water is one of the most influential factors on MXene surface chemistry, which impacts many MXene-based applications. As shown in previous chapters, the high sensitivity of XAS at the Ti L- and O K-edges to local chemical bonds of different intercalated MXenes guides to investigate the nanoconfined water in $Ti_3C_2T_x$ MXene. However, studying nanoconfined water between the $Ti_3C_2T_x$ nanosheets is experimentally challenging and requires careful *in situ* X-ray spectroscopy, microscopy, and diffraction methods at low temperatures. The purposes of this study are shown below:

1- Would it be possible to detect the XAS signature of the nanoconfined water?
2- How would the XAS signature at the O K-edge evolve with temperature?
3- What is the nanoconfined water impact on the electronic structure of the surface Ti atoms (XAS at the Ti L-edge)? Is the Ti oxidation state altered?
4- Is the interlayer spacing changed between the MXene layers? This requires *in situ* XRD data at different temperatures in order to monitor the impact of the nanoconfined water on MXene *d*-spacing.

What is the essence of this chapter?

Unlike bulk water, intercalated water in 2D structures induces many intriguing phenomena and therefore the confinement of water between nano-scale lamellas has attracted attention in physics, biology, electrochemistry, geology and material science [136–138]. Theoretically, adsorbed water at interfaces and confined water are predicted to coexist in many phases [139–142]; however, experimentally it is extremely challenging to capture its structure and identify coexisting metastable phases [143–146]. The impacts of the nanoconfined water molecules next to surfaces is essential to be understood [144,147]. Here we report a remarkable change in the Ti oxidation state and interlayer spacing of $Ti_3C_2T_x$ MXene nanosheets as a function of temperature, which we interpret by a phase transition of the nanoconfined water. *In situ* XA spectra acquired at different temperatures at the O K-edge and Ti L-edge illustrate changes of the nanoconfined water and the accompanied changes in the Ti electronic structure. *In situ* XRD patterns show that the *d*-spacing between the $Ti_3C_2T_x$ nanosheets is enlarged at low temperatures and does not restore its initial value when returning back to room temperature.

6.2 Research Background

What is the common key factor in Ti₃C₂Tₓ MXene-based applications?

The majority of MXene-based applications is strongly affected by nanoconfined water between $Ti_3C_2T_x$ nanosheet flakes, including but not limited to desalination and purification of water [112,115], electromagnetic shielding [148], and EES devices [32,54]. This nanoconfined water is hydrogen (H)-bonded to the –OH functional group of the surface of MXene flakes. Interestingly, the 2D $Ti_3C_2T_x$ nanosheets possess high metallic conductivity combined with negatively charged surfaces of highly hydrophilic nature. Swelling induced by multiple layers of water and/or cations intercalation between $Ti_3C_2T_x$ layers leads to a remarkable increase in the interlayer spacing between the MXene nanosheets (*d*-spacing) [32,43,73,86]. For instance, the delamination process of the $Ti_3C_2T_x$ nanosheets results in a spontaneous intercalation of water and Li^+ between MXene layers [32,43], leading to expansion in the *d*-spacing and thus weakening of interaction between the MXene individual flakes.

Following MXenes discovery in 2011 [23], the nanoconfined water in $Ti_3C_2T_x$ has attracted tremendous attention [86,123,124], but direct experimental evidence of different phases and structure at low temperatures is still missing. At low temperatures, the confined water inside the nanochannels of other materials such as graphene results in 2D ice [143]. The phase and structure of 2D ice in materials other than MXenes were investigated [142–144] by various experimental techniques such as scanning tunneling microscopy (STM), atomic force microscopy (AFM), and transmission electron microscopy (TEM) [143,149]. Also, XAS tool was extensively used to probe the adsorbed and bulk-like water owing to its sensitivity to the strength of the H-bonds between water molecules in different phases [107,150], see Appendix **Figure App. 1**. For example, the H-bonding network is very strong in ice, weaker/partially broken in liquid phase, and even broken (do not exist) in a pure gas phase [151,152]. However, the X-ray based investigation of the inherent nanoconfined water as well as its evolution with temperature in $Ti_3C_2T_x$ MXenes is exceedingly challenging and has not been yet reported.

6.3 *In Situ* XAS Data

To manifest the nanoconfined water signature and its impact on the surface Ti electronic structure, *in situ* spatially-resolved XAS measured at the O K- and Ti L-edge (by using XPEEM sensitivity over $Ti_3C_2T_x$ MXene film, see section 2.2.3) was employed within a temperature

range of 220-300 K. In this context, spatially resolved XPEEM images demonstrate a large area (about 500 μm^2) of a few layers MXene sample. Therefore, as temperature changes, spatially resolved O K-edge images may provide visible changes in the surface oxygen environment of a few-layers of MXene samples. At temperatures below 260 K, the XPEEM micrographs do not show a noticeable change. However, XPEEM micrographs at the O K-edge reveal changes in some surface features starting from 260 K, as shown in **Figure 6.1 a**. In parallel, spatially resolved images at the Ti L-edge also demonstrate changes at temperatures ≥ 260 K, see **Figure 6.1 b**. To better compare, micrographs recorded at 220 K, 260 K, 280 K, and 300K are presented in **Figure 6.1**, however, the complete set of micrographs are shown in **Figure App. 2**. The surface changes represented by bright spots/regions across the entire area of MXene film were observed at T ≥ 260 K. Since the electrochemical performance of an electrode is obtained over large sample area of about few mm^2, the average Ti oxidation state of the whole sample is hence of high importance. A detailed analysis of these bright spots is currently in progress. In the following study, we will concentrate the discussion on changes of $Ti_3C_2T_x$ MXene surface revealed by averaged XA spectra at the O K-edge and Ti L-edge which would deeply interrogate any changes in $Ti_3C_2T_x$ MXene surface features.

6.3.1 O K-edge XA Spectra

Owing to O-containing surface terminations in $Ti_3C_2T_x$ MXene, typical O K-edge XA spectra exhibit two main features known as t_{2g} and e_g peaks at RT [72,74], as discussed in previous chapters. Therefore, the nanoconfined water XA signature would overlap with MXene surface O-containing contribution. The spectra measured at 220 K and 240 K (see **Figure 6.2 a**) exhibit, in addition to a region at about 530.6 eV, a pronounced feature around 541.0 eV. Nevertheless, at temperatures above 260 K, the XA spectra reveal mainly three distinctive peaks at 530.7 eV, 533.9 eV, and 536.8 eV which were not observed at lower temperatures (220 K and 240 K), see **Figure 6.2 a**. On the other hand, the peak at 536.8 eV was observed to shift to lower energies at temperatures above 260 K. Also, other regions probed within the energy range were found to change with temperatures. To precisely allocate peaks/regions within the O K-edge XA spectra at different temperatures shown in **Figure 6.2 a**, peak fitting was implemented. **Figure 6.2 b** demonstrates a representative model of the XA peak fitting data at 270 K to highlight the position of P1–P6. The XA fitting curves recorded at all temperatures are shown in **Figure App. 3**.
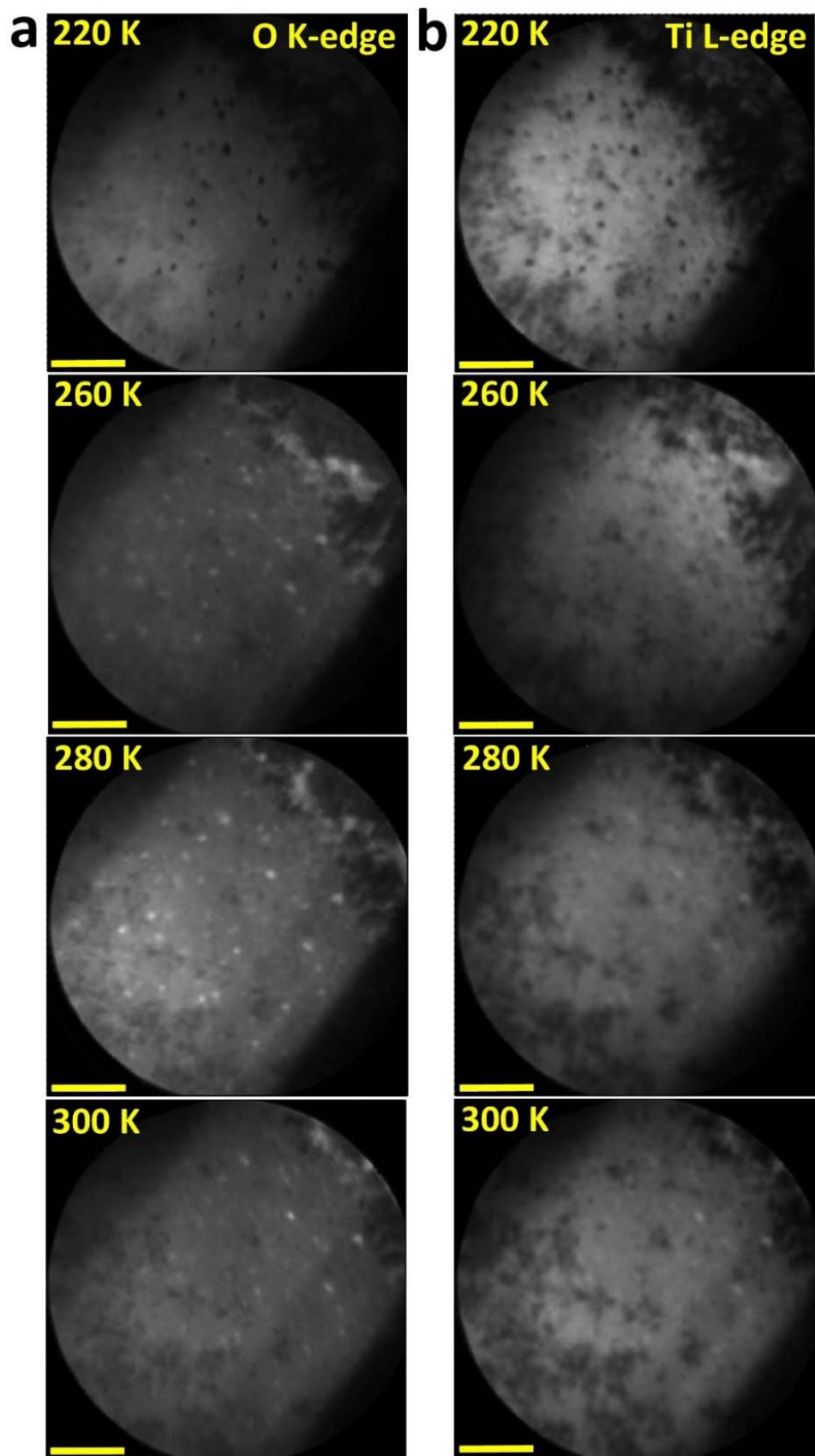
Figure 6.1 XPEEM micrographs of spin-coated $Ti_3C_2T_x$ MXene film measured at 220 K, 260 K, 280 K, and 300 K, mapping MXene sample area of about 500 μm^2. (a) The O K-edge and (b) Ti L-edge images taken at an excitation energy of 536.8 eV and 462.8 eV, respectively. Scale bar shown in all of the XPEEM micrographs is 5 μm.
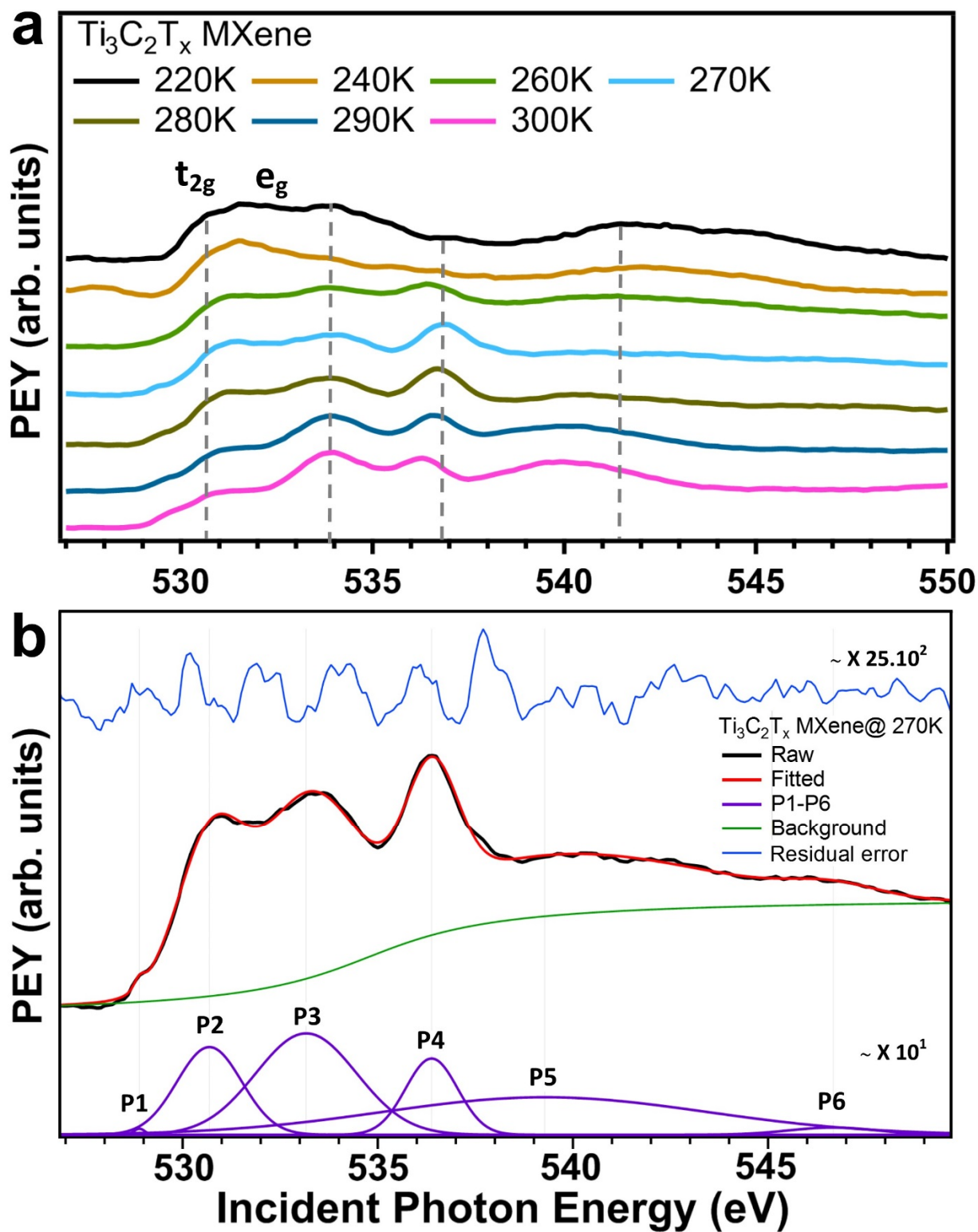
Figure 6.2 *In situ* O K-edge XA spectra of $Ti_3C_2T_x$ MXene measured at different temperatures. (a) The evolution of the nanoconfined water signature with temperatures. The vertical dashed lines highlight visible regions/peaks. (b) A representative XA peak fitting measured at 270 K (this temperature was chosen as a mid-point within the measured temperature range) to unveil all possible peaks within the O K-edge energy range. Please note that the y-axis scale is magnified for residual error and P1-P6 data. The XAS data was recorded in PEY mode and the XA spectra are normalized to the PEY signal above 545 eV.

6.3.2 Peak Fitting of O K-edge XA Spectra

The peak fitting of XA spectra measured between 220 K and 270 K was found to include six peaks (P1–P6) and five peaks (P1–P5) within the temperature range of 280-300 K due to a better fit convergence that results in smallest possible error values, see **Table 6.1**.

Table 6.1 Peak fitting data of the O K-edge XA spectra showing the peak position, FWHM, area, and relative area per each measurement's temperature. Error values are presented in red and considered equal to zero if ≤ 0.05.

#	Parameters	Temperatures (K)						
		220	240	260	270	280	290	300
P1	Position (eV)	530.5 ± 0.1	530.6 ± 0.1	529.2 ± 0.1	529.4 ± 0.0	529.4 ± 0.0	529.5 ± 0.0	529.7 ± 0.0
	FWHM (a.u.)	0.9 ± 0.2	0.8 ± 0.2	0.6 ± 0.3	0.3 ± 0.1	0.5 ± 0.1	0.6 ± 0.1	0.7 ± 0.1
	Area (a.u.)	117.8 ± 68.5	120.6 ± 124.0	9.1 ± 5.2	27.1 ± 8.0	56.2 ± 13.4	105.8 ± 16.0	126.2 ± 37.5
	Rel. A. (a.u.)	0.07	0.07	0.0008	0.002	0.004	0.005	0.008
P2	Position (eV)	531.5 ± 0.1	531.5 ± 0.1	531.0 ± 0.0	531.2 ± 0.0	531.0 ± 0.0	531.0 ± 0.0	531.0 ± 0.0
	FWHM (a.u.)	1.7 ± 0.3	1.4 ± 0.6	1.9 ± 0.0	1.9 ± 0.0	1.8 ± 0.0	1.9 ± 0.0	2.0 ± 0.1
	Area (a.u.)	361.4 ± 123.0	417.3 ± 438.5	1348.7 ± 78.7	2409.3 ± 94.2	2256.2 ± 101.5	2578.5 ± 62.7	2179.4 ± 79.8
	Rel. A. (a.u.)	0.2	0.2	0.1	0.2	0.1	0.2	0.1
P3	Position (eV)	533.7 ± 0.1	533.0 ± 0.5	533.6 ± 0.0	533.7 ± 0.0	533.6 ± 0.0	533.8 ± 0.0	533.8 ± 0.0
	FWHM (a.u.)	3.1 ± 0.2	2.4 ± 1.8	3.9 ± 0.1	3.0 ± 0.1	3.2 ± 0.1	2.9 ± 0.0	2.6 ± 0.0
	Area (a.u.)	715.7 ± 69.9	500.6 ± 519.8	4047.1 ± 148.2	4336.8 ± 158.6	5691.5 ± 128.6	6960.4 ± 71.4	5981.9 ± 101.5
	Rel. A. (a.u.)	0.4	0.3	0.3	0.3	0.4	0.3	0.4
P4	Position (eV)	537.1 ± 0.2	535.5 ± 1.0	536.5 ± 0.0	536.9 ± 0.0	536.7 ± 0.0	536.5 ± 0.0	536.2 ± 0.0
	FWHM (a.u.)	0.4 ± 0.5	2.4 ± 1.2	1.7 ± 0.0	1.5 ± 0.0	1.4 ± 0.0	1.4 ± 0.0	1.5 ± 0.0
	Area (a.u.)	3.7 ± 4.7	176.0 ± 202.8	862.6 ± 46.1	1683.9 ± 53.0	1778.0 ± 49.0	1804.2 ± 36.0	1795.8 ± 56.3
	Rel. A. (a.u.)	0.002	0.1	0.07	0.1	0.13	0.1	0.1

P5	Position (eV)	541.4 ± 0.2	542.0 ± 0.2	540.6 ± 0.0	539.8 ± 0.2	539.9 ± 0.1	539.6 ± 0.0	539.8 ± 0.0
	FWHM (a.u.)	2.5 ± 0.3	3.3 ± 0.5	9.7 ± 0.2	9.8 ± 0.6	6.5 ± 0.2	5.5 ± 0.0	4.3 ± 0.0
	Area (a.u.)	237.8 ± 74.6	349.4 ± 64.0	5283.5 ± 246.5	5178.1 ± 405.1	3283.4 ± 114.9	6329.6 ± 60.0	4865.3 ± 47.0
	Rel. A. (a.u.)	0.1	0.2	0.4	0.4	0.2	0.3	0.3
P6	Position (eV)	544.2 ± 0.4	544.6 ± 0.2	548.3 ± 0.2	547.2 ± 0.1			
	FWHM (a.u.)	3.8 ± 0.7	1.6 ± 0.6	2.3 ± 0.5	2.7 ± 0.4			
	Area (a.u.)	283.0 ± 76.5	50.2 ± 29.7	91.9 ± 37.8	271.9 ± 65.5			
	Rel. A. (a.u.)	0.2	0.03	0.008	0.02			

To better evaluate the changes with temperatures, the area and the relative area of each peak was measured. However, **Table 6.1** shows the main fitting parameters. The evolution of the peak position and area in the temperature range of 220 K to 300 K is shown in **Figure 6.3**. Please note that when the fitting error is smaller than the recorded energy step of 0.1 eV (see **Table 6.1**), the error bars are not included in **Figure 6.3**.
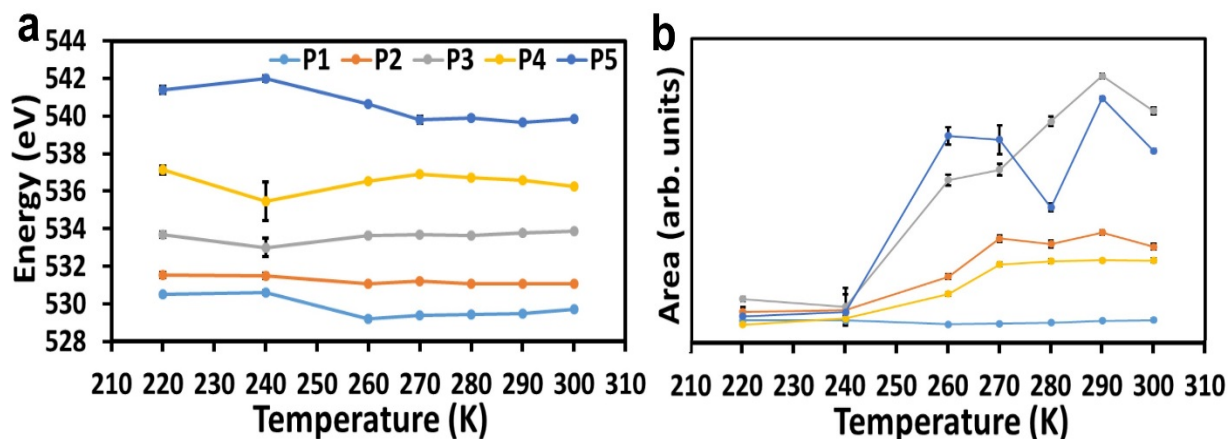
Figure 6.3 The evolution of the O K-edge spectra peak fitting data as a function of temperature with error bars. (a) The peak position trend with temperatures. (b) The corresponding change of the peak area relative to measurement's temperature. For better comparison, this figure highlights the evolution of the fitted peaks that existed in all XA spectra, namely, P1-P5 because the P6 region is not observed at temperatures above 270 K.

At T ≥ 260 K, **Figure 6.3 a** shows that first (P1) and second (P2) peaks demonstrate a significant shift to lower energies of about -1.0 eV and -0.5 eV with a very small error, respectively. However, P1 and P2 reveal no change at T ≤ 240 K. On the other hand, the third (P3), fourth (P4), and fifth (P5) peaks clearly show a change in peak position at T ≥ 260 K. At T ≤ 240 K. The change is either very small or large combined with high error. In particular, P3 and P4 show a comparable trend which demands a careful investigation. In this context, the change in peak position has to be compared to another fitting parameter such as the peak area. This means that the peak area parameter can be used to validate the clear change in peak position at different temperatures.

Figure 6.3 b demonstrates the corresponding peak area together with error bars to highlight the error percentage at different temperatures. Owing to the axis scale, error bars are not present at every single measurement temperature in **Figure 6.3 b**. Thus, a logarithmic scale would clearly help to disclose the error bars especially at T ≤ 240 K, see **Figure App. 4**. In general, unlike P1, the peak area of P2, P3, P4, and P5 was found to be directly proportional to measurement's temperature. Also, the peak area (except P1) was dramatically enlarged at T ≥ 260 K compared to lower temperatures. Regardless of the measurement temperature, the P1 error bar value was found to be large relative to other peaks. Likewise, the P2 error bar is found large especially at T ≤ 240 K. On the other hand, the error bar values of P3, P4, and P5 were relatively small; except at T ≤ 240 K (see **Table 6.1**). However, the interpretation of the variation of P5 area at T ≥ 260 K is complicated and will be clarified below.

To provide a better explanation, the P1-P5 fitting data evolution with temperature needed to be correlated. Since the error bar values of P1 and P2 are found to be very large compared to other peaks, their interpretation will not be discussed here but some ideas will be shown later. A possible interpretation of the P1 and P2 fitting data is presented in Appendix chapter, see page 152. The area error bar of P3 and P4 is found relatively large at T ≤ 240 K, suggesting the growth of P3 and P4 starts at higher temperatures. Regardless of temperature, the P3 position was relatively stable; although its area was dramatically enlarged at T ≥ 260 K. Likewise, P4 area was significantly increased at T ≥ 260 K and its position at 300 K (~536.3 eV) shifts to lower energies by about -0.6 eV compared to measurement recorded at 270 K (~536.9 eV). The P5 region was found to be pronounced around 542.0 eV at T ≤ 240 K and shifts to lower energies to reach ~539.8 eV at 300 K. Furthermore, the area of P5 was dramatically increased

at T ≥ 260 K. However, due to its remarkable broadness, the P5 fitting data is likely affected by contributions originating from various species. This means that P5 area includes an overlap from different features at T ≥ 260 K, which cannot be fully decorrelated at this stage and hence makes it more difficult to discuss.

To assign the peak fitting data of P3 and P4, **Table 6.1** and **Figure 6.3** data was carefully compared to reported values in literature and to XAS data shown in previous chapters. The P3 position was found to be close to 534.0 eV which coincides in energy with the signature of water molecules in gas-phase [107,150] or supercritical water phase [153]. In conjunction with P3, the P4 energy position was found to be close from 536.9 eV at 270 K, which resembles the main-edge water signature in liquid phase. Unlike P3, the P4 position demonstrates -0.6 eV shift to lower energies as going from 270 K to 300 K. This shift is in good agreement with XA main-edge fingerprint of liquid water at elevated temperatures [151,152] and means that the H-bonding network of water molecules is increasingly distorted and/or broken, which may result in non H-bonded water molecules. Importantly, similar to P3, P4 area manifests a remarkable increase above 260 K which suggests a growing role related to water main-edge feature [107,150]. Interestingly, the P5 position is located around 541.0 eV at T ≤ 240 K which can be assigned to the ice phase signature of water (strongly H-bonded water molecules) [107,150]. However, a gradual increase in temperature results in that P5 profile becomes faint and shifts to lower energies, which supports the disappearance of the strongly H-bonded water molecules. The ice phase of water signature vanishes because the strong H-bonding configuration of water molecules is probably transformed into a weaker or partially broken H-bonding network [154].

6.3.3 Discussion of XA Spectra and Peak Fitting Data

Based on the O K-edge XA spectra alongside with the peak fitting data, the t_{2g} and e_g peaks should be located in the energy range between 530.5-532.5 eV. The absence of a well-resolved e_g peak resembles XA spectra signature of ~TiO (Ti^{2+}) species [63,72], see previous chapters. The distinct XA spectral features at 533.9 eV and 536.8 eV can be assigned to (i) pre- and main-edge of H-bonded water (might be supercritical water or liquid water surface) [153] and/or (ii) gas-phase water peaks originated from the antibonding O–H $4a_1$ (534.0 eV) and $2b_2$ (536.0 eV)

orbitals of free water molecules (non H-bonded water) [107,150]. For clarity, the coexistence of liquid and gas phases of water in extremely confined spacing (such as MXene *d*-spacing) is likely not possible, however, oscillation between liquid and vapor phases of the nanoconfined water as a function of time is possible [155]. For simplicity, the coexistence of liquid- and gas-like phase signatures of water described above as (i) and (ii) will be henceforth abbreviated as liquid-gas.

A possible interpretation is that the pronounced region around 541.0 eV (P5) below 260 K can be attributed to post-edge XA characteristic of strongly H-coordinated water molecules, which resembles those in ice [150]. In conjunction with changes revealed by the XPEEM micrograph recorded at 260 K (see **Figure 6.1 a**), the corresponding XA spectrum uncovers a dramatic change related to liquid-gas characteristics (P3 ~533.9 eV and P4 ~536.8 eV). Importantly, the strongly H-coordinated water feature around 541.0 eV becomes noticeably less intense at 260 K, suggesting the inception of ice-thaw. It has to be mentioned that many studies reported that confined water phase transition takes place around 260 K [87,156]. At 270 K, the liquid-gas XA peaks became increasingly apparent whereas the ice feature around 541.0 eV completely vanished when compared to XA spectra measured at lower temperatures, giving rise to the contribution of the non H-bonded water molecules signature.

To carefully control the evolution of the observed features, the sample was progressively annealed at 280 K, 290 K, and 300 K. As the temperature was gradually increased, the P3 and P4 characteristic peaks become more pronounced and the P4 at ~536.8 eV was found to shift by about -0.5 eV to lower energies. This shift of -0.5 eV to lower energies (536.3 eV) is in line with liquid water characteristics at elevated temperatures (gas-like) [151,152], leading to the suggestion that more water molecules would resemble those of gas-like behavior. This can be explained due to the fact the average number of H-bonded water molecules decreases with increasing temperature.

In order to carefully confirm the gradual change in XA spectra at the O K-edge in terms of peak position and shift observed in P3 and P4, **Figure 6.4** shows the O K-edge XA difference spectra relative to the one measured at 260 K. As the temperature increases, the shift to lower energies in P3 and P4 becomes obvious and is highlighted by vertical dashed red lines relative to the grey ones. Furthermore, P3 becomes a well pronounced peak at 300 K relative to the

one measured at 270 K. Unlike P3, at 270 K the P4 was found to be sharp around 537.0 eV (main-edge XA signature of liquid water molecules) while at 300 K reveals a shoulder-like located around 536.2 eV [107,150].
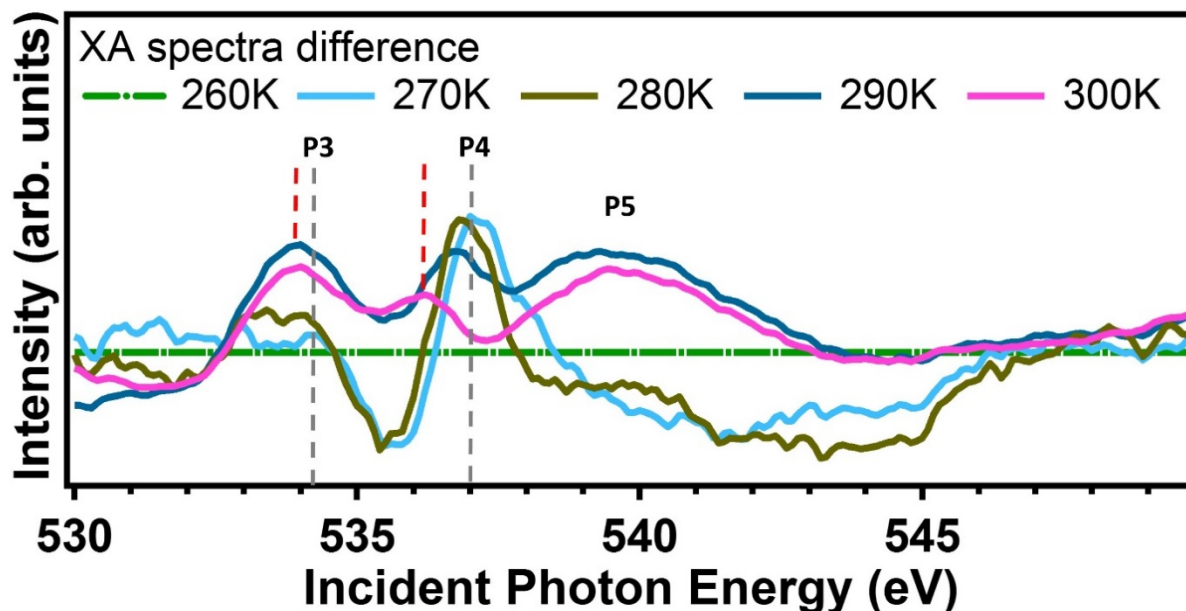
Figure 6.4 O K-edge XA difference spectra relative to the spectrum measured at 260 K, showing three important regions (P3, P4, and P5) within the O K-edge energy range. The grey and red dashed vertical lines are used to illustrate the shift direction with increasing temperature in P3 and P4. The XA difference spectra were obtained by division relative to the spectrum measured at 260 K. The XA difference spectra are normalized to the signal above 545.0 eV.

Thus, the difference of XA spectra at the O K-edge confirms the liquid-gas characteristics of water molecules observed in **Figure 6.2**. In addition, at 300 K a feature at about 539.5 eV suggests a growing oxide signature between TiO (Ti^{2+}) and Ti_2O_3 (Ti^{3+}) species [63]. At 300 K, the change in H-bonding network of water molecules probably affects the Ti oxidation state; as evident by P4 shift to lower energies and the disappearance of the pronounced feature around 541.0 eV (P5) [63]. Therefore, the XA spectra at the Ti L-edge need to be monitored as a function of temperature to disclose the correlation with the oxidation state of the surface Ti atoms in MXene, which is discussed in the next section.

6.3.4 Ti L-edge XA Spectra

To monitor changes due to the oxygen local environment with temperatures on the Ti oxidation state, XA spectra at the Ti L-edge need to be investigated at the same range of temperatures, namely, 220-300 K. **Figure 6.5** shows XA spectra at the Ti L-edge recorded on the same area where the O K-edge measurements are taken from, see **Figure 6.1**. The Ti L-edge spectra of $Ti_3C_2T_x$ MXene at 220 K and 240 K uncover mainly three distinctive features at 457.6 eV, 459.2 eV, and 463.2 eV corresponding to L_3 t_{2g}, L_3 e_g, and L_2 t_{2g} peaks, respectively. The missing of resolved L_2 e_g peak along with a faint shoulder-like L_3 e_g instead of a defined peak indicates a low oxidation state of the surface Ti atoms close to Ti^{2+} species [63,72–74]. The successive heating from 260 K to 300 K demonstrates a shift in the pre-edge onset energy position of about -0.4 eV to lower energies relative to those XA spectra measured below 260 K, indicating a lower Ti oxidation state. This shift to lower energies suggests a change in MXene surface chemistry which is attributed to the hydroxylation of the MXene surfaces following the water phase change. Interestingly, in chapter three a similar effect was observed in the characterization of pristine $Ti_3C_2T_x$ MXene dispersed in water at RT, which we attributed to hydroxylation of MXene surfaces upon dispersion in water [72]. The hydroxylation suggests a charge transfer from the oxygen atoms to the surface Ti atoms in $Ti_3C_2T_x$ MXene at 260 K. The charge transfer here refers to a proton exchange between the nanoconfined water and MXene surfaces, which leads to a charge redistribution in Ti and O bonds of MXenes. The strength of the H-bonding network between water molecules, which evolves as a function of temperature [151,152], most likely affects the surface hydroxylation. Another layer of complexity is that the water molecules in the ice phase are differently charged relative to those in vapor or liquid phases [157]. This leads to anticipate a complex charge transfer and/or electron hopping between water molecules next to $Ti_3C_2T_x$ MXene surfaces at different temperatures, affecting the electronic structure of surface Ti atoms [72,73]. Also, the orientation of water molecules is known to be strongly influenced by nearby charged surfaces [147]. Thus, we can reasonably anticipate a change in MXene surface chemistry.

Please note that the co-intercalated Li^+ ions, as a result of MXene synthesis procedure (see section 2.5.3), are less likely to play a role with respect to the evolution of nanoconfined water with temperature because the bonding between Li^+ and water molecules in the first hydration

shell is much stronger than the H-bonding network of water molecules beyond this shell and is found much less dependent on the temperature [158].
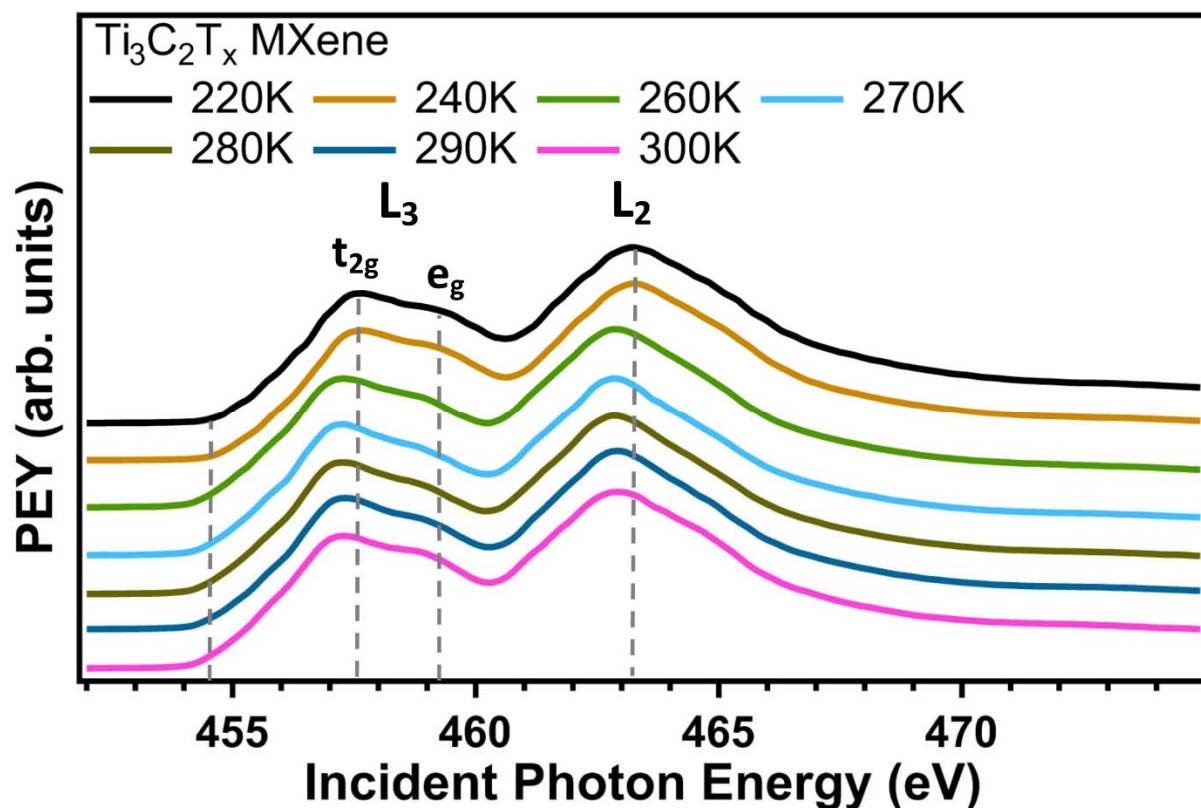
Figure 6.5 *In situ* Ti L-edge XA spectra at different temperatures reveal the impact on the surface Ti atoms in $Ti_3C_2T_x$ MXene in response to the change in the local environment. Typical pre-edge onset energy position, L_3 t_{2g}, L_3 e_g, and L_2 t_{2g} XA features are highlighted by vertical dashed lines. These features were found to shift by -0.4 eV to lower energies from 260 K onwards relative to spectra measured within 220-240 K. The XAS data was recorded in PEY mode and the XA spectra are normalized to the PEY signal above 470.0 eV.

At relatively higher temperatures (300 K), the shift of the pre-edge was found to be irreversible, which indicates that the change in MXene surface chemistry is stable up to RT. However, the stability of the MXene surface chemistry at higher temperature than RT upon the release of the nanoconfined water is essential to be studied.

To probe the thermal stability of MXene surface chemistry and of the nanooconfined water layer, the Ti L-edge measurement was recorded at high temperatures (the related XA O K-edge data at high temperatures are shown in **Figure App 3, 5 and Table App 1**). The high temperatures of 575 K and 773 K were chosen to ensure removal of water molecules. The XA spectra measured at high temperatures are presented in **Figure 6.6** alongside with those recorded at lower temperatures to emphasize the relative shift in energy among each other.

At high temperatures, the XA spectra exhibit resolved peaks of L_3 t_{2g} and e_g features compared to those measured at 220 K and 300 K. Furthermore, L_2 e_g peak was found to be a faint shoulder-like at 575 K and a pronounced shoulder at 773 K relative to the ones measured at 220 K and 300 K. Also, the pre-edge onset energy position was found to shift to higher and lower energies at 773 K and 300 K compared to the one measured at 220 K, respectively.
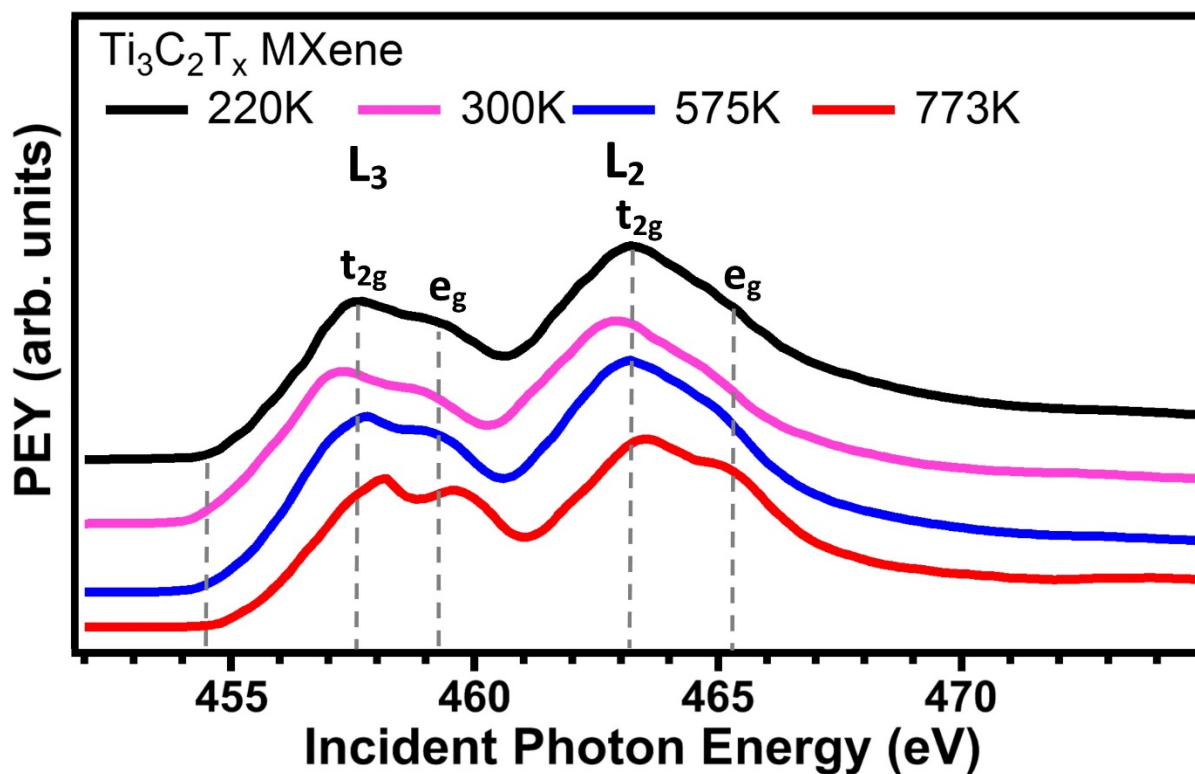
Figure 6.6 Ti L-edge XA spectra of $Ti_3C_2T_x$ MXene recorded at high temperatures of 575 K and 773 K compared to those measured at 220 K and 300 K in order to highlight the impact of the de-intercalation of nanoconfined water on the oxidation state of the surface Ti atoms. The typical pre-edge onset energy position, L_3 t_{2g}, e_g, and L_2 t_{2g}, e_g XA features are highlighted by vertical dashed lines. The XAS data was recorded in PEY mode and the XA spectra were normalized to PEY signal above 470.0 eV.

The XA features highlighted in **Figure 6.6** suggest a difference in the oxidation state of surface Ti atoms in $Ti_3C_2T_x$ MXene. The evolution of $L_{3,2}$ t_{2g} and e_g peaks indicates a higher Ti oxidation state [63,72–74]. The XA features were found to shift by about +0.4 eV to higher energies at 773 K compared to the one measured at 220 K, indicating a higher Ti oxidation state due to de-hydroxylation of MXene surfaces. Although the water molecules between $Ti_3C_2T_x$ nanosheets are significantly released around 423 K [51], the XA measurement at 575 K does not reveal a clear shift to higher energies relative to the one measured at 220 K. However, the $L_{3,2}$ t_{2g} and e_g profiles at 575 K witness changes suggesting a higher Ti oxidation state [72,74]. At 575 K, no clear shift to higher energies was observed (relative to the one measured at 300

K) owing to the fact that the de-intercalation of the nanoconfined water in MXene is fully completed around 673 K [51]. Also, the XA features at 300 K were found shifted to lower energies compared to the one recorded at 220 K, indicating lower surface Ti oxidation state. This lower Ti oxidation state suggests that MXene mostly contain hydroxyl and oxygen surface terminations at 300 K and 220 K, respectively. This change in the surface chemistry is likely taken place by a charge transfer from surface Ti atoms to oxygen atoms in $Ti_3C_2T_x$ MXene at 220 K, owing to the acidic nature of MXene (many protons) [26] and phase change of the nanoconfined water. This would result in a charge transfer from MXene surfaces to the nanoconfined water once transformed into ice, increasing the oxidation state of the surface Ti atoms which causes a shift in XA features to higher energies. Since the nanoconfined water resides between MXene nanosheets, monitoring the interlayer spacing may provide further insight on the structure of the nanoconfined water as discussed in the next section.

6.4 *In Situ* XRD at Low Temperatures

XRD is sensitive to the interlayer spacing in MXene (*d*-spacing) and to the nanoconfined water fingerprint [86,87]. The investigation of the *d*-spacing between $Ti_3C_2T_x$ nanosheets is extremely important as affecting the electrochemical performance [28,32] and nanosheets resistivity [51]. To study the XRD fingerprint of the nanoconfined water in MXene, a customized low temperature-assisted dome-like chamber was utilized, see **Figure 2.7**.

The XRD patterns were recorded at the same temperatures applied for XAS measurements. **Figure 6.7 a** shows *in situ* (002) diffraction order peak of $Ti_3C_2T_x$ MXene within a temperature range of 220-300 K, which provides direct information about the *d*-spacing of $Ti_3C_2T_x$ MXene. The XRD measurement started at RT[1] (#1) and is found at 12.73 Å, as shown in **Table 6.2**. Cooling down to 220 K results in a dramatic shift in the (002) peak to lower 2θ values, signifying an expansion in the *d*-spacing (16.52 Å). This leads to a dramatic difference of 3.79 Å in the *d*-spacing at 220 K relative to the one calculated at RT[1]. Subsequent heating at 240 K, 260 K, and 270 K leads to interlayer spacing of 16.39 Å which is almost analogous to the one measured at 220 K. As the (002) peak is shifted to higher 2θ values at 280 K, 290 K, and 300 K, the interlayer spacing is gradually contracted as shown in **Table 6.2**. However, the interlayer spacing remains larger by 2.04 Å even at 300 K relative to the spacing calculated at RT[1] before the commencement of the cooling-heating cycle. When the cycle is completed, a second profile

recorded at RT and atmospheric conditions (#9) confirms that the (002) peak does not restore its initial value and found to be larger by 2.19 Å relative to RT[1] (#1) measurement.
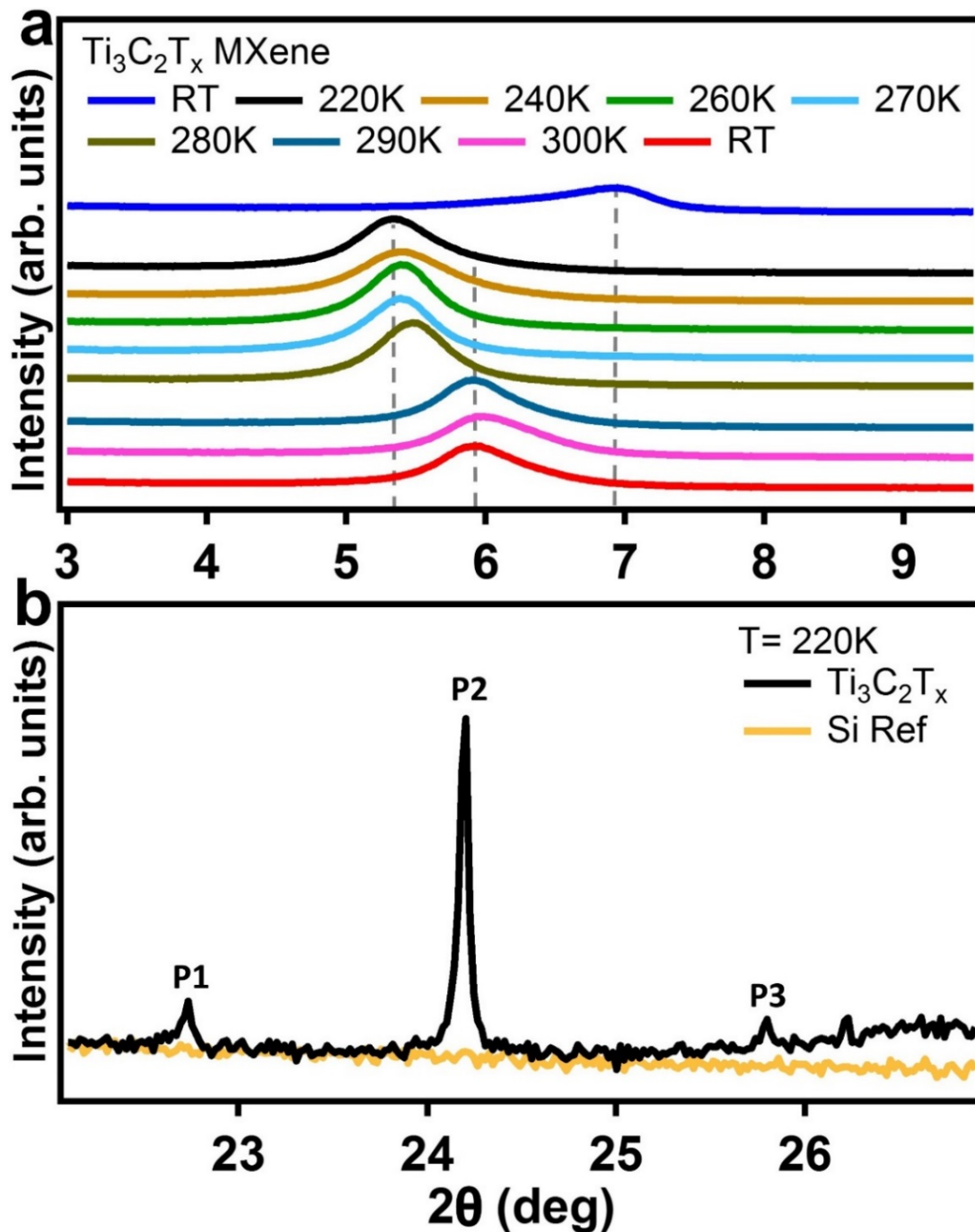
Figure 6.7 *In situ* XRD patterns of drop cast $Ti_3C_2T_x$ MXene on a Si substrate. (a) The response of the (002) diffraction order peak position upon freezing the nanoconfined water at 220 K and 9.5 mbar followed by stepwise heating back to RT. The XRD patterns at RT in blue and red stand for before and after freezing-heating cycle, respectively. (b) The diffraction pattern of frozen nanoconfined water at 220 K and 9.5 mbar shows distinctive ice Bragg peaks (P1, P2, and P3). For comparison, the XRD profile of the Si reference substrate is recorded at 220 K and 7.7 mbar. Vertical dashed lines highlight the significant shift in MXene (002) diffraction order peak to lower 2θ values. Please note that the intensity of panel b is five times smaller than the one in panel a.

106

Table 6.2 The calculation of the interlayer spacing between the $Ti_3C_2T_x$ MXene nanosheets (d-spacing) at different temperatures. The corresponding two theta (2θ) values and the expansion in the d-spacing relative to the first measurement recorded at room temperature (RT[1]) and atmospheric pressure (atm.) are presented. The pressure per each temperature is monitored and is found to increase when the temperature gradually increases as shown below, indicating desorption of some of the nanoconfined water. The room temperature (RT) here is assumed to be 300 K.

#	Temperature (K)	Pressure (mbar)	2θ (deg)	d-spacing (Å)	Difference relative to RT[1] (Å)
1	RT[1]	atm.	6.94	12.73	0.00
2	220	9.5	5.34	16.52	+3.79
3	240	9.5	5.39	16.39	+3.66
4	260	10.6	5.39	16.39	+3.66
5	270	12.3	5.39	16.39	+3.66
6	280	14.3	5.49	16.09	+3.36
7	290	15.3	5.90	14.97	+2.24
8	300	16.0	5.98	14.77	+2.04
9	RT	atm.	5.92	14.92	+2.19
10	220	256.0	5.51	16.03	+3.30

What can be concluded from **Table 6.2** is that, when cycled at 300 K (#8), the difference compared to RT in d-spacing is found to be 2.04 Å, which matches well to the length of the Ti–OH bond ($\sim$2.02 Å) [159]. This probably indicates that MXene surfaces are rearranged to have further hydroxyl functional groups. The d-spacing when cycled back to RT (#9) is found to be 14.92 Å, indicating an expansion of 2.19 Å with respect to the one measured in #1. This seems to indicate that the hydroxylated MXene surfaces facilitate the formation of Ti–O_{water} bonds (2.21 ± 0.02 Å) [159] as the water vapor existed in atmospheric air is anticipated to intercalate between $Ti_3C_2T_x$ nanosheets. Furthermore, the (002) peak at 220 K in #10 does not return to its initial position calculated in #2, suggesting that the internal structure of ice is altered due to a change in MXene surface chemistry. This change in MXene surface chemistry is probably induced by a special reorientation of water molecules established at 220 K (#2). Alternatively, the ice structure is presumably affected by a dissociation of some of the intrinsic MXene nanoconfined water species while heating, as evident by the pressure rise (see #2 to #9), which

cannot be recovered; in this sense the process is not reversible. Therefore, the staggering expansion observed at 220 K (#2) is most likely induced by unique reorientation of water molecules as soon as transformed into ice. Interestingly, the 3.79 Å expansion calculated at 220 K is in perfect agreement with the height of a monolayer of ice [144].

Figure 6.7 b unveils peculiar XRD pattern upon freezing the MXene nanoconfined water at 220 K, showing three diffraction peaks at 2θ values of 22.73°, 24.20°, and 25.79°. These three diffraction peaks were carefully compared to reported values in literature, suggesting ice-related peaks. Recently, another XRD measurements done by our group on different MXene free-standing films (these free-standing films of MXene are synthesized differently though) unveil no ice-related peaks, demanding further investigations. However, if these peaks observed in **Figure 6.7 b** indeed belong to nanoconfined water ice-related peaks then a possible interpretation is as the following:

At first glance, the three distinctive diffraction features observed at 2θ values of 22.73°, 24.20°, and 25.79° can be assigned to the (100), (002), and (101) diffraction order peaks of hexagonal ice (Ih) structure, respectively. However, the higher intensity of the (002) relative to (100) and (101) peaks suggests the occurrence of the (111) diffraction order peak, giving the evidence for the existence of cubic ice (Ic) structure [160].This means that a mixture of Ih and Ic structures is detected in MXene sample. To be confident that the ice signature comes from MXene film, the diffraction pattern of a bare Si substrate was also carried out at 220 K, as shown in **Figure 6.7 b**. The lack of ice-related diffraction peaks in the XRD profile of Si undoubtedly approves that the ice signature comes from the MXene film sample. To further investigate the ice structure, XRD measurements of $Ti_3C_2T_x$ MXene and Si reference substrate were also conducted at 220 K but at higher pressure of 256 mbar, see **Figure 6.8**. Interestingly, **Figure 6.8** reveals a significant difference in terms of XRD peak intensities. The XRD ice-related peak intensity ratios (using peak intensity maxima) were calculated for $Ti_3C_2T_x$ MXene and Si reference samples. Furthermore, XRD peak fitting is essential to validate observations in **Figures 6.7 b** and **6.8**, see section 6.4.1.
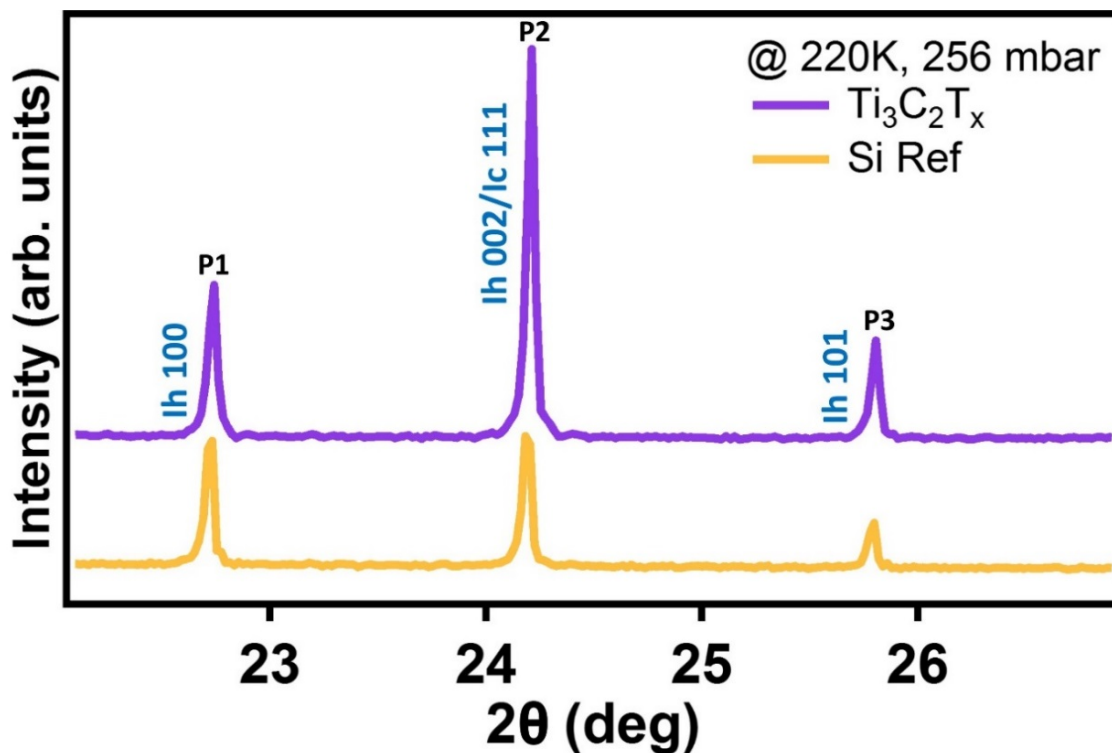
Figure 6.8 *In situ* XRD diffraction pattern recorded at 220 K under pressure conditions of 256 mbar reveals enhanced ice related peaks in Ti$_3$C$_2$T$_x$ MXene. This XRD measurement manifests the impact of further water molecules (ambient air) inside the chilled dome-like chamber and is recorded right after the full XRD cycle measurements described in Table 6.2. For comparison, the XRD profile of the Si reference substrate is also recorded. The 2θ values of the corresponding peaks shown in this figure as well as the peak ratios compared to MXene sample measured at 220 K and 9.5 mbar are presented in Table 6.2.

6.4.1 XRD Peak Fitting

The peak fitting provides, in addition to peak position, the area of each peak to emphasize the peak ratios obtained prior to the peak fitting calculation. To examine the values of peak intensity ratio shown in **Table 6.3**, the peak ratio was also calculated using peak area. To have a direct insight about the difference, the values of peak area ratio are shown between brackets next to ratio values derived from peak intensity maxima, see **Table 6.3**. **Table 6.4** shows the peak fitting data details of ice-related XRD measurements of Ti$_3$C$_2$T$_x$ MXene and Si substrate reference.

As a representative of the performed peak fitting, **Figure 6.9** shows the peak fitting of MXene at 220 K and 9.5 mbar which reveals the position of P1, P2, and P3. The peak fitting of other

samples described in Table 6.4 are shown in **Figure App 6**. Based on the peak fitting data, the peak area ratio values are found in agreement with those derived from peak intensity maxima of $Ti_3C_2T_x$ MXene. The P2/P3 area ratio of the XRD measurement at 220 K and 9.5 mbar is found to be three times larger than the P2/P3 intensity maxima ratio, see **Table 6.3**.

Table 6.3 The relative peak intensity ratio of the ice per each sample measured at 220 K. The ice peaks observed at 2θ values of 22.73° (Ih 100), 24.20° (Ih 002/Ic 111), and 25.79° (Ih 101) are abbreviated as P1, P2, and P3, respectively. The pressure of 256 mbar is obtained by allowing ambient air to be flown in the dome-like chamber prior to recording the XRD pattern. For a direct comparison, the value between brackets ()* shown below stands for peak ratio using peak area instead of peak intensity maxima.

Peak intensity ratio	$Ti_3C_2T_x$ MXene 220 K, 9.5 mbar ()*	$Ti_3C_2T_x$ MXene 220 K, 256 mbar ()*	Si reference substrate 220 K, 256 mbar ()*
P2/P1	4.05 (7.22)	2.47 (2.21)	1.03 (1.12)
P2/P3	5.03 (16.74)	3.79 (3.69)	2.72 (3.37)
P1/P3	1.24 (2.31)	1.53 (1.66)	2.63 (3.00)

Table 6.4 Peak fitting data of ice diffraction order peaks (P1, P2, and P3) observed in MXenes and Si reference substrate. The peak fitting highlights each peak position, area, and relative area (Rel. A) compared to other peaks per similar measurement conditions. For simplicity, the error values are shown in Appendix (**Table App 2**).

	$Ti_3C_2T_x$ MXene@220 K, 9.5 mbar				$Ti_3C_2T_x$ MXene@220 K, 256 mbar				Si ref.@220 K, 256 mbar			
#	2θ	FWHM	Area	Rel. A	2θ	FWHM	Area	Rel. A	2θ	FWHM	Area	Rel. A
P1	22.72	0.06	0.17	0.11	22.72	0.04	2.95	0.26	22.72	0.02	2.29	0.41
P2	24.19	0.05	1.22	0.83	24.20	0.03	6.54	0.58	24.19	0.03	2.57	0.46
P3	25.79	0.04	0.07	0.04	25.79	0.04	1.77	0.16	25.79	0.02	0.76	0.13
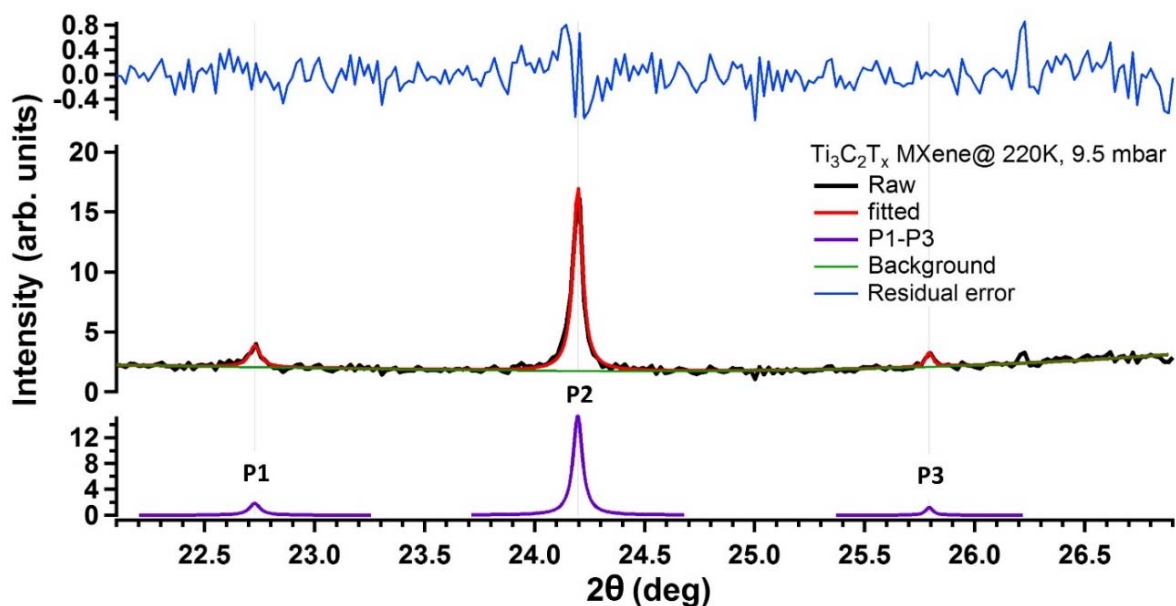
Figure 6.9 A representative peak fitting data of $Ti_3C_2T_x$ MXene measured at 220 K and 9.5 mbar, showing the raw and fitted peaks together with the background and the residual error spectra.

To interpret our data, one should know that in pure Ih structures, the P2 is significantly and slightly smaller than P1 and P3 in intensity, respectively [160]. The prominence of Ic structure, on the other hand, is characterized by higher intensity of P2 compared to P1 and P3 intensities [160]. **Figures 6.7 b** and **6.8** show that P2 is higher in intensity relative to P1 and P3, indicating the coexistence of Ic and Ih structures. This means that the ice diffraction pattern of the nanoconfined water of MXene comprises a mixture of Ih and Ic structures. **Table 6.3** shows that the P2/P1 and P2/P3 ratios of ice structures are found larger than one following the order $MXene_{9.5}$ > $MXene_{256}$ > Si_{256} which indicates systematic increase in the percentage of Ic relative to Ih structure, respectively. It is noteworthy that under ambient air pressure, the formation of the Ic structure is expected upon freezing water vapor [161,162]. At ambient air pressure of 256 mbar, MXene P2/P1 ratio is, however, found remarkably smaller than the one measured at 9.5 mbar which implies that additional water vapor existing in air does not necessarily intercalated, but preferentially forms Ih with certain orientation. The latter is evident as the ratio of P1/P3 is found to be the highest in Si reference substrate compared to MXene samples, as shown in **Table 6.3**. Importantly, the P2/P1 ratio of Si is found to be almost equal one, indicating that the Ih structure is mainly grown on top of the Si reference substrate.

6.4.2 Discussion of XRD Data

What kind of information can be extracted from the discussion of XRD measurements?

First of all, since XRD technique is a bulk-sensitive technique, it is necessary to visualize MXene sample on top of the Si reference substrate. **Figure 6.10** represents a model figure showing possible positions/orientations of drop cast MXene flakes on top of a Si substrate, which may result in microscale voids between MXenes owing to less ordered stack of MXene nanosheets. These voids/pockets can be existed between either different stack of MXene flakes or MXene and Si substrate. These voids may form interconnected channels or mesopores of water [125]. To have a direct comparison, the top panel of **Figure 6.10** shows MXene atomic configuration to highlight the change in the interlayer spacing and the surface chemistry at RT and 220 K. The atomic configuration demonstrates that the interlayer spacing is smaller by 3.8 Å at RT compared to measurement recorded at 220 K. As previously mentioned, the interlayer spacing is likely altered due to the reorientation of water molecules at low temperatures, see section 6.4.

In order to interpret the significant expansion in MXene d-spacing at 220 K, a previous study has shown that water molecules are ordered in layers with hydrogen-down (oxygen-up) orientation fashion and are significantly extending away from negatively charged surfaces [147]. In contrast to those in bulk water, the first layer of water molecules next to charged surfaces was found to extend far away and has a great areal density, implying unique hydrogen-bonding networks. This peculiar behavior of the first water layer is in harmony with our findings and probably explains the significant impact on the interlayer spacing of MXenes. Hence, the unique hydrogen-bonding network as well as the reorientation of water molecules below 260 K drive a remarkable expansion in MXene d-spacing. On the other hand, the surface chemistry is found to be abundant with oxygen and hydroxyl terminations at 220 K and RT, respectively. These surface terminations are observed to be consistent with XAS results as evident by the relative shift of the XA spectra to higher/lower (oxygen/hydroxyl) energies. The change in MXene surface chemistry is caused by a charge transfer and is discussed in detail in section 6.3.4.
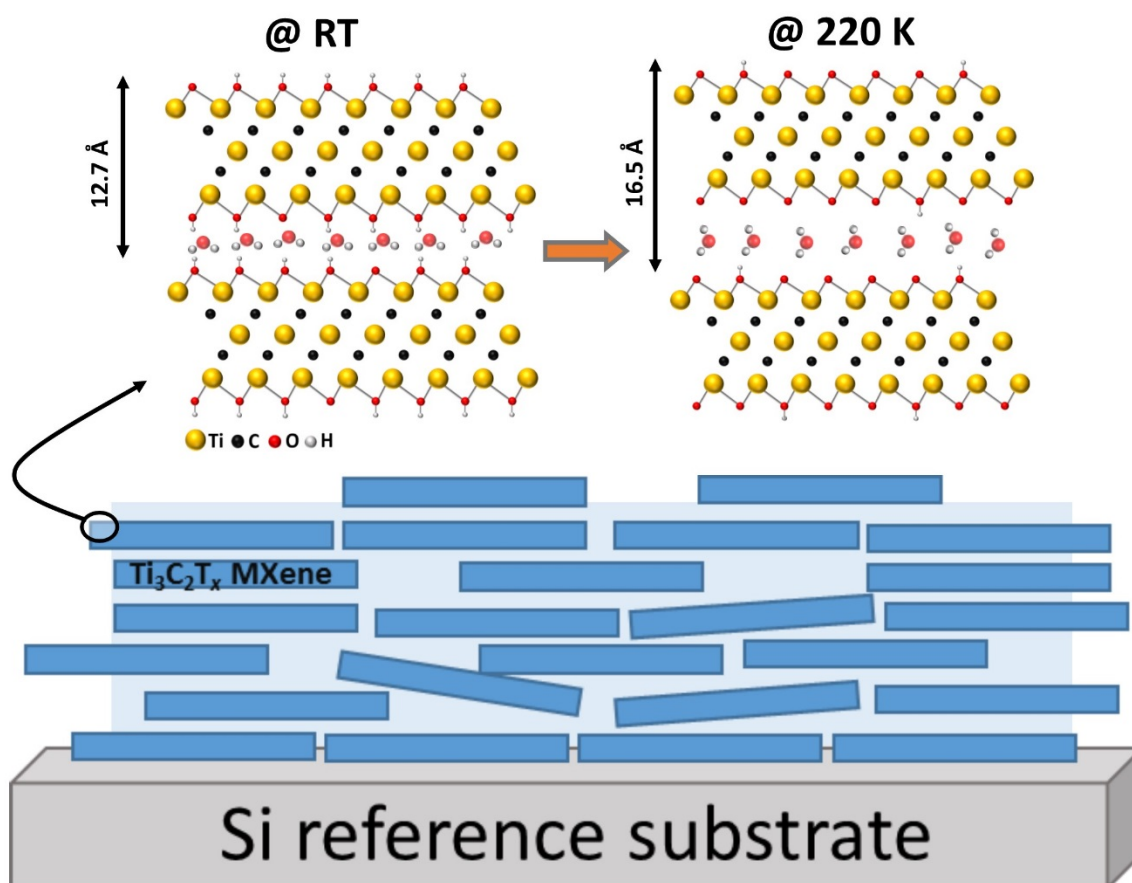
Figure 6.10 A schematic representation of drop cast $Ti_3C_2T_x$ MXene flakes (blue rectangular) on a Si reference substrate (grey rectangular) as a sample ready for XRD measurements. On top, a zoom in of a flake reveals MXene atomic configuration at RT and 220 K to highlight the difference in terms of interlayer spacing and surface chemistry. The MXene flakes in blue denote single or stacking of a few layers of MXene. The voids between different MXene flakes can be accommodated by smaller MXene flakes and/or mesopores of water (light blue background represents, depending on the temperature, the nanoconfined/mesopores water in liquid, solid, and liquid-solid phase). For clarity, this schematic representation is a model figure that shows possible orientations, dimensions, and positions of MXene flakes on a Si substrate, however, MXene flakes may also have many other random orientations, dimensions, and positions different from the one shown in this figure.

One may also argue that the XRD profile of ice cannot be originated from the nanoconfined water located within MXene *d*-spacing as this spacing is enough to accommodate only one or two layers of water. To answer that, XRD pattern can be also acquired from random or MPDO of mono- and bi-hydrated interstratified MXene layers, see section 2.4.1 and **Figure 2.6**. Another important question is that the water that exists in voids/pockets may reveal ice diffraction peaks at low temperatures. If the XRD signature of the ice-related peak ratios observed in MXene$_{9.5}$ sample originates from voids/pockets, a similar XRD signature should be maintained or even enhanced in MXene$_{256}$ sample. The reason is that the amount of water

molecules that existed in air of 256 mbar pressure is significant. This indicates that the ice diffraction pattern observed in MXene$_{9.5}$ sample can be linked to the nanoconfined water upon freezing at 220 K and apparently prefers the Ih 002/ Ic 111 orientations. However, further research is still needed to fully confirm that these XRD ice-related peaks observed in **Figure 6.7 b** are exclusively belong to the nanoconfined water signature upon cooling at 220 K.

6.5 Conclusion

In this work the impact of the nanoconfined water on the interlayer spacing and the surface chemistry was studied by means of XAS and XRD techniques. At different temperatures, the XA spectra show the fingerprint of the nanoconfined water in different phases, see **Figures 6.2 and 6.4**. When the nanoconfined water between MXene nanosheets is initially frozen (strongly H-bonded water molecules), a charge transfer from MXene surfaces to the ice phase of the nanaoconfined water is plausible to take place (de-hydroxylation) [157]. Indeed, owing to the charge transfer, XA spectra at the Ti L-edge reveal a noticeable change, see **section 6.3.4**. As the temperature is gradually ramping up, the ice thaw triggers a reverse charge transfer towards the surfaces of MXene (hydroxylation), suggesting to lower the oxidation state of the surface Ti atoms. Thus, when the ice thaws, the coexistence of water in liquid and gas phases is observed in the XA spectra at the O K-edge. The ice thaw induces a distortion in the local environment of oxygen, which affects MXene surface Ti electronic structure. This means that the phase change of the nanoconfined water (H-bonding network is known to be weakened at elevated temperatures) disrupts the local environment of MXene surfaces. Therefore, the shift of XA characteristic features at the Ti L-edge to higher/lower energies at temperatures below/higher 260 K [151,152] indicates higher/lower oxidation state of MXene surface Ti atoms [63,78]. At high temperatures (above RT) the shift in XA features was found to higher energies, indicating higher Ti oxidation state.

On the other hand, the XRD data show that at gradually heating from 220 K to 300 K uncover that the *d*-spacing shrinks owing to the fact that the hydrogen-bonding between water molecules becomes progressively weaker compared to those in ice. Nonetheless, the *d*-spacing is still larger by 2.19 Å relative to the one calculated first at RT[1], confirming a unique

114

impact not only on the interlayer spacing but also leading to hydroxylation of MXene surfaces. This hydroxylation of MXene surfaces at room temperature is consistent with the shift of the XA features at the Ti L-edge to lower energies. Therefore, as temperature increases, the $Ti_3C_2T_x$ MXene is accordingly altered in terms of surface chemistry, d-spacing, and hydrogen-bonding network of water molecules. These changes are found to be solely related to nanoconfined water phase change. However, further studies, in particular theoretical ones, will be helpful to have a deep understanding about the impact of the hydrogen-bonding network of the nanoconfined water on MXene surfaces.

6.6 Summary

In this study, we discovered unprecedented nanoconfined water-driven changes in the d-spacing and surface chemistry of $Ti_3C_2T_x$ MXene. Up to our knowledge, we are reporting here for the first time the XAS fingerprints of the MXene nanoconfined water at different temperatures. The *in situ* XA spectra at the O K-edge reveal the coexistence of the nanoconfined water in different phases, which triggers lower surface Ti oxidation state. At high temperatures however, the *situ* XA spectra at the Ti L-edge show a shift to higher energies, confirming higher Ti oxidation state upon a complete removal of the nanoconfined water. The shift in XA features is governed by a complicated charge transfer at the MXene-water interface. On the other hand, XRD patterns demonstrate that the d-spacing between the $Ti_3C_2T_x$ nanosheets is drastically expanded upon cooling down to 220 K and does not restore its initial value measured initially at RT. This expansion in the d-spacing suggests a distinctive impact induced by reorientation of the nanoconfined water molecules and alteration in the surface chemistry. It remains an open question how the orientation of the water molecules and especially those forming the first layer adjacent to MXene surfaces behave at different temperatures which requires further experimental and theoretical studies to obtain deeper understanding that guides for future MXene studies.

CHAPTER SEVEN

Conclusion and Outlook

The main focus of this work was to utilize X-ray spectroscopy, microscopy, and diffraction methods to characterize alterations in the surface chemistry of $Ti_3C_2T_x$ MXenes upon changing intercalants (such as urea, Li^+, Na^+, K^+, and Mg^{2+}), environments, and temperatures. Soft X-ray absorption spectroscopy was mainly used at the Ti L-edge and O K-edge to study the Ti oxidation state, which influences the electrochemical performance of $Ti_3C_2T_x$ MXenes. The $Ti_3C_2T_x$ samples were investigated *ex situ* and *in situ* in water and sulfuric acid environments as well as *operando* as an anodic potential was applied. Furthermore, nanoconfined water between $Ti_3C_2T_x$ nanosheets disclosed an impact on MXene surface chemistry and interlayer spacing at low temperatures. Based on the data presented here (chapters three to six), the used techniques have demonstrated great findings not only for characterization purposes of MXene surface chemistry but also offered a guide to enhance their electrochemical performance.

7.1 Summary

Typical layered materials for EES applications, for example graphite, likely suffers from a slow process of cations intercalation. However, the electrochemical performance of $Ti_3C_2T_x$ MXenes in aqueous electrolytes, in particular sulfuric acid, has revealed a remarkable capacity as well as cyclability at low and high rates. This excellent electrochemical performance triggers many studies to have a comprehensive understanding about intercalation, nanoconfined water, and the local chemical bonds that drive the surface chemistry in $Ti_3C_2T_x$ MXenes.

The latest studies about the pseudocapacitive storage mechanisms in 2D and oxide materials such as the $Ti_3C_2T_x$ MXenes were shown in **chapter one**. It does also show the limits and obstacles that the intrinsic pseudocapacitive materials are currently facing. Furthermore, a literature review showed the current studies about the properties of EES devices in general and the substantial progress in the electrochemical performance of $Ti_3C_2T_x$ MXene since its discovery in 2011. The introduction of the advanced X-ray spectroscopy, microscopy, and diffraction techniques used in this PhD work was then addressed in **chapter two**. In addition, this chapter shows the cutting-edge equipment compatible with the aforementioned advanced techniques that help to investigate the surface chemistry and the Ti oxidation state of $Ti_3C_2T_x$ MXene in different environments. The study of MXene in various environments using XAS is extremely challenging and remains poorly investigated.

Indeed, in **chapter three**, the surface chemistry of multilayered $Ti_3C_2T_x$ MXene has witnessed a remarkable difference upon intercalation with urea molecules. Furthermore, drying in air and dispersion in water environments played an important role in changing the Ti oxidation state of $Ti_3C_2T_x$ MXene before and after intercalation. The observation of higher Ti oxidation state after intercalation leads to a significant increase in the electrochemical capacity of urea-intercalated MXene electrode compared to pristine MXene electrode. The higher oxidation state after urea intercalation likely facilitates further reduction in sulfuric acid, which paves the way to higher capacitance. The intercalation of urea as a relatively large molecule compared to cations is utilized as a model here. In **chapter four**, the intercalation of multi-layered $Ti_3C_2T_x$ with various cations such as Li^+, Na^+, K^+, and Mg^{2+} in different environments were studied. Here, the evolution of the oxidation state of the surface Ti atoms in $Ti_3C_2T_x$ MXenes was observed to be affected by cation intercalation as well as exposure to sulfuric acid and is found to be cation-dependent. This chapter shows for the first time the *in situ*/*operando* XAS data at the Ti L-edge of cations-$Ti_3C_2T_x$ in different environments and under anodic applied potential. Accordingly, *in situ* XAS measurements highlight the charge transfer of which the MXene surface has experienced in sulfuric acid. The preliminary electrochemical performance of these multilayered cations-intercalated $Ti_3C_2T_x$ demonstrates a great increase in capacitance.

As MXene-based electrodes consist of many individual MXene particles, the lateral size of an individual $Ti_3C_2T_x$ flakes was reported in a previous study to affect the electrochemical

performance. However, in **chapter five**, the thickness of individual cations-intercalated $Ti_3C_2T_x$ particles was found to affect the Ti oxidation state. By using XPEEM, two individual particles of different thicknesses were chosen and found to alter the Ti oxidation state, leading to expect a change in MXene electrochemical performance. Also, the first observation of the oxygen content distribution across these individual cations-$Ti_3C_2T_x$ particles was reported.

Chapter six reveals peculiar impacts driven by the nanoconfined water on MXene surface chemistry and interlayer spacing. The *in situ* XAS signature of MXene nanoconfined water was revealed upon freezing-heating of MXene sample. As the temperature is gradually increased to reach RT, the *in situ* XAS at the O K-edge enables to monitor the evolution of the nanoconfined water signature. In addition, the *in situ* XAS spectra at the Ti L-edge unveil a shift with respect to each other, indicating a charge transfer between MXene surfaces and the nanoconfined water. The shift of the XA spectra at the Ti L-edge suggests mainly oxygen and hydroxyl surface terminations at 220 K and RT, respectively. At low temperatures, XRD measurements show a significant expansion in the interlayer spacing owing to unique reorientation of the nanoconfined water molecules. Interestingly, the *d*-spacing was found to be significantly enlarged and does not restore its initial value measured before the inception of the cooling-heating cycle at RT. In parallel, the XRD patterns show what could be the fingerprints of cubic and hexagonal ice structures of MXene nanoconfined water. However, further research is still needed to confirm that the ice signature is exclusively related to the nanoconfined water.

7.2 Conclusion and Outlook

The main conclusion of this work is that the oxidation state of the surface Ti atoms plays an essential role in the electrochemical performance of $Ti_3C_2T_x$ MXene. However, the oxidation state of the surface Ti atoms in $Ti_3C_2T_x$ MXene depends on different factors, including but not limited to synthesis procedure, intercalants, nanoconfined water, interlayer spacing, the thickness of the multi-layered MXene particles, and type of electrolytes. The XAS-based characterization enables us to investigate the impact of intercalation, aqueous dispersion environment, thickness of MXene particles, and the nanoconfined water on the MXene Ti oxidation state. Therefore, the impact of each factor on the Ti oxidation state is concluded as following:

- The intercalation is found to affect MXene surface electronic structure. The intercalation of urea molecules between multilayered $Ti_3C_2T_x$ MXene demonstrates a higher Ti oxidation state compared to pristine MXene, resulting in 56% enhancement in the areal capacitance. Also, the cation-intercalation with Li^+, Na^+, K^+, and Mg^{2+} has shown a dramatic alteration in the oxidation state of the surface Ti atoms in $Ti_3C_2T_x$ MXenes and is found to progressively increase with larger cations.

- The dispersion environment of MXene impacts the Ti oxidation state. The initial dispersion of the cation-intercalated $Ti_3C_2T_x$ MXene in H_2SO_4 aqueous solution environment reveals that the oxidation state of the surface Ti atoms remains relatively unaffected compared to pristine MXene. This suggests that the in situ exposure to H_2SO_4 aqueous solution reduces the Ti oxidation state in MXene, suggesting a great impact on the electrochemical performance of MXene. Indeed, a follow-up study by Naguib's group demonstrates that the capacitance was found to be comparable to that of delaminated MXenes and is found to reach 300 F/g for K-$Ti_3C_2T_x$ MXene electrode in 1M H_2SO_4 electrolyte [163].

- The thickness of individual MXene particle is found to influence the Ti oxidation state. Thanks to X-PEEM that enables us to investigate the surface chemistry of individual multi-layered $Ti_3C_2T_x$ MXene particles. Besides the influence of the cation intercalation, the spatially-resolved XA spectra highlights the impact of MXene particle thickness on the Ti oxidation state. It was found that the oxidation state of the surface Ti atoms in Na- and K-$Ti_3C_2T_x$ MXene individual particles is unchanged by particle thickness. However, in case of Li- and Mg-$Ti_3C_2T_x$ MXene, the Ti oxidation state differs between thin and thick particles. Owing to the fact that the Ti oxidation state is unaffected by particle thickness , electrodes constructed from Na- and K-$Ti_3C_2T_x$ MXene particles would have better electrochemical performance compared to Li- and Mg-$Ti_3C_2T_x$ MXene electrodes. Consistent to our results, the recent follow-up study by Naguib's group reveals that the electrochemical performance of Na- and K-$Ti_3C_2T_x$ MXene electrodes is higher compared to Li- and Mg-$Ti_3C_2T_x$ MXene electrodes [163].

- The change in MXene nanoconfined water phase affects the surface chemistry and the interlayer spacing. The spatially-resolved XA spectra at different temperatures uncover the signature of the nanoconfined water between $Ti_3C_2T_x$ MXene nanosheets in different phases, which enable us to detect its impact on the Ti oxidation state. It is found that the Ti oxidation

state becomes higher when the nanoconfined water is in solid phase (frozen) relative to the ones in liquid phase (ice-thaw), suggesting a change in the Ti oxidation state. This leads to conclude that a charge transfer process at low temperatures is taken place from MXene to ice phase nanoconfined water, which results in de-hydroxylation of MXene surfaces and vice versa. As MXene surface functional groups are changed, the hydroxylation (lower oxidation state)/de-hydroxylation (higher oxidation state) process is strongly affecting the Ti oxidation state and thus MXene electrochemical performance.

On the other hand, the XRD data demonstrate that the MXene interlayer spacing becomes larger at low temperatures (ice phase) relative to those measured at relatively higher temperatures (liquid phase). The larger spacing between MXene nanosheets leads to anticipate better electrolyte's proton accessibility, suggesting a boost in the electrochemical performance.

Outlook

Three main targets and their impact on the surface chemistry of $Ti_3C_2T_x$ MXene have been successfully characterized by using X-ray-based techniques. Namely, (i) intercalation, (ii) the local environment, and (iii) the nanoconfined water. With the progress of the characterization of $Ti_3C_2T_x$ in different environments, the X-ray spectroscopy, microscopy, and diffraction techniques have paved the way for further research in future. In particular, the success in finding a link between a higher controlled oxidation state and electrochemical performance in $Ti_3C_2T_x$ MXene inspires lots of possible follow-up experiments such as some of the urgent research that need to be undertaken as follows.

- *Modify the synthesis of $Ti_3C_2T_x$ MXene*. As shown in chapter one, the modification in the synthesis of $Ti_3C_2T_x$ MXene dramatically alters the electrochemical performance. Therefore, based on the XAS results presented in this work, relatively more oxygen-containing surface terminations would lead to better electrochemical properties. For example, another ionic compound salt can be used to promote better redox reactions. In this context, combining X-ray spectroscopic, microscopic, and diffraction methods may offer deep insight into the responsible chemical bonds and guide to better electrochemical properties.

- ***Study of other MXenes than Ti₃C₂Tₓ***. Over the last few years, many different new MXenes were produced. These new MXenes were successfully synthesized from combinations of different transition metals with carbides and/or nitrides such as carbonitride-, Vanadium-, Molybdenum-, and Niobium-based MXenes (**see Figure 1.3**). This leads to plenty of different new promising properties that need to be explored, awaiting further *in situ/operando* XAS and spatially-resolved XA characterization.

- ***Operando XAS measurements of MXenes***. The *in situ* and *operando* work of Ti₃C₂Tₓ MXene in different environment presented in this dissertation require further developments in the electrochemical flow cell in order to enable (i) complete cycling while acquiring XAS data, (ii) using higher concentration of sulfuric acid, (iii) or the use of non-aqueous electrolytes. This would offer in-depth systematic study of the effect of solvent chemistry and how the surface chemistry of MXene would affect the overall electrochemical performance.

- ***Theoretical studies are needed.*** The theoretical study of XA spectra and the nanoconfined water will be helpful to have a deep understanding about the impact of the hydrogen-bonding network of the nanoconfined water on MXene surfaces. For instance, DFT study can be useful to provide a realistic map of surface terminations across the Ti₃C₂Tₓ MXene nanosheets which could guide to predict XA spectra of many MXenes other than Ti₃C₂Tₓ ones. On the other hand, theoretical studies of molecular dynamics (MD) would offer a deep understanding of our data in terms of the impact of the nanoconfined water amount, the hydrogen-bonding network and its interaction with MXene surface functional groups at different temperatures, and cation intercalation including their hydration shell influence.

References

[1]   W.A. Braff, J.M. Mueller, J.E. Trancik, Value of storage technologies for wind and solar energy, Nat. Clim. Chang. 6 (2016) 964–969.

[2]   S. Chu, Y. Cui, N. Liu, The path towards sustainable energy, Nat. Mater. 16 (2016) 16–22.

[3]   P. Simon, Y. Gogotsi, Materials for electrochemical capacitors., Nat. Mater. 7 (2008) 845–54.

[4]   M. Li, J. Lu, Z. Chen, K. Amine, 30 Years of Lithium-Ion Batteries, Adv. Mater. 30 (2018).

[5]   P. Simon, Y. Gogotsi, Perspectives for electrochemical capacitors and related devices, Nat. Mater. 19 (2020) 1151–1163.

[6]   T. Pandolfo, V. Ruiz, S. Sivakkumar, J. Nerkar, General Properties of Electrochemical Capacitors, in: Supercapacitors Mater. Syst. Appl., 2013.

[7]   M. Armand, J.M. Tarascon, Building better batteries, Nature. 451 (2008) 652–657.

[8]   M.S. Islam, C.A.J. Fisher, Lithium and sodium battery cathode materials: Computational insights into voltage, diffusion and nanostructural properties, Chem. Soc. Rev. 43 (2014) 185–204.

[9]   P. Simon, Y. Gogotsi, B. Dunn, Where do batteries end and supercapacitors begin?, Science (80-.). 343 (2014) 1210–1211.

[10]   Y. Jiang, J. Liu, Definitions of Pseudocapacitive Materials: A Brief Review, ENERGY Environ. Mater. 2 (2019) 30–37.

[11]   R. Liu, J. Duay, S.B. Lee, Heterogeneous nanostructured electrode materials for electrochemical energy storage, Chem. Commun. 47 (2011) 1384–1404.

[12]   M.R. Lukatskaya, B. Dunn, Y. Gogotsi, Multidimensional materials and device architectures for future hybrid energy storage, Nat. Commun. 7 (2016).

[13]   R. Yazami, Nanomaterials for lithium-ion batteries: Fundamentals and applications, Pan Stanford Publishing Pte. Ltd., 2013.

[14]   C.K. Chan, H. Peng, G. Liu, K. McIlwrath, X.F. Zhang, R.A. Huggins, Y. Cui, High-performance lithium battery anodes using silicon nanowires, Nat. Nanotechnol. 3 (2008) 31–35.

[15]   D. Pech, M. Brunet, H. Durou, P. Huang, V. Mochalin, Y. Gogotsi, P.L. Taberna, P. Simon, Ultrahigh-power micrometre-sized supercapacitors based on onion-like carbon, Nat. Nanotechnol. 5 (2010) 651–654.

[16]   P. Simon, Y. Gogotsi, Capacitive Energy Storage in Nanostructured Carbon-Electrolyte Systems, Acc. Chem. Res. 46 (2013) 1094–1103.

[17]   B.J. Landi, M.J. Ganter, C.D. Cress, R.A. DiLeo, R.P. Raffaelle, Carbon nanotubes for lithium ion batteries, Energy Environ. Sci. 2 (2009) 638–654.

[18]   Y. Korenblit, M. Rose, E. Kockrick, L. Borchardt, A. Kvit, S. Kaskel, G. Yushin, High-rate electrochemical capacitors based on ordered mesoporous silicon carbide-derived carbon, ACS Nano. 4 (2010) 1337–1344.

[19]   J.P. Zheng, Hydrous Ruthenium Oxide as an Electrode Material for Electrochemical Capacitors, J. Electrochem. Soc. 142 (1995) 2699.

[20]   O. Ghodbane, J.L. Pascal, F. Favier, Microstructural effects on charge-storage properties in MnO2-based electrochemical supercapacitors, ACS Appl. Mater.

Interfaces. 1 (2009) 1130–1139.

[21] V. Augustyn, J. Come, M.A. Lowe, J.W. Kim, P.L. Taberna, S.H. Tolbert, H.D. Abruña, P. Simon, B. Dunn, High-rate electrochemical energy storage through Li+ intercalation pseudocapacitance, Nat. Mater. 12 (2013) 518–522.

[22] J.W. Kim, V. Augustyn, B. Dunn, The effect of crystallinity on the rapid pseudocapacitive response of Nb2O5, Adv. Energy Mater. 2 (2012) 141–148.

[23] M. Naguib, M. Kurtoglu, V. Presser, J. Lu, J. Niu, M. Heon, L. Hultman, Y. Gogotsi, M.W. Barsoum, Two-dimensional nanocrystals produced by exfoliation of Ti3AlC2, Adv. Mater. 23 (2011) 4248–4253.

[24] F. Shahzad, M. Alhabeb, C.B. Hatter, B. Anasori, S.M. Hong, C.M. Koo, Y. Gogotsi, Electromagnetic interference shielding with 2D transition metal carbides (MXenes), Science (80-.). 353 (2016) 1137–1140.

[25] L. Ding, Y. Wei, Y. Wang, H. Chen, J. Caro, H. Wang, A Two-Dimensional Lamellar Membrane: MXene Nanosheet Stacks, Angew. Chemie - Int. Ed. 56 (2017) 1825–1829.

[26] F. Meng, M. Seredych, C. Chen, V. Gura, S. Mikhalovsky, S. Sandeman, G. Ingavle, T. Ozulumba, L. Miao, B. Anasori, Y. Gogotsi, MXene Sorbents for Removal of Urea from Dialysate: A Step toward the Wearable Artificial Kidney, ACS Nano. 12 (2018) 10518–10528.

[27] Y. Xie, M. Naguib, V.N. Mochalin, M.W. Barsoum, Y. Gogotsi, X. Yu, K.W. Nam, X.Q. Yang, A.I. Kolesnikov, P.R.C. Kent, Role of surface structure on li-ion energy storage capacity of two-dimensional transition-metal carbides, J. Am. Chem. Soc. 136 (2014) 6385–6394.

[28] M.R. Lukatskaya, O. Mashtalir, C.E. Ren, Y. Dall'Agnese, P. Rozier, P.L. Taberna, M. Naguib, P. Simon, M.W. Barsoum, Y. Gogotsi, Cation intercalation and high volumetric capacitance of two-dimensional titanium carbide, Science (80-.). 341 (2013) 1502–1505.

[29] C. Eames, M.S. Islam, Ion intercalation into two-dimensional transition-metal carbides: Global screening for new high-capacity battery materials, J. Am. Chem. Soc. 136 (2014) 16270–16276.

[30] M. Naguib, J. Come, B. Dyatkin, V. Presser, P.L. Taberna, P. Simon, M.W. Barsoum, Y. Gogotsi, MXene: A promising transition metal carbide anode for lithium-ion batteries, Electrochem. Commun. 16 (2012) 61–64.

[31] O. Mashtalir, M. Naguib, V.N. Mochalin, Y. Dall'Agnese, M. Heon, M.W. Barsoum, Y. Gogotsi, Intercalation and delamination of layered carbides and carbonitrides, Nat. Commun. 4 (2013) 1716.

[32] B. Anasori, M.R. Lukatskaya, Y. Gogotsi, 2D metal carbides and nitrides (MXenes) for energy storage, Nat. Rev. Mater. 2 (2017) 16098.

[33] Y. Gogotsi, B. Anasori, The Rise of MXenes, ACS Nano. 13 (2019) 8491–8494.

[34] M.R. Lukatskaya, S.M. Bak, X. Yu, X.Q. Yang, M.W. Barsoum, Y. Gogotsi, Probing the Mechanism of High Capacitance in 2D Titanium Carbide Using in Situ X-Ray Absorption Spectroscopy, Adv. Energy Mater. 5 (2015) 1500589.

[35] C.J. Zhang, B. Anasori, A. Seral-Ascaso, S.H. Park, N. McEvoy, A. Shmeliov, G.S. Duesberg, J.N. Coleman, Y. Gogotsi, V. Nicolosi, Transparent, Flexible, and Conductive 2D Titanium Carbide (MXene) Films with High Volumetric Capacitance, Adv. Mater. 29 (2017).

[36] J. Halim, K.M. Cook, M. Naguib, P. Eklund, Y. Gogotsi, J. Rosen, M.W. Barsoum, X-ray photoelectron spectroscopy of select multi-layered transition metal carbides

(MXenes), Appl. Surf. Sci. 362 (2016) 406–417.

[37] O. Mashtalir, M.R. Lukatskaya, A.I. Kolesnikov, E. Raymundo-Piñero, M. Naguib, M.W. Barsoum, Y. Gogotsi, The effect of hydrazine intercalation on the structure and capacitance of 2D titanium carbide (MXene), Nanoscale. 8 (2016) 9128–9133.

[38] M.W. Barsoum, T. El-Raghy, The MAX phases: Unique new carbide and nitride materials: Tertiary ceramics are soft and machinable, yet heat-tolerant, strong and lighweight, Am. Sci. 89 (2001) 334–343.

[39] P. Urbankowski, B. Anasori, T. Makaryan, D. Er, S. Kota, P.L. Walsh, M. Zhao, V.B. Shenoy, M.W. Barsoum, Y. Gogotsi, Synthesis of two-dimensional titanium nitride Ti4N3 (MXene), Nanoscale. 8 (2016) 11385–11391.

[40] R. Meshkian, L.Å. Näslund, J. Halim, J. Lu, M.W. Barsoum, J. Rosen, Synthesis of two-dimensional molybdenum carbide, Mo2C, from the gallium based atomic laminate Mo2Ga2C, Scr. Mater. 108 (2015) 147–150.

[41] J. Halim, S. Kota, M.R. Lukatskaya, M. Naguib, M.Q. Zhao, E.J. Moon, J. Pitock, J. Nanda, S.J. May, Y. Gogotsi, M.W. Barsoum, Synthesis and Characterization of 2D Molybdenum Carbide (MXene), Adv. Funct. Mater. 26 (2016) 3118–3127.

[42] J. Zhou, X. Zha, F.Y. Chen, Q. Ye, P. Eklund, S. Du, Q. Huang, A Two-Dimensional Zirconium Carbide by Selective Etching of Al3C3 from Nanolaminated Zr3Al3C5, Angew. Chemie. 128 (2016) 5092–5097.

[43] M. Ghidiu, M.R. Lukatskaya, M.Q. Zhao, Y. Gogotsi, M.W. Barsoum, Conductive two-dimensional titanium carbide "clay" with high volumetric capacitance, Nature. 516 (2014) 78–81.

[44] M.A. Hope, A.C. Forse, K.J. Griffith, M.R. Lukatskaya, M. Ghidiu, Y. Gogotsi, C.P. Grey, NMR reveals the surface functionalisation of Ti3C2 MXene, Phys. Chem. Chem. Phys. 18 (2016) 5099–5102.

[45] O. Mashtalir, M.R. Lukatskaya, M.Q. Zhao, M.W. Barsoum, Y. Gogotsi, Amine-assisted delamination of Nb2C MXene for li-ion energy storage devices, Adv. Mater. 27 (2015) 3501–3506.

[46] M. Naguib, R.R. Unocic, B.L. Armstrong, J. Nanda, Large-scale delamination of multi-layers transition metal carbides and carbonitrides "mXenes," Dalt. Trans. 44 (2015) 9353–9358.

[47] M. Ghidiu, J. Halim, S. Kota, D. Bish, Y. Gogotsi, M.W. Barsoum, Ion-Exchange and Cation Solvation Reactions in Ti3C2 MXene, Chem. Mater. 28 (2016) 3507–3514.

[48] C. (John) Zhang, L. McKeon, M.P. Kremer, S.H. Park, O. Ronan, A. Seral-Ascaso, S. Barwich, C. Coileáin, N. McEvoy, H.C. Nerl, B. Anasori, J.N. Coleman, Y. Gogotsi, V. Nicolosi, Additive-free MXene inks and direct printing of micro-supercapacitors, Nat. Commun. 10 (2019).

[49] K. Li, M. Liang, H. Wang, X. Wang, Y. Huang, J. Coelho, S. Pinilla, Y. Zhang, F. Qi, V. Nicolosi, Y. Xu, 3D MXene Architectures for Efficient Energy Storage and Conversion, Adv. Funct. Mater. 30 (2020).

[50] Y. Dall'Agnese, M.R. Lukatskaya, K.M. Cook, P.L. Taberna, Y. Gogotsi, P. Simon, High capacitance of surface-modified 2D titanium carbide in acidic electrolyte, Electrochem. Commun. 48 (2014) 118–122.

[51] J.L. Hart, K. Hantanasirisakul, A.C. Lang, B. Anasori, D. Pinto, Y. Pivak, J.T. van Omme, S.J. May, Y. Gogotsi, M.L. Taheri, Control of MXenes' electronic properties through termination and intercalation, Nat. Commun. 10 (2019).

[52] T. Li, L. Yao, Q. Liu, J. Gu, R. Luo, J. Li, X. Yan, W. Wang, P. Liu, B. Chen, W. Zhang, W.

Abbas, R. Naz, D. Zhang, Fluorine-Free Synthesis of High-Purity Ti3C2Tx (T=OH, O) via Alkali Treatment, Angew. Chemie - Int. Ed. 57 (2018) 6115–6119.

[53]   X. Sang, Y. Xie, M.W. Lin, M. Alhabeb, K.L. Van Aken, Y. Gogotsi, P.R.C. Kent, K. Xiao, R.R. Unocic, Atomic defects in monolayer titanium carbide (Ti3C2Tx) MXene, ACS Nano. 10 (2016) 9193–9200.

[54]   M.R. Lukatskaya, S. Kota, Z. Lin, M.Q. Zhao, N. Shpigel, M.D. Levi, J. Halim, P.L. Taberna, M.W. Barsoum, P. Simon, Y. Gogotsi, Ultra-high-rate pseudocapacitive energy storage in two-dimensional transition metal carbides, Nat. Energy. 6 (2017).

[55]   D. University, Entering the Fast Lane-MXene Electrodes Push Charging Rate Limits in Energy Storage, Https://Drexel.Edu/Now/Archive/2017/July/MXene-Electrode/. (2017).

[56]   Z. Lin, D. Barbara, P.L. Taberna, K.L. Van Aken, B. Anasori, Y. Gogotsi, P. Simon, Capacitance of Ti3C2Tx MXene in ionic liquid electrolyte, J. Power Sources. 326 (2016) 575–579.

[57]   N. Jäckel, B. Krüner, K.L. Van Aken, M. Alhabeb, B. Anasori, F. Kaasik, Y. Gogotsi, V. Presser, Electrochemical in Situ Tracking of Volumetric Changes in Two-Dimensional Metal Carbides (MXenes) in Ionic Liquids, ACS Appl. Mater. Interfaces. 8 (2016) 32089–32093.

[58]   X. Wang, T.S. Mathis, K. Li, Z. Lin, L. Vlcek, T. Torita, N.C. Osti, C. Hatter, P. Urbankowski, A. Sarycheva, M. Tyagi, E. Mamontov, P. Simon, Y. Gogotsi, Influences from solvents on charge storage in titanium carbide MXenes, Nat. Energy. 4 (2019) 241–248.

[59]   A. Sarycheva, Y. Gogotsi, Raman Spectroscopy Analysis of the Structure and Surface Chemistry of Ti3C2Tx MXene, Chem. Mater. 32 (2020) 3480–3488.

[60]   C. Zhan, M. Naguib, M. Lukatskaya, P.R.C. Kent, Y. Gogotsi, D.E. Jiang, Understanding the MXene Pseudocapacitance, J. Phys. Chem. Lett. 9 (2018) 1223–1228.

[61]   P. Willmott, An Introduction to Synchrotron Radiation, Wiley, 2019.

[62]   S.M. Bak, R. Qiao, W. Yang, S. Lee, X. Yu, B. Anasori, H. Lee, Y. Gogotsi, X.Q. Yang, Na-Ion Intercalation and Charge Storage Mechanism in 2D Vanadium Carbide, Adv. Energy Mater. 7 (2017) 1700959.

[63]   E. Stoyanov, F. Langenhorst, G. Steinle-Neumann, The effect of valence state and site geometry on Ti L3,2 and O K electron energy-loss spectra of TixOy phases, Am. Mineral. 92 (2007) 577–586.

[64]   T. Petit, J. Ren, S. Choudhury, R. Golnak, S.S.N. Lalithambika, M.F. Tesch, J. Xiao, E.F. Aziz, X-Ray Absorption Spectroscopy of TiO2 Nanoparticles in Water Using a Holey Membrane-Based Flow Cell, Adv. Mater. Interfaces. 4 (2017) 1700755.

[65]   X-Ray Attenuation Length, Https://Henke.Lbl.Gov/Optical_constants/Atten2.Htm. (n.d.).

[66]   Wikipedia, Auger electron vs. fluorescence yields, Https://En.Wikipedia.Org/Wiki/File:Auger_Yield.Svg. (n.d.).

[67]   A. Krol, C.S. Lin, Z.H. Ming, C.J. Sher, Y.H. Kao, C.T. Chen, F. Sette, Y. Ma, G.C. Smith, Y.Z. Zhu, D.T. Shaw, X-ray-absorption studies of Y-Ba-Cu-O and Bi-Sr-Ca-Cu-O films at oxygen K edge by means of fluorescence and total electron yield: A comparison of two techniques, Phys. Rev. B. 42 (1990) 2635–2638.

[68]   M. Abbate, J.B. Goedkoop, F.M.F. de Groot, M. Grioni, J.C. Fuggle, S. Hofmann, H. Petersen, M. Sacchi, Probing depth of soft x-ray absorption spectroscopy measured in total-electron-yield mode, Surf. Interface Anal. 18 (1992) 65–69.

[69]   M. Kasrai, W.N. Lennard, R.W. Brunner, G.M. Bancroft, J.A. Bardwell, K.H. Tan, Sampling depth of total electron and fluorescence measurements in Si L- and K-edge absorption spectroscopy, Appl. Surf. Sci. 99 (1996) 303–312.

[70]   B.H. Frazer, B. Gilbert, B.R. Sonderegger, G. De Stasio, The probing depth of total electron yield in the sub-keV range: TEY-XAS and X-PEEM, Surf. Sci. 537 (2003) 161–167.

[71]   K. Nakanishi, T. Ohta, Improvement of the detection system in the soft X-ray absorption spectroscopy, in: Surf. Interface Anal., 2012: pp. 784–788.

[72]   A. Al-Temimy, B. Anasori, K.A. Mazzio, F. Kronast, M. Seredych, N. Kurra, M.A. Mawass, S. Raoux, Y. Gogotsi, T. Petit, Enhancement of Ti3C2 MXene Pseudocapacitance after Urea Intercalation Studied by Soft X-ray Absorption Spectroscopy, J. Phys. Chem. C. 124 (2020) 5079–5086.

[73]   A. Al-Temimy, K. Prenger, R. Golnak, M. Lounasvuori, M. Naguib, T. Petit, Impact of Cation Intercalation on the Electronic Structure of Ti3C2Tx MXenes in Sulfuric Acid, ACS Appl. Mater. Interfaces. 12 (2020) 15087–15094.

[74]   A. Al-Temimy, F. Kronast, M.A. Mawass, K.A. Mazzio, K. Prenger, M. Naguib, T. Petit, S. Raoux, Spatially resolved X-ray absorption spectroscopy investigation of individual cation-intercalated multi-layered Ti3C2Tx MXene particles, Appl. Surf. Sci. 530 (2020).

[75]   W.S. Yoon, K.Y. Chung, J. McBreen, D.A. Fischer, X.Q. Yang, Electronic structural changes of the electrochemically Li-ion deintercalated LiNi0.8Co0.15Al0.05O2 cathode material investigated by X-ray absorption spectroscopy, J. Power Sources. 174 (2007) 1015–1020.

[76]   F.M.F. De Groot, X-ray absorption and dichroism of transition metals and their compounds, J. Electron Spectros. Relat. Phenomena. 67 (1994) 529–622.

[77]   M.-Y. Hsu, W.-C. Yang, H. Teng, J. Leu, Microstructure and Composition of TiO2 Nanotube Arrays Fabricated with HF and NH4F Electrolytes and Their Evolution during Annealing, J. Electrochem. Soc. 158 (2011) K81.

[78]   S.O. Kucheyev, T. Van Buuren, T.F. Baumann, J.H. Satcher, T.M. Willey, R.W. Meulenberg, T.E. Felter, J.F. Poco, S.A. Gammon, L.J. Terminello, Electronic structure of titania aerogels from soft x-ray absorption spectroscopy, Phys. Rev. B - Condens. Matter Mater. Phys. 69 (2004) 245102.

[79]   F. Kronast, S. Valencia Molina, SPEEM: The photoemission microscope at the dedicated microfocus PGM beamline UE49-PGMa at BESSY II, J. Large-Scale Res. Facil. JLSRF. 2 (2016) A90.

[80]   T. Kachel, The plane grating monochromator beamline U49-2 PGM-1 at BESSY II, J. Large-Scale Res. Facil. JLSRF. 2 (2016).

[81]   Helmholtz Zentrum Berlin, X-PEEM end-station, (n.d.). https://www.helmholtz-berlin.de/forschung/oe/qm/spin-topologie/forschungsgruppen/x-peem/index_en.html.

[82]   Helmholtz Zentrum Berlin, LiXEdrom end-station, (2016). https://www.helmholtz-berlin.de/pubbin/igama_output?modus=einzel&gid=1867&sprache=en.

[83]   C. Schwanke, R. Golnak, J. Xiao, K.M. Lange, Electrochemical flowcell for in-situ investigations by soft x-ray absorption and emission spectroscopy, Rev. Sci. Instrum. 85 (2014) 103120.

[84]   M.P. Seah, W.A. Dench, Quantitative electron spectroscopy of surfaces: A standard data base for electron inelastic mean free paths in solids, Surf. Interface Anal. 1 (1979) 2–11.

[85]   A.D. Dillon, M.J. Ghidiu, A.L. Krick, J. Griggs, S.J. May, Y. Gogotsi, M.W. Barsoum, A.T. Fafarman, Highly Conductive Optical Quality Solution-Processed Films of 2D Titanium Carbide, Adv. Funct. Mater. 26 (2016) 4162–4168.

[86]   S. Célérier, S. Hurand, C. Garnero, S. Morisset, M. Benchakar, A. Habrioux, P. Chartier, V. Mauchamp, N. Findling, B. Lanson, E. Ferrage, Hydration of Ti3C2Tx MXene: An Interstratification Process with Major Implications on Physical Properties, Chem. Mater. 31 (2019) 454–461.

[87]   K. Morishige, H. Iwasaki, X-ray study of freezing and melting of water confined within SBA-15, Langmuir. 19 (2003) 2808–2811.

[88]   C. Zhan, M. Naguib, M. Lukatskaya, P.R.C. Kent, Y. Gogotsi, D.E. Jiang, Understanding the MXene Pseudocapacitance, J. Phys. Chem. Lett. 9 (2018) 1223–1228.

[89]   S.H. Overbury, A.I. Kolesnikov, G.M. Brown, Z. Zhang, G.S. Nair, R.L. Sacci, R. Lotfi, A.C.T. Van Duin, M. Naguib, Complexity of Intercalation in MXenes: Destabilization of Urea by Two-Dimensional Titanium Carbide, J. Am. Chem. Soc. 140 (2018) 10305–10314.

[90]   S. Huang, V.N. Mochalin, Hydrolysis of 2D Transition-Metal Carbides (MXenes) in Colloidal Solutions, Inorg. Chem. 58 (2019) 1958–1966.

[91]   M. Alhabeb, K. Maleski, B. Anasori, P. Lelyukh, L. Clark, S. Sin, Y. Gogotsi, Guidelines for Synthesis and Processing of Two-Dimensional Titanium Carbide (Ti3C2Tx MXene), Chem. Mater. 29 (2017) 7633–7644.

[92]   J. Luo, W. Zhang, H. Yuan, C. Jin, L. Zhang, H. Huang, C. Liang, Y. Xia, J. Zhang, Y. Gan, X. Tao, Pillared Structure Design of MXene with Ultralarge Interlayer Spacing for High-Performance Lithium-Ion Capacitors, ACS Nano. 11 (2017) 2459–2469.

[93]   Y. Gao, L. Wang, Z. Li, Y. Zhang, B. Xing, C. Zhang, A. Zhou, Electrochemical performance of Ti3C2 supercapacitors in KOH electrolyte, J. Adv. Ceram. 4 (2015) 130–134.

[94]   X. Wang, S. Kajiyama, H. Iinuma, E. Hosono, S. Oro, I. Moriguchi, M. Okubo, A. Yamada, Pseudocapacitance of MXene nanosheets for high-power sodium-ion hybrid capacitors, Nat. Commun. 6 (2015).

[95]   J. Li, X. Yuan, C. Lin, Y. Yang, L. Xu, X. Du, J. Xie, J. Lin, J. Sun, Achieving High Pseudocapacitance of 2D Titanium Carbide (MXene) by Cation Intercalation and Surface Modification, Adv. Energy Mater. 7 (2017).

[96]   C. Yang, W. Que, X. Yin, Y. Tian, Y. Yang, M. Que, Improved capacitance of nitrogen-doped delaminated two-dimensional titanium carbide by urea-assisted synthesis, Electrochim. Acta. 225 (2017) 416–424.

[97]   M.L. Baker, M.W. Mara, J.J. Yan, K.O. Hodgson, B. Hedman, E.I. Solomon, K- and L-edge X-ray absorption spectroscopy (XAS) and resonant inelastic X-ray scattering (RIXS) determination of differential orbital covalency (DOC) of transition metal sites, Coord. Chem. Rev. 345 (2017) 182–208.

[98]   L.Y. Gan, D. Huang, U. Schwingenschlögl, Oxygen adsorption and dissociation during the oxidation of monolayer Ti2C, J. Mater. Chem. A. 1 (2013) 13672–13678.

[99]   L.H. Karlsson, J. Birch, J. Halim, M.W. Barsoum, P.O.Å. Persson, Atomically Resolved Structural and Chemical Investigation of Single MXene Sheets, Nano Lett. 15 (2015) 4955–4960.

[100] K.D. Fredrickson, B. Anasori, Z.W. Seh, Y. Gogotsi, A. Vojvodic, Effects of applied potential and water intercalation on the surface chemistry of Ti2C and Mo2C MXenes, J. Phys. Chem. C. 120 (2016) 28432–28440.

[101] S. Zhang, Q. Liu, F. Gao, X. Li, C. Liu, H. Li, S.A. Boyd, C.T. Johnston, B.J. Teppen, Mechanism associated with kaolinite intercalation with urea: Combination of infrared spectroscopy and molecular dynamics simulation studies, J. Phys. Chem. C. 121 (2017) 402–409.

[102] A. Lipatov, M. Alhabeb, M.R. Lukatskaya, A. Boson, Y. Gogotsi, A. Sinitskii, Effect of Synthesis on Quality, Electronic Properties and Environmental Stability of Individual Monolayer Ti3C2 MXene Flakes, Adv. Electron. Mater. 2 (2016) 1600255.

[103] S. Chertopalov, V.N. Mochalin, Environment-Sensitive Photoresponse of Spontaneously Partially Oxidized Ti3C2 MXene Thin Films, ACS Nano. 12 (2018) 6109–6116.

[104] R. Lotfi, M. Naguib, D.E. Yilmaz, J. Nanda, A.C.T. Van Duin, A comparative study on the oxidation of two-dimensional Ti3C2 MXene structures in different environments, J. Mater. Chem. A. 6 (2018) 12733–12743.

[105] C.J. Zhang, S. Pinilla, N. McEvoy, C.P. Cullen, B. Anasori, E. Long, S.H. Park, A. Seral-Ascaso, A. Shmeliov, D. Krishnan, C. Morant, X. Liu, G.S. Duesberg, Y. Gogotsi, V. Nicolosi, Oxidation Stability of Colloidal Two-Dimensional Titanium Carbides (MXenes), Chem. Mater. 29 (2017) 4848–4856.

[106] F.M.F. De Groot, J. Faber, J.J.M. Michiels, M.T. Czyyk, M. Abbate, J.C. Fuggle, Oxygen 1s x-ray absorption of tetravalent titanium oxides: A comparison with single-particle calculations, Phys. Rev. B. 48 (1993) 2074–2080.

[107] P. Wernet, D. Nordlund, U. Bergmann, M. Cavalleri, N. Odelius, H. Ogasawara, L.Å. Näslund, T.K. Hirsch, L. Ojamäe, P. Glatzel, L.G.M. Pettersson, A. Nilsson, The Structure of the First Coordination Shell in Liquid Water, Science (80-.). 304 (2004) 995–999.

[108] M. Naguib, V.N. Mochalin, M.W. Barsoum, Y. Gogotsi, 25th anniversary article: MXenes: A new family of two-dimensional materials, Adv. Mater. 26 (2014) 992–1005.

[109] J.F. Zhu, Y. Tang, C.H. Yang, F. Wang, M.J. Cao, Composites of TiO2 nanoparticles deposited on Ti3C2 mxene nanosheets with enhanced electrochemical performance, J. Electrochem. Soc. 163 (2016) A785–A791.

[110] M. Hu, T. Hu, Z. Li, Y. Yang, R. Cheng, J. Yang, C. Cui, X. Wang, Surface Functional Groups and Interlayer Water Determine the Electrochemical Capacitance of Ti3C2Tx MXene, ACS Nano. 12 (2018) 3578–3586.

[111] Q. Peng, J. Guo, Q. Zhang, J. Xiang, B. Liu, A. Zhou, R. Liu, Y. Tian, Unique lead adsorption behavior of activated hydroxyl group in two-dimensional titanium carbide, J. Am. Chem. Soc. 136 (2014) 4113–4116.

[112] C.E. Ren, K.B. Hatzell, M. Alhabeb, Z. Ling, K.A. Mahmoud, Y. Gogotsi, Charge- and Size-Selective Ion Sieving Through Ti3C2Tx MXene Membranes, J. Phys. Chem. Lett. 6 (2015) 4026–4031.

[113] K.M. Kang, D.W. Kim, C.E. Ren, K.M. Cho, S.J. Kim, J.H. Choi, Y.T. Nam, Y. Gogotsi, H.T. Jung, Selective Molecular Separation on Ti3C2Tx-Graphene Oxide Membranes during Pressure-Driven Filtration: Comparison with Graphene Oxide and MXenes, ACS Appl. Mater. Interfaces. 9 (2017) 44687–44694.

[114] J. Wang, P. Chen, B. Shi, W. Guo, M. Jaroniec, S.Z. Qiao, A Regularly Channeled Lamellar Membrane for Unparalleled Water and Organics Permeation, Angew. Chemie - Int. Ed. 57 (2018) 6814–6818.

[115] S. Hong, F. Ming, Y. Shi, R. Li, I.S. Kim, C.Y. Tang, H.N. Alshareef, P. Wang, Two-Dimensional Ti3C2Tx MXene Membranes as Nanofluidic Osmotic Power Generators, ACS Nano. 13 (2019) 8917–8925.

[116] S.J. Kim, H.J. Koh, C.E. Ren, O. Kwon, K. Maleski, S.Y. Cho, B. Anasori, C.K. Kim, Y.K. Choi, J. Kim, Y. Gogotsi, H.T. Jung, Metallic Ti3C2Tx MXene Gas Sensors with Ultrahigh Signal-to-Noise Ratio, ACS Nano. 12 (2018) 986–993.

[117] E. Lee, A. Vahidmohammadi, B.C. Prorok, Y.S. Yoon, M. Beidaghi, D.J. Kim, Room Temperature Gas Sensing of Two-Dimensional Titanium Carbide (MXene), ACS Appl. Mater. Interfaces. 9 (2017) 37184–37190.

[118] E.S. Muckley, M. Naguib, I.N. Ivanov, Multi-modal, ultrasensitive, wide-range humidity sensing with Ti3C2 film, Nanoscale. 10 (2018) 21689–21695.

[119] E.S. Muckley, M. Naguib, H.W. Wang, L. Vlcek, N.C. Osti, R.L. Sacci, X. Sang, R.R. Unocic, Y. Xie, M. Tyagi, E. Mamontov, K.L. Page, P.R.C. Kent, J. Nanda, I.N. Ivanov, Multimodality of Structural, Electrical, and Gravimetric Responses of Intercalated MXenes to Water, ACS Nano. 11 (2017) 11118–11126.

[120] Q. Gao, J. Come, M. Naguib, S. Jesse, Y. Gogotsi, N. Balke, Synergetic effects of K+ and Mg2+ ion intercalation on the electrochemical and actuation properties of the two-dimensional Ti3C2 MXene, Faraday Discuss. 199 (2017) 393–403.

[121] X. Su, A. Kushima, C. Halliday, J. Zhou, J. Li, T.A. Hatton, Electrochemically-mediated selective capture of heavy metal chromium and arsenic oxyanions from water, Nat. Commun. 9 (2018) 4701.

[122] L. Ding, Y. Wei, L. Li, T. Zhang, H. Wang, J. Xue, L.X. Ding, S. Wang, J. Caro, Y. Gogotsi, MXene molecular sieving membranes for highly efficient gas separation, Nat. Commun. 9 (2018).

[123] N.C. Osti, M. Naguib, K. Ganeshan, Y.K. Shin, A. Ostadhossein, A.C.T. Van Duin, Y. Cheng, L.L. Daemen, Y. Gogotsi, E. Mamontov, A.I. Kolesnikov, Influence of metal ions intercalation on the vibrational dynamics of water confined between MXene layers, Phys. Rev. Mater. 1 (2017) 065406.

[124] N.C. Osti, M. Naguib, A. Ostadhossein, Y. Xie, P.R.C. Kent, B. Dyatkin, G. Rother, W.T. Heller, A.C.T. Van Duin, Y. Gogotsi, E. Mamontov, Effect of Metal Ion Intercalation on the Structure of MXene and Water Dynamics on its Internal Surfaces, ACS Appl. Mater. Interfaces. 8 (2016) 8859–8863.

[125] N. Shpigel, M.D. Levi, S. Sigalov, T.S. Mathis, Y. Gogotsi, D. Aurbach, Direct Assessment of Nanoconfined Water in 2D Ti3C2 Electrode Interspaces by a Surface Acoustic Technique, J. Am. Chem. Soc. 140 (2018) 8910–8917.

[126] T. Okumura, T. Fukutsuka, A. Yanagihara, Y. Orikasa, H. Arai, Z. Ogumi, Y. Uchimoto, Electronic and local structural changes with lithium-ion insertion in TiO2-B: X-ray absorption spectroscopy study, J. Mater. Chem. 21 (2011) 15369–15377.

[127] Y. Liu, F. Zhao, J. Li, Y. Li, J.A. McLeod, L. Liu, Influence of crystal phase on TiO2 nanowire anodes in sodium ion batteries, J. Mater. Chem. A. 5 (2017) 20005–20013.

[128] V. Natu, M. Sokol, L. Verger, M.W. Barsoum, Effect of Edge Charges on Stability and Aggregation of Ti3C2Tz MXene Colloidal Suspensions, J. Phys. Chem. C. 122 (2018) 27745–27753.

[129] V. Natu, M. Clites, E. Pomerantseva, M.W. Barsoum, Mesoporous MXene powders synthesized by acid induced crumpling and their use as Na-ion battery anodes, Mater. Res. Lett. 6 (2018) 230–235.

[130] L. Lorencova, T. Bertok, E. Dosekova, A. Holazova, D. Paprckova, A. Vikartovska, V. Sasinkova, J. Filip, P. Kasak, M. Jerigova, D. Velic, K.A. Mahmoud, J. Tkac, Electrochemical performance of Ti3C2Tx MXene in aqueous media: towards ultrasensitive H2O2 sensing, Electrochim. Acta. 235 (2017) 471–479.

[131] E. Kayali, A. Vahidmohammadi, J. Orangi, M. Beidaghi, Controlling the Dimensions of 2D MXenes for Ultrahigh-Rate Pseudocapacitive Energy Storage, ACS Appl. Mater. Interfaces. 10 (2018) 25949–25954.

[132] V. Augustyn, J. Come, M.A. Lowe, J.W. Kim, P.L. Taberna, S.H. Tolbert, H.D. Abruña, P. Simon, B. Dunn, High-rate electrochemical energy storage through Li + intercalation pseudocapacitance, Nat. Mater. 12 (2013) 518–522.

[133] Y. Gogotsi, P. Simon, True performance metrics in electrochemical energy storage, Science (80-.). 334 (2011) 917–918.

[134] V. Augustyn, P. Simon, B. Dunn, Pseudocapacitive oxide materials for high-rate electrochemical energy storage, Energy Environ. Sci. 7 (2014) 1597–1614.

[135] F.M.F. De Groot, M. Grioni, J.C. Fuggle, J. Ghijsen, G.A. Sawatzky, H. Petersen, Oxygen 1s X-ray-absorption edges of transition-metal oxides, Phys. Rev. B. 40 (1989) 5715–5723.

[136] D. Chandler, Interfaces and the driving force of hydrophobic assembly, Nature. 437 (2005) 640–647.

[137] J. Israelachvili, H. Wennerström, Role of hydration and water structure in biological and colloidal interactions, Nature. 379 (1996) 219–225.

[138] J. Brown, How minerals react with water, Science (80-.). 294 (2001) 67–70.

[139] S. Han, M.Y. Choi, P. Kumar, H.E. Stanley, Phase transitions in confined water nanofilms, Nat. Phys. 6 (2010) 685–689.

[140] N. Giovambattista, P.J. Rossky, P.G. Debenedetti, Phase transitions induced by nanoconfinement in liquid water, Phys. Rev. Lett. 102 (2009).

[141] R. Srivastava, H. Docherty, J.K. Singh, P.T. Cummings, Phase transitions of water in graphite and mica pores, J. Phys. Chem. C. 115 (2011) 12448–12457.

[142] D. Takaiwa, I. Hatano, K. Koga, H. Tanaka, Phase diagram of water in carbon nanotubes, Proc. Natl. Acad. Sci. U. S. A. 105 (2008) 39–43.

[143] G. Algara-Siller, O. Lehtinen, F.C. Wang, R.R. Nair, U. Kaiser, H.A. Wu, A.K. Geim, I. V. Grigorieva, Square ice in graphene nanocapillaries, Nature. 519 (2015) 443–445.

[144] K. Xu, P. Cao, J.R. Heath, Graphene visualizes the first water adlayers on mica at ambient conditions, Science (80-.). 329 (2010) 1188–1191.

[145] D.S. Yang, A.H. Zewail, Ordered water structure at hydrophobic graphite interfaces observed by 4D, ultrafast electron crystallography, Proc. Natl. Acad. Sci. U. S. A. 106 (2009) 4122–4126.

[146] K.T. He, J.D. Wood, G.P. Doidge, E. Pop, J.W. Lyding, Scanning tunneling microscopy study and nanomanipulation of graphene-coated water on mica, Nano Lett. 12 (2012) 2665–2672.

[147] M.F. Toney, J.N. Howard, J. Richer, G.L. Borges, J.G. Gordon, O.R. Melroy, D.G. Wiesler, D. Yee, L.B. Sorensen, Voltage-dependent ordering of water molecules at an electrode-electrolyte interface, Nature. 368 (1994) 444–446.

[148] M. Vural, A. Pena-Francesch, J. Bars-Pomes, H. Jung, H. Gudapati, C.B. Hatter, B.D. Allen, B. Anasori, I.T. Ozbolat, Y. Gogotsi, M.C. Demirel, Inkjet Printing of Self-Assembled 2D Titanium Carbide and Protein Electrodes for Stimuli-Responsive Electromagnetic Shielding, Adv. Funct. Mater. 28 (2018).

[149] R. Ma, D. Cao, C. Zhu, Y. Tian, J. Peng, J. Guo, J. Chen, X.Z. Li, J.S. Francisco, X.C. Zeng, L.M. Xu, E.G. Wang, Y. Jiang, Atomic imaging of the edge structure and growth of a two-dimensional hexagonal ice, Nature. 577 (2020) 60–63.

[150] D. Nordlund, H. Ogasawara, K.J. Andersson, M. Tatarkhanov, M. Salmerón, L.G.M.

Pettersson, A. Nilsson, Sensitivity of X-ray absorption spectroscopy to hydrogen bond topology, Phys. Rev. B - Condens. Matter Mater. Phys. 80 (2009).

[151] A. Nilsson, D. Nordlund, I. Waluyo, N. Huang, H. Ogasawara, S. Kaya, U. Bergmann, L.Å. Näslund, H. Öström, P. Wernet, K.J. Andersson, T. Schiros, L.G.M. Pettersson, X-ray absorption spectroscopy and X-ray Raman scattering of water and ice; an experimental view, J. Electron Spectros. Relat. Phenomena. 177 (2010) 99–129.

[152] I. Waluyo, D. Nordlund, U. Bergmann, D. Schlesinger, L.G.M. Pettersson, A. Nilsson, A different view of structure-making and structure-breaking in alkali halide aqueous solutions through x-ray absorption spectroscopy, J. Chem. Phys. 140 (2014).

[153] P. Wernet, D. Testemale, J.L. Hazemann, R. Argoud, P. Glatzel, L.G.M. Pettersson, A. Nilsson, U. Bergmann, Spectroscopic characterization of microscopic hydrogen-bonding disparities in supercritical water, J. Chem. Phys. 123 (2005).

[154] S. Myneni, Y. Luo, L.Å. Näslund, M. Cavalleri, L. Ojamäe, H. Ogasawara, A. Pelmenschikov, P. Wernet, P. Väterlein, C. Heske, Z. Hussain, L.G.M. Pettersson, A. Nilsson, Spectroscopic probing of local hydrogen-bonding structures in liquid water, J. Phys. Condens. Matter. 14 (2002).

[155] V. Molinero, B.D. Kay, Preface: Special topic on interfacial and confined water, J. Chem. Phys. 141 (2014).

[156] K. Morishige, H. Yasunaga, H. Uematsu, Stability of cubic ice in mesopores, J. Phys. Chem. C. 113 (2009) 3056–3061.

[157] A.J. Lee, S.W. Rick, Characterizing charge transfer at water ice interfaces, J. Phys. Chem. Lett. 3 (2012) 3199–3203.

[158] M. Nagasaka, H. Yuzawa, N. Kosugi, Interaction between Water and Alkali Metal Ions and Its Temperature Dependence Revealed by Oxygen K-Edge X-ray Absorption Spectroscopy, J. Phys. Chem. B. 121 (2017) 10957–10964.

[159] F. Allegretti, S. O'Brien, M. Polcik, D.I. Sayago, D.P. Woodruff, Adsorption bond length for H2O on TiO2(110): A key parameter for theoretical understanding, Phys. Rev. Lett. 95 (2005).

[160] T.L. Malkin, B.J. Murray, A. V. Brukhno, J. Anwar, C.G. Salzmann, Structure of ice crystallized from supercooled water, Proc. Natl. Acad. Sci. U. S. A. 109 (2012) 1041–1045.

[161] F. V. Shallcross, G.B. Carpenter, X-ray diffraction study of the cubic phase of ice, J. Chem. Phys. 26 (1957) 782–784.

[162] W.F. Kuhs, C. Sippel, A. Falenty, T.C. Hansen, Extent and relevance of stacking disorder in "ice Ic," Proc. Natl. Acad. Sci. U. S. A. 109 (2012) 21259–21264.

[163] M.N. K. Prenger, Y. Sun, K. Geneshan, A. Al-Temimy, K. Liang, C. Dun, J. Urban, J. Xiao, T. Petit, A. C. T. van Duin, D. Jiang, Metal Cation Pre-Intercalated Ti3C2Tx MXene as Ultra-High Areal Capacitance Electrodes for Aqueous Supercapacitors, ACS Appl. Energy Mater. 5 (2022) 9373–9382.

[164] T. Fransson, Y. Harada, N. Kosugi, N.A. Besley, B. Winter, J.J. Rehr, L.G.M. Pettersson, A. Nilsson, X-ray and Electron Spectroscopy of Water, Chem. Rev. 116 (2016) 7551–7569.

[165] R. Qiao, Y. De Chuang, S. Yan, W. Yang, Soft X-Ray Irradiation Effects of Li2O2, Li2CO3 and Li2O Revealed by Absorption Spectroscopy, PLoS One. 7 (2012).

Glossary

0D	zero-dimensional
1D	one-dimensional
2D	two-dimensional
AC	activated carbon
AFM	atomic force microscopy
Ag/AgCl	silver-silver chloride
Au	gold
CCD	charge coupled device
C_m	gravimetric specific capacitance
Cr	chromium
CsOH	cesium hydroxide
CV	cyclic voltammogram
DMSO	dimethyl sulfoxide
DFT	density functional theory
ECs	electrochemical capacitors
EDLCs	electric double layer capacitors
EDL	electric double layer
EES	electrochemical energy storage
E_F	fermi energy level
EIS	electrochemical impedance spectroscopy
eV	electron volt
EY	electron yield
F/g	farads per gram

F/cm²	farad per square centimeter
F/cm³	farad per cubic centimeter
FY	fluorescence yield
g/cm³	gram per cubic centimeter
h	hour
HCl	hydrochloric acid
HF	hydrofluoric acid
HM	hydrazine monohydrate
H₂SO₄	sulfuric acid
KOAc	potassium acetate
KOH	potassium hydroxide
LIB	Li-ion batteries
LiCl	lithium chloride
LiF	lithium fluoride
LiOH	Lithium hydroxide
LTO	lithium titanium oxide
MCP	micro-channel plates
MPDO	maximum possible degree of ordering
mL/min	milliliter per minute
MΩ.cm	Mega Ohm centimeter
MD	Molecular dynamics
NaOH	sodium hydroxide
NAP	near ambient pressure
NMR	nuclear magnetic resonance
PEEK	polyether ether ketone
PEY	partial electron yield
PFY	partial fluorescence yield

pH	potential of hydrogen
Pt	Platinum
RH	relative humidity
rpm	revolutions per minute
s	second
STM	scanning tunneling microscopy
TBAOH	tetrabutylammonium hydroxide
TEM	transmission electron microscopy
TEY	total electron yield
TFY	total fluorescence yield
UHV	ultra-high vacuum
Wh kg^{-1}	watt hour per kilogram
W kg^{-1}	watt per kilogram
XA	X-ray absorption
XAS	X-ray absorption spectroscopy
XRD	X-ray diffraction
XPEEM	X-ray photoemission electron microscopy

# List of Figures

List of Tables

Appendix

Figure App. 1 The signature of X-ray absorption spectra of different water phases. Ice phase grown on BaF_2 at 144 K (black), liquid phase at 299 K (blue), and gas phase (red). Reproduced with permission from Ref. [164].
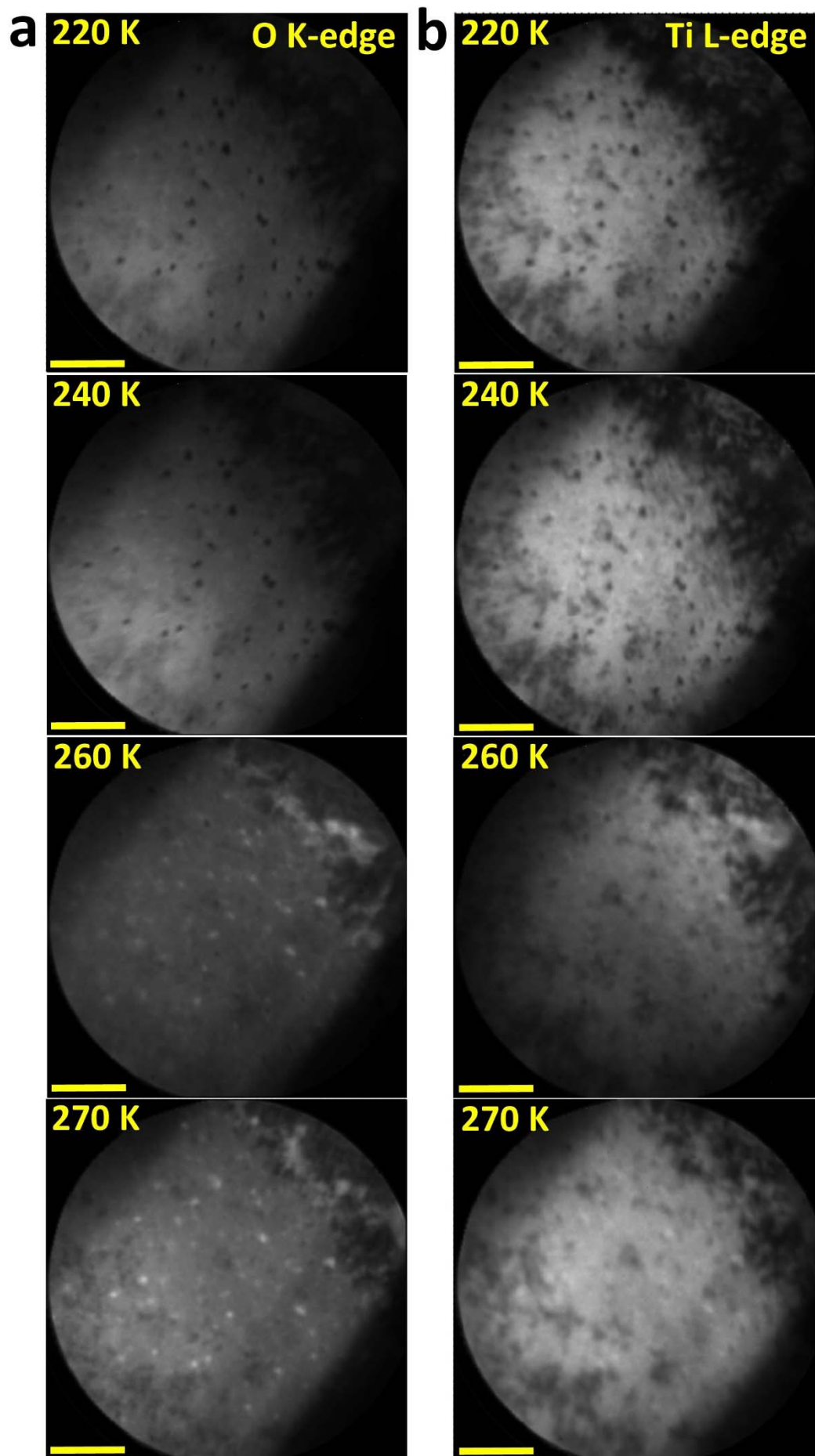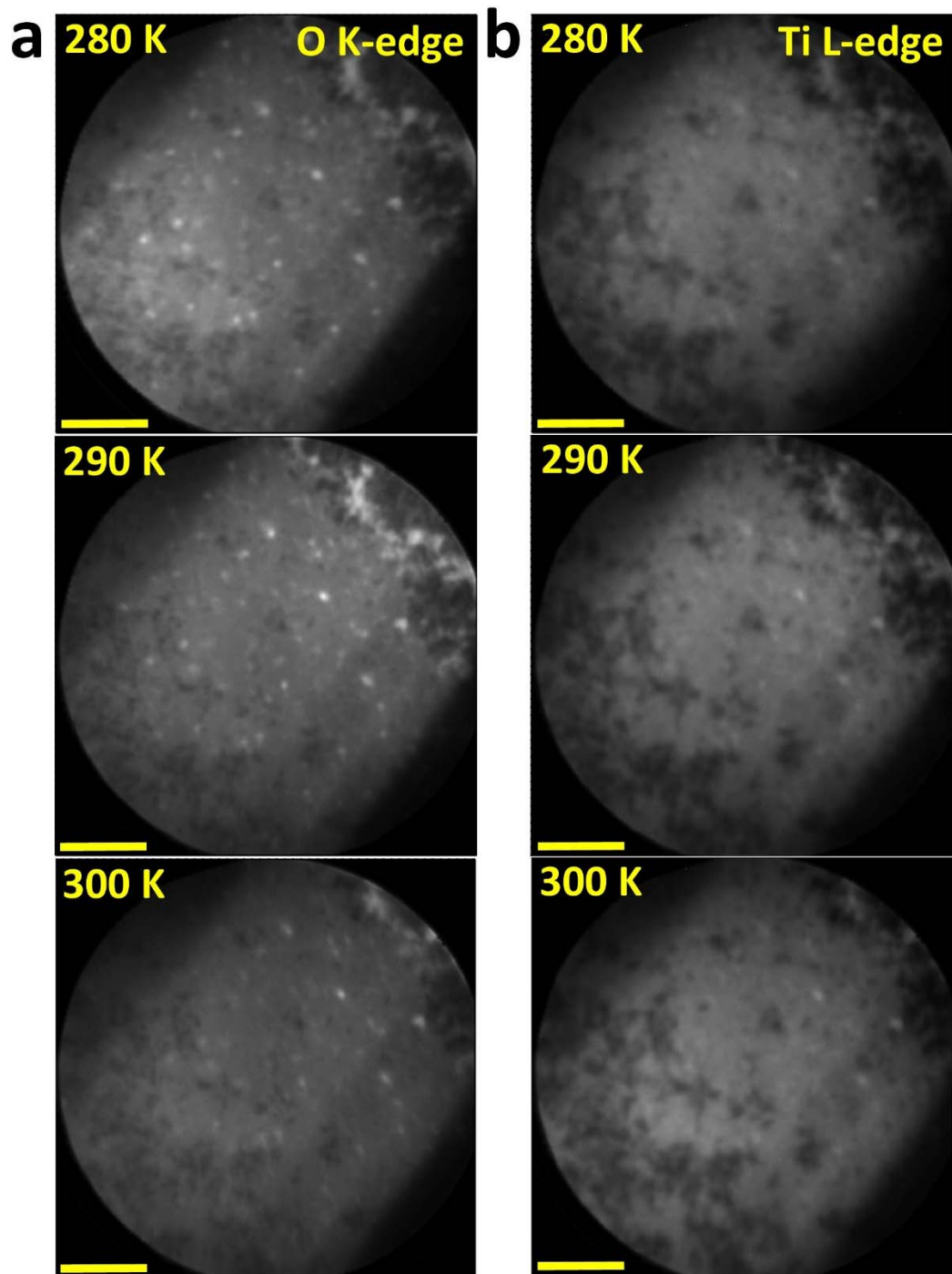
Figure App. 2 XPEEM micrographs of spin-coated Ti$_3$C$_2$T$_x$ MXene film measured at temperatures of 220 K, 240 K, 260 K, 270 K, 280 K, 290 K, and 300 K (page 142 and 143), mapping MXene sample area of about 500 μm^2. (a) The O K-edge and (b) Ti L-edge images taken at an excitation energy of 536.8 eV and 462.8 eV, respectively. Scale bar shown in XPEEM micrographs is 5 μm.
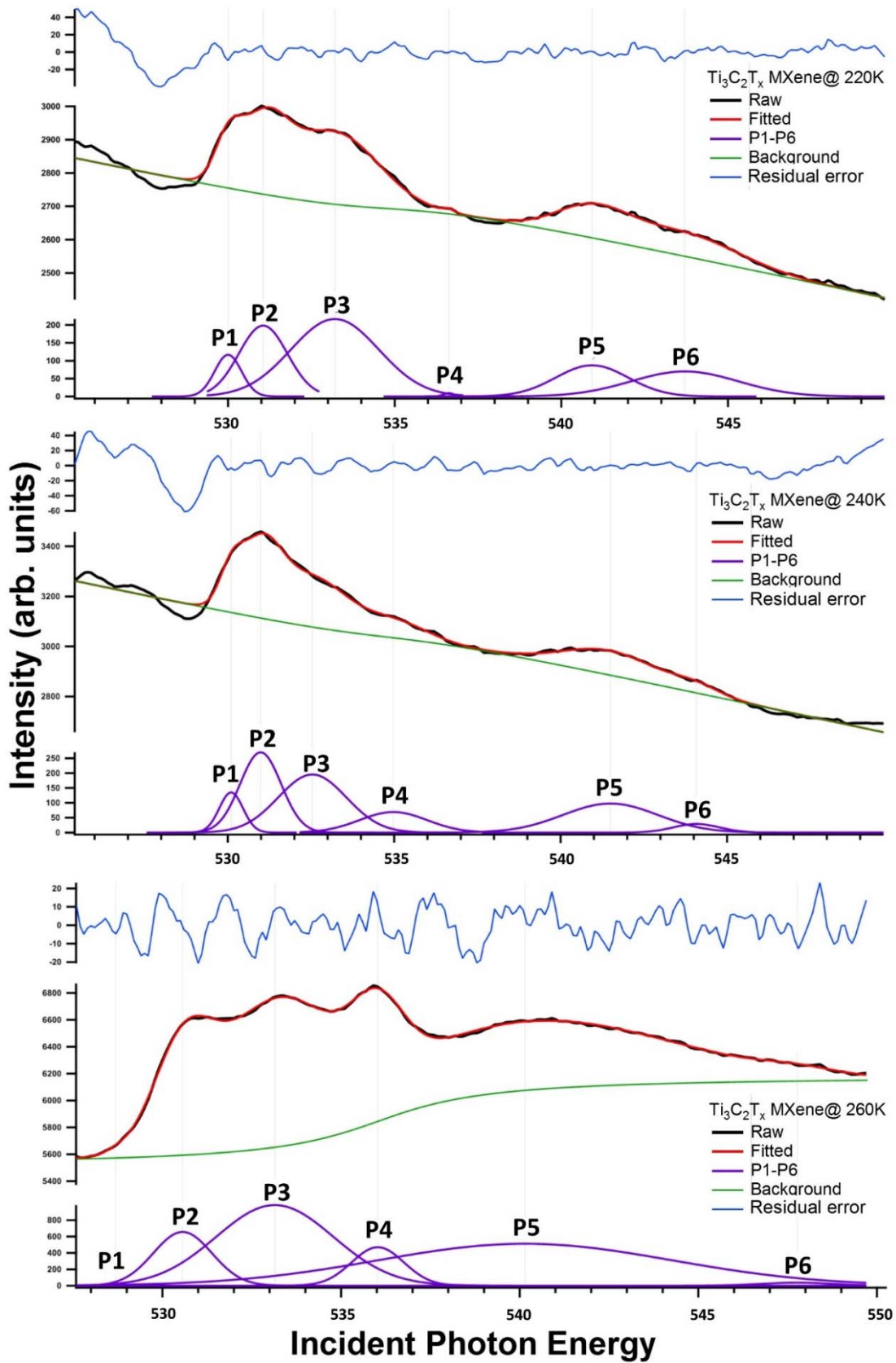
Figure App. 3 (set one) XA peak fitting of measurements recorded at 220 K, 240 K, and 260 K to highlight all possible peaks within the O K-edge energy range.

Figure App. 3 (set two) XA peak fitting of measurements recorded at 270 K, 280 K, and 290 K to highlight all possible peaks within the O K-edge energy range.

Figure App. 3 (set three) XA peak fitting of measurements recorded at 300 K, 575 K, and 773 K to highlight all possible peaks within the O K-edge energy range.
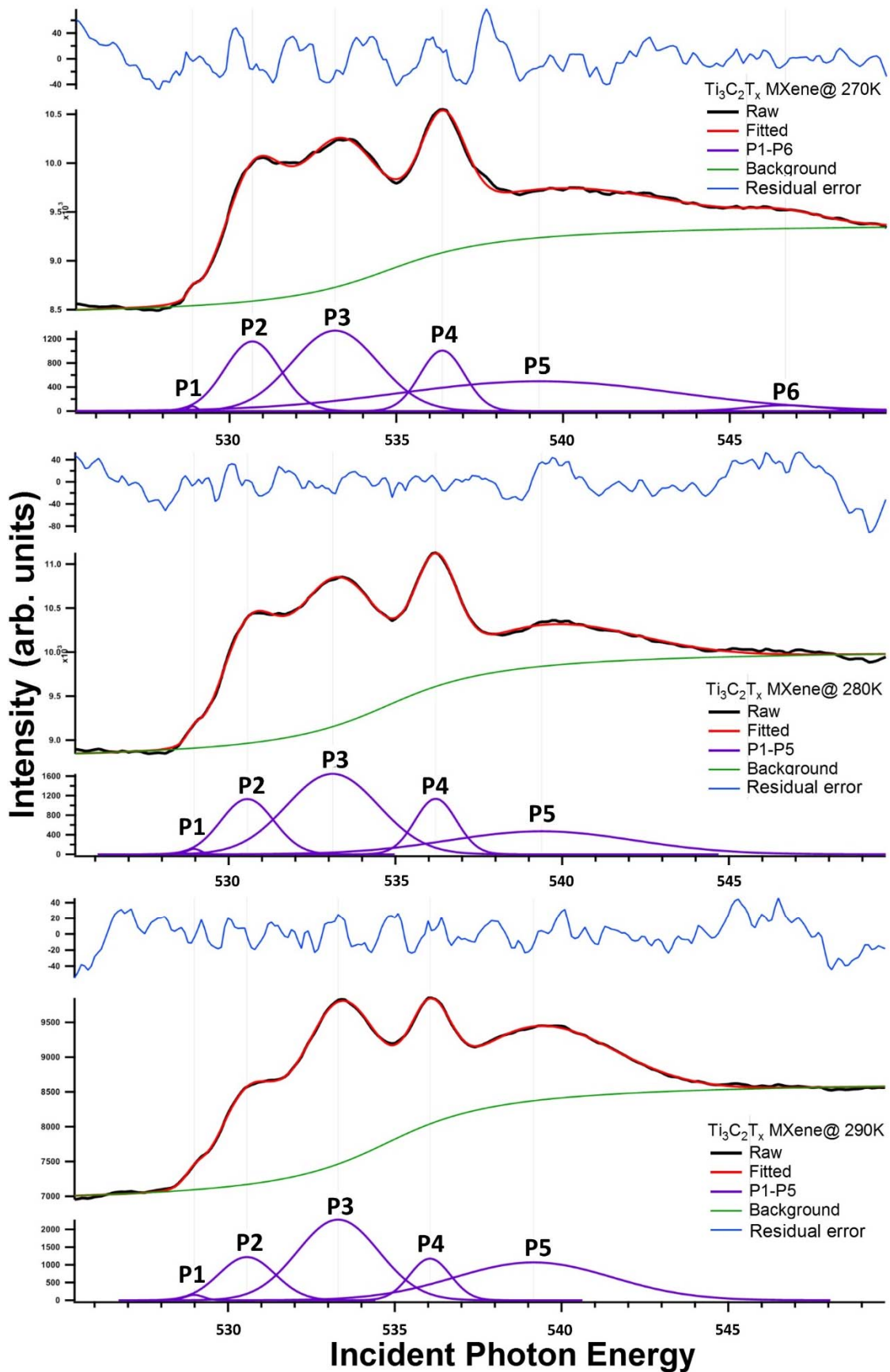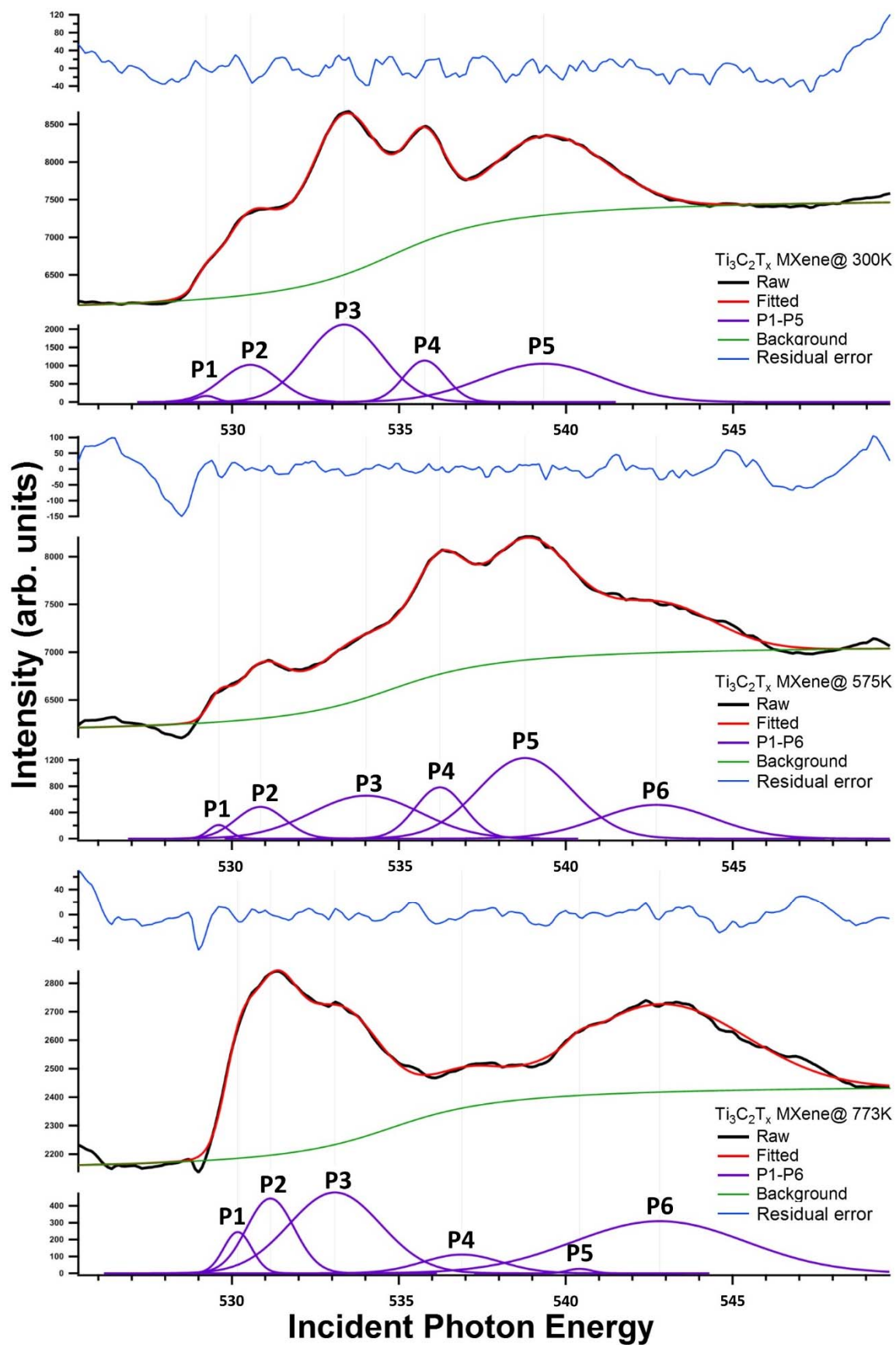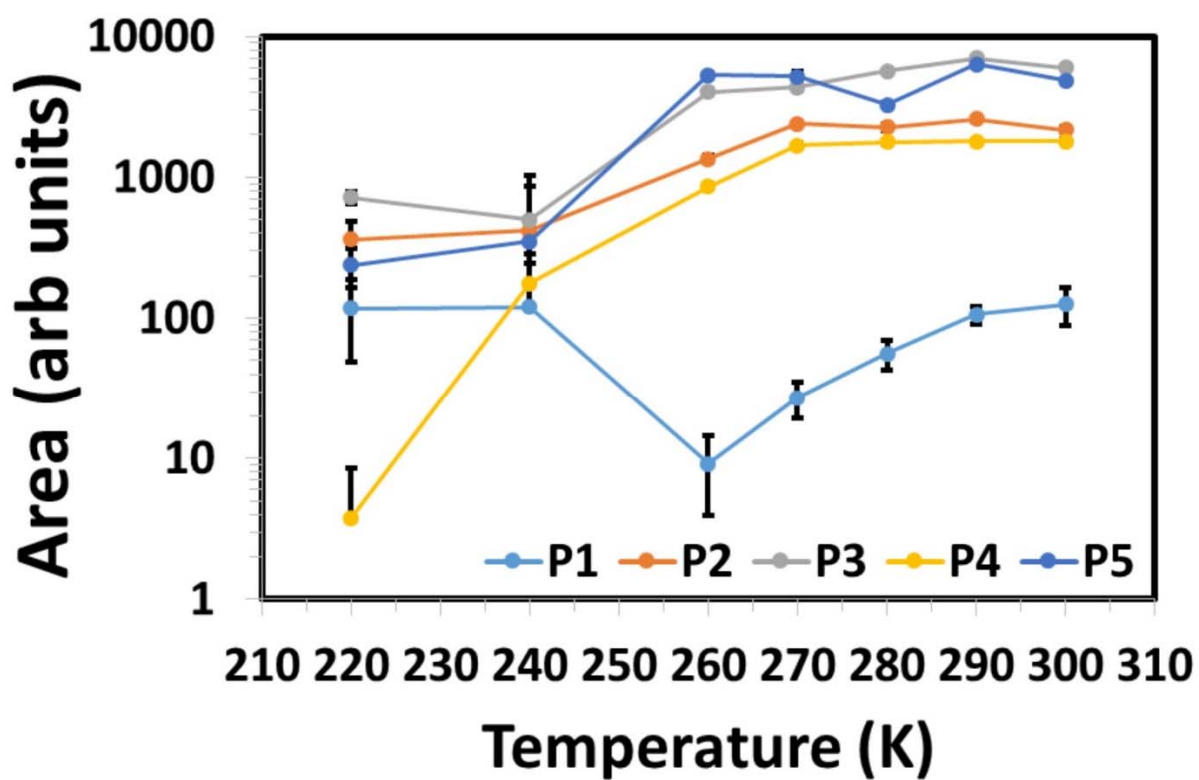
Figure App. 4 XPEEM micrographs of spin-coated Ti$_3$C$_2$T$_x$ MXene film measured at temperatures of 220 K, 240 K, 260 K, 270 K, 280 K, 290 K, and 300 K (page 142 and 143), mapping MXene sample area of about 500 µm^2. (a) The O K-edge and (b) Ti L-edge images taken at an excitation energy
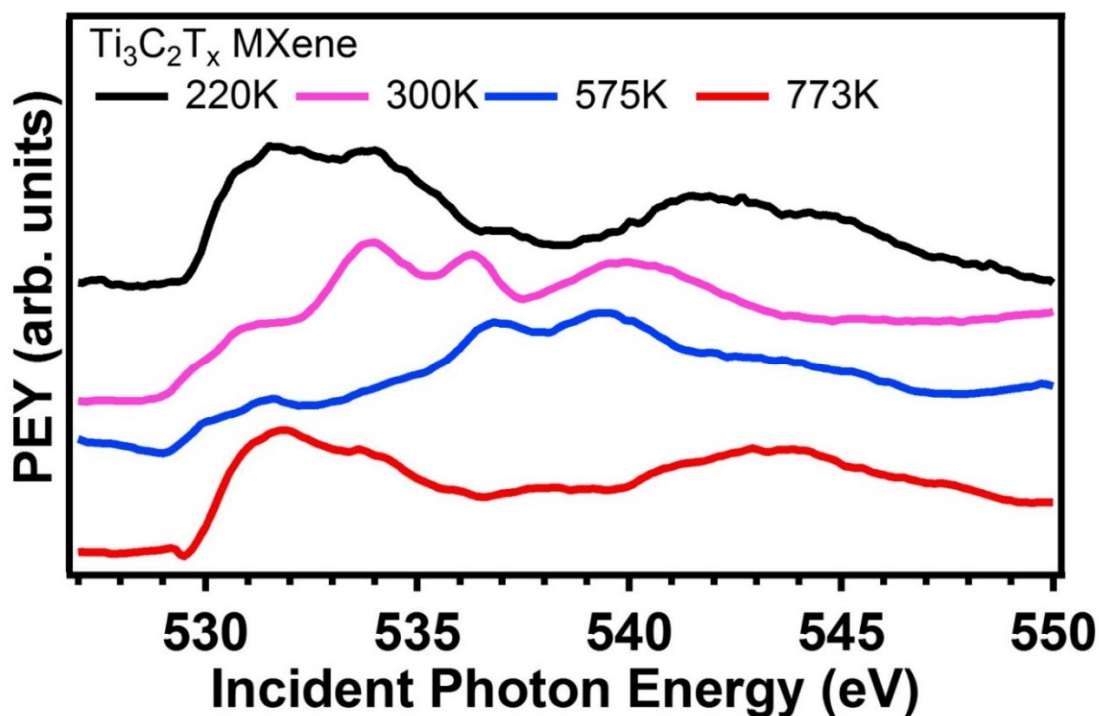
Figure App 5 O K-edge XA spectra of $Ti_3C_2T_x$ MXene measured at high temperatures of 575 K and 773 K compared to those measured at 220 K and 300 K to highlight the impact of the de-intercalation of nanoconfined water. The XAS data was recorded in PEY mode and the XA spectra are normalized to the PEY signal above 545 eV.

Table App. 1

	XAS fitting data at high temperatures							
	575 K				**773 K**			
#	Position	FWHM	Area	Rel. Area	Position	FWHM	Area	Rel. Area
P1	530.1 ± 0.05	0.7 ± 0.1	163.5 ± 59.3	0.01	530.6 ± 0.05	1.0 ± 0.1	258.7 ± 129.5	0.05
P2	531.3 ± 0.1	1.7 ± 0.2	886.1 ± 214.5	0.1	531.6 ± 0.1	1.6 ± 0.3	791.7 ± 293.0	0.1
P3	534.5 ± 0.2	3.8 ± 0.8	2673.1 ± 618.0	0.2	533.6 ± 0.1	3.2 ± 0.3	1646.5 ± 238.0	0.3
P4	536.7 ± 0.0	1.7 ± 0.1	1448.2 ± 376.3	0.1	537.4 ± 0.2	2.7 ± 0.3	325.5 ± 60.1	0.06
P5	539.3 ± 0.1	3.3 ± 0.2	4329.8 ± 289.8	0.3	540.9 ± 0.1	0.8 ± 0.3	23.6 ± 13.3	0.004
P6	543.2 ± 0.1	4.0 ± 0.2	2203.5 ± 211.0	0.2	543.3 ± 0.1	6.0 ± 0.2	2002.8 ± 96.5	0.4

Table App. 2

#	Ti₃C₂Tₓ MXene@220 K, 9.5 mbar				Ti₃C₂Tₓ MXene@220 K, 256 mbar				Si ref.@220 K, 256 mbar			
	2θ	FWHM	Area	Rel. A	2θ	FWHM	Area	Rel. A	2θ	FWHM	Area	Rel. A
P1	22.7 ±0.0	0.06 ±0.0	0.2 ±0.02	0.1	22.7 ±0.0	0.04 ±0.0	2.9 ±0.1	0.2	22.7 ±0.0	0.03 ±0.0	2.3 ±0.1	0.4
P2	24.2 ±0.0	0.05 ±0.0	1.2 ±0.02	0.8	24.2 ±0.0	0.03 ±0.0	6.5 ±0.1	0.6	24.2 ±0.0	0.03 ±0.0	2.6 ±0.1	0.4
P3	25.8 ±0.0	0.04 ±0.0	0.07 ±0.02	0.04	25.8 ±0.0	0.04 ±0.0	1.8 ±0.1	0.2	25.8 ±0.0	0.02 ±0.0	0.7 ±0.1	0.1

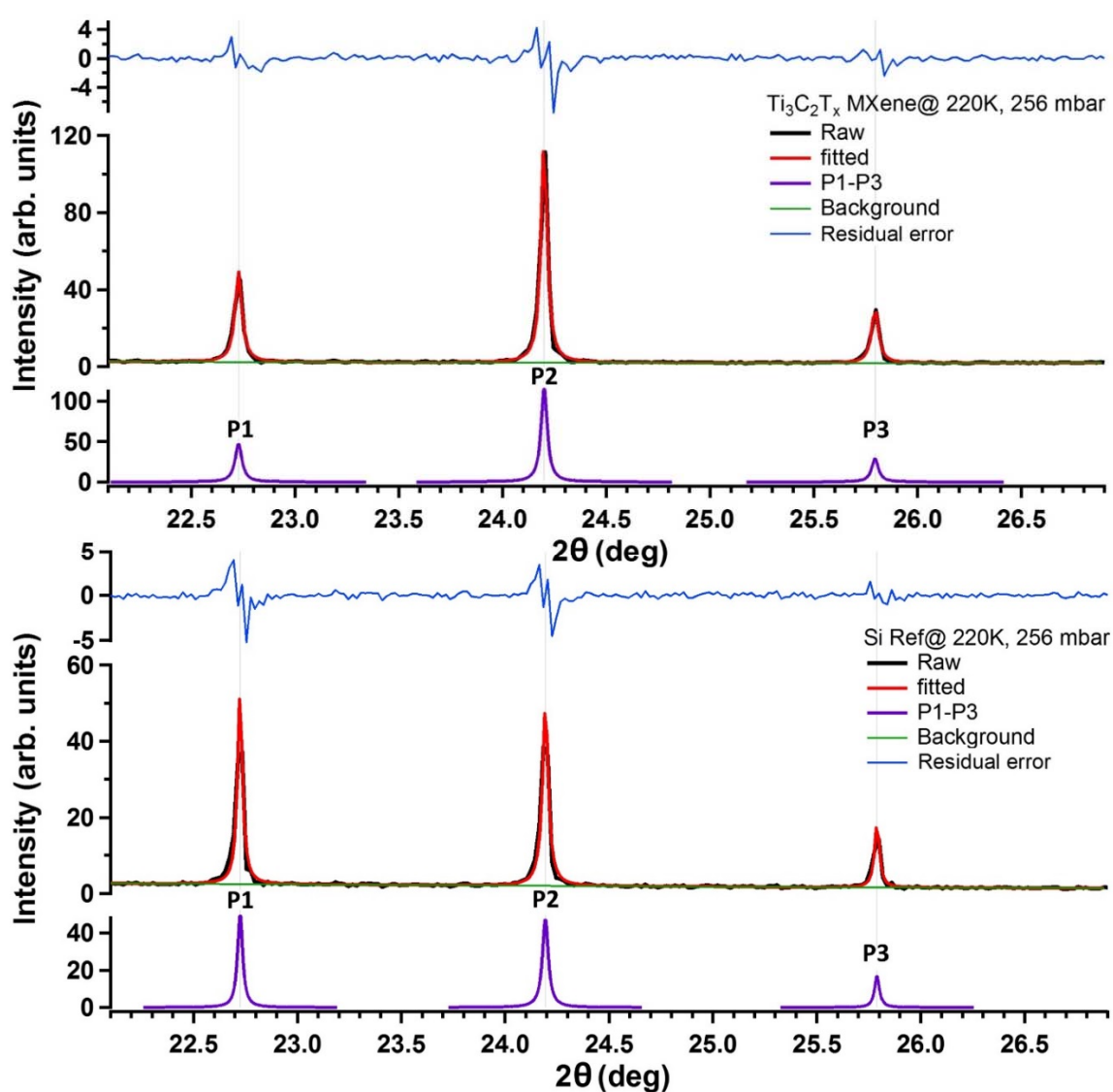**Figure App. 6** Peak fitting data of Ti₃C₂Tₓ MXene and Si reference measured at temperature and pressure conditions of 220 K and 256 mbar, respectively, showing the raw and fitted peaks together with the background and the residual error spectra.

Possible interpretation of P1 and P2

The P1 positon of 530.5 eV can be attributed to the t_{2g} peak. However, P1 was found to be shifted by about -1.0 eV to lower energies at T ≥ 260 K which resembles the shift in oxide species of higher Ti oxidation state [63]. If this large shift at T ≥ 260 K is indeed related to the t_{2g} peak, then P1 should remain well pronounced. Since P1 area becomes less intense at T ≥ 260 K, the shift of about -1.0 eV cannot be assigned to the t_{2g} peak. Therefore, t_{2g} peak is probably turned into a shoulder-like rather than a resolved peak owing to that the area of other peaks become significantly larger relative to P1 area at T ≥ 260 K, see **Table 6.1**.

Since P2 is located at 531.5 eV below 260 K, P2 cannot be linked to the signature of e_g peak which is kown to be found above 532.5 eV [72–74], as discussed in sections 4.4 and 5.4. Also, the peak fitting shows that the position of P2 is separated by about +1.0 eV compared to P1 which refutes the link to e_g peak signature [63,78] and hence may indicate a relation to Li–O bond signature [73], see **Figure 4.4**. Likewise, the significant shift of P1 below 529.5 eV may suggest a signature of Li oxide species [165]. As discussed in section 2.5.3, Li oxide residual species may have originated from the synthesis procedure of this MXene sample.

Selbstständigkeitserklärung

Name: Al-Temimy
Vorname: Ameer

Ich erkläre gegenüber der Freien Universität Berlin, dass ich die vorliegende Dissertation selbstständig und ohne Benutzung anderer als der angegebenen Quellen und Hilfsmittel angefertigt habe. Die vorliegende Arbeit ist frei von Plagiaten. Alle Ausführungen, die wörtlich oder inhaltlich aus anderen Schriften entnommen sind, habe ich als solche kenntlich gemacht. Diese Dissertation wurde in gleicher oder ähnlicher Form noch in keinem früheren Promotionsverfahren eingereicht.

Mit einer Prüfung meiner Arbeit durch ein Plagiatsprüfungsprogramm erkläre ich mich einverstanden.

Datum: 12.09.2023 Unterschrift: _____Ameer Al-Temimy_____

· ·

Declaration of authorship

Name: Al-Temimy
First name: Ameer

I declare to the Freie Universität Berlin that I have completed the submitted dissertation independently and without the use of sources and aids other than those indicated. The present thesis is free of plagiarism. I have marked as such all statements that are taken literally or in content from other writings. This dissertation has not been submitted in the same or similar form in any previous doctoral procedure.

I agree to have my thesis examined by a plagiarism examination software.

Date: 12.09.2023 Signature: _____Ameer Al-Temimy_____